MASARYK UNIVERSITY
Faculty of Science
Department of Theoretical Physics and Astrophysics

HABILITATION

From supermassive black holes to the large-scale structure of the Universe

Norbert Werner

2016

Abstract:

The Lambda Cold Dark Matter (ΛCDM) model has been shown to be remarkably successful in describing many aspects of our Universe, which is dominated by dark energy and dark matter. However, the physical processes associated with the evolution of the baryonic matter are complex and still poorly understood. In the course of structure formation, only a small fraction of the baryons turned into stars - most remain in a diffuse intergalactic medium (IGM). The growth of galaxies is regulated by feedback processes, such as energy and momentum input from supernovae, and jets and winds of accreting supermassive black holes. These processes, collectively called galactic feedback, can limit further gravitational collapse, and thus a detailed knowledge of how they work is essential for our understanding of galaxy formation and evolution. Here I present my study of the intimate connection between the IGM, star formation and the growth of supermassive black holes in the most massive galaxies.

Keywords: clusters of galaxies, giant elliptical galaxies, large-scale structure, intergalactic medium, active galactic nuclei, chemical enrichment, feedback, supernovae, cosmology, X-ray astronomy

Contents

Chapter 1

Introduction

The Lambda Cold Dark Matter (ΛCDM) model has been shown to be remarkably successful in describing many aspects of our Universe, which is dominated by dark energy and dark matter. However, the physical processes associated with the evolution of the baryonic matter are complex and still poorly understood. In the course of structure formation, only a small fraction of the baryons turned into stars - most remain in a diffuse intergalactic medium (IGM). My research focuses on the intimate connection between the IGM, star formation and the growth of supermassive black holes in the most massive galaxies.

The growth of galaxies is regulated by feedback processes, such as energy and momentum input from supernovae, and jets and winds of accreting supermassive black holes, also called active galactic nuclei (AGN). This galactic feedback stops the inward flow of gas onto galaxies, heats the interstellar medium, preventing it from cooling and forming further stars, and ejects baryons back into the surrounding IGM, most of which is relatively hot in the low redshift Universe. These processes can limit further gravitational collapse, and thus a detailed knowledge of how they work is essential for our understanding of galaxy formation and evolution. I study the stellar and AGN feedback using data across a wide range of wavelengths, including the radio, infrared, optical, ultraviolet, and with a particular emphasis on the X-ray band.

The IGM has very low densities and therefore it is mostly difficult to observe. However, in the gravitational potentials of giant elliptical galaxies, groups and clusters of galaxies, the density and temperature of the IGM becomes high enough to emit observable X-ray radiation. This hot IGM, that in galaxy clusters is called the intra-cluster medium (ICM), has temperatures of $T_{\rm e} \sim 5^6$–10^8 K (0.5–10 keV) and densities declining from $n \sim 10^{-2}$ cm^{-3} near the cluster centers to 10^{-4} cm^{-3} in the outskirts. It consists of completely ionized hydrogen and helium, with highly ionized heavier elements of roughly the Solar abundance in the centre, decreasing to about one third of the Solar metallicity in the outskirts. Most of its observed continuum emission is due to the interaction of electrons and ions, which leads to the bremsstrahlung emission of X-ray photons. De-excitation of the ions of heavier elements, leading to transitions to the K- and L-shells, may result in observable line emission in the X-ray band. The ICM is in a collisional ionization equilibrium, where the ionization and recombination rates are entirely determined by collisions, and is optically thin (the radiation fields in clusters

do not affect its ionization state). The shape of observed X-ray spectra is therefore completely determined by the ICM temperature and metallicity. The normalization of the observed spectrum is proportional to the emission measure $EM = \int n_{\rm p}\, n_{\rm e}\, {\rm d}V$, where $n_{\rm p}$ and $n_{\rm e}$ are the proton and electron number densities and V is the volume of the emitting region.

The research presented in the enclosed papers is in a large part based on deep observations of galaxy clusters with the US-led *Chandra* X-ray observatory, European-led *XMM-Newton* satellite, and the Japan-led *Suzaku* mission, using X-ray spectroscopy as the main tool to asses the physical properties of the hot plasma. I also present work based on radio data from the Giant Metrewave Radio Telescope (GMRT) and the Jansky Very Large Array (VLA), far-infrared data obtained by the *Herschel* Space Observatory, and optical data from various facilities including the SOAR telescope and the *Hubble Space Telescope*.

Using my expertise in high-resolution X-ray spectroscopy, and a broad experience in both the acquisition and interpretation of multi-wavelength data, I address here the following key questions:

1. How do black holes regulate the growth of structure?

It is now well established that black holes play a vital role in the evolution of their host galaxy. There are two major mechanisms through which AGN can strongly affect their surrounding environment: one is radiative AGN feedback, where the radiation from vigorously accreting black holes couples with the cold gas in the host galaxy; the other is the so-called radio-mechanical feedback, where jets from AGN accreting at a modest rate heat or push the gas out.

Here, I discuss the radio-mechanical feedback mode, which is thought to dominate the evolution of massive galaxies over the past 10 billion years. In the absence of heating, the hot ($\sim 10^7$ K) X-ray emitting haloes surrounding giant elliptical galaxies (either haloes of their own, or because they are part of a group or cluster of galaxies) would cool radiatively and form stars, building much larger galaxies than are seen. However, X-ray studies with *Chandra* and *XMM-Newton* have shown that the expanding, AGN jet inflated, bubbles filled by relativistic plasma (seen as 'radio lobes' by radio telescopes) displace the hot gas, creating cavities in the X-ray emitting plasma (e.g. McNamara et al. 2005, see the left panel of Fig. 1) and drive weak shocks that heat the surrounding medium isotropically, preventing it from cooling.

In the first and second enclosed paper (Chapter 2 and 3), we show that in their wakes, the rising bubbles filled by relativistic plasma uplift low entropy gas from the innermost regions of their host galaxies mixing it with the ambient hot medium. The total gas mass uplifted by the buoyantly rising relativistic plasma in M 87 is $\sim$ 6–9×10^9 $M_\odot$ (see the right panel of Fig. 1), which shows that the AGN is capable to strip the galaxy of its lowest entropy gas, preventing star-formation (see Chapter 2 for details). On the other hand, in Chapter 3 we show that the uplift and displacement of the low entropy gas from the direct vicinity of the central AGN can temporarily break

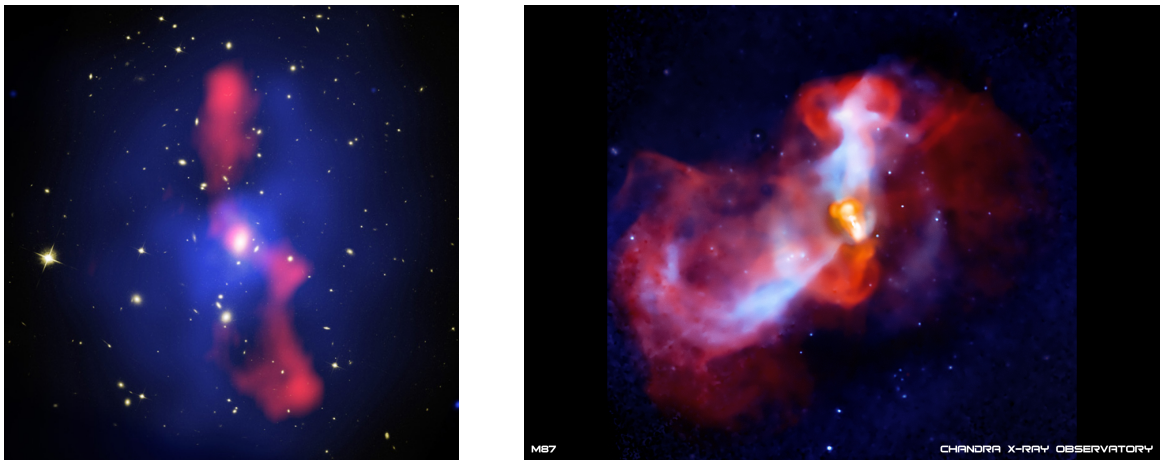

Figure 1.1: *Left panel:* Composite optical, X-ray (blue), radio (red) image of the galaxy cluster MS0735.6+7421. X-ray observations with *Chandra* have shown that jets from the central AGN inflate bubbles filled by relativistic, radio-emitting plasma that displace the hot gas, creating cavities in the X-ray images of galaxy clusters (McNamara et al. 2005). *Right panel:* In its wake, the buoyantly rising relativistic, radio-emitting plasma injected by the AGN jets, uplifts large amounts of low entropy X-ray emitting gas (shown in white), preventing it from cooling and forming stars. (From our press release by the Chandra X-ray Center)

the feedback cycle and lead to cooling without triggering an AGN feedback response and resulting in star formation that is offset from the center of the galaxy. The observed unchecked cooling where a black hole is offset from the cooling gas solidifies the idea that AGN play a key role in maintaining the cooling/heating balance in cluster cores.

Radio-mechanical AGN feedback appears to maintain a long-lived delicate balance between heating and cooling in the hot X-ray emitting atmospheres of massive galaxies, groups, and clusters of galaxies. However, there is very little consensus on how this balance is maintained and how cooled or cooling gas fuels the AGN. To create a feedback loop, the thermal state of the hot atmosphere must influence the power output of the AGN. A particularly important outstanding question, addressed by my research, is therefore: How does AGN feedback operate across spatial scales of over 8 orders of magnitude - from the immediate vicinity of the black hole to a scale of several hundreds of kpc in clusters of galaxies? The feedback loop is maintained most naturally if the supermassive black hole is fueled by gas from the hot atmosphere at a rate that depends on the thermal state of the gas. The remarkable similarity of the hot X-ray emitting atmospheres surrounding some of the nearest brightest giant elliptical galaxies (see the enclosed paper in Chapter 4) is consistent with a picture of hot accretion leading to jet heating, which creates an energy balance where heating and cooling are in equilibrium, keeping the hot galactic atmospheres in a steady state.

As these jet inflated bubbles expand and rise buoyantly in the hot plasma, they drive gas motions, including turbulence. A critical, missing piece in our picture of AGN feedback have been observational measurements of gas motions, because the spectral

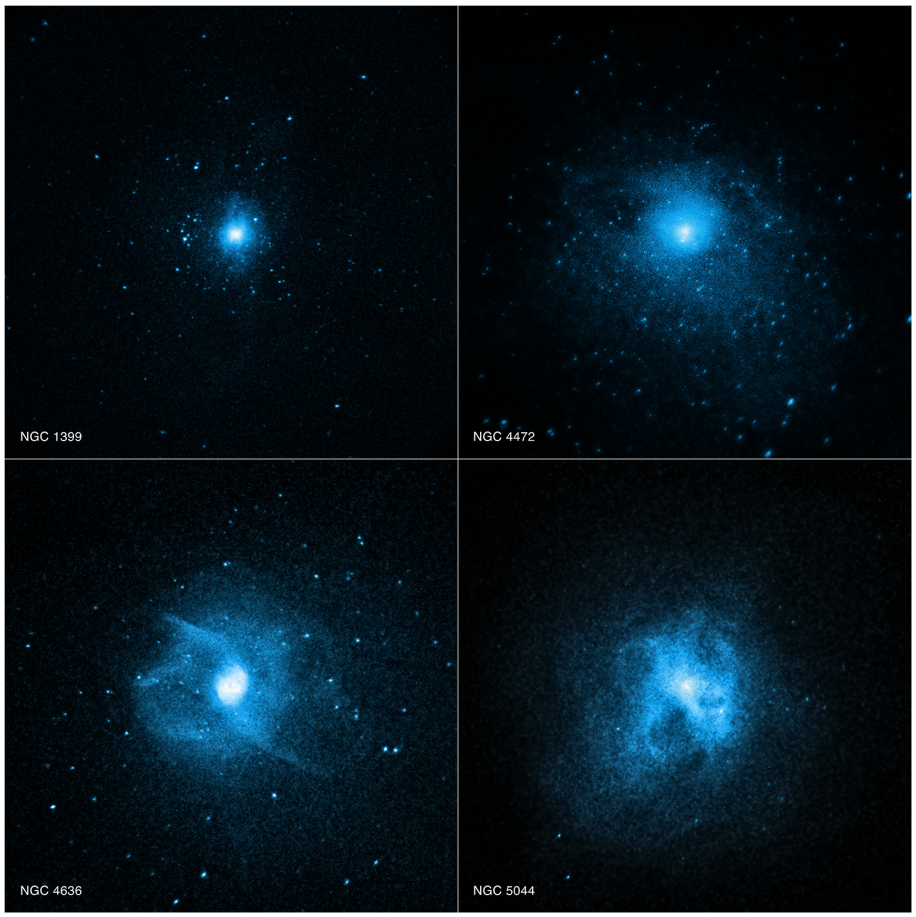

Figure 1.2: The X-ray emitting hot plasma in the centers of galaxies where our *Herschel* observations revealed cold gas (including NGC 4636 and NGC 5044) appears to be much more disturbed than in the cold gas-free systems (such as NGC 4472 and NGC 1399). This is a sign that outbursts from the central black hole have occurred, possibly driven, in part, by clumpy, cold gas that has been pulled onto the black hole. These outbursts dump most of their energy into the center of the galaxy, where the cold gas is located. By stirring and partially destroying the cold gas, this energy deposition may prevent the cold gas from cooling sufficiently to form stars. (From our press release by the Chandra X-ray Center)

resolution of the CCD-type detectors used on the *XMM-Newton*, *Chandra*, and *Suzaku* satellites is insufficient to measure the velocity broadening of spectral lines. The intensity of some spectral lines in the X-ray bright cores of elliptical galaxies, groups and clusters of galaxies is suppressed by resonance scattering (line photons get absorbed and quickly re-emitted in a different direction). Since the optical depth of a resonance line depends on the characteristic velocity of small-scale motions, its measurement allows us to determine turbulence independently of line broadening (Gilfanov et al. 1987). In the fourth enclosed paper (Chapter 5), we developed a new technique where we measure the resonance scattering of X-ray spectral lines observed with the reflection grating spectrometers on the *XMM-Newton* satellite to determine the AGN induced turbulence in the hot plasma surrounding giant elliptical galaxies. This powerful technique provided the first observational constraints on velocities in the hot plasma in these systems. Turbulence in the ICM continues to be of major interest for the understanding of the evolution of galaxy clusters. Recently, we found strong indications that turbulent heat dissipation may be of crucial importance for the heating of the ICM (Zhuravleva et al. 2014a).

A missing key ingredient in our models is the lack of knowledge of the microphysical properties of the hot IGM/ICM, which determine its thermal conductivity and viscosity. This limits our understanding of how the energy from accreting black holes couples with the hot diffuse ICM - e.g. how do gas motions driven by the rising bubbles dissipate into heat and how is the heat distributed across the ICM. The hot ICM is permeated by weak, tangled magnetic fields and as such its microphysics remains untreatable in a purely theoretical way. New observational constraints are essential if we are to make progress. The spectacular, sub-arcsecond imaging capabilities of the *Chandra* X-ray Observatory will remain unsurpassed for at least the next 20 years, and ultra-deep observations with this instrument still provide opportunities for breakthroughs in our understanding of the microphysics of the hot plasma. In the enclosed paper presented in Chapter 6, I present a deep, 500 ks, legacy-class *Chandra* observation of the nearest, best resolved cold front in the sky, which lies 90 kpc to the north of M87. Cold fronts are believed to be due to the sloshing (or swirling) of the gas in the gravitational potential of clusters and they are known to be remarkably sharp, with gas density and temperature discontinuities at least several times sharper than the Coulomb mean free path. Because this observation provided an extraordinary improvement in resolution, resolving scales smaller than 80 pc, it allowed us to place crucial constraints on fundamental physical processes shaping cold fronts, such as: growth of hydrodynamic instabilities in the ICM (placing constraints on viscosity), suppression of thermal conductivity, and structure of intra-cluster magnetic fields. The observation of the Ophiuchus cluster described in Chapter 7 indicates that thermal conduction in the hot ICM is not suppressed completely. The data also show evidence for both Rayleigh-Taylor and Kelvin-Helmholtz instabilities, implying relatively low ICM viscosity. These observations provide important constraints for the models of the evolution of baryons in cosmological simulations.

However, many central group/cluster galaxies are also surrounded by spectacular, filamentary nebulae containing large amounts of cold and ionized gas. Because of the presence of many different gas and plasma phases in these systems, the use of multi-

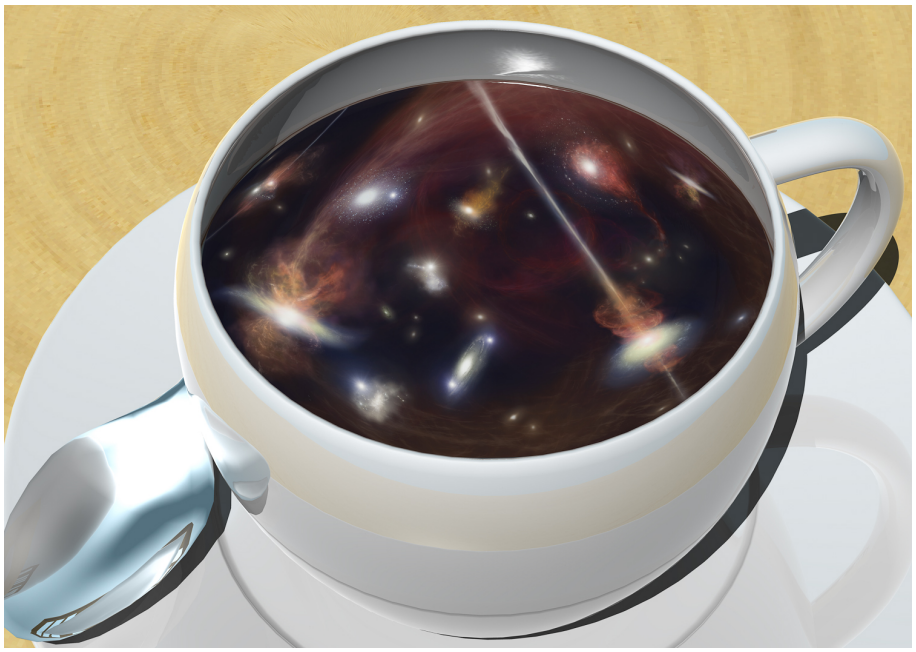

Figure 1.3: The combined energy of supernova explosions and accreting supermassive black holes at redshifts 2–4 (before the period of cluster formation) must have been strong enough to expel most of the metals from the galaxies at early times, and enrich and mix the intergalactic gas. Exploding supernovae and accreting black holes were the spoon that mixed the metals into the intergalactic medium. (From our JAXA press release)

wavelength data is crucial, if we wish to understand how heating and cooling operate throughout the putative AGN feedback loop. The enclosed papers in Chapters 8 and 9 report the results of our multi-wavelength survey of some of the nearest brightest giant elliptical galaxies using far-infrared spectral imaging with *Herschel* PACS, optical narrow band imaging and spectroscopy with the SOAR telescope, and X-ray spectral imaging with *Chandra*. We find a dichotomy, where some of the systems are cold-gas-free and others harbor relatively large quantities of cold gas which is produced chiefly by thermally unstable cooling from the hot phase (see Fig. 2). The jets in these systems appear to couple efficiently to the cold gas phases and our observations indicate that radio-mechanical AGN feedback is likely to play a crucial role in clearing giant elliptical galaxies of their cold gas, keeping them red and dead. Intriguingly, our analysis also revealed indications for an anti-correlation between jet power and cold molecular gas content, favoring hot accretion models.

2. How did the star formation and chemical enrichment of the Universe proceed?

Supernovae inject large amounts of energy into the surrounding medium and enrich it with heavy elements (collectively called metals). The deep gravitational potential wells of galaxy clusters keep all of the metals ever produced by the stellar populations

of the member galaxies, making them archeological treasure troves to study the integrated history of star-formation. The dominant fraction of metals in clusters currently resides within the hot X-ray emitting IGM (for a review see Werner et al. 2008).

Most of the chemical elements with prominent line emission in the X-ray band, from O up to Ni, are produced by supernovae. The observed equivalent widths of the emission lines can be directly converted into elemental abundances. While core-collapse supernovae produce large amounts of O, Ne, and Mg, Type Ia supernovae produce large quantities of Fe, Ni, and Si-group elements, but very little O, Ne, and Mg.

Our groundbreaking studies of the outskirts of galaxy clusters (see Simionescu et al. 2011, 2013, 2015; Urban et al. 2011, 2014; Werner et al. 2013) have allowed us to measure the ICM metallicity out to the virial radii of the Perseus and Virgo clusters. These observations provide important hints that activity of accreting supermassive black holes also played an important role in the distant past. In the enclosed paper in Chapter 10, we show that the measured iron abundance has about a third of the Solar value and its distribution is remarkably uniform both as a function of radius and azimuth out to the cluster outskirts. This homogeneous distribution requires that most of the metal enrichment of the intergalactic medium occurred before clusters formed, probably more than ten billion years ago, during the period of maximal star formation and black hole activity. The combined energy of supernova explosions and AGN must have been strong enough to expel most of the metals from the galaxies at early times, and enrich and mix the intergalactic gas. This gas was later accreted by clusters and virialized (increasing its entropy through shock heating) to form the present ICM. Observations of the Virgo Cluster, that also allow us to measure the abundances of Si, S, and Mg out to the outskirts (Simionescu et al. 2015), show that the chemical composition of the intra-cluster medium is constant on large scales and is generally consistent with that of our own Galaxy.

Chapter 2

Feedback under the microscope: heating, gas uplift, and mixing in the nearest cluster core

N. Werner[1], *A. Simionescu*[1], *E. T. Million*[1], *S. W. Allen*[1], *P. E. J. Nulsen*[2], *A. von der Linden*[1], *S. M. Hansen*[3], *H. Böhringer*[4], *E. Churazov*[5,6], *A. C. Fabian*[7], *W. R. Forman*[2], *C. Jones*[2], *J. S. Sanders*[7], *and G. B. Taylor*[8]

[1]Kavli Institute for Particle Astrophysics and Cosmology, Stanford University, 382 Via Pueblo Mall, Stanford, CA 94305-4060, USA
and SLAC National Accelerator Laboratory, 2575 Sand Hill Road, Menlo Park, CA 94025, USA
[2]Harvard-Smithsonian Center for Astrophysics, 60 Garden St., Cambridge, MA 02138, USA
[3]University of California Observatories & Department of Astronomy, University of California, Santa Cruz, CA 95064, USA
[4]Max-Planck-Institut für extraterrestrische Physik, Giessenbachstr, 85748 Garching, Germany
[5]Max-Planck-Institut für Astrophysik, Karl-Schwarzschild-Strasse 1, 85741 Garching, Germany
[6]Space Research Institute (IKI), Profsoyznaya 84/32, Moscow 117810, Russia
[7]Institute of Astronomy, Madingley Road, Cambridge CB3 0HA
[8]Department of Physics and Astronomy, University of New Mexico, Albuquerque, NM 87131, USA

Published in the Monthly Notices of the Royal Astronomical Society, volume 407, pages 2063–2074, 2010

Abstract

Using a combination of deep (574 ks) *Chandra* data, *XMM-Newton* high-resolution spectra, and optical Hα+[N II] images, we study the nature and spatial distribution of the multiphase plasma in M 87. Our results provide direct observational evidence of 'radio mode' AGN feedback in action, stripping the central galaxy of its lowest entropy gas and therefore preventing star-formation. This low entropy gas was entrained with and uplifted by the buoyantly rising relativistic plasma, forming long "arms". A number of arguments suggest that these arms are oriented within 15°–30° of our line-of-sight. The mass of the uplifted gas in the arms is comparable to the gas mass in the approximately spherically symmetric 3.8 kpc core, demonstrating that the AGN has a profound effect on its immediate surroundings. The coolest X-ray emitting gas in M 87 has a temperature of $\sim$0.5 keV and is spatially coincident with Hα+[N II] nebulae, forming a multiphase medium where the cooler gas phases are arranged in magnetized filaments. We place strong upper limits of 0.06 $M_{\odot}$/yr (at 95 per cent confidence) on the amount of plasma cooling radiatively from 0.5 to 0.25 keV and show that a uniform, volume-averaged heating mechanism could not be preventing the cool gas from further cooling. All of the bright Hα filaments in M 87 appear in the downstream region of the $<$ 3 Myr old shock front, at smaller radii than $\sim$0.6′. We suggest that shocks induce shearing around the filaments, thereby promoting mixing of the cold gas with the ambient hot ICM via instabilities. By bringing hot thermal particles into contact with the cool, line-emitting gas, mixing can supply the power and ionizing particles needed to explain the observed optical spectra. Furthermore, mixing of the coolest X-ray emitting plasma with the cold optical line emitting filamentary gas promotes efficient conduction between the two phases, allowing non-radiative cooling which could explain the lack of X-ray gas with temperatures under 0.5 keV.

2.1 Introduction

If the energy radiated away at the centres of so-called "cool-core" clusters of galaxies, which show sharp X-ray surface brightness peaks and central temperature dips, came only from the thermal energy of the hot, diffuse intra-cluster medium (ICM), the ICM would cool and form stars at rates orders of magnitude above what the observations suggest (see Peterson & Fabian 2006, for a review). It is currently believed that the energy which offsets the cooling is provided by the interaction between the active galactic nuclei (AGN) in the central dominant galaxies and the ICM (see Churazov et al. 2000, 2001, 2002; McNamara & Nulsen 2007, for a review). Through a tight feedback loop, it is thought that the AGN can provide enough energy to prevent catastrophic cooling. Recent deep observations of nearby bright cooling core clusters such as Perseus, M 87, Centaurus, and Hydra A revealed AGN induced weak shocks and sound waves with sufficient energy flux to counterbalance the radiative cooling (Sanders & Fabian 2007; Forman et al. 2005; Sanders & Fabian 2008; Nulsen et al. 2005; Simionescu et al. 2009a). To the first order it is thus understood where the energy comes from and how it gets transported. However, the detailed physics of the AGN/ICM interaction is not yet

clear.

M 87, the central dominant galaxy of the Virgo cluster, at a distance of only 16.1 Mpc (Tonry et al. 2001) is the nearest, X-ray bright cool core. It is an ideal system for detailed studies of the energy input from the AGN to the hot, cooling ICM. After the Perseus cluster, M 87 is the second brightest extended extragalactic object in soft X-rays. The most striking X-ray features in M 87 are its two "X-ray arms", first detected by Feigelson et al. (1987) using *Einstein Observatory* data and later studied in detail by Böhringer et al. (1995) using *Rosat* and VLA radio observations. The X-ray arms extend to the East and Southwest from the centre of the galaxy and they spatially correlate with the radio emission. Böhringer et al. (1995) found that the X-ray arms are due to cooler gas, possibly uplifted from the centre of the galaxy. These results and the subsequent high-quality radio data by Owen et al. (2000) led Churazov et al. (2001) to argue that the X-ray and radio morphology can be explained by bubbles of radio-emitting plasma rising buoyantly through the hot ICM. These rising bubbles entrain and uplift cooler gas from the centre of the galaxy, which then further adiabatically cools. Churazov et al. (2001) suggested that the buoyantly rising bubbles dissipate energy into sound waves, internal waves, turbulent motion in the wake, and potential energy of the uplifted gas, all of which could provide heating to the cooling core region (see also e.g. Brüggen & Kaiser 2002; Kaiser 2003; Brüggen 2003; De Young 2003; Ruszkowski et al. 2004a,b; Heinz & Churazov 2005).

Observations with *Chandra* and *XMM-Newton* greatly enhanced our view of M 87. Using *XMM-Newton* observations, Belsole et al. (2001), Matsushita et al. (2002), and Molendi (2002) showed that the regions associated with radio arms have two-temperature (in the ranges of $kT \sim 0.8$–1 keV and $kT \sim 1.6$–2.5 keV) or multi-temperature structure. However, plasma below 0.8 keV is largely absent (Böhringer et al. 2002; Sakelliou et al. 2002). Young et al. (2002) analyzed an early, relatively short (40 ks) *Chandra* observation which showed cavities and edges in the hot plasma. They compared the X-ray morphology with the 6 cm radio (Hines et al. 1989) and Hα+[N II] emission (Sparks et al. 1993) and showed that the optical filaments lie outside of X-ray cavities filled with radio plasma; some are along the edges of the cavities, and several optical filaments coincide with knots of cooler X-ray gas. Using a longer ($\sim$150 ks) *Chandra* observation, Sparks et al. (2004) studied the relation of the X-ray and optical filaments and concluded that electron conduction from the hot X-ray emitting plasma to the cooler phase provides a quantitatively acceptable energy source for the optical filaments. Using the same *Chandra* data, Forman et al. (2005) identified shock fronts associated with an AGN outburst about 1–2×10^7 yr ago. They argued that shock fronts may be the most significant channel for heating (i.e., entropy increase) of the ICM near to the AGN.

Subsequent *Chandra* observations increased the total exposure time to 500 ks, which allowed Forman et al. (2007) to resolve a web of filamentary structure in both X-ray arms. Both arms show narrow filaments, with a length-to-width ratio of up to $\sim$50. However, while the Southwestern arm has only a single set of filaments, the Eastern arm shows multiple sets of filaments and bubbles, increasing in scale with the distance from the centre. The high spatial resolution of *Chandra* also highlights the fact that while the Eastern X-ray arm is cospatial with the radio arm, the radio emission bends around and avoids the Southwestern X-ray arm. A residual image of M 87 showing

Table 2.1: Summary of the *Chandra* observations. Colums list the observation ID, detector, observation mode, exposure after cleaning, and observation date.

Obs. ID	Detector	Mode	Exposure (ks)	Obs. date
2707	ACIS-S	FAINT	82.9	Jul. 6 2002
3717	ACIS-S	FAINT	11.1	Jul. 5 2002
5826	ACIS-I	VFAINT	126.8	Mar. 3 2005
5827	ACIS-I	VFAINT	156.2	May 5 2005
5828	ACIS-I	VFAINT	33.0	Nov. 17 2005
6186	ACIS-I	VFAINT	51.5	Jan. 31 2005
7210	ACIS-I	VFAINT	30.7	Nov. 16 2005
7211	ACIS-I	VFAINT	16.6	Nov. 16 2005
7212	ACIS-I	VFAINT	65.2	Nov. 14 2005

the inner cavities and the X-ray arms obtained using all *Chandra* ACIS-I data is shown in Fig. 2.1 (from Million et al. 2010a), together with the 90 cm radio image by Owen et al. (2000). The temperature structure and metallicity of the X-ray arms was studied in detail by Simionescu et al. (2008) using deep (120 ks) *XMM-Newton* data. These authors confirmed that the arms are multiphase with a temperature distribution between 0.6–3.2 keV. This temperature distribution is also consistent with that found by spectral fits to the *XMM-Newton* Reflection Grating Spectrometer (RGS) data (Werner et al. 2006), which show the presence of weak Fe XVII lines. Simionescu et al. (2008) estimate the total mass of gas below 1.5 keV, most of which was uplifted by the AGN, as $5 \times 10^8\ M_\odot$.

In this paper, we study for the first time the detailed nature and the spatial distribution of the multiphase plasma associated with the X-ray arms. *Chandra* allows us to study detailed structure in the cooler phases at a much higher spatial resolution than is possible with *XMM-Newton*. Our data allow us to sample well the small substructure seen in the *Chandra* images, map the spatial distribution of the individual temperature components and compare it with new Hα images obtained at the *Lick Observatory*, and archival data from the *Hubble Space Telescope (HST)*. In Section 2, we describe the data reduction and analysis; in Section 3, we present the results of the observations; in Section 4, we determine the physical properties of the cooler plasma phases and discuss the uplift of the low entropy gas from the bottom of the gravitational potential well, and effects of shocks and mixing. Finally, in Section 5, we summarize our conclusions.

A distance to M 87 of 16.1 Mpc (Tonry et al. 2001) implies a linear scale of 4.7 kpc arcmin^{-1}. All errors are quoted at the 68 per cent confidence level for one interesting parameter.

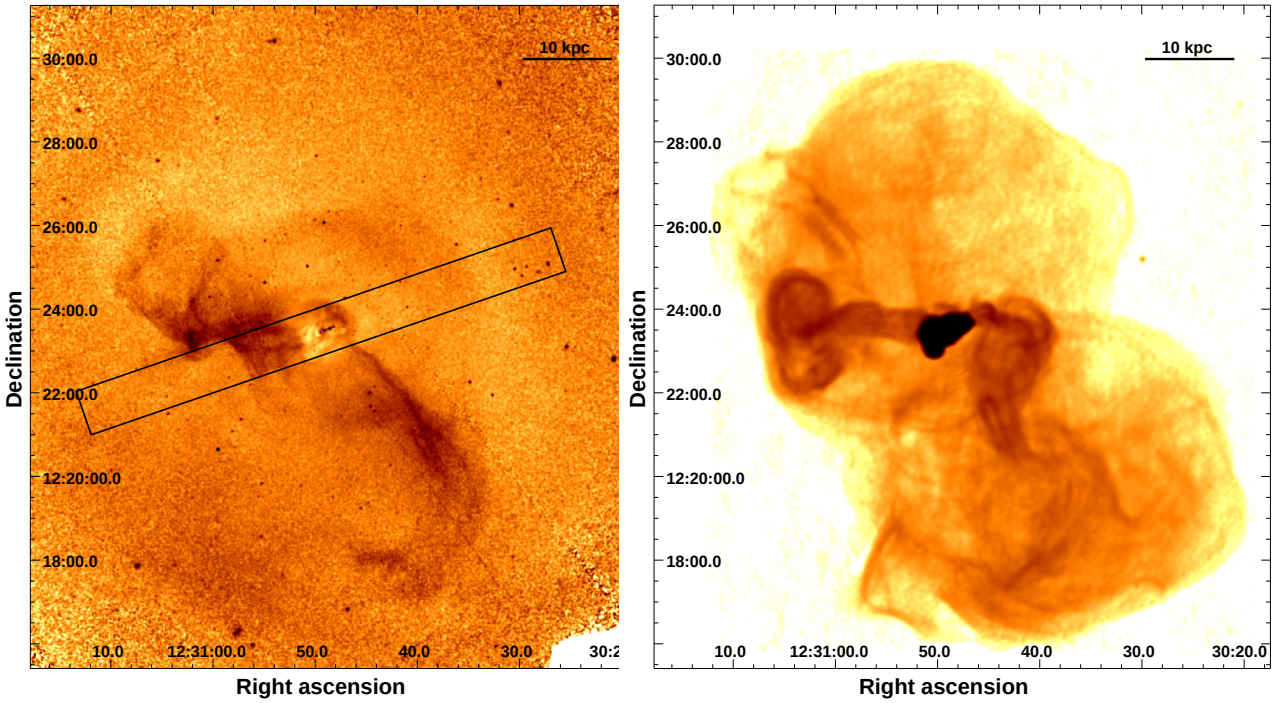

Figure 2.1: *Left panel:* Relative deviations of the surface brightness from a double beta model fit to the *Chandra* 0.6–2.0 keV image of M 87, obtained by coadding all ACIS-I observations (see Paper II for details). The cavities in the core and the two X-ray arms are clearly visible. The *XMM-Newton* RGS extraction region is overplotted. *Right panel:* The 90 cm radio image by Owen et al. (2000). Two flows (radio arms) emerge from the inner-jet region, one directed Eastward (spatially coincident with the X-ray arm) and the other directed to the Southwest. While the Eastern radio arm ends in edge-brightened torus-like vortex rings, the Southwestern radio arm develops a S-shaped Southward twist. Both radio arms are immersed in a pair of large, partially overlapping radio lobes. Both panels show the same $14.6' \times 15.8'$ field.

2.2 Data reduction and analysis

2.2.1 *Chandra* data

The *Chandra* observations of M 87 were taken between July 2002 and November 2005 using the Advanced CCD Imaging Spectrometer (ACIS). The observations are listed in Table 9.2. The total net exposure time after cleaning is 574 ks. We follow the data reduction procedure described in Million et al. (2010a), hereafter referred to as Paper II (see also Million & Allen 2009; Million et al. 2010b).

The individual regions for the spectral analysis were determined using the Contour Binning algorithm (Sanders 2006), which groups neighboring pixels of similar surface brightness until a desired signal-to-noise threshold is met. In order to have small enough regions to resolve substructure and still have enough counts to fit a simple multi-temperature model, we adopted a signal-to-noise ratio of 50. The total number of regions in this analysis is $\sim$6000, with a total number of $\sim$15,000,000 net counts.

Background spectra for the appropriate detector regions were extracted from the blank-sky fields available from the Chandra X-ray Center. These were normalized by the ratio of the observed and blank-sky count rates in the $9.5 - 12$ keV band (the statistical uncertainty in the observed $9.5 - 12$ keV flux is less than 5 per cent in all cases). The background level in these observations is low and represents only a marginal source of systematic uncertainty in the determined quantities.

Spectral modeling has been performed with the SPEX package (Kaastra et al. 1996, SPEX uses an updated version of the MEKAL plasma model with respect to XSPEC). We analyze data in the 0.6–7.0 keV band. To investigate the multi-temperature structure and map the spatial distribution of plasmas at different temperatures, we fit to each bin a model consisting of collisionally ionized equilibrium plasmas at four fixed temperatures, with variable normalizations and common metallicity. This method was introduced by Sanders et al. (2004) in the analysis of deep *Chandra* observations of the Perseus cluster. For M 87, the temperatures are fixed at 0.5, 1.0, 2.0, and 3.0 keV. The temperatures of the coolest and hottest components were selected based on previous multi-temperature analysis of *XMM-Newton* RGS and EPIC data (Werner et al. 2006; Simionescu et al. 2008). We also searched for a 0.25 keV component in our spectral fits, but did not detect any emission at this temperature. The temperatures of the individual spectral components are sufficiently far apart that the spectral analysis can constrain their emission measures if they are simultaneously present in the same extraction region. The overall metallicity in each region is free to vary. The O/Fe ratio is fixed at 0.59 Solar, Ne/Fe at 1.20 Solar, and the Mg/Fe at 0.60 Solar, as determined from *XMM-Newton* RGS spectra (Werner et al. 2006). The Galactic absorption toward M 87 is modelled as neutral gas with Solar abundances with a column density fixed at $N_{\rm H} = 1.94 \times 10^{20}$ cm^{-2}, the value determined by the Leiden/Argentine/Bonn (LAB) Survey of Galactic H I (Kalberla et al. 2005). Throughout the paper, abundances are given with respect to the "proto-solar values" by Lodders (2003), which are for O, Ne, and Fe approximately 30 per cent lower than the values given by Anders & Grevesse (1989).

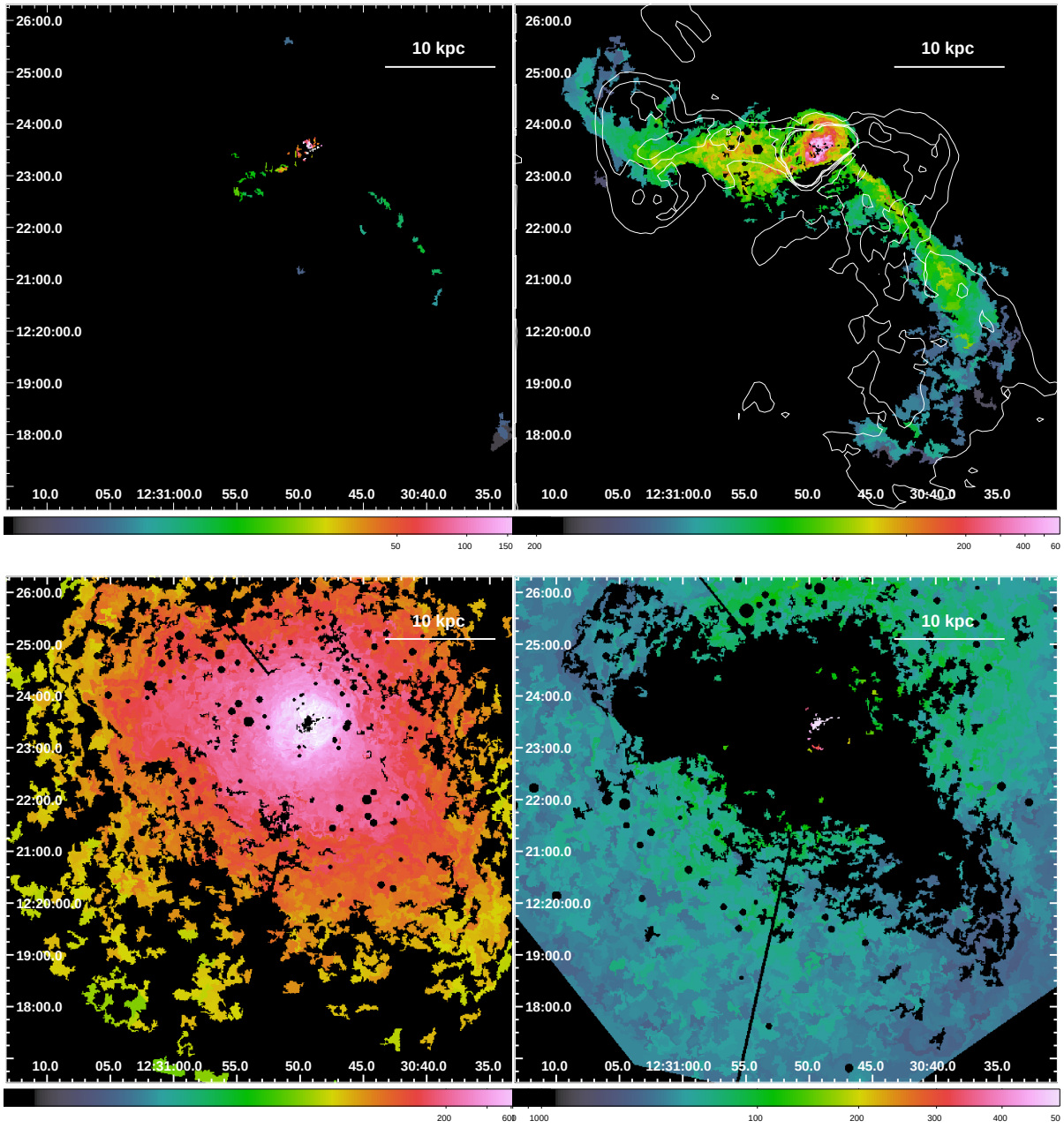

Figure 2.2: Spatial distribution of the emission measure, $Y = \int n_{\rm H} n_{\rm e} {\rm d}V$, (in 10^{58} cm^{-3} arcsec^{-2}) of the 0.5 keV (upper left), 1.0 keV (upper right), 2.0 keV (bottom left), and 3.0 keV (bottom right) plasma detected at 99.7 per cent confidence. On the upper right panel, we over-plotted the contours of the 90 cm radio image (Owen et al. 2000). All the panels show the same $10.45' \times 9.75'$ field. For a zoomed in version of the spatial distribution of 0.5 keV plasma in the core see the right panel of Fig. 3.1.

2.2.2 *XMM-Newton* RGS data

The multi-temperature structure of the hot plasma in and around M 87 exhibits a complex set of spectral lines that cannot be modelled by a single-temperature spectral model (Sakelliou et al. 2002; Werner et al. 2006). In order to confirm that our simple four-temperature model describes the temperature structure of M 87 well, we fit the same model to the *XMM-Newton* RGS spectra.

The *XMM-Newton* RGS data were obtained in January 2005, with a net exposure time of 84 ks. The data were processed as described in Werner et al. (2006). Spectra were extracted from a $1.1'$ wide extraction region, centred at the core of the galaxy. Because the RGS operates without a slit, it collects all photons from within the $1.1' \times \sim 12'$ field of view. Line photons originating at angle $\Delta\theta$ (in arcminutes) along the dispersion direction are shifted in wavelength by $\Delta\lambda = 0.138\Delta\theta$ Å. Therefore, every line is broadened by the spatial extent of the source. To account for this spatial broadening in our spectral model, we produce a predicted line spread function (LSF) by convolving the RGS response with the surface brightness profile of the galaxy derived from the EPIC/MOS1 image along the dispersion direction. Because the radial profile of a particular spectral line can be different from the overall radial surface brightness profile, the line profile is multiplied by a scale factor s, which is the ratio of the observed LSF to the expected LSF. This scale factor is a free parameter in the spectral fit.

We fit the spectra in the 8–38 Å band with the same four-temperature model fitted to the *Chandra* data, with an additional 0.25 keV component included to determine an upper limit on the amount of such cool plasma. We have also separately fitted the RGS data with a model consisting of four isobaric cooling flows with elemental abundances tied between the models (similar to one of the models used for the Centaurus cluster in Sanders et al. 2008). In this case, we model separately gas cooling from 3 keV to 2 keV, from 2 keV to 1 keV, from 1 keV to 0.5 keV, and from 0.5 keV to 0.25 keV. The central AGN cannot be excluded from the RGS data of the core of the galaxy and also needs to be accounted for. We model the AGN spectrum with a power-law of a photon index $\gamma = 1.95$ and a 2–10 keV luminosity of $L_X = 1.15 \times 10^{42}$ erg s^{-1} (Werner et al. 2006).

2.2.3 Hα data

Narrow-band Hα imaging (central wavelength 6606 Å, FWHM 75 Å) of M 87 was carried out using the *Shane* 3 m telescope at *Lick Observatory* on March 26th, 2009. The total integration time was 24 ks, split into 20 exposures using a dither pattern with $\sim$ 5 arcsec offsets. We also acquired 1200 seconds of *R* band imaging, also split into 20 exposures. The data were processed using the pipeline of Erben et al. (2005). A constant background was subtracted, estimated from the region of the image with the lowest counts. The images were registered with `scamp` (Bertin 2006), and resampled and combined with `swarp` (Bertin et al. 2002). The seeing of the coadded images is about 2 arcsec.

To study the morphology of the brighter Hα filaments in the cluster core, we have also analyzed two Hα images available in the *HST* archive. Both images were taken with WFPC2, placing the core onto the Planetary Camera. The Southeastern region

was imaged with the Wide Field Camera for only 2700 seconds (proposal ID: 5122, PI Ford), and is not as deep as our ground-based image. The Northwestern region was imaged significantly longer (13900 seconds, proposal ID: 6296, PI Ford).

2.3 Results

2.3.1 Spatial distribution of the X-ray gas

Fig. 7.4 shows the spatial distribution of the emission measures for the four individual temperature components (0.5, 1.0, 2.0, and 3.0 keV) obtained from the *Chandra* data. The top left panel shows an interesting result: the map reveals the presence of gas with a temperature of $kT \sim 0.5$ keV to the North of the jet in the core of the galaxy, in the Southwestern arm, and in a horseshoe like filament to the Southeast of the core outside of the mushroom shaped Eastern radio arm (radio contours are overplotted in the top right panel of Fig. 7.4). No 0.5 keV gas with significance higher than 3σ is present within the Eastern radio arm. While all the detected 0.5 keV plasma in the core and in the Southeastern horseshoe is within the RGS extraction region (see the left panel of Fig. 2.1), the Southwestern arm is outside of the area covered by the present RGS data.

The spatial distribution of the $\sim$1 keV plasma seen in the top right panel of Fig. 7.4 correlates with the radio emission and is very similar to the morphology of the X-ray arms seen clearly in Fig. 2.1. In the core, the 1 keV plasma forms a prominent ridge to the North of the AGN, which is cospatial with 0.5 keV plasma and Hα+[N II] emission (see below). Based on two-temperature spectral fits to *XMM-Newton* data it has been shown that the X-ray arms are relatively isothermal at $\sim$1 keV (Molendi 2002; Simionescu et al. 2008) and our spectral fits to the Southwestern X-ray arm confirm that its temperature is constant as a function of radius (see Fig. 2.3). Most of the Eastern radio arm contains $\sim$1 keV plasma, a large amount of which is also present to the South of the "stem of the radio mushroom" where the 0.5 keV horseshoe is observed. The brightest part of the Southwestern radio arm is not spatially coincident with the 0.5 keV and 1 keV plasma, but it bends around the cooler X-ray gas. On the Southwest, just outside of the core region, the 1 keV plasma forms a narrow and remarkably straight and smooth filament, which broadens with increasing distance from the core. At the projected radius of $\sim 3'$, which is the approximate distance of the circular shock front described in Paper II and by Forman et al. (2007), the distribution of 1 keV gas broadens, and at $4.5'$ it starts to bend to the Southeast.

The spatial distribution of the plasma at $\sim$ 2 keV is, in comparison, remarkably symmetric and only slightly elongated in the direction of the X-ray arms. A knot of $\sim$3 keV plasma is present at the inner edge of the X-ray cavity South of the core, at the bottom of the bright radio cocoon, which Forman et al. (2005) identified as a "bud". This 3 keV plasma is most probably associated with a shock front at the radius of $0.6'$ (Forman et al. 2007, Paper II, see also the right panel of Fig. 2.5).

The fraction of the emission measure of cooler gas (1 keV and 0.5 keV) in the X-ray arms with respect to the total emission measure is 10–35 per cent, consistent with the results obtained by fitting a differential emission measure distribution to *XMM-*

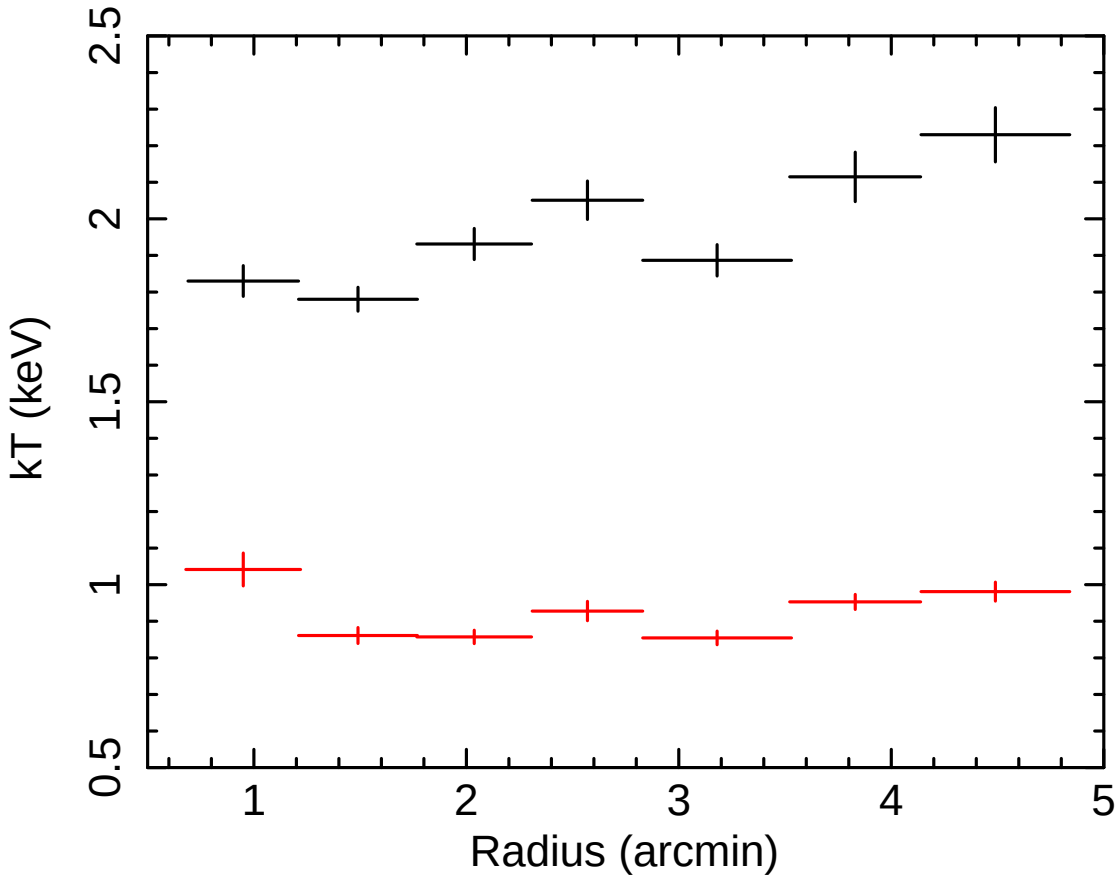

Figure 2.3: The temperature profile of the Southwestern X-arm fitted with a two-temperature model. While the temperature of the hotter component shows a slight radial increase (black data points) the radial distribution of the cooler temperature component (red data points) looks remarkably flat at around 1 keV. If the uplift were adiabatic, the temperature of the cooler gas within the arm would be radially decreasing.

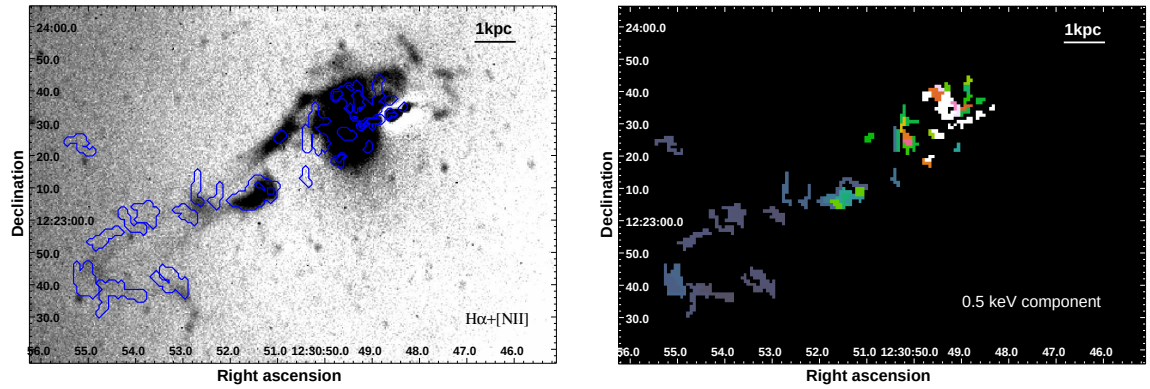

Figure 2.4: The Hα emission (left panel) and plasma at $\sim$0.5 keV (right panel; blue contours in the left panel) spatially correlate in the core and form a horseshoe like feature to the Southeast of the core. The right panel is a zoomed in version of the top left panel of Fig. 7.4. Both panels show the same $2.7' \times 1.85'$ field.

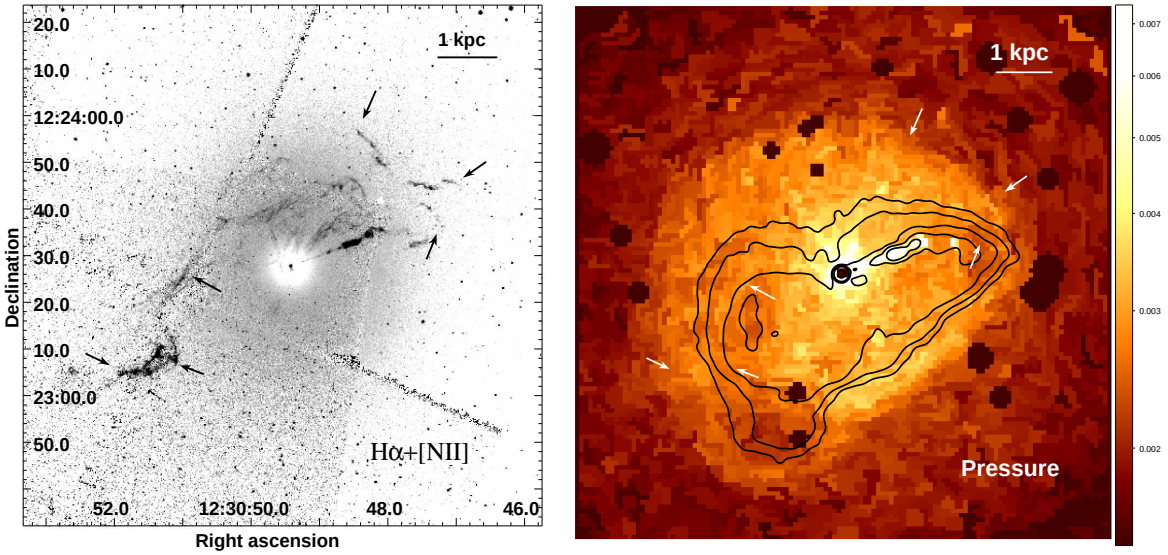

Figure 2.5: *Left panel:* Hα image of the innermost $2' \times 2'$ region of M 87, divided by the best fit De Vaucouleurs profile, obtained by *HST*. *Right panel: Chandra* pressure map (in units of keV cm^{-3} $\times \left(\frac{1}{2\mathrm{Mpc}}\right)^{-1/2}$, see Paper II for details on producing the pressure map) of the same inner $2' \times 2'$ region overplotted with the 6 cm radio emission contours from Hines et al. (1989). The pressure map clearly shows a discontinuity, a likely shock front, at a radius of $0.6'$. The Hα image shows that all the bright Hα filaments appear in the downstream region of the shock. The arrows identify the bright Hα features furthest from the centre, at the edges of apparently underpressured X-ray cavities, and a bright Hα "knee" on the Southeast.

Newton data by Simionescu et al. (2008). The spatial distribution of the coolest gas phases is also in good agreement with that found in the *XMM-Newton* data analysis (Simionescu et al. 2008), but is revealed by *Chandra* with a strikingly better spatial resolution.

The elemental abundances obtained from the fits are likely to be biased due to the limitations of our model, which has its temperatures fixed at specific values (detailed study of the metallicity will be presented in Million et al. in prep.; see also Paper II and Simionescu et al. 2008).

2.3.2 Morphology of the Hα nebulae: new clues about their powering

The left panel of Fig. 3.1 shows an excerpt of the Hα+[N II] image obtained at the *Lick Observatory* after subtraction of the scaled *R*-band continuum image. Owing to the large depth, our data reveal a previously undiscovered horseshoe-like filament of Hα+[N II] emission to the Southeast of the core. The feature is detected at a mean level of 5σ above the sky. Fig. 3.1 shows that the spatial distribution of the Hα+[N II] emission is remarkably similar to that of the 0.5 keV plasma, both in the core and in the Southeastern horseshoe like region. Except for a small knot of Hα+[N II] emission in the "cap of the mushroom" (see Gavazzi et al. 2000), the Eastern radio arm is devoid of observable Hα filaments. As mentioned above, the Eastern radio arm is also devoid of any detectable 0.5 keV emission. Our *Lick Observatory* data (Fig. 3.1) and the *HST* data (Fig. 2.5) unfortunately do not cover the Southwestern X-ray arm.

Fig. 2.5 shows an Hα image for the innermost $2' \times 2'$ region of M 87 from *HST* next to a pressure map obtained in Paper II by using *Chandra* data. In the pressure map we see a discontinuity, likely shock front, at $0.6'$ and several underpressured regions filled with radio emitting plasma, as shown by the contours of 6 cm radio emission from Hines et al. (1989). Assuming that this inner shock propagates at an approximately constant velocity of 1000 km s^{-1}, it originated in an AGN outburst $\sim$2.8 Myr ago. Interestingly, all the bright Hα emission is within the inner higher pressure region surrounded by the shock front at $0.6'$. Some filaments appear to be parallel to the shock front, others seem to lie at the edges of cavities, while the filament to the Southeast of the core is perpendicular to the shock front, bright in the downstream region and faint in the upstream. Upstream of the shock front, the Southeastern Hα filament continues at a much lower surface brightness and forms the prominent horseshoe. On the Hα image, we identify with arrows the bright features furthest from the centre, at the edges of X-ray cavities, and a bright Hα "knee" on the Southeast. The same arrows are plotted in the pressure map.

2.3.3 High-resolution *XMM-Newton* RGS spectra

To confirm the presence of the coolest gas phases indicated by fitting the *Chandra* data and to verify that the simple four-temperature model fits the data sufficiently well, we also analyze the *XMM-Newton* RGS high-resolution line spectra. The results of the

five-temperature fit to the RGS data are listed in Table 3.3 and the best fit model to the spectra is shown in Fig. 3.7.

The emission measures for the 2 keV and 1 keV phases obtained by the RGS are consistent with those from the *Chandra* maps for the area covered by the gratings. The emission measure of the 0.5 keV phase obtained using the RGS is higher by a factor of 3 than the value from the *Chandra* map. The sensitivity of *Chandra* in the 0.6–7 keV band to 0.5 keV emission in these moderate S/N spectra is limited and if we only consider regions where the 0.5 keV component was detected at larger than the 99.7% confidence level then we miss the cool emission in some regions. By including all regions detected at the 68% confidence the 0.5 keV features in the map become wider and the agreement between the emission measures from *Chandra* and RGS improves.

The lack of O VII lines provides strong constraints on the amount of 0.25 keV plasma. The 95 per cent upper limit for its emission measure is lower by a factor of 11 than the emission measure of the 0.5 keV plasma.

To get constraints on the amount of radiative cooling, we also fit the RGS spectra with a set of cooling flow models (see Table 3.3). If the plasma would cool isobarically in the absence of heating, the best fit mass deposition rates would be the same in the different temperature ranges. However, the mass deposition rates are decreasing as a function of temperature and for the gas cooling from 0.5 keV to 0.25 keV we determine a tight 95 per cent upper limit of $\dot{M} = 0.06\ M_{\odot}/\mathrm{yr}$.

2.4 Discussion

2.4.1 Orientation of the X-ray arms

The inferred properties of the X-ray arms depend critically on their orientation with respect to our line-of-sight. Based on *HST* observations of the superluminal motion in the jet of M 87, Biretta et al. (1999) concluded that the position angle of the jet is $< 19^{\circ}$ from our line-of-sight. The two large, partially overlapping, outer radio lobes of M 87 (the diffuse structures which embed the more collimated, brighter radio arms seen in the right panel of Fig. 2.1 and in Owen et al. 2000) are also probably oriented close to our line-of-sight. It is likely that the Southern radio lobe is positioned towards us and the Northern lobe is oriented away from us. This picture is supported by the observation of polarized flux from the Southern lobe (Andernach et al. 1979), which shows that the Faraday depth towards it is likely to be small. The radius of the large lobes/bubbles is $\sim$22 kpc and their approximate centres are in projection 26 kpc apart. Assuming that the physical distance between the centres of the bubbles is at least twice their radius, a conservative limit for the orientation of the axis along which the bubbles rise is $< 35^{\circ}$ from our line-of-sight. The Southwestern radio arm appears to "merge" into the Southern lobe indicating that its orientation is similar to that of the two large bubbles. Although the relation of the Eastern radio arm to the outer lobe is less clear, the most likely orientation of both X-ray and radio arms is approximately anti-parallel and far from the plane of the sky.

Table 2.2: Best fit parameters for a five-temperature fit and a four-cooling-flow model fit to the high-resolution RGS spectra extracted from a 1.1′ wide region centred on the core of M 87. Emission measures, $Y = \int n_{\rm H} n_{\rm e} {\rm d}V$, are given in 10^{63} cm^{-3}. The scale factor s is the ratio of the observed LSF to the expected LSF based on the overall radial surface brightness profile. The upper limits are quoted at their 95 per cent confidence level. Abundances are quoted with respect to the proto-solar values of Lodders (2003).

Parameter	5T-model	4-c.f. model
$Y_{0.25\rm keV}$	< 0.07	–
$Y_{0.5\rm keV}$	0.79 ± 0.05	–
$\dot{M}_{0.5-0.25keV}$	–	< 0.06
$Y_{1.0\rm keV}$	7.1 ± 0.3	–
$\dot{M}_{1.0-0.5keV}$	–	0.90 ± 0.03
$Y_{2.0\rm keV}$	56.3 ± 1.3	–
$\dot{M}_{2.0-1.0keV}$	–	3.79 ± 0.25
$Y_{3.0\rm keV}$	< 2.4	–
$\dot{M}_{3.0-2.0keV}$	–	6.03 ± 0.21
s	2.21 ± 0.10	2.19 ± 0.11
C	0.75 ± 0.21	0.82 ± 0.22
N	1.9 ± 0.3	2.0 ± 0.3
O	0.79 ± 0.04	0.84 ± 0.04
Ne	1.92 ± 0.13	1.92 ± 0.13
Mg	1.25 ± 0.15	1.26 ± 0.13
Fe	1.33 ± 0.04	1.39 ± 0.05
Ni	0.9 ± 0.3	0.9 ± 0.3

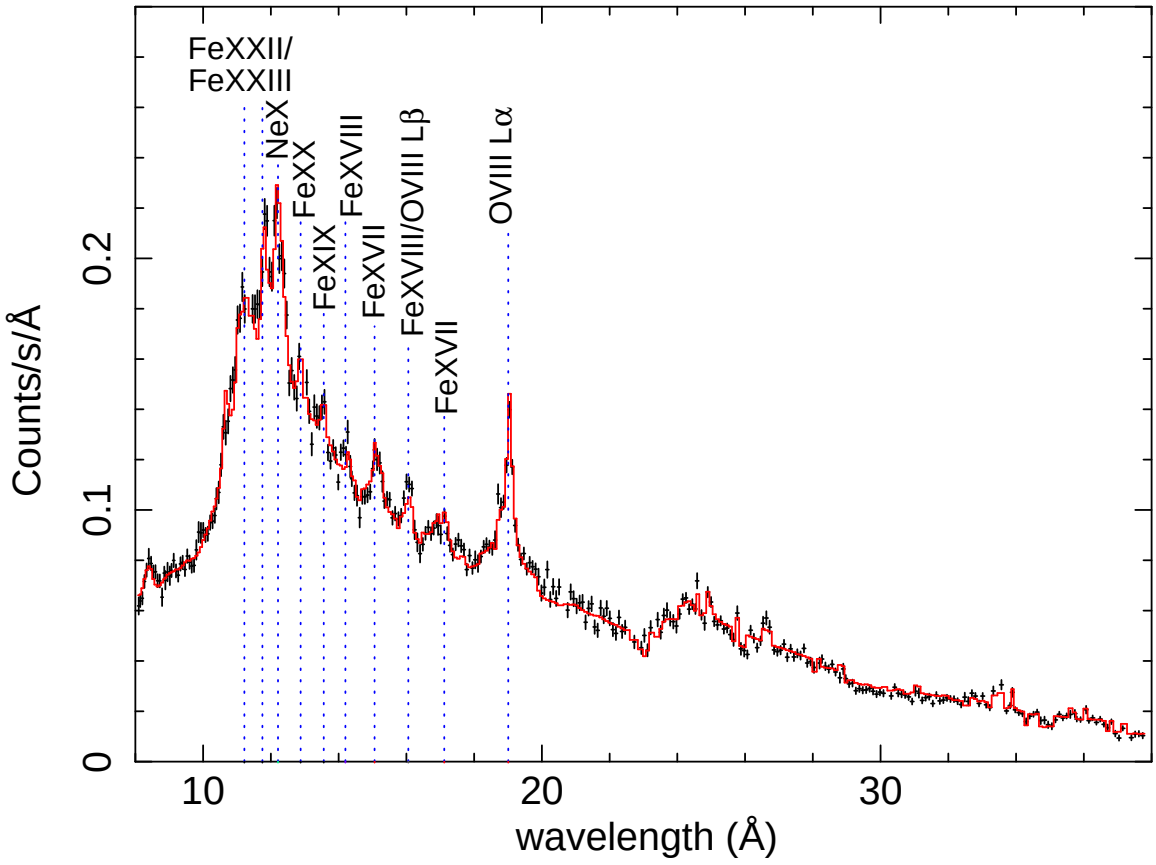

Figure 2.6: The first order RGS spectrum extracted from a 1.1′ wide region centred on the core of M 87. The continuous line represents the best fit model to the spectrum.

2.4.2 Physical properties and origin of the X-ray arms

We determine the properties of the X-ray arms for three different orientation angles (15°, 30°, and 90°) from our line-of-sight. For each orientation, we determine the radial profiles of the gas mass, entropy, and cooling time for the different phases (see Fig. 4.6). We assume that all the gas phases are in equilibrium with the ambient pressure at the given distance from the centre. The radial distribution of the ambient pressure is determined using the deprojected temperature and electron density profiles parametrized by equations (6) and (7) in Churazov et al. (2008). Using this pressure profile $p(r)$, we calculate the electron number density profile $n_{\rm e}(r) = p(r)/(kT)$ of the $kT = 0.5$ keV and 1 keV plasmas. Using these density profiles and the best fit emission measures, $Y = \int n_{\rm H} n_{\rm e} {\rm d}V$, for each extraction region, we determine the volumes which the cooler phases occupy: $V = Y/(n_{\rm H} n_{\rm e})$, where $n_{\rm H} = n_{\rm e}/1.2$ is the hydrogen number density for collisionally ionized plasma with Solar metallicity.

The line-of-sight depths, l, of the emitting volumes, V, shown in Fig. 2.8, are then calculated as $l = V/A$, where A is the area on the sky of the given extraction region. The corresponding gas masses are calculated as $M = 1.4 n_{\rm H} m_{\rm p} V$ (where $m_{\rm p}$ is the proton mass), only in the spatial regions where their presence was determined with better than 3σ significance. The cumulative radial gas mass profiles are shown in the bottom panel of Fig. 4.6. The middle panel of this figure shows the radial entropy profiles calculated as $S = kT/n_{\rm e}^{2/3}$. The top panel shows the cooling time profiles calculated as the gas enthalpy divided by the energy lost per unit volume of the plasma:

$$t_{\rm cool} = \frac{\frac{5}{2}(n_{\rm e} + n_{\rm i})kT}{n_{\rm e} n_{\rm i} \Lambda(T)}, \tag{2.1}$$

where the ion number density $n_{\rm i} = 0.92 n_{\rm e}$ and $\Lambda(T)$ is the cooling function for Solar metallicity tabulated by Sutherland & Dopita (1993). Cooling functions based on more up to date plasma codes (Schure et al. 2009) predict for the 0.5 keV plasma a 9 per cent higher cooling rate.

If the arms lie in the plane of the sky, then the small line-of-sight depths of the emitting volumes in Fig. 2.8 indicate that the 1 keV gas is not volume filling at most radii, including the core of the galaxy. The 1 keV gas is then made of small blobs and filaments with an entropy smaller than the lowest entropy of the ambient medium in the centre of the galaxy (see Fig. 4.6). This would mean, as pointed out by Molendi (2002), that the cool blobs/filaments can hardly originate from the adiabatic evolution of the hot-phase gas entrained by buoyant radio bubbles, as suggested by Churazov et al. (2001). However, if the arms are oriented close to our line-of-sight, the physical picture changes.

For the likely angles of 15°–30° from our line-of-sight, both the radial distribution of the gas entropy and the distribution of the depths of the emitting volumes of the 1 keV component give a more consistent picture with other observables. The 1 keV plasma appears to be mostly volume filling, except in regions where the X-ray images reveal cavities. Its cooling time is $>1.5 \times 10^8$ yr, which is comparable to or longer than the uplift time. Moreover, by taking the projection effects properly into account, the apparent large angle between the current direction of the jet and the Southwestern arm

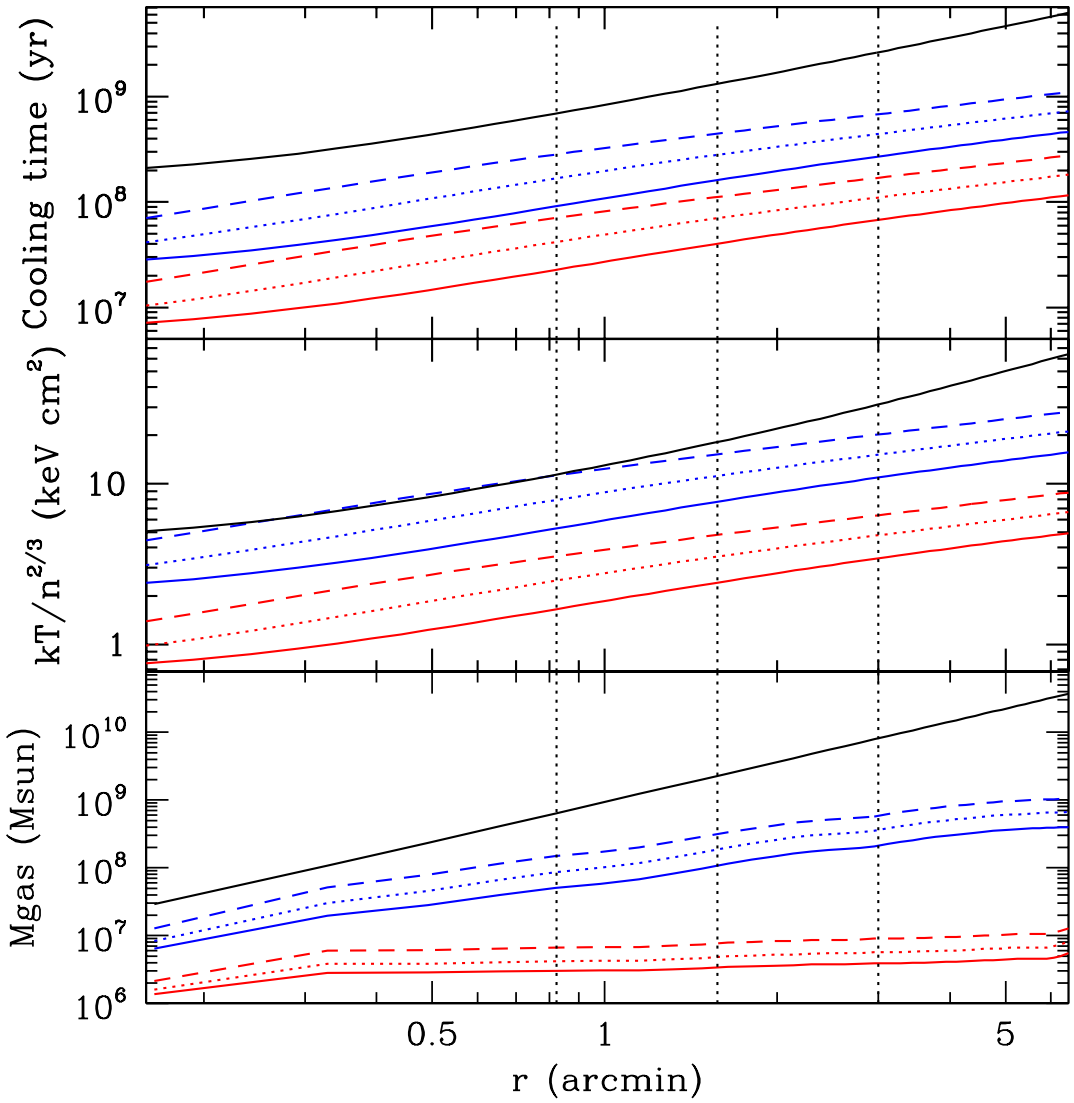

Figure 2.7: Cumulative gas mass, entropy ($S = kT/n^{2/3}$), and radiative cooling time of the 0.5 keV phase (red lines), 1.0 keV phase (blue lines), and the ambient ICM (black lines) as a function of projected radius for orientation angles of 15° (dashed lines), 30° (dotted lines), and 90° (full lines) from our line-of-sight. For the deprojected density and temperature profiles of the ambient ICM we assume the profiles parametrized by equations (6) and (7) in Churazov et al. (2008). The cooler gas phases are assumed to be in pressure equilibrium with the ambient medium (see text for details). The vertical dotted lines denote the radii of the outer edge of the ridge of multiphase gas North of the jet, the end of the Southeastern horseshoe, and the radius of the shock at $\sim 3'$, which corresponds to the projected radius of the inner edge of the "cap of the mushroom" of the Eastern arm.

translates into a much smaller physical angle. The inferred spatial distribution of the depths of the emitting volumes (see Fig. 2.8) indicates that the orientation angle of the filament is not constant and at certain positions the arms are folded along our line-of-sight. The Southwestern arm appears to be folded at the projected radius of $3.4'$, where the arm divides into two filaments (see Fig. 2.1). The Eastern arm appears to have folds at $\sim 2.1'$ and its line-of-sight depth increases in the cap of the mushroom. We caution that because of the strongly simplified assumptions the values for the depths quoted in the figures are approximate numbers only.

If the uplift of the low entropy plasma were strictly adiabatic, then the temperature of the arms would decrease as a function of radius. However, as shown by Molendi (2002), Simionescu et al. (2008), and in Fig. 2.3 using a two-temperature model, the average temperature of the arms is remarkably constant. The constant temperature implies rising entropy with radius and suggests that conduction plays an important role in the thermal evolution of the arms.

The estimated total mass of 1 keV gas in the arms is between 6–9 $\times 10^8$ $M_\odot$, which given the uncertainties is remarkably similar to the total gas mass of 6.3×10^8 $M_\odot$ within the innermost 3.8 kpc region ($0.8'$ in the plane of the sky), where the X-ray emission is relatively spherically symmetric. Outside of this radius, all the $\sim$1 keV gas is distributed along the two X-ray arms. If the entropy of the arms is increasing due to heat conduction, then most of the 6–9$\times 10^8$ $M_\odot$ of $\sim$1 keV plasma might have been uplifted from within the innermost approximately spherical 3.8 kpc region of the galaxy. While this is a large fraction of the total gas mass in the core of the cluster, it is only a fraction of the uplifted gas mass observed in more massive clusters; e.g. the inferred mass of the uplifted gas in Hydra A is 1.6–6.1 $\times 10^9$ $M_\odot$ (Simionescu et al. 2009b). Though seen with great clarity in our study, the physics of gas uplift in M 87 is by no means extreme. Many brightest cluster galaxies can be expected to be similarly efficient in evacuating their lowest entropy plasma during AGN outbursts.

By assuming that the outer radio halo is a spherical bubble of hot plasma undergoing a steady energy input from the jet, Owen et al. (2000) estimated its age to $\sim 10^8$ yr. However, if the radio halo consists of two bubbles rising buoyantly in the hot ICM, then the outer radio lobes are likely to be older. The age of the radio and X-ray arms estimated by Churazov et al. (2001) is a few times 10^7 yr. However, if the whole Southwestern arm originated in a single uplift following an AGN outburst, then for an orientation angle of $<30^\circ$ from our line-of-sight, its length is >60 kpc, which assuming an uplift velocity of 400 km s^{-1} implies an age of $>1.5 \times 10^8$ yr. The age of the observed structures is thus greater than previously thought.

2.4.3 Implications for gas motions in the ICM

The NW edge of the Southwestern X-ray arm is remarkably smooth out to the radius of $\sim 3.3'$ and the filament is surprisingly straight for a distance of over $2'$. This strongly suggests that the gas motions cannot be very turbulent in either phase. The lack of strong turbulence in the ICM has been inferred previously based on the straightness of the Hα filaments in the Perseus cluster (Fabian et al. 2003b), and strong upper limits on turbulent velocities were placed based on resonance scattering in NGC 4636

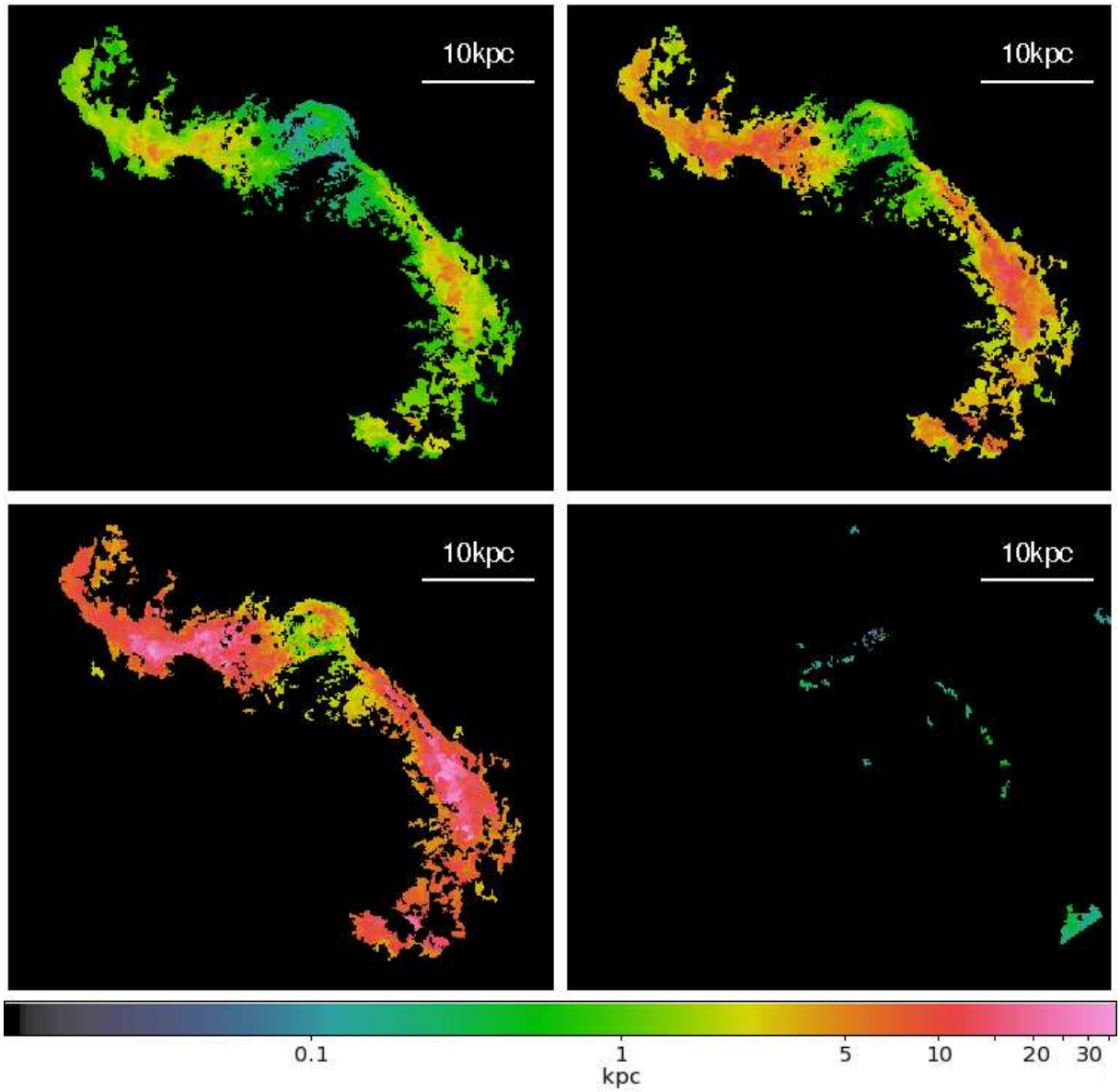

Figure 2.8: Maps of the line-of-sight depths in kpc for the emitting volumes of 1 keV plasma for orientation angles of 90° (top left panel), 30° (top right panel), and 15° (bottom left panel) from our line-of-sight. The map on the bottom right panel shows the line-of-sight depth distribution of the 0.5 keV component for an orientation angle of 30° from our line-of-sight. All the panels show the same $10.36' \times 9.25'$ field.

(Werner et al. 2009) and turbulent line broadening in Abell 1835 (Sanders et al. 2010b). The bending of the X-ray arms of M 87 at larger radii might be caused by gas sloshing, which creates a spiral like shearing motion pattern in the ICM which is the most obvious at the two opposite and staggered cold fronts seen at 7′ to the Southeast (Simionescu et al. 2007) and at 19′ to the North (Simionescu et al. 2010). The sloshing induced shearing motions might also generate mixing of the ∼1 keV gas with the ambient ICM at large radii.

2.4.4 The coolest X-ray emitting phase

The total mass of ∼0.5 keV gas in M 87 is at least $7 \times 10^6\ M_\odot$. Because we calculate the mass of the 0.5 keV component only in spatial regions where it was detected at higher than the 99.7 per cent confidence, this value is a conservative lower limit. The inferred small line-of-sight depths of the emitting volumes of the 0.5 keV component imply that the coolest X-ray emitting gas is not volume filling, but forms a multi-phase medium together with both the hotter X-ray emitting and the cold Hα emitting gas phases. Soft band X-ray images (Forman et al. 2007) reveal that this cooler phase forms a network of filaments, which spatially coincide with *H*α filaments (Sparks et al. 2004, see also Fig. 3.1). Relatively cool ($\sim$ 0.5 keV) X-ray gas associated with Hα filaments has also been observed in the Perseus cluster and in 2A 0335+096 (Sanders & Fabian 2007; Sanders et al. 2009).

One of the most prominent regions in M 87 occupied by multiphase plasma is a ridge to the North of the jet, which contains 2 keV, 1 keV, 0.5 keV, and Hα gas. This region is just outside of the inner radio cocoon and possibly contributes to the confinement of the radio plasma on the Northern side and to the depolarization seen there by Owen et al. (1990). The depolarization of the radio emission in this region overlapping with the filaments indicates that the magnetic fields are disordered on scales less than 0.1 kpc. Therefore, it is likely that the Hα filaments consist of many narrow magnetized threads, which are not perfectly aligned and are small compared to the observed beam. Depolarization of the radio emission at regions containing Hα and soft X-ray emission has been previously observed in the Centaurus cluster (Taylor et al. 2007).

Limits on cooling and constraints on viable heating mechanisms

Even though the cooling time of the ∼0.5 keV gas is relatively short (see the top panel of Fig. 4.6), no X-ray emitting plasma below 0.5 keV is observed in M 87. The 95 per cent confidence upper limit for the emission measure of 0.25 keV plasma based on the non-detection of O VII lines with RGS is $Y = \int n_{\rm H} n_{\rm e} {\rm d}V = 7 \times 10^{61}\ {\rm cm}^{-3}$, which is only 9 per cent of the emission measure of the 0.5 keV plasma. Therefore, assuming pressure equilibrium between different gas phases, the mass of the 0.25 keV phase is at least 22 times lower than the mass of the 0.5 keV plasma. Assuming the 1 keV gas is isobarically cooling to 0.5 keV, its best fit mass deposition rate is $\dot{M} = 0.9\ M_\odot\ {\rm yr}^{-1}$, which is 15 times larger than the 95 per cent confidence upper limit for the mass deposition rate from 0.5 keV to 0.25 keV. The upper limits on gas cooling below 0.5 keV rely on the O VII lines and thus on the O abundance of the cool gas, which we assumed to be the

same as that of the hotter phase which is fairly constant across the core (Werner et al. 2006). For significant amounts of gas cooling radiatively below 0.5 keV to be present in the core, without detectable O VII emission, the O abundance of the cooling plasma would have to be unrealistically low. The lack of larger amounts of gas radiatively cooling below 0.5 keV implies the presence of heating. A similar temperature floor at $\sim$0.5 keV is observed in the Perseus cluster, Centaurus cluster, 2A 0335+096, Abell 262, Abell 3581, and HCG 62, (Sanders & Fabian 2007; Sanders et al. 2008, 2009, 2010a).

The energy emitted per unit volume in a blob of 0.5 keV gas, that is in pressure equilibrium with the surrounding 1 keV and 2 keV gas, is 4.8 times larger than the energy emitted by the neighboring volume of gas at 1 keV and 30 times larger than for the gas at 2 keV. Therefore, any heating process preventing the coolest gas phase from cooling below the $\sim$0.5 keV temperature floor and providing energy uniformally in a volume-averaged way would overheat the surrounding gas and is ruled out by the data. The mechanism that heats the coolest gas clearly provides more energy per unit volume to cooler, denser phases than it does to the hotter phases.

An alternative explanation is that the coolest X-ray plasma cools non-radiatively by mixing. Sanders et al. (2010a) reached similar conclusions for a sample of cool core clusters. The coolest X-ray plasma in M 87 might cool non-radiatively by mixing with the cold optical line emitting filamentary gas, allowing efficient conduction between the two phases (Fabian et al. 2002; Soker et al. 2004). As indicated by the fact that all the bright Hα+[N II] filaments end at the innermost shock front, this mixing might be promoted by the shock, which induces enhanced shearing motions, and might also power the detected optical and UV line emission (see the next section).

2.4.5 The nature of the Hα filaments

The optical emission line filaments in M 87 are likely due to cooled gas, enriched by dust from stellar mass loss (Sparks et al. 1993), which has been uplifted by the buoyant relativistic plasma, together with the coolest X-ray emitting phase. The total mass of the $\sim 10^4$ K Hα emitting gas in the filament system in M 87 is estimated to be of the order of 10^5–10^7 $M_\odot$ (Sparks et al. 1993), which is comparable to the mass of $\sim$0.5 keV gas. However, the total mass of cold neutral and molecular gas based on the upper limits on CO emission within the bright Hα emitting regions is at most only a few times 10^6 $M_\odot$ (Salomé & Combes 2008). This implies that the Hα emitting gas is not a thin skin on the underlying clouds of neutral and molecular gas as in the Perseus cluster, where the inferred total mass of the cold gas is as high as $\sim 4\times10^{10}$ $M_\odot$ (Salomé et al. 2006). Recently, Sparks et al. (2009) discovered filaments of C IV emission in M 87, with a total power of 1.1×10^{39} erg s^{-1}, arising from gas at a temperature of $\sim 10^5$ K, which spatially coincides with the Hα filaments on all scales. This detection indicates that the cool and hot gas phases are in thermal communication. The emission strengths are consistent with thermal conduction, which would create this intermediate temperature phase at the interface of the hot ICM and the cooler gas. However, even though conduction can quantitatively provide the energy seen in the form of line emission (Sparks et al. 2004), it would have to proceed at close to the Spitzer or saturated levels to power the filaments. The very thin and long Hα filaments are magnetized (see Sect. 2.4.4 and

Fabian et al. 2008) and the likely orientation of the magnetic fields parallel to the interface of the cold and hot phase would largely suppress the level of conduction. Thus it seems unlikely that thermal conduction alone can explain the optical line emission.

All of the bright Hα emission in M 87 is observed in the downstream region of the innermost $<$3 Myr old shock front, within a radius of $\sim 0.6'$. This suggests that the Hα emission in M 87 is somehow related to shocks in the ICM. The passage of a shock accelerates the intra-cluster medium, but because of the large density contrast the relatively cool Hα emitting gas is left behind, resulting in a sudden strong shear around the filaments. It is likely that such shear promotes mixing of the cold gas with the ambient hot ICM via instabilities. Ferland et al. (2009) recently showed that the spectra of optical filaments observed around the central galaxies of cooling core clusters can be explained if the filaments are heated by ionizing particles, either conducted from the surrounding regions or produced in situ by MHD waves. By facilitating contact between the hot thermal particles and the cold gas, mixing can supply the power and the ionizing particles needed to explain the optical line emission spectrum. Mixing of X-ray emitting plasma with the cold gas also naturally explains the presence of the $\sim 10^5$ K intermediate temperature gas phase. If the coolest X-ray emitting gas cools by mixing with the filamentary gas behind the shock front and conductively connects with it (e.g. Begelman & Fabian 1990; Soker et al. 2004), then its thermal energy will be radiated away in the UV band, in the optical Hα+[N II], and most likely at infrared wavelengths in the presence of dust.

2.4.6 Implications for galaxy formation models

The series of recent 'radio' or 'jet'-mode AGN outbursts in M 87, revealed in exquisite detail by the *Chandra* data, by no means represent a unique or extreme phenomenon. For example, a complete, flux-limited study of eighteen optically and X-ray bright, nearby galaxies, including M 87, by Dunn et al. (2010) shows that 17/18 sources exhibit some form of current radio activity associated with the central AGN (see also Best et al. 2005; Dunn & Fabian 2006, 2008; Sun 2009). Allen et al. (2006) also show that the efficiency with which the accretion of hot gas powers jets in giant ellipticals, including M 87, is remarkably uniform. Our results for the nearest, brightest cluster core show that even the current, relatively modest level of radio mode AGN activity has been sufficient to remove a sizeable fraction of the coolest, lowest entropy gas from the central galaxy. This is the material that would have cooled to form stars (e.g. Peterson & Fabian 2006). Our results therefore provide direct evidence that radio mode AGN input has a profound effect on the ability of large galaxies to form stars from their surrounding X-ray emitting halos.

2.5 Conclusions

Using a combination of deep (574 ks) *Chandra* data, *XMM-Newton* high-resolution spectra, and optical Hα+[N II] images, we have performed an in-depth study of AGN

feedback in M 87. Accounting for the fact that the long X-ray and radio "arms" are seen in projection with likely angles of $\sim 15^\circ$–30° from our line-of-sight, we find that:

- The mass of the uplifted low entropy gas in the arms is comparable to the gas mass in the approximately spherically symmetric 3.8 kpc core, demonstrating that the AGN has a profound effect on its immediate surroundings. This result has important implications for understanding AGN feedback in galaxy formation models (e.g. Croton et al. 2006; De Lucia & Blaizot 2007; Sijacki et al. 2007).

- The coolest detected X-ray plasma, with a temperature of $\sim$0.5 keV, the Hα+[N II] emitting gas, and the UV emitting gas are cospatial, and appear to be arranged in magnetized filaments within the hot ambient atmosphere, forming a multi-phase medium.

- We do not detect X-ray emitting gas with temperatures below $\sim$0.5 keV. To remain in steady state and at constant pressure, the filaments of 0.5 keV gas would require a 5 times higher heating rate than the 1 keV gas, and 30 times stronger heating than 2 keV plasma. Thus, a uniform, volume-averaged heating mechanism would overheat the surrounding gas and can be ruled out in M 87.

- All of the bright Hα and UV filaments are seen in the downstream region of the < 3 Myr old shock front, within a radius of $\sim 0.6'$. This argues that the generation of Hα and UV emission in M 87 is related to shocks in the ICM.

Based on these observations we propose that shocks induce shearing around the denser gas filaments, thereby promoting mixing of the cold gas with the ambient hot ICM via instabilities. This process may both provide a mechanism for powering the optical line emission and explain the lack of plasma with temperature under 0.5 keV:

- By helping to get hot thermal particles into contact with the cool, line-emitting gas, mixing can supply the power and the ionizing particles needed to explain the optical spectra of the Hα+[N II] nebulae (see Ferland et al. 2009).

- Mixing of the coolest X-ray emitting plasma with the cold optical line emitting filamentary gas promotes efficient conduction between the two phases, allowing the X-ray gas to cool non-radiatively, which may explain the lack of gas with temperatures under 0.5 keV.

Acknowledgments

Support for this work was provided by the National Aeronautics and Space Administration through Chandra/Einstein Postdoctoral Fellowship Award Number PF8-90056 and PF9-00070 issued by the Chandra X- ray Observatory Center, which is operated by the Smithsonian Astrophysical Observatory for and on behalf of the National Aeronautics and Space Administration under contract NAS8-03060. This work was supported in part by the US Department of Energy under contract number DE-AC02-76SF00515.

SMH is supported by the National Science Foundation Postdoctoral Fellowship program under award number AST-0902010.

Chapter 3

Violent interaction between the AGN and the hot gas in the core of the galaxy cluster Sérsic 159-03

N. Werner[1], *M. Sun*[2], *J. Bagchi*[3], *S. W. Allen*[1], *G. B. Taylor*[4], *S. K. Sirothia*[5], *A. Simionescu*[1], *E. T. Million*[6], *J. Jacob*[7], *M. Donahue*[8]

[1]Kavli Institute for Particle Astrophysics and Cosmology, Stanford University, 452 Lomita Mall, Stanford, CA 94305-4085, USA
and SLAC National Accelerator Laboratory, 2575 Sand Hill Road, Menlo Park, CA 94025, USA
[2]Department of Astronomy, University of Virginia, P.O. Box 400325, Charlottesville, VA 22904-4325, USA
[3]Inter University Center for Astronomy and Astrophysics (IUCAA), Post Bag 4, Ganeshkhind, Pune 411 007, India
[4]Department of Physics and Astronomy, University of New Mexico, Albuquerque, NM 87131, USA
[5]National Centre for Radio Astrophysics, Tata Institute of Fundamental Research, Post Bag 3, Ganeshkhind, Pune 411007, India
[6]Department of Physics and Astronomy, University of Alabama, Box 870324, Tuscaloosa, AL 35487, USA
[7]Department of Physics, Newman College, Thodupuzha 685 585, India
[8]Physics&Astronomy Department, Michigan State University, East Lansing, MI 48824-2320, USA

Published in the Monthly Notices of the Royal Astronomical Society, volume 415, pages 3369–3379, 2011

Abstract

We present a multi-wavelength study of the energetic interaction between the central active galactic nucleus (AGN), the intra-cluster medium (ICM), and the optical emission line nebula in the galaxy cluster Sérsic 159-03. We use X-ray data from *Chandra*, high resolution X-ray spectra and UV images from *XMM-Newton*, Hα images from the *SOAR* telescope, *HST* optical imaging, and *VLA* and *GMRT* radio data. The cluster center displays signs of powerful AGN feedback, which has cleared the central regions ($r < 7.5$ kpc) of dense, X-ray emitting ICM. X-ray spectral maps reveal a high pressure ring surrounding the central AGN at a radius of $r \sim 15$ kpc, indicating an AGN driven weak shock. The cluster harbors a bright, 44 kpc long Hα+[N II] filament extending from the centre of the cD galaxy to the north. Along the filament, we see low entropy, high metallicity, cooling X-ray gas. The gas in the filament has most likely been uplifted by 'radio mode' AGN activity and subsequently stripped from the galaxy due to its relative southward motion. Because this X-ray gas has been removed from the direct influence of the AGN jets, part of it cools and forms stars as indicated by the observed dust lanes, molecular and ionized emission line nebulae, and the excess UV emission.

3.1 Introduction

Supermassive black holes (SMBH) play a crucial role in galaxy formation. The correlation between the mass of the central SMBH and the bulge mass of their host galaxies suggests that their evolution is tightly coupled (Magorrian et al. 1998). Outbursts of accreting SMBH (referred to as active galactic nuclei or AGN) disturb and heat the surrounding gas, lowering the accretion rate and, in some cases, driving so much gas out of the galaxy that the star formation is drastically reduced.

The most dramatic portrayal of the interaction between AGN and their surroundings can be seen in the distribution of X-ray emitting gas in nearby giant ellipticals and clusters of galaxies. *Chandra* X-ray images have revealed giant cavities and shocks in the hot gas produced by repeated outbursts of the central AGN (e.g. Fabian et al. 2003a; Nulsen et al. 2005; Forman et al. 2005). These AGN outbursts in principle provide enough power to offset radiative losses, suppress cooling, and prevent further star formation in the dense cores of clusters of galaxies (see e.g. McNamara & Nulsen 2007). Detailed X-ray imaging and 2D spectral mapping of cooling cores with cavities, X-ray bright filaments, and shock fronts, provides the most reliable means of measuring the energy injected into the hot intra-cluster medium (ICM) by AGN, and is a powerful tool to study the physics of the AGN feedback in general (see e. g. Randall et al. 2011a; Million et al. 2010a; Werner et al. 2010; Simionescu et al. 2009b).

Here we present a detailed multi-wavelength study of AGN feedback processes in the core of the nearby (z=0.0564; Maia et al. 1987), relatively poor, low mass cluster of galaxies Sérsic 159-03 (A S1101). The thermal properties and chemical enrichment of the hot ICM in this cooling core cluster have been studied in detail using *XMM-Newton* (Kaastra et al. 2001, 2004; de Plaa et al. 2006). Compared to other cooling core clusters,

Table 3.1: Summary of the radio observations. Columns list the central frequency, the telescope array, the resolution of the beam, its position angle, the rms noise, and the observing date.

Frequency (MHz)	Array	Resolution (arcsec)	P.A. (deg)	rms Noise (μJy beam^{-1})	Obs. date
244	*GMRT*	20.04×8.92	11.0	1420	2007 November 2, 3
325	*GMRT*	17.67×9.08	-179.4	352	2009 May 16,17
617	*GMRT*	8.29×3.13	9.7	250	2009 May 09,11
1400	*VLA*-B	10×4	0.0	64	2006 August 8
8400	*VLA*-B	3.1×0.72	8.3	21	2006 August 8

where the central temperature drops to $\sim$1/3 of the peak ambient value, Sérsic 159-03 has a relatively modest (factor of 1.5) temperature drop in the core (Sun 2009). The radio properties of this cluster have been reported by Bîrzan et al. (2008), in the study of a sample of 24 cooling cores. The bright optical emission line nebulae in the core of the cluster have been studied in detail by Crawford & Fabian (1992) and more recently by Oonk et al. (2010) using integral field spectroscopy.

Throughout the paper we adopt a flat $\Lambda_{\rm CDM}$ cosmology with $H_0 = 70\,{\rm km\,s^{-1}\,Mpc^{-1}}$ and $\Omega_M = 0.3$, which implies a linear scale of 1.2 kpc arcsec^{-1} at the cluster redshift of $z = 0.0564$ (Maia et al. 1987). Throughout the paper, abundances are given with respect to the solar values by Grevesse & Sauval (1998). All errors are quoted at the 68 per cent confidence level.

3.2 Data reduction and analysis

3.2.1 Optical, Hα, and UV data

To study the optical properties of the central cluster galaxy, we analyzed a 600 s observation available in the *Hubble Space Telescope (HST)* archive (proposal ID: 8719). The image was taken with WFPC2 using the F555W filter and placing the galaxy onto the WF3 chip.

Narrow-band optical imaging was performed with the 4.1 m *Southern Astrophysics Research Telescope (SOAR)* telescope on September 13, 2009 (UT) using the *SOAR* Optical Imager (SOI). The night was photometric with a seeing of around 1″. We used the 6916/78 CTIO narrow-band filter for the Hα+[N II] lines, and the 6738/50 filter for the continuum. We took four 1200 s exposures with the 6916/78 filter and four 750 s exposures with the 6738/50 filter. We reduced each image using the standard procedures in the `IRAF MSCRED` package using EG 274 as a spectroscopic standard. The pixels were binned 2×2, for a scale of 0.154″ per pixel. More details on the SOI data reduction can be found in Sun et al. (2007).

We also analyzed near Ultra Violet data obtained by the *XMM-Newton* Optical Monitor on 2002 November 20–21. Exposures were taken with the UVW1 (2400–3600 Å) and UVW2 (1800–2400 Å) filters.

3.2.2 Radio data

The summary of radio observations with the *Giant Metrewave Radio Telescope (GMRT)*[1] and the *Very Large Array (VLA)*, including the observation date, obtained beam, and rms noise, is shown in Table 9.2. The strong, stable calibrator 3C 48 was used for absolute flux density and bandpass calibration at all frequencies. We tied the final flux density scale to the standard 'Baars-scale' (Baars et al. 1977). The *VLA* data were obtained in the B configuration. Their calibration was performed using `AIPS` (Greisen 2003) in the standard fashion, while imaging and self-calibration were performed using `Difmap` (Shepherd et al. 1995).

The *GMRT* data were reduced using `AIPS++` (version: 1.9). After applying bandpass corrections to the phase calibrator, gain and phase variations were estimated, and flux density, bandpass, gain and phase calibration were applied. The data for antennas with high errors in antenna-based solutions were examined and flagged over certain time ranges. Some baselines were also flagged based on closure errors on the bandpass calibrator. Channel and time-based flagging of data points corrupted by radio frequency interference (RFI) was applied using a median filter with a 6σ threshold. Residual errors above 5σ were also flagged after a few rounds of imaging and self calibration. The system temperature ($T_{\rm sys}$) was found to vary with antenna, the ambient temperature and elevation (Sirothia 2009). In the absence of regular $T_{\rm sys}$ measurements for *GMRT* antennas, this correction was estimated from the residuals of corrected data with respect to the model. The corrections were then applied to the data. The final images were made after several rounds of phase self calibration, and one round of amplitude self calibration, where the data were normalized by the median gain for all the data.

3.2.3 *Chandra* X-ray data

The *Chandra* observations of Sérsic 159-03 were taken in August 2009 using the Advanced CCD Imaging Spectrometer (ACIS). The total net exposure time after cleaning is 89.6 ks. We follow the data reduction procedure described in Million et al. (2010b) and Million et al. (2010a). Background spectra were extracted from the appropriate recent blank-sky fields available from the Chandra X-ray Center. These were normalized by the ratio of the observed and blank-sky count rates in the 9.5–12 keV band.

Background subtracted images were created in 13 narrow energy bands, spanning 0.5–7.5 keV. These were flat fielded with respect to the median energy for each image. The blank sky background fields were processed in an identical way to the source observation and reprojected to the same coordinate system. The background subtracted and exposure corrected images were co-added to create the broad band images.

For the spectral analysis, point sources were excluded. The individual regions for the 2D spectral mapping were determined using the Contour Binning algorithm (Sanders 2006), which groups neighboring pixels of similar surface brightness until a desired

[1]The *GMRT* is a national facility operated by the National Centre for Radio Astrophysics of the TIFR, India.

signal-to-noise threshold is met. In order to have small enough regions to resolve substructure and still have enough counts to achieve better than 7 per cent accuracy in the temperature determination, we adopted a signal-to-noise ratio of 35 ($\sim$1230 counts per region). Separate photon-weighted response matrices and effective area files were constructed for each region analyzed.

Spectral modeling has been performed with the SPEX package (SPEX uses an updated version of the MEKAL plasma model with respect to XSPEC, Kaastra et al. 1996) in the 0.6–7.0 keV band. To each bin we fitted a model consisting of absorbed (Galactic $N_{\rm H} = 1.14 \times 10^{20}$ cm^{-2}, based on the LAB survey of H I by Kalberla et al. 2005) collisionally ionized equilibrium plasmas with temperature, spectral normalization (emission measure), and metallicity as free parameters. The new Galactic absorption column density value for Sérsic 159-03 by Kalberla et al. (2005) is significantly lower than the older measurements by Dickey & Lockman (1990), which indicated $N_{\rm H} = 1.79 \times 10^{20}$ cm^{-2}. Using the new absorption values the X-ray spectra of the cluster core do not show the excess soft X-ray emission reported by Bonamente et al. (2005) and Werner et al. (2007).

3.2.4 *XMM-Newton* RGS data

The hot plasma in the core of Sérsic 159-03 exhibits a complex multi-temperature structure (de Plaa et al. 2006). In order to determine the amount of low-temperature cooling X-ray gas in the core and obtain upper limits on the mass deposition rate, we analyze high spectral resolution *XMM-Newton* Reflection Grating Spectrometer (RGS) X-ray data.

The *XMM-Newton* RGS data were obtained on November 20–21 2002, with a net exposure time of 86.3 ks. The data were processed as described in de Plaa et al. (2006). Spectra were extracted from a $4'$ wide extraction region, centred on the optical centre of the galaxy. Because the RGS operates without a slit, it collects all photons from within the $4' \times \sim 12'$ field of view. Line photons originating at angle $\Delta\theta$ (in arcminutes) along the dispersion direction are shifted in wavelength by $\Delta\lambda = 0.138\Delta\theta$ Å. Therefore, every line is broadened by the spatial extent of the source. To account for this spatial broadening in our spectral model, we produce a predicted line spread function (LSF) by convolving the RGS response with the surface brightness profile of the cluster derived from the EPIC/MOS1 image along the dispersion direction. Because the radial profile of a particular spectral line can be different from the overall radial surface brightness profile, the line profile is multiplied by a scale factor s, which is the ratio of the observed LSF to the expected LSF. This scale factor is a free parameter in the spectral fit. We fit the spectra in the 8–28 Å band.

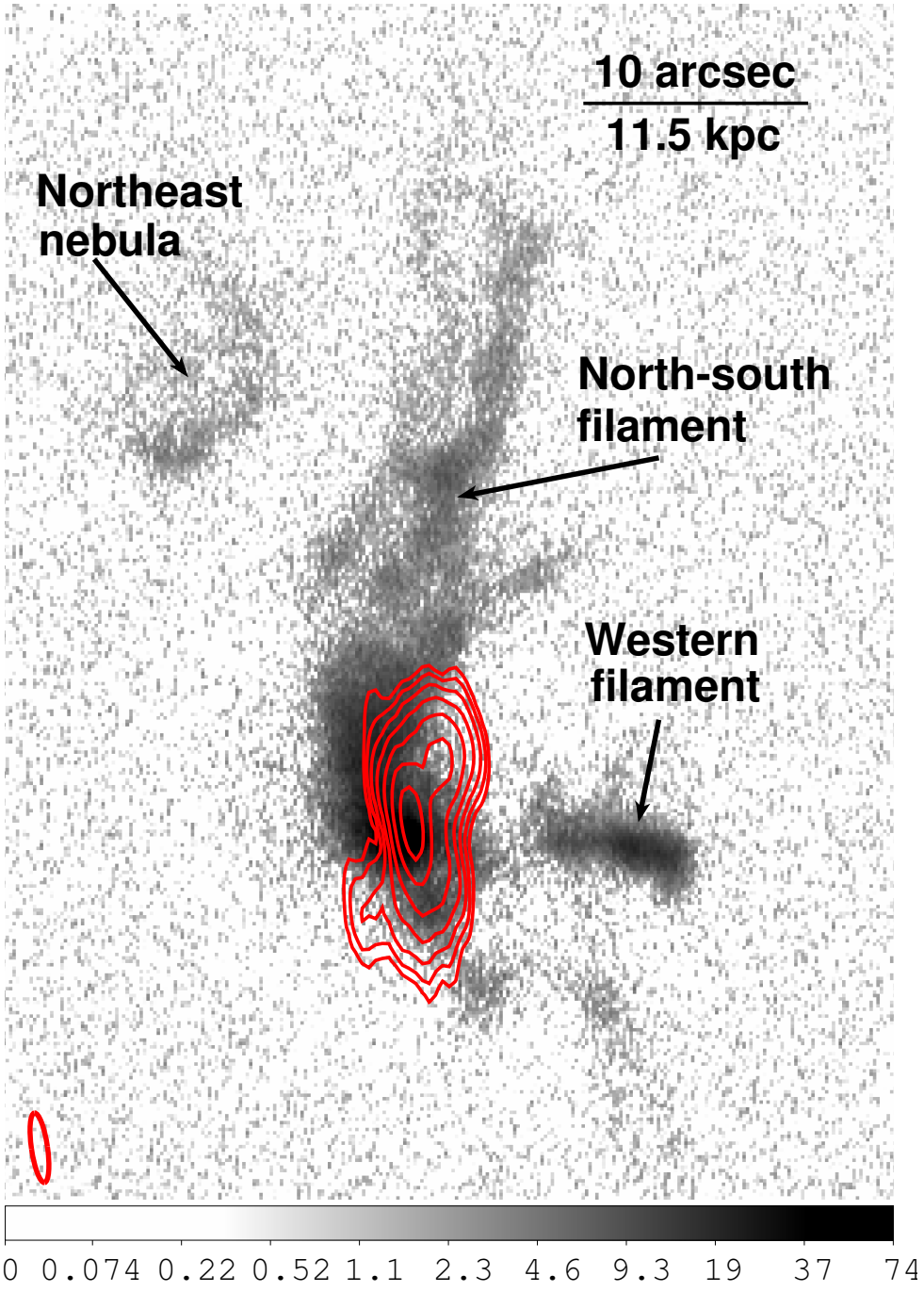

Figure 3.1: Hα+[N II] image obtained with the 4.1 m *SOAR* telescope. The image shows a large 44 kpc long north-south filament, a smaller western filament, and a separate nebula at the northeast. The northern end of the large filament separates into two parallel structures. The contours of the 8.4 GHz radio emission are over-plotted in red and the beam size is indicated by the red ellipse in the bottom left corner. The outermost radio contour is at 0.12 mJy beam^{-1} and the levels increase logarithmically to the innermost contour which is at 4.0 mJy beam^{-1}.

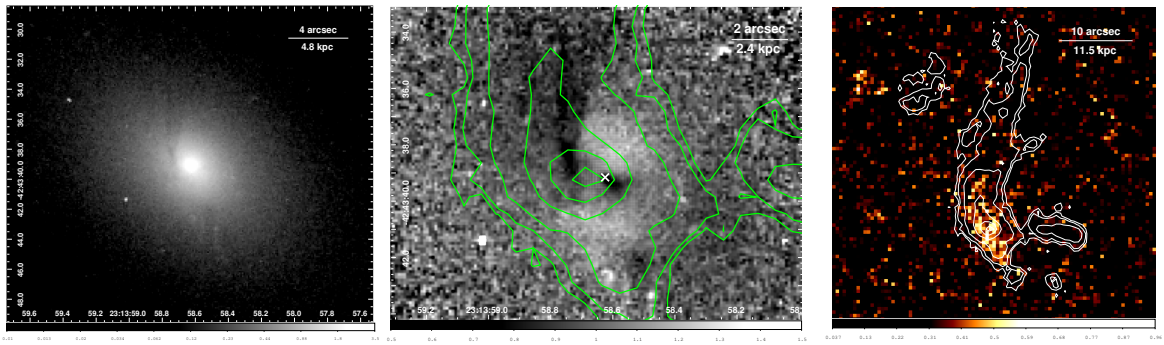

Figure 3.2: *Left panel: HST* image of the central cluster galaxy of Sérsic 159-03 with clear dark dust bands. *Middle panel:* The *HST* image divided by the best fit 2D elliptical de Vaucouleurs model of the galaxy. The white "X" mark indicates the optical center of the galaxy. A 4.5 kpc long dust lane displaced to the east and extending to the north is clearly visible. The inner region of the galaxy is disturbed and not well described by the de Vaucouleurs profile. The green contours show the isophotes of the Hα+[N II] filaments (see Fig. 3.1). *Right panel:* *XMM-Newton* Optical Monitor UVW2 (1800–2400 Å) image of of the core of the galaxy with the Hα contours over-plotted. The UV emission clearly extends along the brightest region of the Hα filament.

3.3 Results

3.3.1 Optical and UV properties

The cooling core of Sérsic 159-03 harbors a remarkable Hα+[N II] emission line filament system shown in Fig. 3.1. This system of emission line nebulae consists of a large 44 kpc long north-south filament extending to the radius of 35 kpc in the north and a smaller western structure extending out to 16 kpc. The total Hα+[N II] flux is 5.9×10^{-14} erg s^{-1} cm^{-2}. Assuming $[\mathrm{N\,II}]_{6583\mathring{A}}/\mathrm{H}\alpha = 1$ and $[\mathrm{N\,II}]_{6548\mathring{A}}/[\mathrm{N\,II}]_{6583\mathring{A}} = 0.35$, the total H$\alpha$ flux is $\sim 2.5 \times 10^{-14}$ erg s^{-1} cm^{-2}. The total luminosity of the Hα line emission (with the [N II] flux excluded) is $L_{\mathrm{Hff}} = 2 \times 10^{41}$ ergs s^{-1}. Our measured Hα flux is higher than the flux $f_{\mathrm{H}\alpha} = 1.79 \pm 0.15 \times 10^{-14}$ erg s^{-1} cm^{-2} measured by McDonald et al. (2010), who used a filter with a 10 times narrower bandpass targeting only the Hα emission lines. A separate nebula can be seen 25 kpc to the northeast of the core.

Assuming a volume filling fraction of unity, a cylindrical geometry in the Hα bright regions, optically thin ionized gas, isotropic radiation, and case B recombination at 10^4 K (Bland-Hawthorn & Maloney 1999), the total mass of the Hα emitting gas is about 2.7×10^9 $M_\odot$. However, these optical filaments most likely consist of many thin threads with very small volume filling fractions (e.g. Fabian et al. 2008). The inferred mass is therefore likely to be significantly overestimated.

The giant elliptical galaxy in the core of Sérsic 159-03 has its major axis aligned in the northeast-southwest direction (left panel of Fig. 3.2). The *HST* data reveal a

Table 3.2: Radio flux densities. The flux densities obtained by *GMRT* and *VLA* are from this work, the values obtained at 408 MHz and 843 MHz by *MOST* are from the MRC (Large et al. 1981) and SUMSS surveys (Bock et al. 1999; Mauch et al. 2003). The flux density at 4.75 GHz obtained by *ATCA* is from Hogan et al. in preparation.

Frequency (MHz)	Array	Flux density (Jy)
244	*GMRT*	3.360 ± 0.20
325	*GMRT*	2.024 ± 0.20
408	*MOST*	1.390 ± 0.10
617	*GMRT*	0.786 ± 0.05
843	*MOST*	0.472 ± 0.014
1425	*VLA*-B	0.235 ± 0.020
4752	*ATCA*	0.0469 ± 0.007
8400	*VLA*-B	0.0313 ± 0.005

4.5 kpc long dust lane extending from the centre to the north, coincident with the bright Hα emitting gas. It is displaced to the east from the core of the galaxy by about 1.2″ ($\sim$1.4 kpc). The dust lane is clearly visible in the middle panel of Fig. 3.2, where the *HST* image is divided by the best fit 2D elliptical de Vaucouleurs model. This ratio image also uncovers a fainter dust lane to the south of the core. The over-subtraction of the emission from center of the galaxy by the model shows that the surface brightness of the stellar core is flatter than the de Vaucouleurs profile. We do not detect optical emission from the AGN.

Near Ultra Violet images (NUV) from the *XMM-Newton* Optical Monitor show diffuse emission which is co-spatial with the dust lanes and the emission line nebulae, providing a strong indication for current star-formation (right panel of Fig. 3.2). After correcting for coincidence, dead-time loss, and time sensitivity degradation, the total UVW1 luminosity within a radius of 7 arcsec is 3.7×10^{42} ergs s^{-1}. Based on Cardelli et al. (1989), the Galactic extinction in the UVW1 band was assumed to be 0.07 mag and the unknown internal extinction was set to zero. We measured the 2MASS J-band luminosity within the same aperture and subtracted the contribution from the passive stellar population from the empirical $L_{\rm UVW1} - L_{\rm J}$ relation derived by Hicks & Mushotzky (2005). We find a net NUV luminosity excess of $\sim$$2.3\times10^{42}$ ergs s^{-1}. Without correcting for internal extinction, we obtain a UVW2-UVW1 color $\sim$0.4 mag.

3.3.2 Radio morphology

The contours of the 8.4 GHz radio emission in Fig. 3.1 and 3.3 resolve the source into an S-shape, oriented primarily north-south, with a compact central feature of flux density 6.3 mJy/beam, which is approximately the fifth of the total radio flux at this frequency. The jets seem to start out in the northeast-southwest direction, before bending clock-

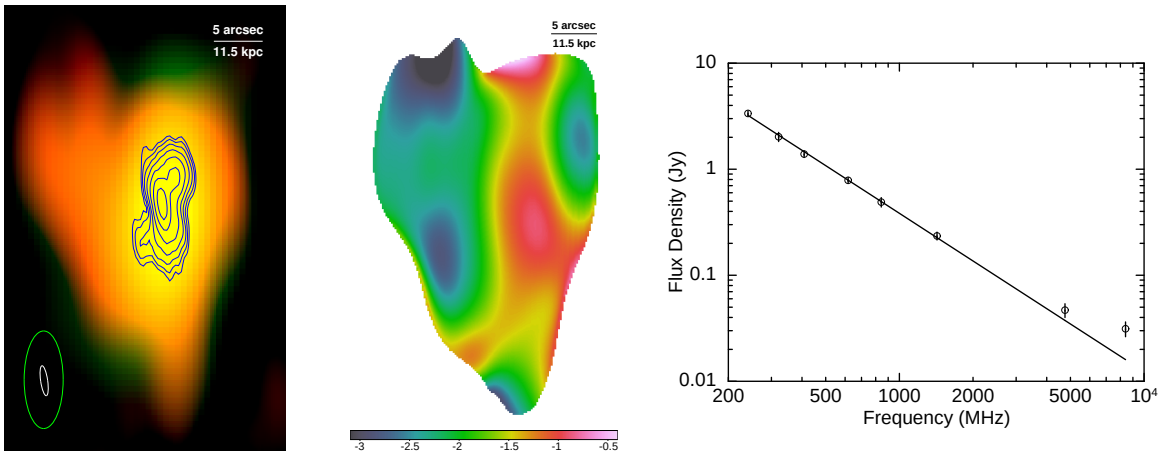

Figure 3.3: *Left panel:* Red+green color image, produced from the radio data at 617 MHz (red) and 1.4 GHz (green), with the 8.4 GHz radio contours overplotted. The beam sizes of the 8.4 GHz and 1.4 GHz radio emission are indicated by the white and green ellipses in the bottom left corner. The outermost contour of the 8.4 GHz radio emission is at 0.12 mJy beam^{-1} and the levels increase logarithmically to the innermost contour which is at 4.0 mJy beam^{-1}. *Central panel:* Spectral index map produced by combining the 617 MHz *GMRT* and the 1.4 GHz *VLA* radio data. The radio maps show the innermost 0.5×0.78 arcmin^2 region of the cluster. The radio maps at the two frequencies have been matched in resolution. *Right panel:* The broad band radio spectrum between 244 MHz and 8.4 GHz. The radio spectrum between 244 MHz and 1.4 GHz can be described by the overplotted power-law $S_\nu \propto \nu^{-\alpha}$ with index $\alpha = 1.49$.

wise. The centers of the radio and optical emission are well aligned. At 1.4 GHz the total flux density is ∼230 mJy and shows a core with an extension ∼12 arcseconds to the east (see the white contours in Fig. 3.4). In the 617 MHz *GMRT* radio map, the morphology of the radio emission is nearly identical to 1.4 GHz. The extension to the east is also detected at 617 MHz and seems to be divided into two filaments. The lower frequency GMRT radio maps do not significantly resolve the radio source.

In the left panel of Fig. 3.3 we show a red+green color image, produced from the radio data at 617 MHz (red) and 1.4 GHz (green) with the contours of the 8.4 GHz radio emission overplotted. This combined radio image clearly shows the extension to the east. The central panel of Fig. 3.3 shows the spectral index map of the core of Sérsic 159-03 produced by combining the 617 MHz *GMRT* and the 1.4 GHz *VLA* radio data. Only data above 2 mJy/beam at 617 MHz and 0.2 mJy/beam at 1.4 GHz were included. To the east, north-east and north-west of the core the radio emission has a very steep spectrum described by a power-law $S_\nu \propto \nu^{-\alpha}$ with index $\alpha > 2.2$. The spectrum of the central region is flatter with index $\alpha \sim 1$.

In Table 3.2 we show the integrated radio flux densities at five different frequencies obtained with *GMRT* and *VLA*. We also list the published flux densities obtained by the MRC survey at 408 MHz (Large et al. 1981) and by the SUMSS survey at 843 MHz (Bock et al. 1999; Mauch et al. 2003) performed with the *Molonglo Observatory Synthesis Telescope (MOST)*. The integrated flux density at 4.75 GHz obtained by the *Australia Telescope Compact Array (ATCA)* is from Hogan et al. in preparation. The broad band radio spectrum is shown in the right panel of Fig. 3.3. Between 244 MHz and 1.4 GHz the integrated spectrum can be described by a power-law $S_\nu \propto \nu^{-\alpha}$ with $\alpha = 1.49$. At high frequencies, between 4.8 GHz and 8.4 GHz, however, the best fit power-law is significantly flatter with index $\alpha = 0.71$.

3.3.3 X-ray imaging: a disturbed morphology

The X-ray data show no evidence for a point source associated with the central radio source. Assuming a power-law like spectrum with a photon index $\Gamma = 2.0$, a conservative upper limit on the X-ray flux in the 2–10 keV band is $f_X = 2.3 \times 10^{-15}$ erg s^{-1} cm^{-2}. The large scale X-ray emission from the cluster is elongated in the same northeast-southwest direction as the major axis of the cD galaxy. The X-ray emission does not show obvious sharp surface brightness discontinuities, indicative of cold fronts due to sloshing gas.

While the large scale X-ray morphology of Sérsic 159-03 is relatively relaxed, its core is strongly disturbed. The brightest, densest X-ray emitting gas is displaced northward from the centre of the cD galaxy to a radius of $r \sim 8$ kpc. In the top left panel of Fig. 3.4, we show the smoothed *Chandra* image of the cluster core in the 0.5–7.5 keV band. The black cross indicates the position of the central AGN. In the top right panel, we show the same image, with the contours of the Hα+[N II] emission over-plotted in black, and the contours of the 8.4 GHz and 1.4 GHz radio emission over-plotted in blue and white, respectively. The lower panels of Fig. 3.4 show the same *Chandra* images divided by their best fit 2D elliptical double beta model. The images shows a bright ridge of dense thermal X-ray gas displaced by about 8 kpc to the north of the AGN and a clumpy

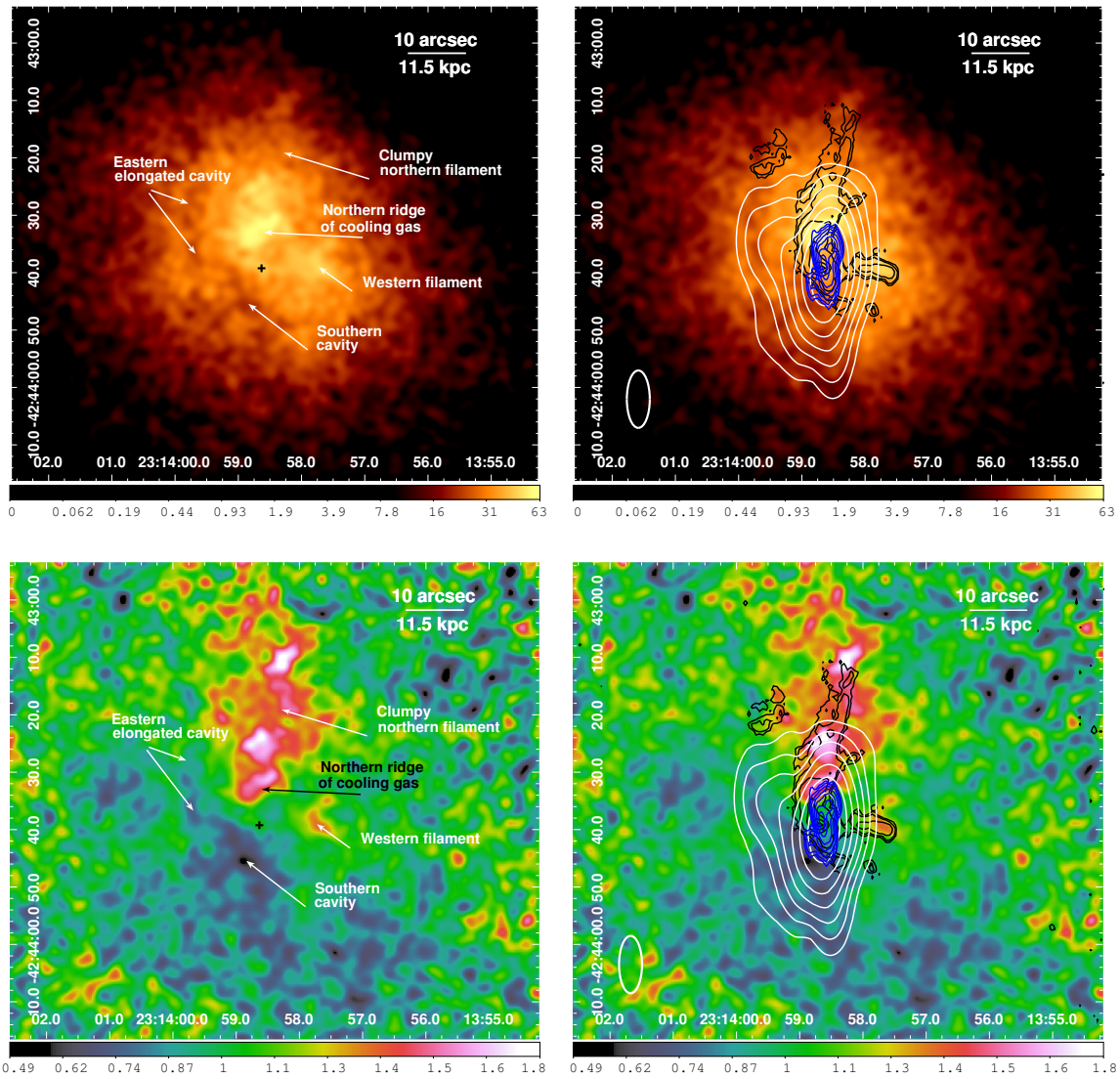

Figure 3.4: *Top left panel:* Background subtracted, flat-fielded *Chandra* X-ray image of the core of Sérsic 159-03 in the 0.5–7.5 keV band. The cross indicates the position of the central radio source. *Top right panel:* The same *Chandra* image with over-plotted contours of the 8.4 GHz (blue) and 1.4 GHz (white) radio emission, and with the contours of the Hα+[N II] line emission (black). The beam size of the 1.4 GHz radio emission is indicated by the white ellipse in the bottom left corner. The outermost radio contour is at 0.3 mJy beam^{-1} and the levels increase logarithmically to the innermost contour which is at 137.7 mJy beam^{-1}. The contours of the 8.4 GHz radio emission are the same as in Fig. 3.1 and 3.3. The dense cooling gas is displaced to the north of the centre of the galaxy and the region within $r \lesssim 7.5$ kpc is void of dense gas. *Lower left panel:* The *Chandra* image divided by the best fit 2D elliptical double beta model. Note the clear structure to the north. *Lower right panel:* The same ratio image with the contours of the radio and Hα+[N II] emission over-plotted. The images have been smoothed with a Gaussian kernel.

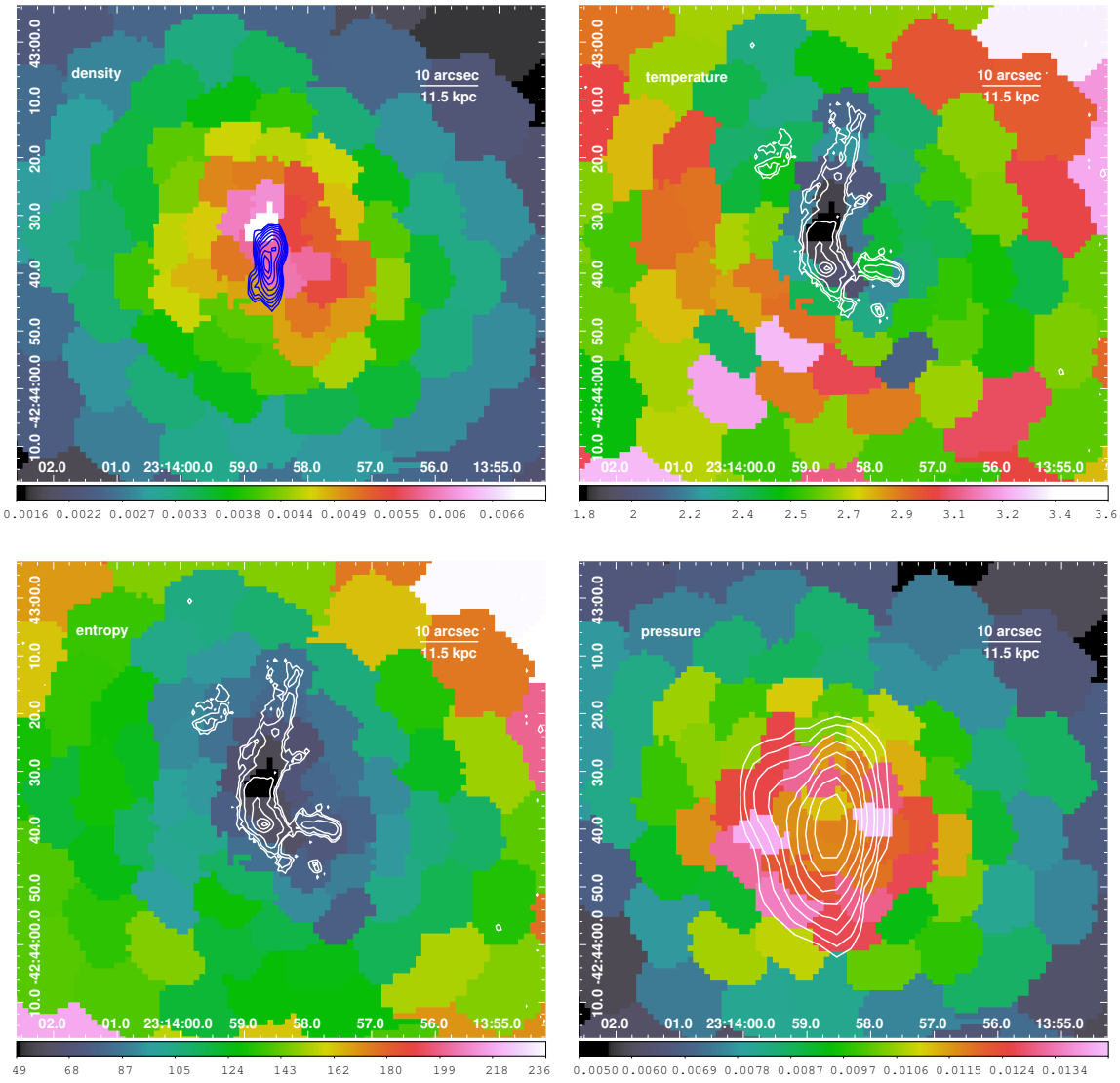

Figure 3.5: 2D maps of density (in units of $\mathrm{cm}^{-3} \times \left(\frac{l}{2\mathrm{Mpc}}\right)^{-1/2}$; top left panel), temperature (in units of keV; top right panel), pressure (in units of keV $\mathrm{cm}^{-3} \times \left(\frac{l}{2\mathrm{Mpc}}\right)^{-1/2}$; lower right panel), and entropy (in units of keV $\mathrm{cm}^{2} \times \left(\frac{l}{2\mathrm{Mpc}}\right)^{1/3}$; lower left panel). The maps were obtained by fitting each S/N$\sim$35 region independently with a single temperature thermal model, yielding 1σ fractional uncertainties of $\sim$7–10 per cent on the temperature. The contours of the Hα+[N II] optical line emission are over-plotted on the temperature and entropy maps. The contours of the 8.4 GHz and 1.4 GHz radio emission are over-plotted on the density and pressure map, respectively.

X-ray filament extending along the Hα filament to 31 kpc beyond this ridge. Another X-ray filament extends to the west and coincides with the western optical emission line nebula.

The ridge of dense, thermal X-ray emitting gas to the north of the AGN seems to be interacting with, and confining, the 8.4 GHz radio emitting plasma (blue contours in Fig. 3.4). The jets appear distorted by the interaction with the dense cooling gas. The 1.4 GHz radio plasma also appears deflected by the ridge of dense gas to the east, where it fills a gap - an elongated cavity - in the X-ray surface brightness distribution. This elongated cavity is possibly composed of two cavities. The X-ray surface brightness drops sharply to the southeast of the AGN, forming an apparent cavity with a radius of $\sim$11 kpc, filled by 1.4 GHz radio emission. This drop in surface brightness is spatially coincident with the sharp southeastern edge of the bright emission line nebulae.

3.3.4 Thermodynamic properties of the core

The disturbed morphology of the cluster core is also reflected in the 2D maps of density, temperature, entropy, and pressure shown in Fig. 3.5. The ICM spatially associated with the large north-south Hα filament has a relatively low projected temperature (top right panel of Fig. 3.5). The high density (top left panel of Fig. 3.5) and low temperature of this feature translate into low entropy (lower left panel of Fig. 3.5). The western filament, on the other hand, has a significantly higher temperature and entropy.

The projected thermal pressure peaks in an approximate ring surrounding the core at a radius of $r \sim 15$ kpc (lower right panel of Fig. 3.5). The pressure in this ring consisting of over fifteen independently fitted adjacent regions is approximately 20 per cent higher than in the center, indicating an AGN driven weak shock. The maps reveal that the relatively over-pressured gas to the southeast of the core has approximately 1.2 times higher temperature than the surrounding gas, which is consistent with the hotter gas having been compressed and heated by an AGN driven shock.

The metallicity of the ICM along the Hα+[N II] filaments is higher by $\sim$0.3 Solar than that of the surrounding plasma (see Fig. 3.6). The metallicity increase is not significant in any single region, the error on the metallicity in every region is $\sim$0.20 Solar. However, the fact that the increase is seen in 5 independently fitted adjacent regions along the filament makes this result interesting. The apparent metallicities of the bright northern ridge of cooling plasma and of the core are, however, low. It has been shown that the metallicity is sensitive to the modeling of the underlying temperature structure and, if multi-temperature plasma is modeled with a single-temperature spectral model, the metallicity of gas can be significantly underestimated (e.g. Buote 2000a). The low metallicities of these features thus indicate the presence of multi-phase gas.

3.3.5 High resolution X-ray spectra

In order to determine whether cooling X-ray gas with $kT < 1$ keV is present in the core of the cluster, we examine the *XMM-Newton* RGS spectra (see Fig. 3.7) to search for low

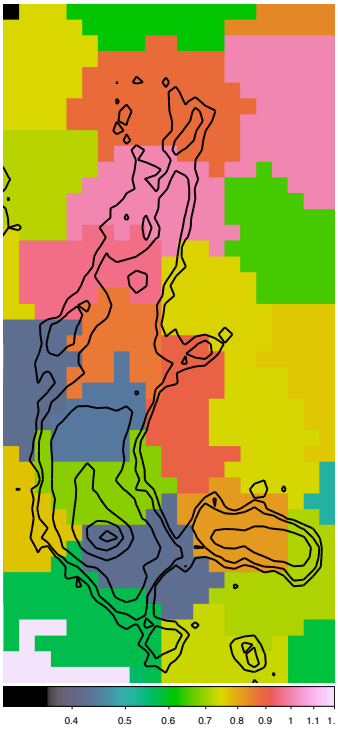

Figure 3.6: Metallicity map of the core of the cluster with the contours of the Hα+[N II] optical line emission over-plotted. The metallicity of the ICM along the filament is higher than that of the surrounding medium. The apparent metallicity of the bright 'northern ridge' and of the core is low, indicating the presence of multi-phase gas.

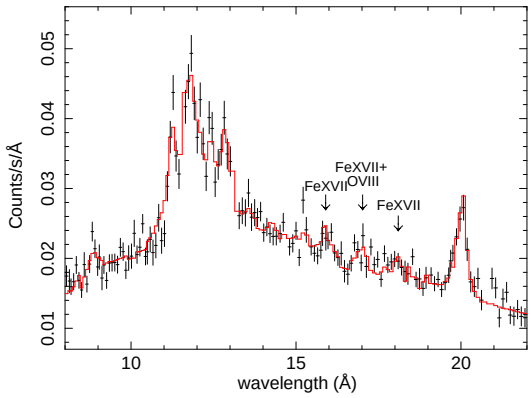

Figure 3.7: The first order *XMM-Newton* RGS spectrum extracted from a 4′ wide region centred on the core of Sérsic 159-03. The continuous line represents the best fit model to the spectrum. Fe XVII lines emitted by plasma with $kT < 0.9$ keV are clearly visible in the spectrum.

Table 3.3: Best fit parameters for a four-temperature fit and a CIE+two-cooling-flow model fit to the high-resolution RGS spectra extracted from a $4'$ wide region centred on the core of Sérsic 159-03. Emission measures, $Y = \int n_{\rm H} n_{\rm e} {\rm d}V$, are given in 10^{66} cm^{-3}. Radiative cooling rates are given in $M_\odot$ yr^{-1}. The scale factor s is the ratio of the observed LSF to the expected LSF based on the overall radial surface brightness profile. The upper limits are quoted at their 95 per cent confidence level. Abundances are quoted with respect to the values of Grevesse & Sauval (1998).

Parameter	4T-model	CIE+c.f.+c.f. model
$Y_{0.25{\rm keV}}$	0.05 ± 0.04	–
$Y_{0.75{\rm keV}}$	0.19 ± 0.03	–
$Y_{1.5{\rm keV}}$	0.7 ± 0.3	–
$Y_{3.0{\rm keV}}$	12.1 ± 0.3	–
Y_{CIE}	–	12.3 ± 0.2
$\dot{M}_{1.9-0.5{\rm keV}}$	–	82 ± 11
$\dot{M}_{0.5-0.1{\rm keV}}$	–	< 25
kT (keV)	–	3.05 ± 0.16
s	1.12 ± 0.13	1.13 ± 0.11
O	0.39 ± 0.04	0.43 ± 0.04
Ne	0.43 ± 0.12	0.44 ± 0.11
Fe	0.78 ± 0.04	0.82 ± 0.06

temperature line emission (primarily Fe XVII) tracing rapidly cooling gas. We fit the RGS data with a model consisting of collisionally ionized equilibrium plasmas at four fixed temperatures (0.25 keV, 0.75 keV, 1.5 keV, and 3 keV) with variable normalizations and common metal abundances. The abundances of O, Ne, Mg, and Fe are free parameters in the fit. Our fit confirms the presence of relatively cool, $kT < 1$ keV plasma. Based on the lack of O VII line emission however, which is emitted at $kT < 0.4$ keV, we place a strong upper limit on the amount of gas cooling radiatively to very low temperatures. Our 90 per cent confidence upper limit on the emission measure of gas with $kT = 0.25$ keV is $Y = \int n_{\rm H} n_{\rm e} dV = 9 \times 10^{64}$ cm^{-3}, which is about 50 per cent of the best fit emission measure for the 0.75 keV gas.

In order to place constraints on the amount of cooling in the cluster core we fit the RGS spectra with a separate model consisting of thermal plasma in collisional ionization equilibrium and two isobaric cooling flow models. The first cooling flow model is used to account for gas with temperatures between $kT_{\rm upper} = 1.9$ keV and $kT_{\rm Lower} = 0.5$ keV, which appears to be the 'temperature floor' in several cooling core clusters (Sanders et al. 2009, 2010a; Werner et al. 2010). The second cooling flow model is used to place an upper limit on the radiative cooling rate from 0.5 keV down to cold gas. While in the temperature range of 1.9–0.5 keV the data are formally consistent with a radiative cooling rate of $\dot{M} = 82 \pm 11\ M_\odot$ yr^{-1}, the 95 per cent confidence upper limit for radiative cooling from 0.5 keV to lower temperatures is only 25 $M_\odot$ yr^{-1}.

3.4 Discussion

3.4.1 Displacement of gas from the cD galaxy

The core of Sérsic 159-03 has a remarkably complex and rich morphology at all wavelengths. It displays signs of a powerful AGN feedback. The central regions of the galaxy ($r < 7.5$ kpc) are cleared of the densest, X-ray emitting ICM and the cluster core displays a massive, bright Hα filament extending northward from the centre of the cD galaxy to a radius of 35 kpc. This long filament is reminiscent of that in Abell 1795 (Fabian et al. 2001; Crawford et al. 2005; McDonald & Veilleux 2009).

While the densest cooling X-ray plasma has been pushed away and uplifted from the cooling core by the radio jets to a radius of at least $r \sim 8$ kpc, the brightest core of the Hα emission is not displaced from the galactic nucleus. The most likely reason is that the Hα emitting gas is only a thin layer on an underlying large reservoir of dense atomic and molecular gas at the base of the galaxy potential, which is difficult to uplift entirely. Observations of K-band emission lines of molecular and ionized hydrogen with the SINFONI integral field spectrograph reveal extended filaments in the core of Sérsic 159-03, tracing closely each other and the Hα emission (Oonk et al. 2010). The line-of-sight velocities, as measured by Oonk et al. (2010), show a striking east/west dichotomy, suggesting that part of the velocity vector of the jets, which push and uplift the gas, is oriented along our line of sight. The gas to the east of the stellar core has a radial velocity of $\sim$200 km s^{-1} with respect to the cD galaxy, which seems to be decreasing with the distance from the nucleus. The observed interaction between the

radio jets and the Hα emitting gas (see Fig. 3.1) indicates that the gas is being pushed out by the radio jets and is not falling in along our line of sight.

The radial velocity distribution of the gas along the western filament goes smoothly from about -200 km s^{-1} to +50 km s^{-1} with increasing distance from the core, indicating circular motion, which is consistent with the uplift scenario, but not with an alternative scenario of a simple infall from the surrounding hot X-ray halo.

The morphology of the cooling filamentary gas indicates relative gas motions with the ambient ICM moving toward the northwest, dragging and bending the Hα filament. The gas uplifted by the jet in the southwestern direction has been dragged to the west and the gas uplifted towards northeast has been displaced in the north-northwestern direction. These relative gas motions are most likely the result of the south-southeastward peculiar motion of the cD galaxy.

Relatively cool X-ray gas is present along the whole northern filament of Sérsic 159-03, but the correlation between the Hα and soft X-ray emission is not perfect. We see clumps of dense, cooling X-ray emitting plasma at $\sim$8 kpc and at $\sim$17 kpc, but no obvious Hα peaks at the same locations. The 'northern ridge' at $r \sim 8$ kpc has the coldest projected temperature and lowest entropy. The X-ray filament extends to the north by about 3 kpc further than the observed Hα filament. The relatively low temperature and entropy, and high metallicity of the filament compared to the ambient plasma (see Fig. 3.5 and 3.6) indicate that the filamentary system has been uplifted and stripped from the cD galaxy. The western Hα+[N II] filament is also surrounded by bright, dense X-ray emitting gas, but its projected temperature is $\sim$0.8 keV higher. The western filament might have been shock heated or its gas might have gotten mixed with the hotter ambient plasma.

Gas uplift by buoyant radio-emitting plasma, supplied by the jets of the AGN, has also been observed in other cooling core clusters. Detailed spectroscopic mapping of the cooling core of the Virgo Cluster, centered on M87, shows clearly that radio mode AGN feedback is highly efficient in stripping the core of the galaxy of its lowest entropy gas (Werner et al. 2010). The total mass of uplifted gas in M87 is 6–9$\times 10^8$ $M_\odot$, which is similar to the current gas mass within its innermost $r \sim 3.8$ kpc region. The disruption of the core of Sérsic 159-03 is considerably larger than that of M87, but by no means extreme. The AGN feedback in the Hydra A cluster is responsible for the uplift of a few times 10^9 $M_\odot$ of low entropy plasma (Simionescu et al. 2009a). Recently, Ehlert et al. (2011a) presented a multi-wavelength study of the cluster MACS J1931.8-2634 where extreme AGN feedback with a jet power of $P_{\rm jet} \sim 10^{46}$ erg s^{-1} and the sloshing gas disrupted the core, separating it into two X-ray bright ridges, which are currently at a distance of $\sim$25 kpc from the core.

3.4.2 Cooling of the displaced gas and star-formation

To the north of the AGN, we see cooling X-ray plasma displaced by about 8 kpc from the nucleus, producing a prominent bright ridge which confines the high frequency radio plasma. The northern X-ray filament extends 31 kpc beyond this ridge. The relatively dense uplifted X-ray emitting gas, which is removed from the direct influence of the AGN jets, will cool in the absence of heating and eventually form stars. Multiphase

cooling X-ray gas, displaced from the center of the cD galaxy and spatially coincident with Hα emission, has also been seen in the Ophiuchus Cluster, in Abell 2052, and in MACS J1931.8-2634 (Million et al. 2010a; Edwards et al. 2009; de Plaa et al. 2010; Ehlert et al. 2011a).

Assuming that the filament has been uplifted at half of the sound speed (at 400 km s^{-1}), the age of the filament will be $\sim 10^8$ yr. That is approximately equal to the cooling time of 1 keV plasma in pressure equilibrium with the ambient ICM at the observed location. The *XMM-Newton* RGS spectra clearly reveal Fe XVII line emission associated with gas cooling to $kT < 1$ keV. The 95 per cent confidence upper limit on radiative cooling below 0.5 keV is 25 $M_\odot$ yr^{-1}.

The densest and coolest X-ray emitting clumps, in particular the bright multiphase 'northern ridge', will cool and form narrow Hα emitting filaments (e.g. see simulations by Sharma et al. 2010), along which some of the gas might eventually fall back towards the cluster centre. It is possible that a significant fraction of the Hα emitting gas in the northern filament at large radii is due to the cooling of the uplifted X-ray emitting plasma. The cold gas is likely to go on to eventually form stars. The *XMM-Newton* OM UVW2 and *Galex* images (McDonald et al. 2010) indicate that the UV emission is extended along the brightest regions of the northern Hα filament, indicating ongoing star formation.

The *HST* images show that the brightest regions of the filament are dusty. An infrared survey with the *Spitzer Space Telescope*, however, did not detect the system at 70μm (Quillen et al. 2008) indicating that the filaments do not contain an exceptionally large amount of warm dust. The excess UV emission from the cD galaxy corresponds to a star-formation rate of $\sim$2.3 $M_\odot$ yr^{-1} for the assumed Salpeter IMF. Assuming the Kennicutt (1998) relation, SFR $(M_\odot \text{ yr}^{-1}) = 7.9 \times 10^{-42}$ ($L_{\mathrm{H}\alpha}$/erg s^{-1}), and neglecting intrinsic extinction due to dust, the measured Hα luminosity corresponds to a star-formation rate of 1.5 $M_\odot$ yr^{-1}. Accounting for internal extinction would further increase the intrinsic Hα and NUV fluxes. Star-formation, however, is most likely not the only heating and ionizing source in the cluster center.

The large turbulent velocities and the elevated [N II]/Hα ratio of $\sim$1.5 in the nucleus (Crawford & Fabian 1992) indicates that the interaction with the radio jets contributes strongly to the heating of the gas in the center. The [N II]/Hα line ratios of 0.6 in the western filament are relatively high as well (Crawford & Fabian 1992), indicating the presence of an additional non-ionizing source of energy at larger radii (see e.g. Ferland et al. 2009).

Based on the data for M87, Werner et al. (2010) proposed that the Hα filaments in its core may be powered by shock induced mixing of cold gas with the surrounding ICM (see Begelman & Fabian 1990). By bringing the hot thermal particles into contact with the cool gas, mixing can supply the power and ionizing particles to explain the observed spectra. Hot ICM electrons that penetrate into the cold gas excite the molecular hydrogen and deposit heat. This scenario has been explored theoretically by Ferland et al. (2008, 2009), who studied heating by cosmic-rays, which affect the cooler ionized and neutral components in a similar way to hot ICM electrons. The fact that the soft X-ray emission traces the Hα emitting gas suggests that this process could be responsible for part of the Hα+[N II] line emission, part of the UV emission, and for

the non-radiative cooling of the coldest X-ray gas in Sérsic 159-03.

The most similar known X-ray/Hα filament system is observed in Abell 1795. In that cluster the filament extends for 50 kpc. The cD galaxy at the head of this filament is moving with respect to the ICM and the emission line nebula may originate from a runaway cooling of the hot X-ray emitting gas in the wake of that motion (Fabian et al. 2001; Markevitch et al. 2001; McDonald & Veilleux 2009). The filamentary system in Sérsic 159-03, however, is most likely the result of AGN driven uplift and ram pressure stripping from the cD galaxy. The filament in Abell 1795 is composed of a pair of thin $w < 1$ kpc intertwined Hα+[N II] filaments (McDonald & Veilleux 2009), spatially coincident with relatively cool X-ray emitting gas (Fabian et al. 2001), and with chains of FUV-bright young star clusters condensing from the cooling gas in the filament (Crawford et al. 2005; McDonald & Veilleux 2009). The northern end of the large Hα filament in Sérsic 159-03 separates into two narrow, parallel structures. Given a better spatial resolution, we would most likely resolve the filament into more thin threads. As discussed by Fabian et al. (2008) for the emission line nebulae in the core of the Perseus Cluster, the thin thread-like filamentary structures are most likely stabilized by magnetic fields. These magnetic fields might be possible to detect using Faraday Rotation against the polarized jet emission (as has been done for the filaments in the Centaurus Cluster by Taylor et al. 2007).

3.4.3 The powerful radio mode AGN

The core of Sérsic 159-03 harbors a powerful radio mode AGN. Inflating the southern cavity, which has a radius of $\sim$11 kpc and is approximately spherical, in the surrounding medium with a thermal pressure of $p = 0.065$ keV cm^{-3}, required a $4pV$ work of about 7×10^{58} ergs, indicating powerful jets. However, no optical or X-ray point source is presently seen at the position of the radio bright AGN. Using the 'Black hole fundamental plane' relation of Merloni et al. (2003), for a 10 mJy core flux at 4.75 GHz and for a black hole mass of 6×10^8 $M_\odot$ (determined from the K-band bulge luminosity by Rafferty et al. 2006), the expected X-ray core flux is 2.4×10^{-13} erg s^{-1} cm^{-2}. This value is two orders of magnitude higher than our conservative upper limit of 2.3×10^{-15} erg s^{-1} cm^{-2}. The observed scatter around the 'Black hole fundamental plane' is, however, large. The radio luminosities of some other well known brightest cluster galaxies (e.g. NGC 1275) also show similar offsets with respect to the expected relation.

The radio morphology is similar to 4C26.42 in Abell 1795 (Liuzzo et al. 2009) and it is also reminiscent of PKS 1246-410 in the Centaurus Cluster (Taylor et al. 2007). The distortion of the jets, and the change in the axis from N-S to E-W, is most likely due to the strong interactions with the dense gas. The velocity dispersion of the NIR emission lines, which sharply increases in the nuclear region (Oonk et al. 2010) shows that the interaction of the jets with the cold gas is the strongest within the innermost 2 kpc region. The presence of cold, high density material in the cluster core is likely to decelerate the jets, which might entrain thermal gas, slow down to subsonic velocities, and continue to rise buoyantly. Such deceleration due to strong interaction with dense gas on small scales has been seen using VLBA observations in Hydra A (Taylor 1996)

and Abell 1795 (Liuzzo et al. 2009). While the 1.4 GHz and 617 MHz radio plasmas appear to be deflected by the dense 'northern ridge of cooling plasma' to the east, forming the 'eastern elongated X-ray dark cavity', the younger radio jet seen at 8.4 GHz is being deflected to the northwest where it is likely to continue to buoyantly rise along the short axis of the cluster. The 8.4 GHz southern jet is being deflected by the Hα emitting gas to the southeast where it is partly filling the 'southern X-ray cavity'.

Between 244 MHz and 1.4 GHz the integrated radio emission in the cluster core has a remarkably steep power-law spectrum $S_\nu \propto \nu^{-\alpha}$ with index $\alpha = 1.49$. At higher frequencies, however, the radio spectrum flattens to index $\alpha = 0.71$. At the 4.75 GHz *ATCA* radio map (Hogan et al. in prep.), the radio morphology is very similar to that at 8.4 GHz, indicating that the flatter part of the integrated radio emission originates in the $\sim$10 kpc scale inner lobes (see the contours in the left panel of Fig. 3.3) where active jets are injecting relativistic particles. At the lower frequencies the radio emission is more extended, indicating an older population of electrons. The spectral index map produced from the 617 MHz and 1.4 GHz radio data (central panel of Fig. 3.3) shows that while in the central regions $\alpha \sim 1$, to the east, where the radio plasma seems to be filling the elongated cavity, the spectral index steepens to $\alpha > 2$. The spectral index also steepens in the northwest, where the plasma fills a region with a relative deficit in X-ray surface brightness. This radio plasma is most likely buoyant and exerting work on the surrounding medium.

The steep integrated spectrum of the radio source is similar to radio mini-halos found within the cooling radius of some clusters (e.g Ferrari et al. 2008). The morphology of the extended radio emission, however, indicates that it is due to the plasma from the radio jets which have been decelerated, deflected and confined by the interaction with the dense gas. A steep radio spectral index has been found in other cooling core clusters (e.g., PKS 0745-191, A2029, A4059, A2597 Taylor et al. 1994; Pollack et al. 2005) and taken as an indicator of confinement.

Our thermodynamic maps show that the projected thermal pressure peaks in an approximate ring surrounding the AGN. The pressure in the ring is approximately 20 per cent higher than in the center, indicating the presence of an AGN driven shock front. The high pressure region to the south of the AGN is hotter in multiple independently fitted adjacent regions than the plasma both outside and inside this feature. The observed projected temperature jump of $\Delta T \sim 1.2$ suggests a shock with a Mach number of $M \sim 1.5$. The complex X-ray morphology with a cavity inside the shock front unfortunately prevents a more precise modeling of the shock. The relatively modest, factor of 1.5, temperature drop in the core of this cluster (Sun 2009) also points towards a relatively strong AGN feedback activity. AGN induced shocks, which may be the most significant channel for heating of the ICM near to the AGN, have also been observed around M87 in the center of the Virgo Cluster and in Hydra A, (Forman et al. 2005; Million et al. 2010a; Nulsen et al. 2005; Simionescu et al. 2009b).

3.5 Conclusions

We performed a multi-wavelength study of the energetic interaction between the central AGN, the ICM, and the optical emission line nebula in the galaxy cluster Sérsic 159-03. We conclude that:

- Powerful 'radio mode' AGN feedback and possible ram pressure cleared the central region of the cD galaxy ($r < 7.5$ kpc) of the cooling low entropy X-ray gas.
- This low entropy, high metallicity, relatively cool X-ray gas lies along the bright, 44 kpc long Hα+[N II] filament extending from the centre of the cD galaxy to the north.
- As indicated by the observed dust lanes, molecular and ionized emission line nebulae, and the excess UV emission, part of this displaced gas, which is removed from the direct influence of the AGN, cools and forms stars.
- The pressure map shows evidence for an AGN induced weak shock at a radius of $r = 15$ kpc and the X-ray images reveal cavities indicating past powerful AGN activity with an energy of $\sim 7 \times 10^{58}$ ergs. At low frequencies, the radio source has an unusually steep spectrum with $\alpha = 1.5$ indicating aging and confinement by the ambient gas.

Acknowledgments

We thank Alastair Edge and Michael Hogan for providing the reduced 4.75 GHz *ATCA* radio data and for helpful discussions. We thank Seth Bruch and Emily Wang for their help with the *SOAR* observations. Support for this work was provided by the National Aeronautics and Space Administration through Chandra/Einstein Postdoctoral Fellowship Award Number PF8-90056 and PF9-00070 issued by the Chandra X-ray Observatory Center, which is operated by the Smithsonian Astrophysical Observatory for and on behalf of the National Aeronautics and Space Administration under contract NAS8-03060, and by the *Chandra* grants GO0-11019X and GO0-11139X. This work was supported in part by the U.S. Department of Energy under contract number DE-AC02-76SF00515. The Very Large Array is part of the National Radio Astronomy Observatory. The National Radio Astronomy Observatory is a facility of the National Science Foundation operated under a cooperative agreement by Associated Universities, Inc. We thank the staff of the *GMRT* that made these observations possible. The *SOAR* Telescope is a joint project of Conselho Nacional des Pesquisas Cientficas e Tecnologicas CNPq-Brazil, The University of North Carolina Chapel Hill, Michigan State University, and the National Optical Astronomy Observatory.

Chapter 4

On the thermodynamic self-similarity of the nearest, most relaxed, giant ellipticals

N. Werner[1], *S. W. Allen*[1], *A. Simionescu*[1]

[1]Kavli Institute for Particle Astrophysics and Cosmology, Stanford University, 452 Lomita Mall, Stanford, CA 94305-4085, USA
and SLAC National Accelerator Laboratory, 2575 Sand Hill Road, Menlo Park, CA 94025, USA

Published in the Monthly Notices of the Royal Astronomical Society, volume 425, pages 2731–2740, 2012

Abstract

We present detailed spatially resolved measurements of the thermodynamic properties of the X-ray emitting gas in the inner regions of the five nearest, X-ray and optically brightest, and most X-ray morphologically relaxed giant elliptical galaxies known. Beyond the innermost region at $r \gtrsim 1$ kpc, and out to $r \sim 6$ kpc, the density, pressure, entropy, and cooling time distributions for the X-ray emitting gas follow remarkably similar, simple, power-law like distributions. Notably, the entropy profiles follow a form $K \propto r^{\alpha}$, with an index $\alpha = 0.92$-1.07. The cumulative hot X-ray emitting gas mass profiles and the gas-mass to stellar-light ratios of all five galaxies are also similar. Overall the observed similarity of the thermodynamic profiles in this radial range argues that, in these systems, relativistic jets heat the gas at a similar rate averaged over time scales longer than the cooling time $t_{\rm cool} \gtrsim 10^8$ yr. These jets are powered by accretion from the hot gas, or material entrained within it, onto the central super-massive black hole. This jet heating creates an energy balance where heating and cooling are in equilibrium, keeping the hot galactic atmospheres in a 'steady-state'. Within $r \lesssim 1$ kpc,

Table 4.1: Summary of the *Chandra* observations. Columns list the distances of the galaxies, the angular scales per kpc at the corresponding distances, the B-band optical and bolometric X-ray luminosities (O'Sullivan et al. 2001), radio luminosities at 1.4 GHz (Condon et al. 1998, 2002), the line-of-sight Galactic absorbing hydrogen column densities, $N_{\rm H}$, in their directions (Kalberla et al. 2005), observation identifiers, and exposure times after cleaning.

Galaxy	Distance (Mpc)	Scale (arcsec kpc^{-1})	$L_{\rm B}$ ($10^{10}L_{\odot}$)	$L_{\rm X}$ (10^{41} erg s^{-1})	$L_{\rm R}$ (10^{38} erg s^{-1})	$N_{\rm H}$ (cm^{-2})	Obs. ID	Exposure (ks)
NGC4472 (M49)	16.7*	12.4	8.7	2.96	1.20	1.53	321	19.1
			5.8				11274	39.7
NGC4649 (M60)	16.5*	12.5		2.05	0.13	2.04	8182	49.5
							8507	17.5
NGC1399	20.9*	9.9	4.4	5.68	1.52	1.50	319	49.9
							4172	36.7
							9530	59.3
NGC1407	28.8†	7.2	7.4	1.95	1.23	5.42	791	32.5
NGC4261	31.6†	6.5	5.1	1.63	329.52	1.75	9569	100.9

†Tonry et al. (2001)
*Blakeslee et al. (2009)

this similarity breaks down: the observed entropy profiles show well resolved flattening and the values differ from system to system substantially. The accretion rate onto the black hole and the AGN activity, heating the interstellar medium, must therefore vary significantly on time scales shorter than $t_{\rm cool} = 10^7$–10^8 yr.

4.1 Introduction

X-ray studies with *Chandra* and *XMM-Newton* have shown that relativistic jets, produced by accreting supermassive black holes (SMBH) at the centres of galaxies, groups and clusters, interact strongly with their environments, driving shocks (e.g. Forman et al. 2005, 2007; Nulsen et al. 2005; Simionescu et al. 2009b; Million et al. 2010d) and inflating bubbles of relativistic plasma in the surrounding X-ray emitting gas (e.g. Churazov et al. 2000; Fabian et al. 2003a, 2006; Bîrzan et al. 2004; Dunn et al. 2005; Dunn & Fabian 2006, 2008; Forman et al. 2005, 2007; Rafferty et al. 2006; McNamara & Nulsen 2007). These bubbles rise buoyantly and can entrain and uplift large quantities of low entropy gas from the innermost regions of their host galaxies (Simionescu et al. 2008, 2009a; Werner et al. 2010, 2011). All of this activity is believed to take place in a tight feedback loop, where the hot interstellar medium (ISM), which is observable in the X-ray band, cools and accretes onto the central SMBH (referred to as active galactic nucleus or AGN), leading to the formation of jets which heat the surrounding gas and drive the above phenomena (for a review see McNamara & Nulsen 2007; Gitti et al. 2012). This heating acts to lower the accretion rate, reducing the feedback, until the accretion eventually builds up again. AGN feedback appears to play an important role in regulating the 'cooling cores' of galaxy clusters and the formation and evolution of massive galaxies (e.g. Peterson & Fabian 2006; Croton et al. 2006; De Lucia & Blaizot

2007; Sijacki et al. 2007). Although much has been learned about AGN feedback, many questions regarding the remarkable balance between heating and cooling remain.

Nearby giant ellipticals are in many respects low redshift proxies for more distant and more luminous cluster cooling cores, allowing us to study AGN feedback 'in closeup'. Another key advantage is that the binding energy per particle is lower in galaxies: a given amount of AGN heating therefore affects the gas in galaxies more obviously than in clusters. By observing a sample of nearby, X-ray bright galaxies with a high degree of completeness, and with data of sufficient quality to map the detailed thermodynamic properties, we can hope to gain important insight into the physics of AGN feedback, its duty cycle, and its role in galaxy formation.

One of the most useful thermodynamic quantities in studying the impact of cooling and feedback in galaxies, groups, and clusters of galaxies is the gas entropy which, by rewriting the adiabatic index in terms of X-ray observables, can be defined as $K = kTn_{\rm e}^{-2/3}$, where kT is the temperature and $n_{\rm e}$ is the electron density of the X-ray emitting gas. Because entropy can only be changed by gains and losses of energy, it traces the thermal history of the gas. The radial profiles of entropy in statistical samples of galaxy clusters and groups have been analyzed by Pratt et al. (2006, 2010), Cavagnolo et al. (2009) and Sun et al. (2009). However, a detailed study of the thermodynamic properties of giant ellipticals, reaching down to sub-kpc scales, has not been performed.

Here we present detailed, spatially resolved measurements of the key thermodynamic properties (density, temperature, pressure, entropy, cooling time, and gas mass) of the X-ray emitting gas in the innermost regions of the five nearest, X-ray and optically brightest, and most morphologically relaxed giant elliptical galaxies known. All of these galaxies have deep *Chandra* observations, as well as exquisite optical and multi-wavelength data.

In Sect. 9.1.1, we describe our sample, the reduction of the X-ray data, and the spectral analysis. In Sect. 9.3, we present the measurements of both the 2D distributions and the deprojected radial profiles of the key thermodynamic properties. We show, for the first time, that the azimuthally averaged gas density, pressure, cooling time, and entropy profiles of relaxed giant elliptical galaxies are in the radial range $1 \lesssim r \lesssim 6$ kpc remarkably similar. Based on these results, in Sect. 9.4 we present some new insights into the likely thermal history of the X-ray emitting atmospheres of the galaxies. In Sect. 9.5, we summarize our conclusions.

4.2 Sample selection, data reduction, and analysis

4.2.1 Sample selection and its properties

Our target list is drawn from the parent sample of Dunn et al. (2010), who identified the optically-brightest ($B_{\rm T} \leq 13.5$ mag) and X-ray brightest ($F_{\rm X} > 10^{-12}$ erg cm^{-2} s^{-1} in the 0.1–2.4 keV band) giant elliptical galaxies within a distance $d \leq 100$ Mpc and with declination $dec \geq -45$ degrees. Motivated by a goal to resolve the innermost thermodynamic structure in detail, from this list we select only those systems with

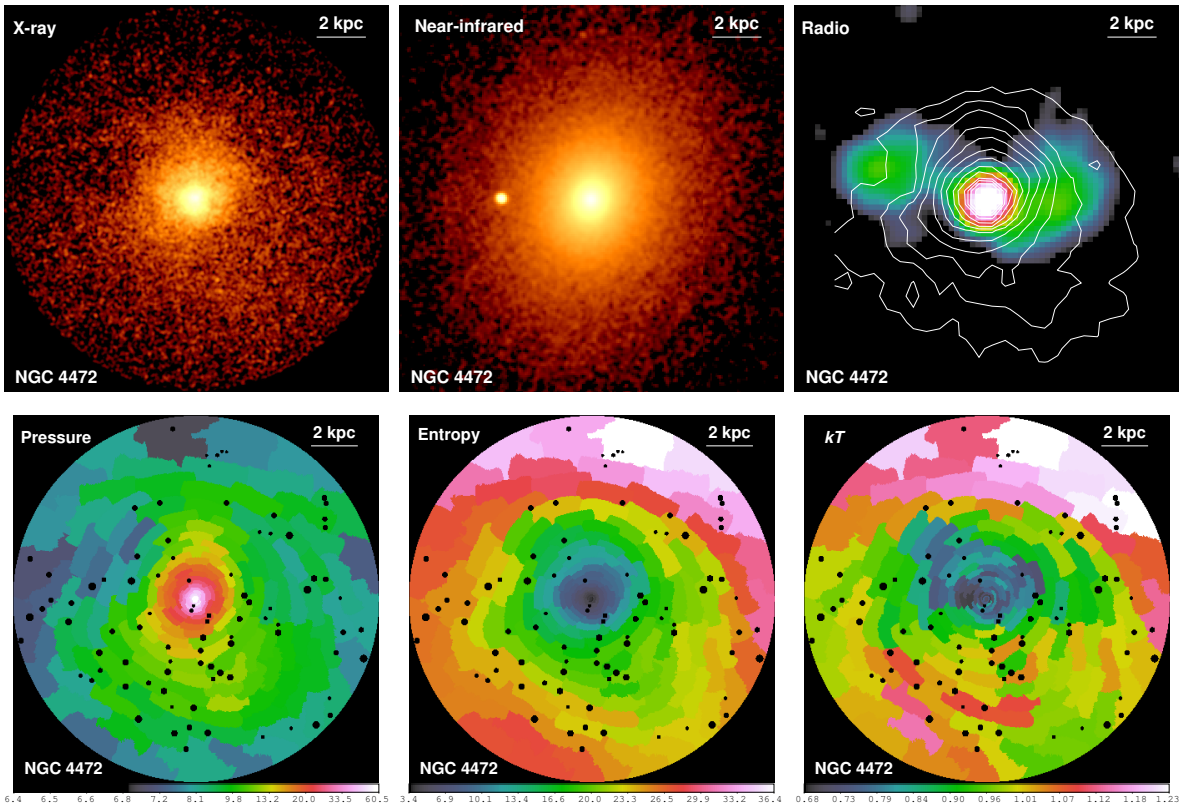

Figure 4.1: *Top panels: Chandra* X-ray image of NGC 4472 in the 0.5–2 keV band (left panel); K-band near-infrared image from the Two Micron All-Sky Survey (2MASS; central panel); VLA 1.4 GHz radio map obtained in the C-configuration from Dunn et al. (2010) with the X-ray contours over-plotted (right panel). The images are shown in on a logarithmic scale. *Bottom panels:* 2D map of pressure (in units of keV cm^{-3} $\times \left(\frac{l}{20\mathrm{kpc}}\right)^{-1/2}$; left panel), entropy (in units of keV cm^2 $\times \left(\frac{l}{20\mathrm{kpc}}\right)^{1/3}$; central panel), and temperature (in units of keV; right panel). The maps were obtained by fitting each region independently with a single temperature thermal model, yielding 1σ fractional uncertainties of $\sim$3–5 per cent in temperature, entropy, and pressure. Point sources were excluded from the spectral analysis and therefore appear as black circles on the maps.

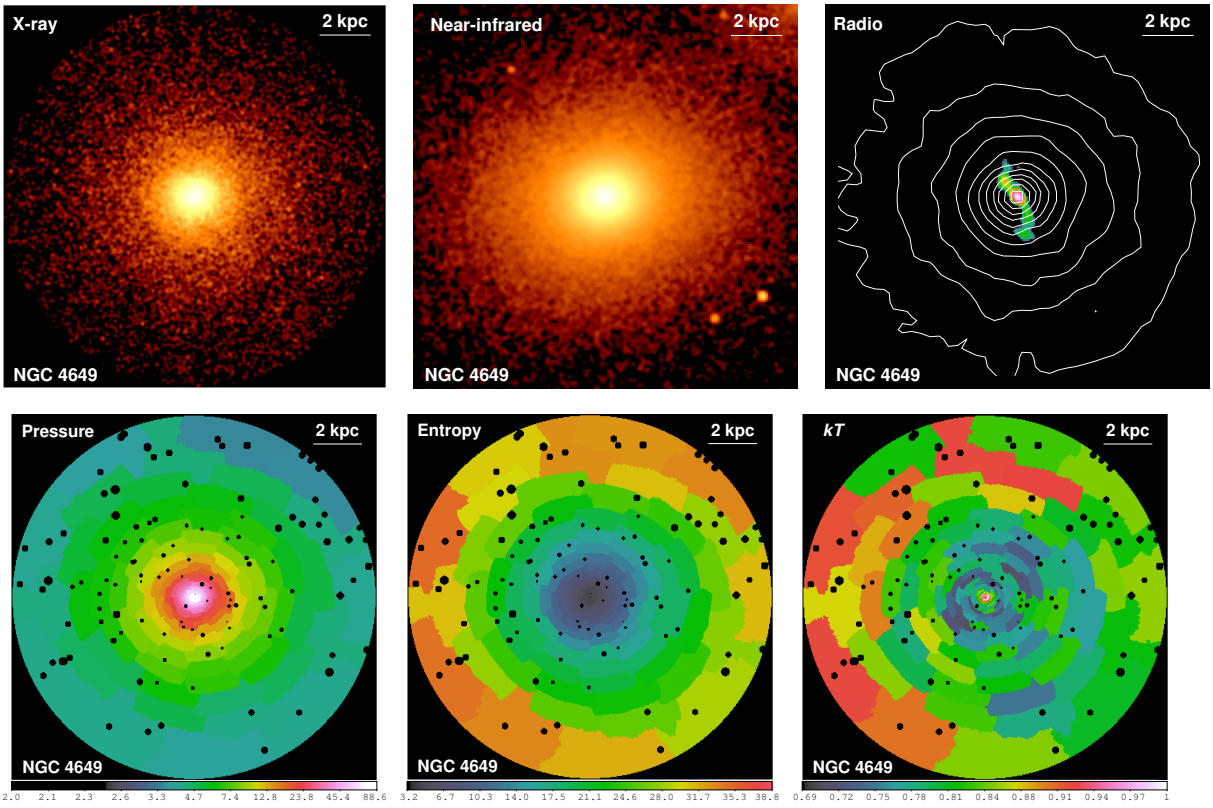

Figure 4.2: As Fig. 4.1, but for NGC 4649. The VLA 1.4 GHz radio map was obtained in the B-configuration (Dunn et al. 2010).

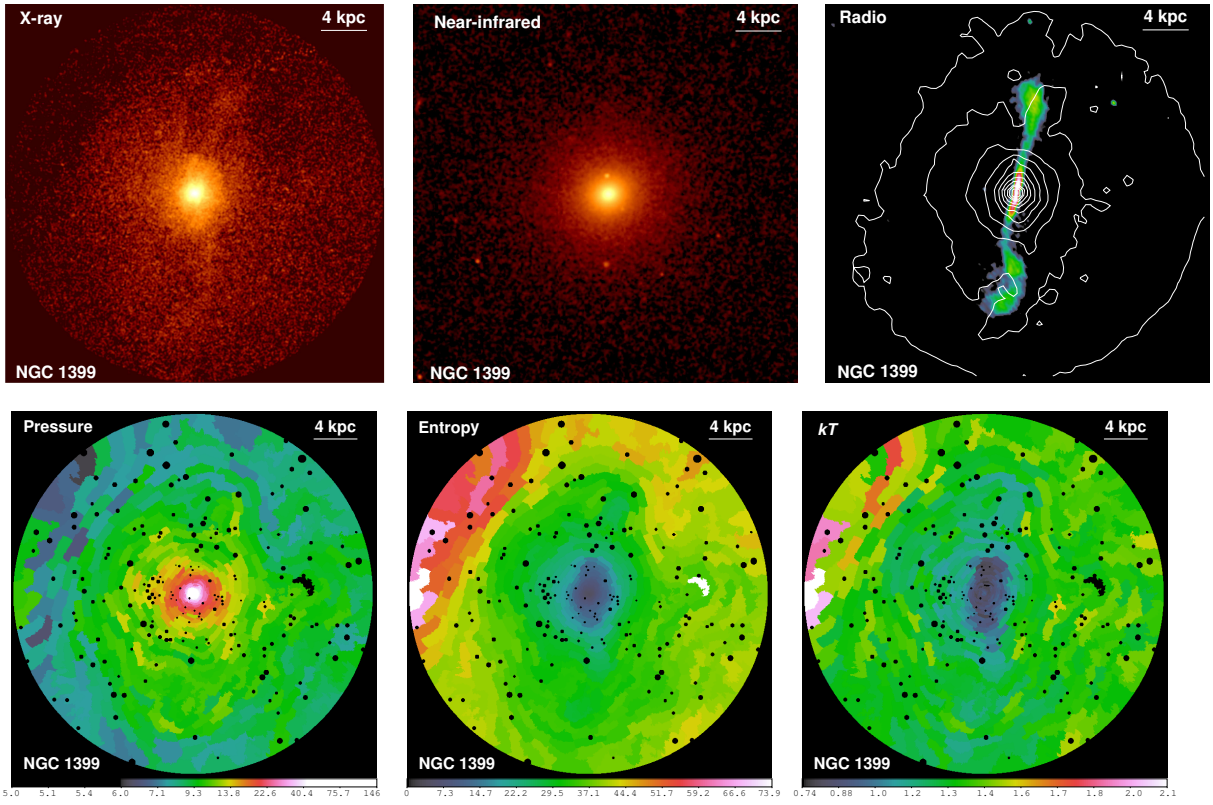

Figure 4.3: As Fig. 4.1, but for NGC 1399. The VLA 1.4 GHz radio map was obtained in the H-configuration (hybrid A and B configuration; Dunn et al. 2010).

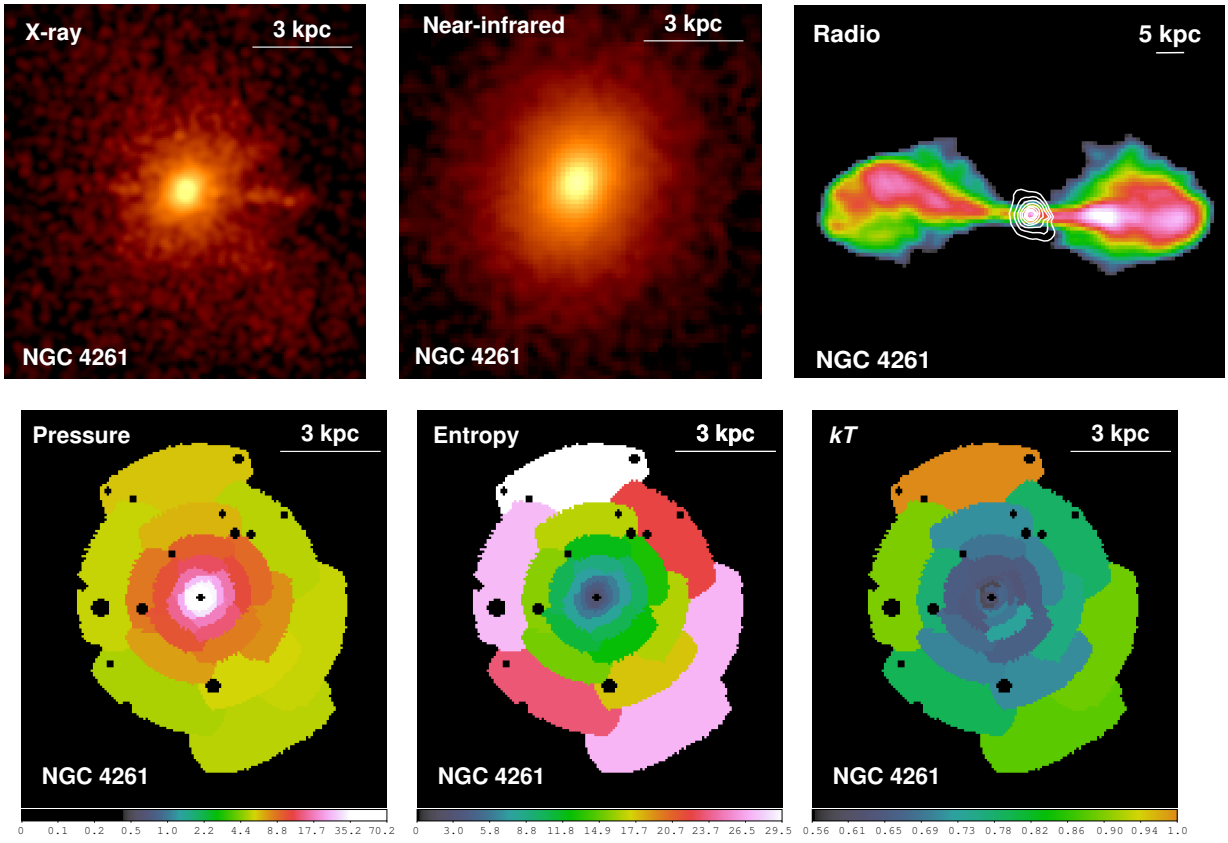

Figure 4.4: As Fig. 4.1, but for NGC 4261.

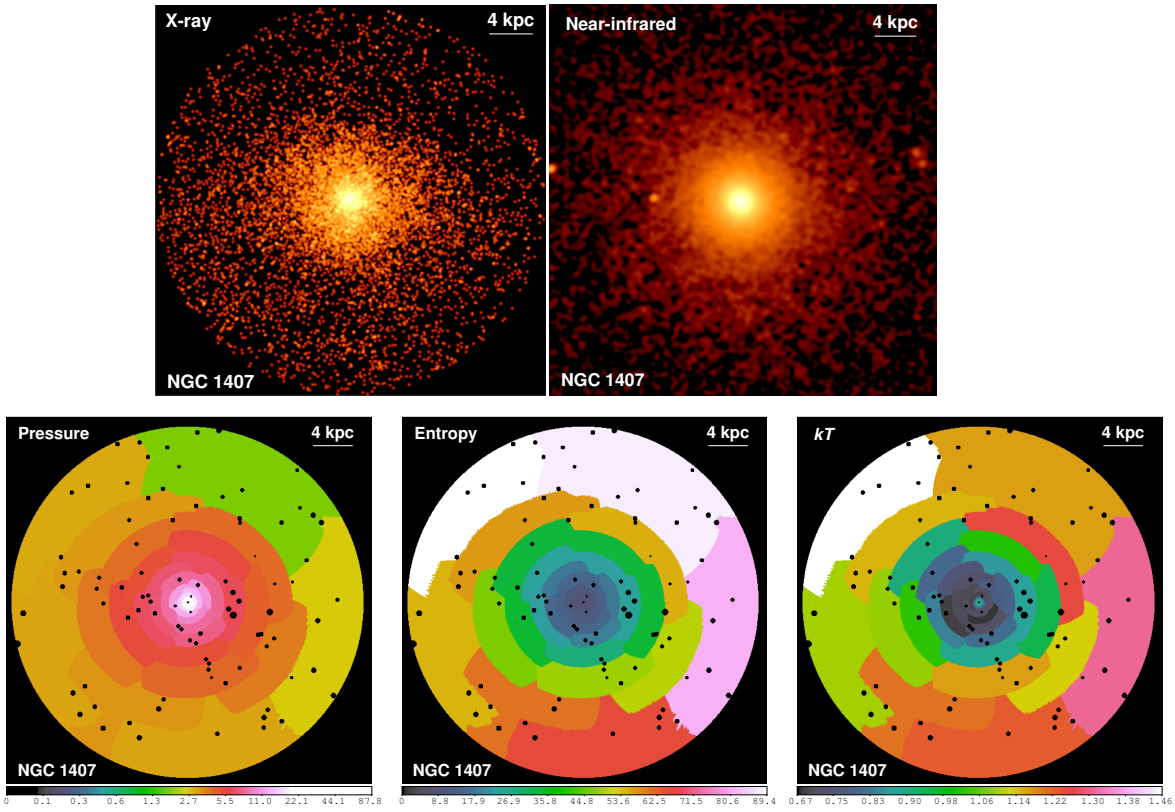

Figure 4.5: As Fig. 4.1, but for NGC 1407.

distance $d < 35$ Mpc. From the resulting sample of thirteen galaxies, we select those systems that appear the most morphologically relaxed at X-ray wavelengths (i.e. symmetric and undisturbed in their *Chandra* images). The highly symmetric morphologies of these galaxies ensure that their deprojected thermodynamic properties can be determined as robustly as possible. Five galaxies meet these criteria. Their X-ray, near-infrared, and radio images (except for NGC 1407, for which we do not have spatially resolved radio data) are shown in Figs. 4.1–4.5 and their properties are summarized in Table 9.2.

As seen in the X-ray images (the reduction of the X-ray data is described in Sect. 4.2.2), NGC 4649 and NGC 1407 are highly symmetric. Although NGC 1399, NGC 4472, and NGC 4261 do display slight departures from spherical symmetry, they are still among the most X-ray morphologically relaxed giant elliptical galaxies known. The faintest galaxy in our sample is NGC 4261, with a bolometric X-ray luminosity of $L_X = 1.63 \times 10^{41}$ erg s^{-1} and flux of 1.36×10^{-12} erg s^{-1} cm^{-2}. Our relatively high luminosity limit restricts the contamination of the detected X-ray emission by an unresolved population of X-ray binaries (see Sect. 4.2.2 for details). The relatively high X-ray fluxes of our sources, combined with their proximity ensure that we can measure the thermodynamic properties down to sub-kpc radii.

The processed near-infrared K-band images obtained with the Two Micron All-Sky Survey (2MASS) shown in the upper central panels of Figs. 4.1–4.5 were downloaded from the NASA/IPAC Infrared Science Archive[1] (Jarrett et al. 2003). They show that the stellar light and by implication the star-mass distribution in all of the galaxies is highly symmetric with no indications for disturbance or star-formation. The galaxies do not, in general, show detectable dust lanes or H I emission and their stellar populations are old and red (Serra & Oosterloo 2010). NGC 4261 does show a nuclear disk of gas and dust in the innermost $r \sim 100$ pc (see Jaffe et al. 1993; Jaffe & McNamara 1994) containing $(5.4 \pm 1.8) \times 10^4\ M_\odot$ of molecular and atomic hydrogen (Ferrarese et al. 1996); however, cool gas or dust has not been detected elsewhere in NGC 4261 (Serra & Oosterloo 2010; Combes et al. 2007). All five galaxies are essentially 'red and dead'.

All five galaxies have central, active radio jets, but their observed radio powers and morphologies span a wide range, as indicated by the radio luminosities listed in Table 9.2 and by the radio maps in Figs. 4.1–4.4 (see also Dunn et al. 2010). NGC 4261 is the most powerful radio source, with jets that puncture through the X-ray emitting galactic atmosphere to form giant lobes in the surrounding intra-group medium (IGM). NGC 1399 has ∼10 kpc long radio jets with lobes that also appear to be depositing energy away from the centre of the galaxy. The radio lobes of NGC 4472, and of the 10 times less radio luminous NGC 4649, are seen at smaller radii. For NGC 1407, we do not presently have high quality radio data, but its radio luminosity is similar to those of NGC 4472 and NGC 1399 (see Table 9.2), clearly indicating the presence of jets.

[1] http://irsa.ipac.caltech.edu/

4.2.2 *Chandra* data reduction and analysis

Data reduction

Our analysis of the *Chandra* data follows the data reduction procedures described in Million et al. (2010c) and Million et al. (2010d). The standard level-1 event lists were reprocessed using the CIAO (version 4.3) software package, including the latest gain maps and calibration products. Bad pixels were removed and standard grade selections applied. The data were cleaned to remove periods of anomalously high background. The net exposure times after cleaning are summarized in Table 9.2. Background images and spectra were extracted from the blank-sky fields available from the Chandra X-ray Center. These were cleaned in an identical way to the source observations, reprojected to the same coordinate system, and normalized by the ratio of the observed to blank-sky count rates in the 9.5–12 keV band.

Background subtracted images were created in 6 narrow energy bands, spanning 0.5–2.0 keV. These were flat fielded with respect to the median energy for each image and then co-added to create the broad band X-ray images shown in Figs. 4.1–4.5.

Identification of point sources was performed using the CIAO task WAVDETECT. These were excised from the images in Figs. 4.1–4.5 and substituted by local backgrounds. Point sources were also excluded from all regions used for spectral analysis. Separate photon-weighted response matrices and effective area files were constructed for each spectral region.

Spectral analysis

Our spectral analysis was separated into two parts. In the first part, 2D maps of projected thermodynamic quantities were made. The individual regions for the 2D spectral mapping were determined using the Contour Binning algorithm (Sanders 2006), which groups neighboring pixels of similar surface brightness until a desired signal-to-noise threshold is met. In order to have small enough regions to resolve substructure, yet still have enough counts to achieve better than 5 per cent accuracy in the temperature measurements, we adopted a signal-to-noise ratio of 18 ($\sim$320 counts per region). We modeled the spectra extracted from each spatial region with the SPEX[2] package (Kaastra et al. 1996, SPEX is faster, uses an updated version of the MEKAL plasma model with respect to XSPEC, though provides consistent results). Because the spectral band above 2 keV is dominated by background in low temperature galaxies, the spectral fitting was performed in the 0.6–2.0 keV band. The spectrum for each region was fitted with a model consisting of an absorbed single-phase plasma in collisional ionization equilibrium, with the temperature and spectral normalization (emission measure) as free parameters. The line-of-sight absorption column densities, $N_{\rm H}$, were fixed to the values determined by the Leiden/Argentine/Bonn radio survey of H I (Kalberla et al. 2005, see Table 9.2).

After the point source removal, the contribution from an unresolved population of low mass X-ray binaries (LMXB) to the X-ray emission is insignificant. We per-

[2]www.sron.nl/spex

formed fits, where we included power-law emission components with photon indices $\Gamma = 1.56 - 1.80$, which were shown to describe well the population of low-luminosity LMXB (Irwin et al. 2003; Kim & Fabbiano 2004). Such additional power-law emission is not detected significantly in the galaxies and including it in the spectral fitting does not significantly affect the measured thermodynamic properties of the hot ISM (we note that this conclusion does not change if we extend the fitted band to 7 keV).

The largest systematic uncertainty in the measured densities stems from the metallicity measurements. When fitting the spectra of thermal plasmas with kT in the range $\sim$0.5–1.0 keV, the emission measure and metallicity typically anti-correlate. In regions with complicated temperature structure the metallicity is often biased low and consequently the emission measure is biased high (e. g. Buote 2000b; Werner et al. 2008). Moreover, for spectra with relatively low numbers of counts, the statistical uncertainties on the metallicity are high and multi-temperature model fits are unfeasible. Therefore, our 2D maps of thermodynamic properties were produced with the metallicity fixed to 0.5 Solar (throughout the paper, metal abundances are given with respect to the Solar values by Grevesse & Sauval 1998). If the metallicity is underestimated/overestimated by a factor of 2 in the model, the density will be overestimated/underestimated by a factor of $\sim$1.35.

In the second stage of our analysis, we measured azimuthally-averaged, deprojected radial profiles of thermodynamic quantities. We extracted spectra from concentric annular regions at least 1 arcsec wide, with a signal-to-noise ratio of at least 18 ($\sim$320 counts). The deprojected profiles of thermodynamic properties were obtained with the XSPEC (version 12.5 Arnaud 1996) spectral fitting package, using the projct model. The combined set of azimuthally averaged spectra extracted from concentric annuli was modeled in the 0.6–2.0 keV band simultaneously to determine the deprojected electron density (n_e) and temperature (kT_e) profiles. The emission from each spherical shell was modeled with a photoelectrically absorbed (Balucinska-Church & McCammon 1992) APEC thermal plasma model (Smith et al. 2001, using AtomDB v2.0.1). Deprojected densities were determined in 14–27 shells, and temperatures in 7–10 regions, depending on the galaxy. For each galaxy we fitted two metallicity values, one for the shells outside the radius of $\sim$1 kpc and another value for the shells in the central regions of the galaxies.

For all spectral fitting, we employ the extended C-statistics available in XSPEC and SPEX. All errors are quoted at the 68 per cent confidence level for one interesting parameter ($\Delta C = 1$).

4.3 Thermodynamic measurements

4.3.1 2D distribution of thermodynamic properties

The lower panels of Figs. 4.1–4.5 show 2D maps of projected electron pressures ($n_e kT_e$), entropies ($kT_e / n_e^{\frac{2}{3}}$), and temperatures (kT_e). The projected electron densities were determined assuming a fixed line of sight of column depth $l = 20$ kpc.

The 2D distributions of the pressures are approximately spherically symmetric in the cores of all five galaxies, consistent with the X-ray emitting gas being in approximate hydrostatic equilibrium. The most obvious departure from spherical symmetry is seen in NGC 4472 in the areas spatially coincident with the radio lobes at radii $r \sim 4$ kpc, where the projected thermal pressure drops by 10–25 per cent.

The spatial distribution of the projected entropy appears spherically symmetric in 4/5 systems, the exception being NGC 1399 where the entropy distribution beyond $r \sim 1.5$ kpc is elongated, with lower entropy gas extended along the radio jets. Overall, however, in all cases, the lowest entropy gas resides in the innermost cores of the galaxies, as expected for convective stability. The regions of relatively high entropy at $r > 6$ kpc, to the north of NGC 4472 and NGC 1407, and to the east of NGC 1399, indicate that these galaxies are moving through the ambient medium.

The observed temperature distributions of the galaxies appear less symmetric. In NGC 4472 we see cooler plasma extended along the eastern radio lobe, and in NGC 1399 the low temperature ISM is distributed along the radio jets. The lowest projected temperatures of the galactic atmospheres are in the range 0.6–0.75 keV. Such low ISM temperatures are not, however, always seen in the densest, central regions. Three out of five galaxies (NGC 4649, NGC 1407, and NGC 1399) show a significant temperature *increase* in their cores. The clearest central temperature increase is seen in NGC 4649, arguably the most morphologically relaxed galaxy in our sample.

4.3.2 Azimuthally-averaged, deprojected thermodynamic properties

The relatively undisturbed X-ray morphologies and high degree of azimuthal symmetry observed in the distributions of projected thermodynamic quantities confirms that the five systems in this study are among the most dynamically relaxed giant elliptical galaxies in the local Universe. All systematic uncertainties associated with deprojection analyses, carried out under the assumption of spherical symmetry and of a single-phase nature at each radius, are therefore minimized for these systems. We have determined the azimuthally-averaged deprojected radial profiles of electron density ($n_{\rm e}$), temperature ($kT_{\rm e}$), and metallicity (Z) from the *Chandra* data. Using these quantities we also determine the deprojected radial profiles for the cumulative gas mass, entropy ($K = kT_{\rm e}/n_{\rm e}^{\frac{2}{3}}$), electron pressure ($P_{\rm e} = n_{\rm e}kT_{\rm e}$), and cooling time. We define the cooling time as the gas enthalpy divided by the energy radiated per unit volume of the plasma:

$$t_{\rm cool} = \frac{\frac{5}{2}(n_{\rm e} + n_{\rm i})kT}{n_{\rm e}n_{\rm i}\Lambda(T)}, \tag{4.1}$$

where the ion number density $n_{\rm i} = 0.92n_{\rm e}$, and $\Lambda(T)$ is the cooling function for Solar metallicity tabulated by Schure et al. (2009). Cooling functions based on older plasma codes (Sutherland & Dopita 1993) predict a 9 per cent lower cooling rate for 0.5 keV plasma.

Our main result from the deprojection analysis is that beyond the central $r \sim 1$ kpc, and out to the radii $r \lesssim 6$ kpc, the cumulative gas mass, density, pressure, entropy, and cooling time distributions for the X-ray emitting gas follow remarkably similar

radial profiles (see Fig. 4.6). The observed cumulative gas mass within $r = 8$ kpc is $\sim 5.8 \times 10^8\ M_\odot$ with a system-to-system dispersion of 10 per cent. The entropy profiles follow a simple, power-law form $K \propto r^\alpha$ with an index $\alpha = 0.92$-1.07. The weighted system-to-system dispersions in entropy at $r = 1$ kpc and at $r = 5$ kpc are only 14 per cent and 17 per cent, respectively. The density profiles follow the form $n_e \propto r^{-\beta}$ with an index $\beta = 1.1$–1.46 and with a system-to-system dispersion of 10 per cent at $r = 5$ kpc. The pressure profiles have an approximate power-law form of $P_e \propto r^{-\gamma}$ with an index $\gamma = 0.93$–1.43 and with a system-to-system dispersion of 13 per cent at $r = 5$ kpc. The thermodynamic profiles of NGC 4261 can be well described with power-law relations all the way down to the smallest radii measured.

In the absence of heating, cooling in the central regions of these galaxies would be strong: within the radius $r \lesssim 4$ kpc, the cooling times in all five galaxies are $t_{\rm cool} < 1$ Gyr. Within $r \lesssim 1$ kpc of the center, the cooling times are $t_{\rm cool} < 10^8$ yr, and less than a few 10^7 yr within 0.5 kpc.

All five galaxies show a flattening of their central entropy profiles within $r \lesssim 1$ kpc. In contrast to the remarkable similarity in the thermodynamic profiles at larger radii ($1 \lesssim r \lesssim 6$ kpc), within this innermost $r \lesssim 1$ kpc region the entropies of the galaxies also show a significant system-to-system scatter of 40 per cent at $r = 0.2$ kpc. The system with the least central flattening of the entropy distribution is NGC 4261, where the entropy drops to $K_0 = 0.88 \pm 0.02$ keV cm^2 at 0.23 kpc. The largest core entropy of $K_0 = 4.1 \pm 0.5$ keV cm^2 at $r = 0.27$ kpc is observed in NGC 1407.

The temperature profiles of the galaxies exhibit significant system-to-system scatter. Interestingly the temperature profiles for NGC 4649, NGC 1399, and NGC 1407 show clear temperature increase in the central regions, which may be associated with repeated shock activity increasing the entropy of the gas. In contrast, the radial temperature distributions in the centres of NGC 4472 and NGC 4261 are relatively flat.

The best fit metallicities of the hot ISM within $r \sim 1$ kpc are $Z \sim 0.5$ Solar, except for NGC 1399 which has a core metallicity of $Z \sim 0.85$ Solar. Beyond this innermost region ($1 < r < 6$ kpc) the metallicities of NGC 4649 and NGC 4261 are $Z \sim 0.3$ Solar; NGC 1407 has $Z \sim 0.75$ Solar, and the metal abundances of NGC 1399 and NGC 4472 are $Z \sim 1$ Solar. The systematic uncertainties on the metallicity measurements of $kT \lesssim 1$ keV plasma with CCD type detectors are, however, unfortunately still significant.

To verify that the spectroscopically measured temperatures, and other thermodynamic quantities, determined in azimuthally averaged annular regions are approximately unbiased with respect to the true average values at a given radius, we have compared their results with the average values determined from all bins at the same radii in the 2D maps. We find no significant differences between the values found by fitting spectra extracted from circular annuli and the azimuthally averaged values determined from 2D maps at any radius.

The obtained deprojected density and temperature profiles are broadly consistent with the previously published results in the literature (e.g. Humphrey et al. 2006, 2009; Churazov et al. 2010).

4.4 Discussion

Beyond the innermost core, at $r \gtrsim 1$ kpc and out to at least $r \sim 6$ kpc, the X-ray emitting hot gas mass profiles and thermodynamic profiles exhibit remarkable self-similarity. The density, entropy, pressure, and cooling time distributions follow simple, power-law forms. The total gravitating mass at these radii is also similar in all five galaxies, and is dominated by their stellar populations (Humphrey et al. 2006; Das et al. 2010). The mass fraction of hot X-ray emitting gas in this radial range is small, of the order of $f_{\rm gas} \lesssim 2 \times 10^{-3}$. Because the hot ISM represents a minor and essentially dynamically insignificant fraction of the total mass of the galaxies, the observed similarity of the hot gas mass and its thermodynamic profiles is surprising and reflects a deep and long term stability of energy input from the AGN and from the stellar populations. Interestingly, the ratio of the cumulative gas mass within $r < 8$ kpc to the total B-band luminosity for the galaxies in our sample spans a relatively small range of $M_{\rm gas}/L_{\rm B} = 7.1 - 11.3 \times 10^{-3}\ M_{\odot}/L_{\odot}$.

4.4.1 Universal thermodynamic profiles

The similarity of the thermodynamic properties of the gaseous atmospheres of our galaxy sample has important implications for the evolution of giant ellipticals. The cooling time of the hot gas in the central regions is short (see left panel of Fig. 4.6) and in the absence of heating this gas will cool and form stars (e.g. Peterson & Fabian 2006). The X-ray spectra of these galaxies, however, lack the expected strong O VII lines associated with gas cooling below $T \sim 5 \times 10^6$ K (see e.g. Sanders & Fabian 2011). Moreover, their stellar populations are old, showing no evidence for recent star-formation, and no significant central atomic or molecular reservoirs of cooled gas are detected (Serra & Oosterloo 2010). All of this indicates that the gas has been kept from cooling.

Type Ia supernovae are expected to explode in giant elliptical galaxies at a rate of 0.166 per 100 yr per $10^{10}\ L_{\rm B\odot}$ (Cappellaro et al. 1999), releasing $\sim 10^{51}$ ergs of energy per supernova. In principle, this can provide a heating rate of 1.6×10^{41} erg s^{-1} within $r \lesssim 6$ kpc, which is of the same order of magnitude as the X-ray luminosity within the same region. However, to approximately balance the radiative cooling, the energy released by supernovae would have to couple to the X-ray emitting gas with a 100 per cent efficiency, which seems unlikely. The dominant source of heating is instead likely to be the central AGN.

As indicated by the observed radio morphologies, the jets and lobes driven by the central AGN interact with and mechanically heat the ISM out to a radius of several kpc. A complete, flux-limited study of 18 nearby, X-ray bright, optically bright giant elliptical galaxies by Dunn et al. (2010) shows that 17/18 systems exhibit some form of current radio activity associated with the central AGN (see also Best et al. 2005; Dunn & Fabian 2006, 2008; Sun 2009). Such observations imply that active 'radio-mode' AGN feedback is not a rare and sporadic phenomenon, but rather represents the default state for large elliptical galaxies. Allen et al. (2006) demonstrate a tight correlation between the Bondi accretion rates of hot gas and the observed jet power in such ellipticals. This

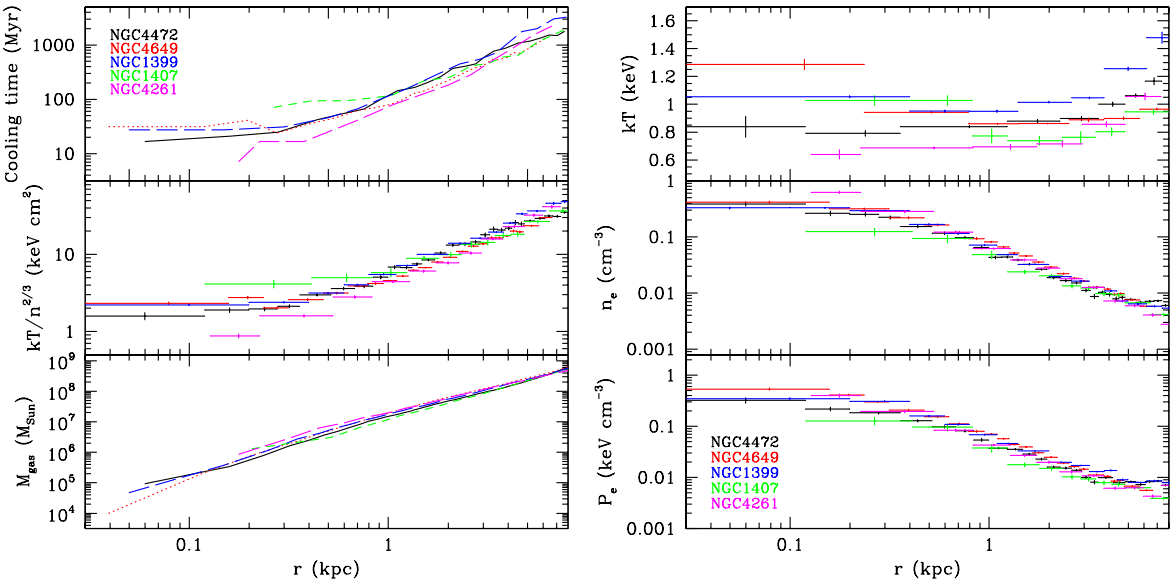

Figure 4.6: *Left panel:* Radial distributions of cooling times, entropies, and cumulative gas masses for our sample of 5 nearby giant elliptical galaxies. *Right panel:* Radial distributions of the deprojected temperatures, electron densities, and electron pressures.

argues that AGN feedback is likely controlled by the accretion of hot gas, or multi-phase gas entrained within it. The similarity of the observed thermodynamic profiles reported here supports this, and argues that relativistic jets, produced by accretion onto the central SMBH, heat the gas at a similar and constant rate averaged over time scales longer than the cooling time, $t_{\rm cool} \gtrsim 10^8$ yr. This jet heating creates an energy balance where heating and cooling are in approximate equilibrium, keeping the hot galactic atmospheres in a near 'steady-state'. Importantly, the observed 'steady-state' also indicates that the time averaged accretion rate onto the SMBH is intimately connected to the conditions of the hot X-ray emitting gas phase on spatial scales of several kpc.

The jet-powers estimated from the energies and timescales required to inflate the bubbles of relativistic radio-emitting plasma are $P_{\rm jet} \sim 8 \times 10^{42}$ ergs s^{-1} in NGC 4472 (Allen et al. 2006); $P_{\rm jet} \sim 1.3 \times 10^{42}$ ergs s^{-1} in NGC 4649 and $P_{\rm jet} \sim 2.2 \times 10^{42}$ ergs s^{-1} in NGC 1399 (Shurkin et al. 2008); and $P_{\rm jet} > 10^{43}$ ergs s^{-1} in NGC 4261 (O'Sullivan et al. 2011). In NGC 4472, NGC 4649, and NGC 1399 the energy required to keep the hot ISM within $r \lesssim 6$ kpc from cooling is only 2.5–10 per cent of the estimated jet-power, and in NGC 4261, which is the system with the most powerful radio source in our sample, this energy is less than 1 per cent of the power output of the AGN. In NGC 4261 the jets penetrate through the hot galactic corona and form lobes which deposit most of their energy into the surrounding intergalactic medium (O'Sullivan et al. 2011).

Although we do not see evidence for shocks currently propagating through the X-ray atmospheres of the galaxies in our sample, repeated AGN induced shocks most likely do contribute to the heating of the hot ISM. Detailed studies of the giant elliptical galaxy NGC 5813 revealed that the total energy in shocks driven by the expand-

ing bubbles can be 1/2–3 times the total internal energy of the cavities (Randall et al. 2011b). The total jet power in these systems is therefore most likely even higher than the estimates provided above. Interestingly, despite the fact that the fraction of the estimated 'current' jet-power that is needed in each case to keep the hot ISM from cooling varies from galaxy to galaxy by an order of magnitude, the observed similarity of the thermodynamic properties, including the gas mass and entropy, argues that the energy deposited into the ISM within $r \lesssim 6$ kpc must be similar and steady, to keep the hot galactic atmospheres in a 'steady-state'.

4.4.2 Heating in the innermost $r \lesssim 1$ kpc

As shown in Sect 9.5, the entropy and cooling time profiles show well resolved flattening at radii $r \lesssim 1$ kpc. This flattening, combined with the short cooling times of $t_{\rm cool} < 10^8$ yr, implies that the gas at these radii has been heated by AGN activity relatively recently. Radiative cooling will reduce the entropy of the central gas, and in order to offset such cooling and flatten the profiles a heating mechanism is required. Heating by repeated AGN induced weak shocks is likely to be the most significant channel for entropy increase of the hot plasma near to the AGN. Shock heating, which increases the entropy by ΔS, will offset the radiative heat loss by $\Delta Q = T\Delta S$ (where T is the temperature of the gas). Examples of pronounced, ongoing AGN induced shock heating have been studied in detail in M 87 (Forman et al. 2005, 2007; Million et al. 2010d) and in NGC 5813 (Randall et al. 2011b).

The steepest central entropy distribution is seen in NGC 4261, where the entropy continues to drop all the way in to the centre of the system. The fact that the central entropies at $r < 1$ kpc, where $t_{\rm cool} < 10^8$ yr, are substantially different from system to system indicates that the accretion rate onto the black hole and the resulting jet-power, heating the ISM, varies significantly on time scales shorter than a few 10^7 yr.

Given the remarkable similarity of the profiles at $r > 1$ kpc our analysis suggests that the application of hydrostatic mass analyses to the regions of those galaxies from 1–6 kpc are likely to be relatively accurate (e. g. Humphrey et al. 2006; Churazov et al. 2008, 2010). Humphrey et al. (2008, 2009) extend their hydrostatic mass analyses all the way into the cores of their target galaxies, arguing that in some systems, most notably in NGC 4649, relative hydrostatic equilibrium applies all the way to small radii allowing to infer directly the mass of the central SMBH. The increased system-to-system scatter in our observed central gas entropy indicates that caution should be employed when extending such analyses to the inner 1 kpc, where feedback may induce significant thermodynamic variations on timescales as short as a few 10^6 yr.

4.4.3 The origin of the hot gas

There are three possible explanations for the origin of the hot gas in giant ellipticals: first, it could be leftover baryonic material from the process of galaxy formation. In this case, the similarity of the gas mass to stellar light ratios in the galaxies would indicate similar star formation and feedback histories. Second, some fraction of the X-ray emit-

ting gas could have been accreted from the surrounding large scale environment. If this process is important, then the gas mass to stellar light ratios would depend strongly on the large scale environments of the galaxies and would therefore be expected to exhibit significant system-to-system variation, which is not seen in our sample[3]. A third possibility is that stellar mass loss contributes significantly to the X-ray halos (for a review see Mathews & Brighenti 2003). In this process, gas from the outer layers of evolved stars is mixed and assimilated into the hot phases of the galaxies (Mathews 1990). Hydrodynamic simulations of the gas ejected by red giant stars and planetary nebulae have been performed by Parriott & Bregman (2008) and Bregman & Parriott (2009). These simulations predict that about 75 per cent of the ejecta produced by red giant stars moving supersonically relative to the ambient medium will be shock heated to approximately the temperature of the hot ISM. However, the products of stellar mass loss evidently do not thermalize universally in all environments. The presence of dust and PAHs in the dense cooling cores of some galaxy clusters suggests that in those systems much of the ejected stellar gas remains cool (Voit & Donahue 2011; Donahue et al. 2011). The high ambient pressures in the cores of galaxy clusters with massive cooling cores might be promoting more rapid radiative cooling of the products of stellar mass loss. However, none of our galaxies lie at the centers of massive cooling cores.

While we cannot at present discriminate clearly whether original baryonic matter left over from the process of galaxy formation or the products of stellar mass loss dominate the X-ray emitting material within $1 < r < 8$ kpc, the remarkable similarity of the thermodynamic and gas mass profiles, and gas mass to stellar light ratios in the systems presented here provides an important, new constraint.

4.5 Conclusions

We performed a detailed spatially resolved study of the thermodynamic properties of the X-ray emitting gas in the inner regions of the five nearest, X-ray and optically brightest, and most morphologically relaxed giant elliptical galaxies at X-ray wavelengths. Our main conclusions may be summarized as follows:

- Beyond the innermost central region, at $r \gtrsim 1$ kpc and out to $r \sim 6$ kpc, the radial profiles of density, pressure, cooling time, and entropy of these galaxies follow remarkably similar, simple, power-law like distributions. The entropy profiles follow a form $K \propto r^{\alpha}$ with an index $\alpha = 0.92$-1.07, with a system to system dispersion at a given radius of only $\sim$15 per cent. The cumulative hot X-ray emitting gas mass profiles and the gas-mass to stellar-light ratios of all five galaxies are also similar.

- The observed similarity of the thermodynamic profiles in this radial range argues that, in these systems, relativistic jets heat the gas at a similar rate averaged over

[3]The gas mass fractions around the brightest cluster galaxies of cooling core clusters are significantly higher than those of the galaxies investigated in this paper (e. g. Allen et al. 2008). Most of the gas in those systems likely originates from the surrounding intra-cluster medium.

time scales longer than the cooling time $t_{\rm cool} \gtrsim 10^8$ yr. This jet heating creates an energy balance where heating and cooling are in equilibrium, keeping the hot galactic atmospheres in a 'steady-state'.

- The entropy profiles show well resolved flattening at radii $r \lesssim 1$ kpc. In contrast to the remarkable similarity at larger radii ($1 \lesssim r \lesssim 6$ kpc), the central entropy value differs from system to system, with a scatter of 40 per cent at 0.2 kpc. The accretion rate onto the black hole and the AGN activity, heating the ISM, must therefore vary significantly on time scales shorter than $t_{\rm cool} = 10^7$–10^8 yr.
- Our results support the picture in which the jets associated with the central AGN are powered by the accretion of hot gas, or the material entrained within it.

Acknowledgments

We thank Robert Dunn for providing us the radio data for NGC 4472, NGC 4649, and NGC 1399. We thank Payel Das for providing us stellar mass and dark matter profiles for the galaxies. We thank Paul Nulsen and Mark Voit for inspiring discussions. Support for this work was provided by the National Aeronautics and Space Administration through Chandra/Einstein Postdoctoral Fellowship Award Number PF8-90056 and PF9-00070 and through the Chandra Award Number GO9-0088X issued by the Chandra X-ray Observatory Center, which is operated by the Smithsonian Astrophysical Observatory for and on behalf of the National Aeronautics and Space Administration under contract NAS8-03060. SWA acknowledges support from the U.S. Department of Energy under contract number DE-AC02-76SF00515

Chapter 5

Constraints on turbulent pressure in the X-ray halos of giant elliptical galaxies from resonant scattering

N. Werner[1], *I. Zhuravleva*[2], *E. Churazov*[2,3], *A. Simionescu*[4], *S. W. Allen*[1], *W. Forman*[5], *C. Jones*[5], *J.S. Kaastra*[6,7]

[1]Kavli Institute for Particle Astrophysics and Cosmology, Stanford University, 452 Lomita Mall/mc 4085, Stanford, CA 94305, USA
[2]Max-Planck-Institut für Astrophysik, Karl-Schwarzschild-Strasse 1, 85741 Garching, Germany
[3]Space Research Institute (IKI), Profsoyznaya 84/32, Moscow 117810, Russia
[4]Max-Planck-Institut für Extraterrestrische Physik, Giessenbachstr, 85748 Garching, Germany
[5]Harvard-Smithsonian Center for Astrophysics, 60 Garden St., Cambridge, MA 02138, USA
[6]SRON Netherlands Institute for Space Research, Sorbonnelaan 2, 3584 CA Utrecht, the Netherlands
[7]Sterrenkundig Instituut, Universiteit Utrecht, P.O. Box 80000, 3508 TA Utrecht, the Netherlands

Published in the Monthly Notices of the Royal Astronomical Society, volume 398, pages 23–32, 2009

Abstract

The dense cores of X-ray emitting gaseous halos of large elliptical galaxies with temperatures $kT \lesssim 0.8$ keV show two prominent Fe XVII emission features, which provide a sensitive diagnostic tool to measure the effects of resonant scattering. We present here high-resolution spectra of five bright nearby elliptical galaxies, obtained with the Reflection Grating Spectrometers (RGS) on the *XMM-Newton* satellite. The spectra for

the cores of four of the galaxies show the Fe XVII line at 15.01 Å being suppressed by resonant scattering. The data for NGC 4636 in particular allow the effects of resonant scattering to be studied in detail and to prove that the 15.01 Å line is suppressed only in the dense core and not in the surrounding regions. Using deprojected density and temperature profiles for this galaxy obtained with the *Chandra* satellite, we model the radial intensity profiles of the strongest resonance lines, accounting for the effects of resonant scattering, for different values of the characteristic turbulent velocity. Comparing the model to the data, we find that the isotropic turbulent velocities on spatial scales smaller than ≈1 kpc are less than 100 km s^{-1} and the turbulent pressure support in the galaxy core is smaller than 5% of the thermal pressure at the 90% confidence level, and less than 20% at 95% confidence. Neglecting the effects of resonant scattering in spectral fitting of the inner 2 kpc core of NGC 4636 will lead to underestimates of the chemical abundances of Fe and O by ∼10–20%.

5.1 Introduction

The hot intra-cluster medium and the hot halos around giant elliptical galaxies are usually assumed to be optically thin. Although this assumption is valid for most of the emitted X-ray photons, at the energies of the strongest resonant transitions, the hot plasma can be optically thick (Gilfanov et al. 1987). The transition probabilities of strong resonance lines are large and, if the column density of the ion along a line of sight is sufficiently high, photons with the energies of these resonance lines will get absorbed and, within a short time interval, reemited in a different direction. Because of the short time between absorption and emission, this process can be regarded as scattering. Since resonant scattering in clusters and elliptical galaxies will cause the radial intensity profile of an emission line to become weaker in the centre and stronger outside, it can also lead to an underestimate of metal abundances in the dense cores and a corresponding overestimate in the surrounding region. This effect is, however, not expected to be large. Sanders & Fabian (2006) found that metallicities in cluster cores could be underestimated by at most 10% due to resonant scattering.

Gilfanov et al. (1987) pointed out that since the optical depth τ in the core of a resonance line depends on the characteristic velocity of small-scale motion, measurements of τ give important information about the turbulent velocities in the hot plasma. Measuring the level of resonant scattering in clusters and giant elliptical galaxies is thus a good way to constrain the energy in turbulence and the turbulent pressure support. The first constraints on turbulent velocities using resonant scattering were obtained for the Perseus cluster by Churazov et al. (2004). Using XMM-Newton EPIC data, they compared the relative fluxes of the 1s–2p and 1s–3p He-like Fe lines in the core and in an annulus surrounding the core of the Perseus cluster. The expected optical depth of the 6.7 keV 1s–2p Fe XXV resonance line is much larger than that of the 1s–3p line, therefore the ratio provides information about the level of resonant scattering. Churazov et al. (2004) found no evidence for resonant scattering in Perseus, indicating that differential gas motions on scales smaller than ∼100 kpc in the core of the cluster must have a range of velocities of at least half of the sound speed. Independently, using the

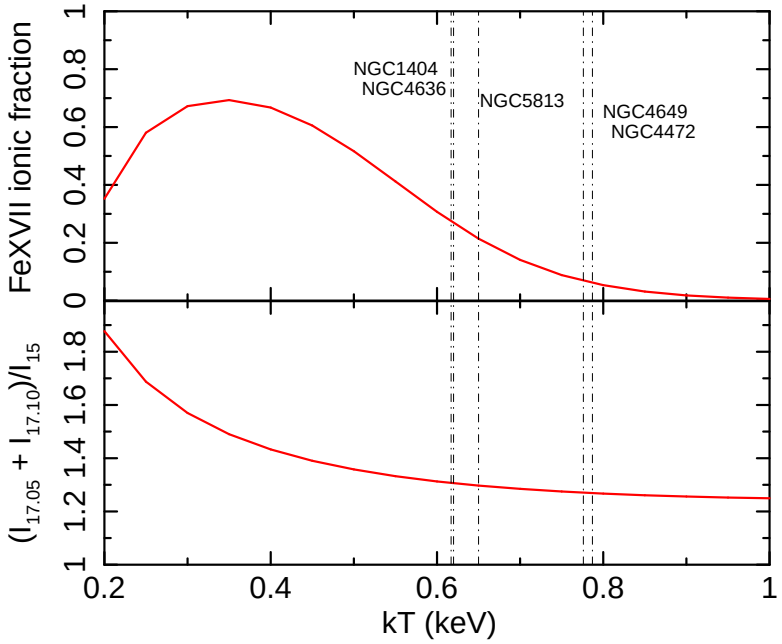

Figure 5.1: Fraction of Fe in the form of Fe XVII and the theoretical line ratio $(I_{\lambda 17.05} + I_{\lambda 17.10})/I_{\lambda 15.01}$ for an optically thin plasma as a function of the plasma temperature. The vertical lines mark the RGS measured temperatures of the five galaxies in our sample.

same data, Gastaldello & Molendi (2004) reached similar conclusions.

The most sensitive spectral lines to determine the level of resonant scattering are the Fe XVII lines at 15.01 Å (2p–3d) and the unresolved blend of the same ion at 17.05 and 17.10 Å (2p–3s). The optical depth is directly proportional to the column density of the ion and the oscillator strength of the given transition. While the oscillator strength of the 15.01 Å line is $f = 2.73$, and thus the line is expected to have a relatively large optical depth, the oscillator strength of the 17.05 Å line is $f = 0.12$ and the optical depth of this line blend is negligible (the oscillator strength of the 17.10 Å line is of the order of 10^{-8})[1]. Because of this dramatic difference in expected optical depths, and the fact that both lines originate from the same ion of the same element, the Fe XVII lines provide, in principle, an excellent diagnostic tool to measure the magnitude of resonant scattering. At the relatively low temperatures of hot halos around giant elliptical galaxies, ∼0.6–0.8 keV, both lines are very strong and, in this temperature range, their expected intensity ratios have only a very weak dependence on temperature (see Fig. 5.1, Doron & Behar 2002). Therefore, any observed spatial dependence of the intensity ratios is unlikely to be due to gradients in temperature or Fe abundance in the

[1] http://cxc.harvard.edu/atomdb/WebGUIDE/index.html

Table 5.1: List of the galaxies in the sample, with their distance (luminosity distances, obtained from the NASA/IPAC Extragalactic Database, http://nedwww.ipac.caltech.edu/), corresponding linear scale per arcminute, Galactic $N_{\rm H}$ value (Kalberla et al. 2005), average temperature measured by *ROSAT*. The last two columns give the total and filtered RGS exposure times, respectively.

galaxy	distance	scale	$N_{\rm H}$	kT	Exp. time	Clean time
	Mpc	kpc/arcmin	10^{20} cm^{-2}	keV	ks	ks
NGC 4636	17.5	5.1	1.90	0.55*	64406	58205
NGC 5813	29.9	8.7	4.37	0.52†	36708	29899
NGC 1404	25.5	7.4	1.51	0.60*	55032	17231
NGC 4649	19.8	5.8	2.1	0.78*	54210	46096
NGC 4472	18.4	5.4	1.53	0.88*	111033	81850

* O'Sullivan et al. (2003)
† Reiprich & Böhringer (2002)

hot plasma, making these lines especially clean diagnostic tools. The Fe XVII line ratios in extended objects can be measured with the *XMM-Newton* Reflection Grating Spectrometers (RGS, den Herder et al. 2001). Xu et al. (2002) reported the first and so far only radial profile of the $(I_{\lambda 17.05} + I_{\lambda 17.10})/I_{\lambda 15.01}$ ratio for the X-ray luminous elliptical galaxy NGC 4636, which indicates the presence of resonant scattering. Attempts to measure resonant scattering in NGC 5044 and M 87, which are hotter and more massive systems with weaker Fe XVII lines, were not successful (Tamura et al. 2003; Werner et al. 2006).

Here we follow up on the work by Xu et al. (2002), by reporting the Fe XVII $(I_{\lambda 17.05} + I_{\lambda 17.10})/I_{\lambda 15.01}$ line ratios measured in the cores of five nearby bright elliptical galaxies observed with *XMM-Newton* RGS: NGC 4636, NGC 5813, NGC 1404, NGC 4649, and NGC 4472. In Sect. 2 we describe the sample and observations; in Sect. 3 we discuss the details of the data analysis; and in Sect. 4 we present the results of the observations. We focus our attention on NGC 4636, for which data are of very high quality. Because NGC 4636 is X-ray bright, has a relatively long exposure and a favorable temperature, for this system we can measure and compare the observed line ratios in the core and surrounding regions. In Sect. 5 we present a model for the radial profile of the 15.01 Å line in NGC 4636 for different values of turbulent velocities, derived using deprojected density and temperature profiles from *Chandra* data. Comparing this model to the data, we place constraints on the characteristic velocity of isotropic turbulence in the core of the galaxy. Implications of the results are discussed in Sect. 6.

Throughout the paper, abundances are given with respect to the "proto-solar values" by Lodders (2003). All errors are quoted at the 68% confidence level for one interesting parameter ($\Delta C = 1$; for C statistics).

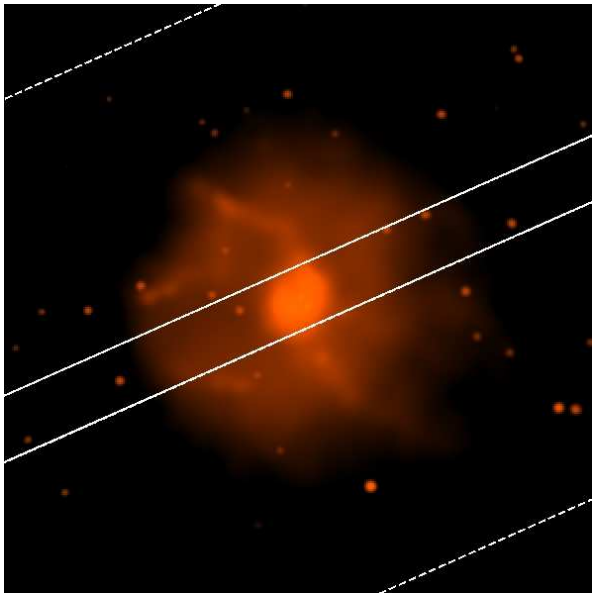

Figure 5.2: *Chandra* image of NGC 4636 with the RGS extraction regions over-plotted. The central extraction region is 0.5′ wide (indicated by full lines), the two extraction regions next to the core (between the full and dashed lines) are 2.25′ wide. The image was extracted in the 0.5–2.0 keV band, cleaned and adaptively smoothed.

5.2 Sample and XMM-Newton observations

We have analyzed a sample of five nearby, giant elliptical galaxies observed with *XMM-Newton* RGS. The sample is listed in Table 5.1. The galaxies were selected based on their relatively low core temperatures, at which a significant fraction of Fe is expected to be in the form of Fe XVII (see Fig. 5.1), their large X-ray fluxes, and strongly peaked surface brightness distributions, which are necessary to obtain RGS spectra with sufficient statistics. The sample contains both relatively relaxed galaxies and systems showing very clear signs of interaction between the hot halo gas and central Active Galactic Nucleus (AGN). In Figs. 5.2 and 9.6 we show 0.5–2.0 keV *Chandra* images of the galaxies in our sample with the RGS extraction regions overplotted. The images show that the cores of NGC 4649, NGC 4472, and NGC 1404 are *relatively* relaxed (although on larger scales NGC 1404 shows a prominent cold front to the Northwest, and NGC 4649 and NGC 4472 harbor central radio sources, which exhibit interaction with the hot gas, Shurkin et al. 2008; Biller et al. 2004). NGC 4636 and NGC 5813, on the other hand, look much more disturbed, with obvious signs of recent episodes of interaction between the hot plasma and the AGN. NGC 4636 has a very dense core and

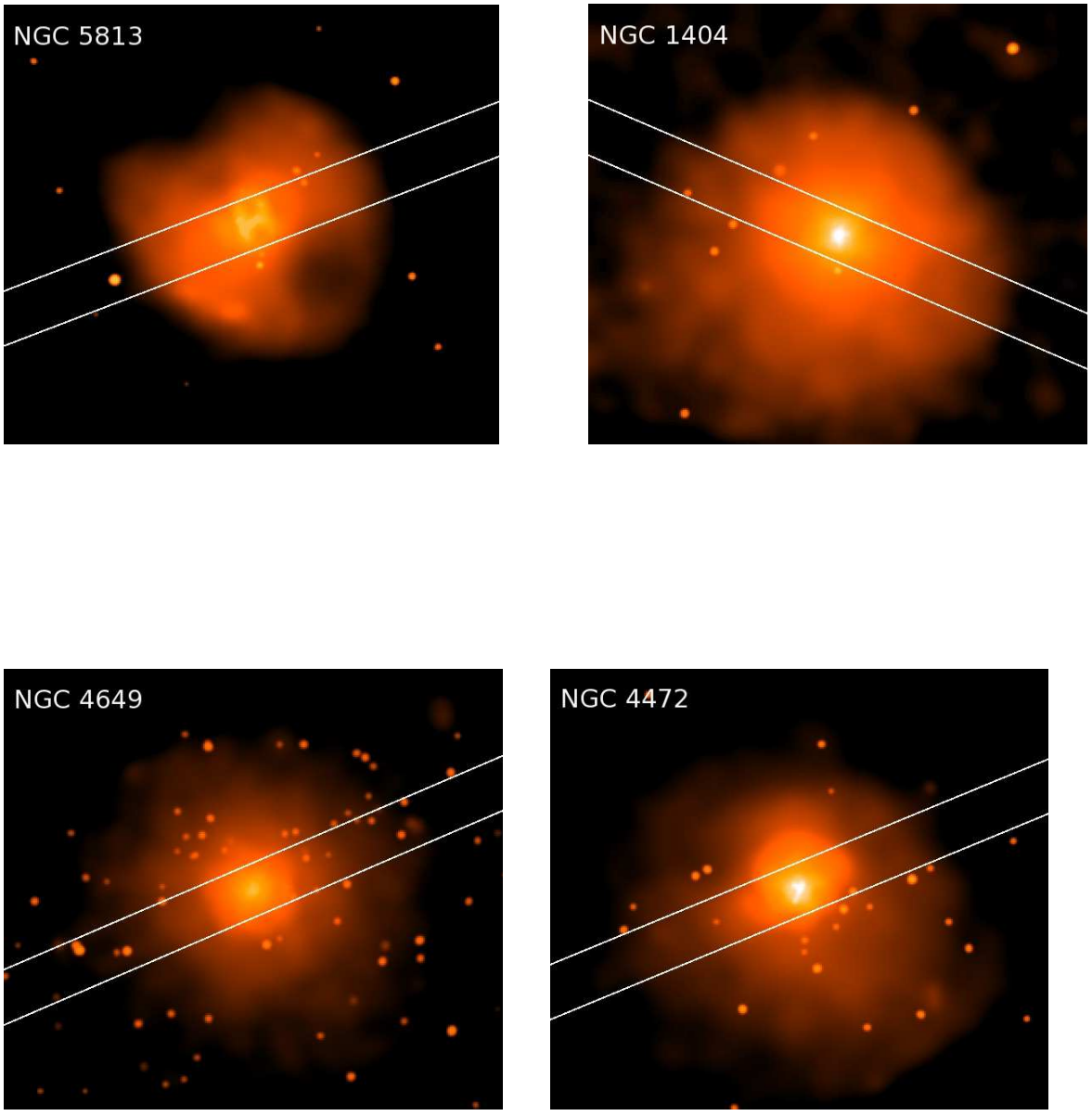

Figure 5.3: *Chandra* images of the giant elliptical galaxies in our sample with overplotted RGS extraction regions (see also Fig. 5.2). The extraction regions are 0.5′ wide. While the core of NGC 5813 is strongly disturbed, the cores of the other three galaxies are relatively relaxed. The images were extracted in the 0.5–2.0 keV band, cleaned and adaptively smoothed.

Table 5.2: The best fit parameters for a single-temperature, optically thin plasma model fitted to the *XMM-Newton* RGS spectra extracted from 0.5′ wide regions centred on the cores of the galaxies. For NGC 4636 we also show the results from fits to spectra extracted from two 2.25′ wide regions surrounding the core (see Fig. 5.2). The 13.8–15.5 Å part of the spectrum, where the strongest Fe XVII and Fe XVIII resonance lines are present was initially excluded from the fits. Fluxes are given in the 0.3–2.0 keV band. The emission measure is defined as $Y = \int n_{\rm e} n_{\rm H} dV$. The scale factor s is the ratio of the observed LSF width to the expected LSF for a flat abundance distribution. Abundances are quoted with respect to the proto-solar values of Lodders (2003). The last three rows list the best fit line ratios in the full spectral band (after the Fe XVII ion was set to zero in the model and replaced by gaussian lines), the theoretical line ratios predicted for an optically thin plasma, and the derived level of suppression of the 15.01 Å line, $(I/I_0)_{15.01\mathring{A}}$.

galaxy	NGC 4636 core	NGC 4636 outer reg.	NGC 5813	NGC 1404	NGC 4649	NGC 4472
flux (10^{-12} erg cm^{-2})	1.75 ± 0.08	2.57 ± 0.17	1.47 ± 0.12	1.08 ± 0.11	1.63 ± 0.10	1.44 ± 0.08
Y (10^{64} cm^{-3})	0.47 ± 0.02	0.46 ± 0.03	1.01 ± 0.10	0.50 ± 0.05	0.31 ± 0.03	0.34 ± 0.02
kT (keV)	0.606 ± 0.006	0.695 ± 0.004	0.645 ± 0.008	0.608 ± 0.009	0.774 ± 0.007	0.781 ± 0.006
s	0.40 ± 0.04	1.02 ± 0.04	0.87 ± 0.11	0.97 ± 0.22	0.69 ± 0.21	0.79 ± 0.12
N	1.3 ± 0.3	1.5 ± 0.4	2.0 ± 0.8	2.3 ± 0.8	1.3 ± 0.7	1.3 ± 0.5
O	0.44 ± 0.05	0.61 ± 0.06	0.53 ± 0.09	0.58 ± 0.10	0.61 ± 0.15	0.53 ± 0.07
Ne	0.31 ± 0.08	0.39 ± 0.18	0.33 ± 0.19	0.81 ± 0.22	1.31 ± 0.35	1.18 ± 0.22
Fe	0.52 ± 0.03	0.92 ± 0.06	0.75 ± 0.09	0.67 ± 0.08	0.87 ± 0.18	0.83 ± 0.08
$[\lambda 17/I_{\lambda 15}]_{\rm observed}$	2.04 ± 0.21	1.28 ± 0.13	1.99 ± 0.34	1.98 ± 0.29	1.25 ± 0.28	2.24 ± 0.34
$[\lambda 17/I_{\lambda 15}]_{\rm predicted}$	1.31	1.31	1.30	1.31	1.27	1.27
$I_{15.01}/I_{0\ 15.01}$	0.64 ± 0.07	1.02 ± 0.10	0.65 ± 0.11	0.66 ± 0.10	1.02 ± 0.23	0.57 ± 0.09

X-ray bright arm-like structures which might have been produced by shocks (Jones et al. 2002). The core of NGC 5813 is highly disturbed with most of the hot gas being pushed into dense sheets by the rising bubbles of relativistic plasma.

Currently the best data set for the study of resonant scattering is that for NGC 4636. The X-ray halo of this galaxy has a conveniently low temperature, at which ∼26% of Fe is in the form of Fe XVII, a very dense core and a deep *XMM-Newton* observation, which also allows us to extract spectra from outside the core region with reasonably good statistics in the Fe XVII lines. Using a deep *Chandra* observation of this galaxy we derive deprojected density and temperature profiles which we use to model radial intensity profiles for the strongest resonance lines, taking into account the effects of resonant scattering for different assumed values of turbulent velocities.

5.3 Data analysis

5.3.1 *XMM-Newton* RGS data analysis

We processed the RGS data using version 8.0.0 of the *XMM-Newton* Science Analysis System (SAS), and extracted spectra using the method described by Tamura et al. (2001). To minimize the contamination by soft-protons from Solar flares, we extracted

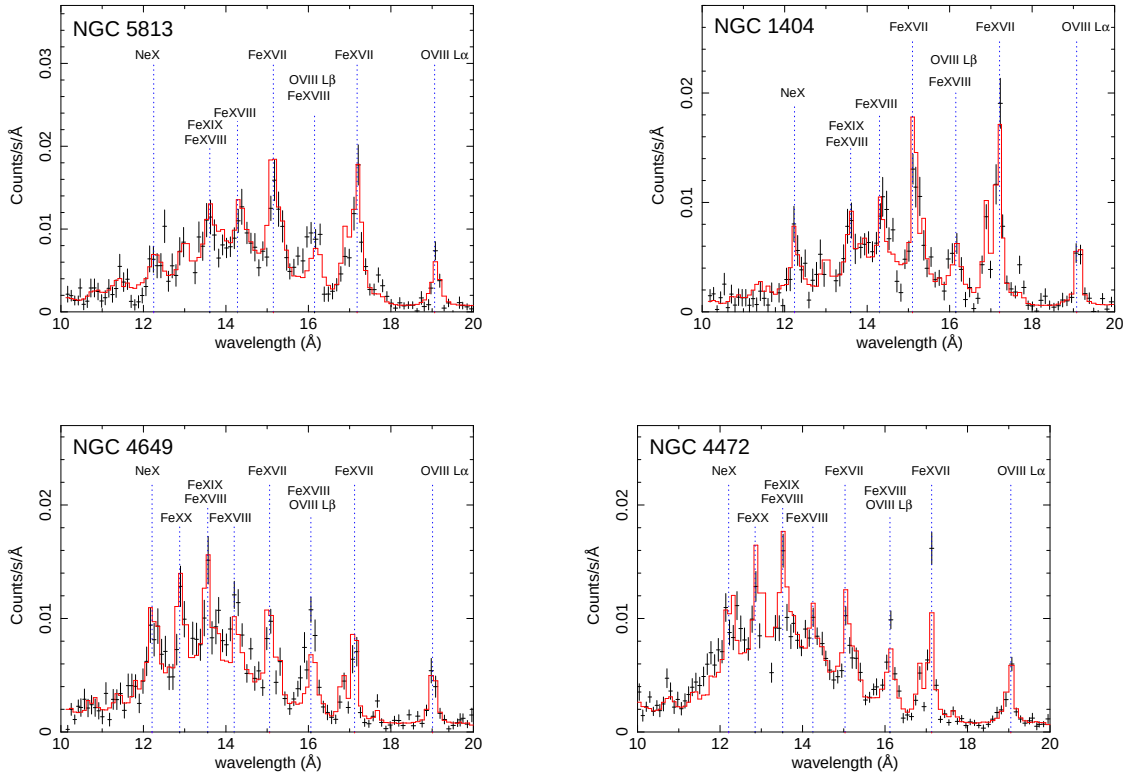

Figure 5.4: RGS spectra for NGC 5813, NGC 1404, NGC 4649, and NGC 4472. The spectra were extracted from 0.5′ wide extraction regions centred on the cores of the galaxies. The full line indicates the best-fit optically-thin single-temperature plasma model. The 13.8–15.5 Å part of the spectrum, where the strongest Fe XVII and Fe XVIII resonance lines are present, was excluded from these spectral fits.

a light curve for each dataset using events on CCD 9 of the RGS, outside the central region, with a distance larger than 30″ from the dispersion axis, and excluded time intervals with elevated count rates. The original exposure time and the total time after cleaning are listed in Table 5.1. The flares in the observation of NGC 1404 were weak and we obtain the same best fit spectral parameters for both the filtered and unfiltered data set. Therefore, for this galaxy we used the full observation. Because emission from the galaxies fills the entire field of view of the RGS, the background cannot be estimated from a region on the detector away from the source. Therefore, we modeled the background using the standard RGS background model for extended sources available in SAS (rgsbkgmodel, Gonzaléz-Riestra 2004).

The effects of resonant scattering are most significant in the centermost parts of the galaxies, where the density is highest. Therefore, we extract spectra from narrow 30″ wide bands centred on the cores of the galaxies, probing regions within radii of 1.3–2.2 kpc (depending on distance) in the cross dispersion direction of the RGS. We extract and fit both first and second order spectra. Because the RGS operates without a slit, it collects all photons from within the $0.5' \times \sim 12'$ field of view. Line photons originating at angle $\Delta\theta$ (in arcminutes) along the dispersion direction, will be shifted in wavelength by

$$\Delta\lambda = 0.138\,\Delta\theta\ \mathring{A}. \tag{5.1}$$

Therefore, every line will be broadened by the spatial extent of the source. To account for this broadening in our spectral model, for each RGS spectrum, we produce a predicted line spread function (LSF) by convolving the RGS response with the surface brightness profile of the galaxy derived from the EPIC/MOS1 image in the 0.8–1.4 keV band along the dispersion direction. Because the radial profile of a particular spectral line can be different from the overall radial surface brightness profile (e.g. in the presence of metallicity gradients), the line profile is multiplied by a scale factor s, which is the ratio of the observed LSF width to the expected LSF for a flat abundance distribution. This scale factor is a free parameter in the spectral fit.

For the spectral modeling of the RGS data we use the SPEX package (Kaastra et al. 1996). Spectral fitting of the RGS data is done in the 10 Å to 28 Å band. We model the emission of the observed galaxies as optically thin plasmas in collisional ionization equilibrium, absorbed by neutral Galactic gas with Solar abundances. For each object we fix the Galactic column density to the value determined by the Leiden/Argenitine/Bonn (LAB) Survey of Galactic H I (Kalberla et al. 2005). For the emission of the elliptical galaxies we assume a single-temperature plasma. Using more complicated multi-temperature models does not improve the fits and differential emission measure models always converge to a simple single-temperature approximation. The spectral normalization, plasma temperature, and the abundances of N, O, Ne, and Fe are free parameters in the fit. For the spectral fitting we use C-statistics.

5.3.2 *Chandra* analysis of NGC 4636

We reprocessed the *Chandra* observations of NGC 4636 (OBSID 3926 and 4415) applying the latest CTI and time-dependent gain calibrations using standard methods (see

Vikhlinin et al. 2005, for more details). In brief, we performed the usual filtering by grade, excluded bad/hot pixels and columns, removed cosmic ray 'afterglows', and applied the VF mode filtering. We excluded data with anomalously high background. The remaining exposure time for NGC 4636 is 150.4 ks. The background files were processed in the same manner as the observations. An additional background component is produced during the 41 ms of the 3.2 s nominal exposure readout of the ACIS CCDs, while the chips are exposed to the sky. This small contribution of the source flux, 1.3%, is uniformly re-distributed along the readout direction and is subtracted using the technique described by Markevitch et al. (2000). The blank-field background is also renormalized by reducing its integration time by 1.3% to account for this additional subtraction.

As the final step in data preparation (see Churazov et al. 2008, for more details), we computed, for each X-ray event, the ratio of the effective area (a function of photon energy and position) to that at a predefined energy and position:

$$\eta = A(E, x_d, y_d) / A_0(E), \tag{5.2}$$

where $A(E, x_d, y_d)$ includes mirror and detector efficiencies (including non-uniformity of the detector quantum efficiency and the time and spatially dependent contamination on the optical blocking filter). Finally, for each event list, we make an exposure map that accounts for all position dependent, but energy independent, efficiency variations across the focal plane (e.g., overall chip geometry, dead pixels or rows, and variation of telescope pointing direction). We use these data in Sect. 5.5 to derive deprojected gas density and temperature profiles.

5.4 Observations of resonant scattering

The results from the spectral fitting of the *XMM-Newton* RGS data with an optically thin single-temperature plasma model are shown in Table 5.2. The 13.8–15.5 Å part of the spectrum, where the strongest Fe XVII and Fe XVIII resonance lines are present, was initially excluded from this fit. These lines are expected to be suppressed by resonant scattering and this suppression, which is not accounted for in the plasma model, could slightly bias the best fit spectral parameters. After obtaining the best fit, we freeze the temperature and Fe abundance of the thermal component, set the abundance of the Fe XVII ion to zero in the model, add narrow Gaussians at the wavelength of the strongest Fe XVII lines (restframe wavelengths of 15.01 Å, 17.077 Å, 15.30 Å, and 16.80 Å) and re-fit the full 10–28 Å spectral band. Freezing the temperature and the Fe abundance is necessary because by setting the Fe XVII ion to zero and replacing it with Gaussians in the model we lose important constraints on these parameters. The line normalisations, the continuum level (normalisation of the thermal component), the abundances of the other elements and the broadening factor s are free parameters. In the error calculation, we also marginalise over the uncertainties of the temperature and Fe abundance as determined in the initial fit. We determine the best fitting normalisations for these Gaussians and the value of $(I_{\lambda 17.05} + I_{\lambda 17.10}) / I_{\lambda 15.01}$ (the 17.05 and 17.10 Å lines are blended and we fit them with a single Gaussian at 17.077 Å). We divide the

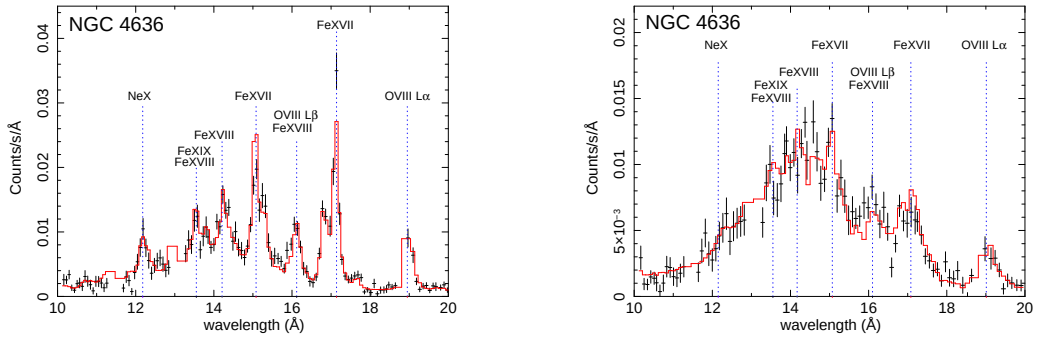

Figure 5.5: *XMM-Newton* RGS spectra extracted from a 0.5′ wide extraction region centered on the core of NGC 4636 (left panel) and from two 2.25′ wide extraction regions surrounding the core (right panel). The ratios of the Fe XVII lines at 15.01 and ∼17 Å change. The full line indicates the best fit optically thin single-temperature plasma model. The 13.8–15.5 Å part of the spectrum, where the strongest Fe XVII and Fe XVIII resonance lines are present, was excluded from these spectral fits.

theoretical ratio $(I_{\lambda 17.05} + I_{\lambda 17.10})/I_{\lambda 15.01}$ by the measured value, which, assuming the lines at ∼17 Å are optically thin, gives us the level at which the 15.01 Å line is suppressed, $(I/I_0)_{15.01\mathring{A}}$. These values are listed in Table 5.2. In four out of five galaxies the line ratios are significantly higher (observed values ∼ 2.0) than the expected theoretical value for an optically thin plasma of 1.27–1.31, indicating that the 15.01 Å line is optically thick. In NGC 4649, the line ratios are consistent with the 15.01 Å line being optically thin.

A number of factors argue that the observed high $(I_{\lambda 17.05} + I_{\lambda 17.10})/I_{\lambda 15.01}$ line ratio is due to resonant scattering. The $(I_{\lambda 17.05} + I_{\lambda 17.10})/I_{\lambda 15.01}$ line ratio in an optically thin plasma can reach values ∼ 1.9 only for temperatures as low as 0.2 keV (see Fig. 5.1, Doron & Behar 2002), which is much lower than the observed temperatures of the galaxies. Moreover, if the plasma in the cores of the galaxies were multiphase with an additional 0.2 keV component, which would alter the Fe XVII line ratios, then we would also observe other strong lines (e.g. O VII), which we do not. Another possibility to obtain such high line ratios in an optically thin plasma is non-equilibrium ionization (NEI). However, NEI effects are unlikely in the dense plasma in cores of giant elliptical galaxies because, due to the high density, the equilibration time is short. If the higher-than-expected line ratios were due to incomplete atomic physics in the current spectral models, then they should not change as a function of radius. This can be directly verified in NGC 4636, which has the best combination of X-ray flux, temperature, and exposure. The data for this galaxy allow us to extract spectra and determine the $(I_{\lambda 17.05} + I_{\lambda 17.10})/I_{\lambda 15.01}$ line ratios in the combined spectrum from two regions surrounding the core at 15″–150″ from the centre of the galaxy, in the crossdispersion direction of the RGS (see Fig. 5.2). We follow here the same fitting procedure as for the cores of the galaxies. The best fitting results are shown in the third column of Table 5.2. The off-centre line ratios are consistent with the 15.01 Å line being optically

Table 5.3: Oscillator strengths and optical depths for the strongest X-ray lines in the spectrum of NGC 4636 for Mach numbers 0.0, 0.25, 0.5, 0.75. The expected suppression due to resonant scattering $(I/I_0)_{\rm cir}$ gives the value integrated within a radius of 2 kpc from the centre of the galaxy. The approximate values $(I/I_0)_{\rm RGS}$ were obtained by integrating within an "effective extraction region" which is 0.5′ wide and 3′ long. The metallicity is assumed to be constant with the radius.

Ion	λ (Å)	f	$M = 0.0$			$M = 0.25$			$M = 0.5$			$M = 0.75$		
			τ	$(I/I_0)_{\rm cir}$	$(I/I_0)_{\rm RGS}$	τ	$(I/I_0)_{\rm cir}$	$(I/I_0)_{\rm RGS}$	τ	$(I/I_0)_{\rm cir}$	$(I/I_0)_{\rm RGS}$	τ	$(I/I_0)_{\rm cir}$	$(I/I_0)_{\rm RGS}$
Fe XVII	15.01	2.73	8.8	0.47	0.69	3.6	0.59	0.79	1.9	0.68	0.85	1.3	0.76	0.89
Fe XVII	17.05	0.12	0.5	0.89	0.95	0.2	0.95	0.98	0.1	0.97	0.99	0.07	0.98	0.99
Fe XVIII	14.20	0.57	1.3	0.72	0.87	0.5	0.86	0.94	0.3	0.91	0.96	0.2	0.95	0.98
Fe XVIII	16.08	0.005	0.01	0.99	1.00	0.005	0.99	1.00	0.003	1.00	1.00	0.002	1.00	1.00
O VIII Lα	18.96	0.28	1.2	0.74	0.87	0.8	0.81	0.91	0.5	0.88	0.94	0.3	0.91	0.96

thin in this region. The difference in the spectra of the core and surrounding regions of NGC 4636 can be seen clearly in Fig. 5.5. While the 15 Å line is suppressed in the centre, it may be slightly enhanced outside the dense core.

The best fit line broadening scale factor s indicates that in NGC 4636 the distribution of the line producing ions is more peaked than the surface brightness, suggesting that the distribution of metals is centrally peaked. In the other systems this effect is smaller and less significant.

5.5 Modelling of resonant scattering in NGC 4636

To gain a better understanding of the observed line ratios, we simulate the effects of resonant scattering on the radial intensity profiles of the strongest X-ray emission lines in NGC 4636. For this we use the deprojected temperature and density profiles measured with *Chandra*.

In our deprojection analysis, we follow the approach described by Churazov et al. (2008). We assume spherical symmetry, but make no specific assumption about the form of the underlying gravitational potential. For a given surface brightness profile in $n_{\rm a}$ annuli, we choose a set of $n_{\rm s}$ ($n_{\rm s} \leq n_{\rm a}$) spherical shells with the inner radii $r({\rm i})$, ${\rm i} = 1, \ldots, n_{\rm s}$. The gas emissivity $\mathcal{E}$ is assumed to be uniform inside each shell, except for the outermost shell, where the gas emissivity is assumed to decline as a power law of radius: $\mathcal{E} = \mathcal{E}_{\rm out} r^{-6\beta_{\rm out}}$, where $\beta_{\rm out}$ is a parameter. The deprojection process is a simple least square solution to determine the set of emissivities in the set of shells (along with the emissivity normalization $\mathcal{E}_{\rm out}$ of the outer layers) that provides the best description of the observed surface brightness. The emissivity of each shell can then be evaluated as an explicit linear combination of the observed quantities. Since the whole procedure is linear, the errors in the observed quantities can be propagated straightforwardly. With our definition of η (see subsection 5.3.2), the projection matrix does not depend on energy. Therefore, the deprojection in *any energy band* is precisely that used to deproject the surface brightness. Thus, we can accumulate a set of spectra (corrected for background and readout) for each of the $n_{\rm a}$ annuli, and apply the deprojection to

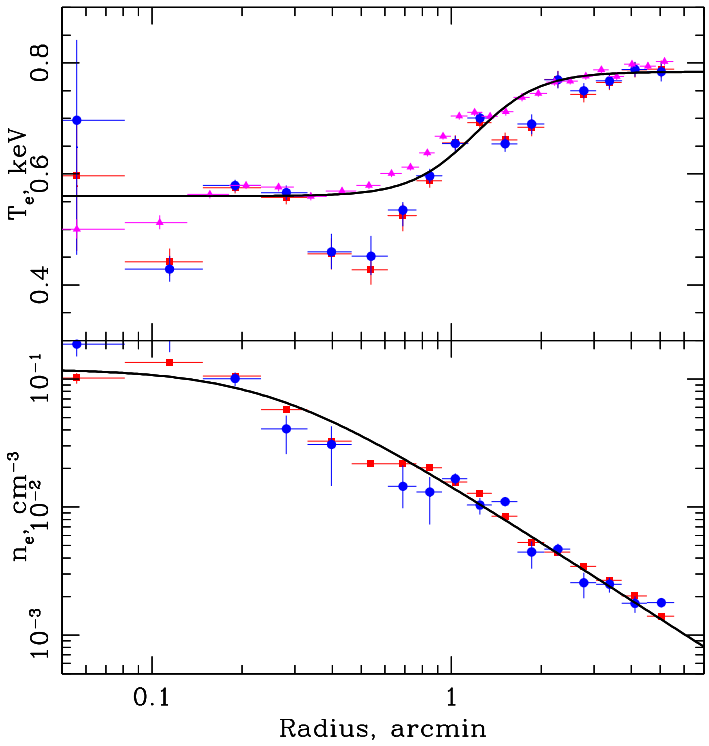

Figure 5.6: Observed radial profiles of the electron density and temperature used to model resonant scattering in NGC 4636. The blue circles and red squares indicate the deprojected profiles determined from *Chandra* data with metallicity as a free parameter in the fit and with metallicity fixed to 0.68 Solar, respectively. The magenta triangles show the projected radial temperature profile with the metallicity as a free parameter in the fit. The solid lines show the parametrization of the gas density and gas temperature profiles given in eqs. 5.3 and 5.4.

determine the emissivities of each shell in each of the ACIS energy channels.

The *Chandra* data were modeled using XSPEC V12 (Arnaud 1996) and the APEC model (Smith et al. 2001). The gas temperature and normalization were free parameters in the model. The heavy element abundance was either a free parameter in the fit or fixed to 0.68 Solar (as determined from a spectral fit to *Chandra* data extracted within the radius of $1'$ from the centre of NGC 4636). The metallicity profile in NGC 4636 has large uncertainties, because the metal abundance distribution in the deprojected *Chandra* spectra has a large scatter as a result of noise enhancement during deprojection coupled with the limited spectral resolution of the CCDs.

The electron density profile was derived from the spectral normalization, fixing the proton to electron ratio to 0.83. Fig. 5.6 shows the deprojected electron density (lower panel) and the temperature (upper panel) as a function of distance from the centre of the galaxy. The circles and squares show the deprojected profiles for metallicity as a free parameter and for metallicity fixed to 0.68 Solar, respectively. The triangles show the projected temperature profile with the metallicity as a free parameter.

Based on the observed radial distributions of electron density $n_{\rm e}$ and temperature $kT_{\rm e}$ in NGC 4636, we adopt the following approximate forms for the deprojected density and temperature profiles:

$$n_{\rm e} = 1.2 \times 10^{-1} \left[1 + \left(\frac{r}{0.25'}\right)^2\right]^{-0.75} \ {\rm cm}^{-3}, \tag{5.3}$$

and

$$kT = 0.56 \frac{1 + 1.4(r/1.2')^4}{1 + (r/1.2')^4} \ {\rm keV}. \tag{5.4}$$

We consider two possible radial behaviors for metallicity: a simple constant abundance of 0.68 Solar; and a centrally peaked abundance distribution, which is more consistent with the best fit *XMM-Newton* RGS line profile ($s = 0.40 \pm 0.04$). In the latter case we approximate the metallicity profile with the following function:

$$Z = 0.95 \frac{2 + (r/0.8')^3}{1 + (r/0.8')^3} - 0.4. \tag{5.5}$$

We calculate the optical depth of the 15 Å line from the centre of the galaxy to infinity, $\tau = \int n_{\rm i} \sigma_0 {\rm d}r$, where $n_{\rm i}$ is the ion concentration and σ_0 is the cross section at the line centre, which for a given ion is

$$\sigma_0 = \frac{\sqrt{\pi} h r_{\rm e} c_{\rm s} f}{\Delta E_{\rm D}}, \tag{5.6}$$

where the Doppler width is given by

$$\Delta E_{\rm D} = E_0 \left(\frac{2kT_{\rm e}}{A m_{\rm p} c_{\rm s}^2} + \frac{V_{\rm turb}^2}{c_{\rm s}^2} \right)^{1/2}. \tag{5.7}$$

In these equations r_e is the classical electron radius, f is the oscillator strength of a given atomic transition, E_0 is the rest energy of a given line, A is the atomic mass of the corresponding element, m_p is the proton mass, c_s is the sound speed, and V_{turb} is the characteristic velocity of isotropic turbulence. $V_{turb} \equiv \sqrt{2}V_{1D,turb}$, where $V_{1D,turb}$ is the velocity dispersion in the line of sight due to turbulence. Using the adiabatic sound speed, $c_s = \sqrt{\gamma\, k\, T\, /\, \mu\, m_p}$, the expression for the broadening can be rewritten as

$$\Delta E_D = E_0 \left[\frac{2kT_e}{A m_p c_s^2} (1 + \frac{\gamma}{2\,\mu} A M^2) \right]^{1/2}, \tag{5.8}$$

where $\mu = 0.6$ is the mean particle mass, γ is the adiabatic index, which for ideal monatomic gas is 5/3, and $M = V_{turb}/c_s$ is the corresponding Mach number. The line energies and oscillator strengths were taken from ATOMDB[2] and the NIST Atomic Spectra Database[3].

The resonant scattering effect has been calculated using Monte-Carlo simulations, as described by Churazov et al. (2004). We model the hot halo as a set of spherical shells and obtain line emissivities for each shell using the APEC plasma model (Smith et al. 2001). We account for scattering by assuming a complete energy redistribution and dipole scattering phase matrix. The line of Fe XVII has a pure dipole scattering phase matrix. In Fig. 5.7 we show the optical depth of the 15.01 Å Fe XVII line as a function of radius, for various turbulent velocities, assuming the peaked Fe abundance distribution. For higher turbulent velocities, the optical depth becomes smaller. In Fig. 5.8 we show the ratio of the 15.01 Å line intensity calculated including the effect of resonant scattering to the line intensity without accounting for resonant scattering for various turbulent velocities, both for constant and peaked iron abundance distributions. The figure clearly shows the effect of the resonant scattering: in the core of the galaxy the intensity of the line is suppressed, whereas in the surrounding regions the intensity of the line rises. The effect is more prominent in the case of the centrally peaked Fe abundance distribution, where the central suppression is larger and the enhancement in the outer part is stronger.

We compare the models of resonant scattering with the observations and determine the systematic uncertainties involved by simulating spectra corresponding to each of these models, which are then fit in the same way as the observed data. To this end, we multiply the surface brightness profile of NGC 4636 with the theoretical suppression profiles for the 15.01 Å line (Fig. 5.8) to determine the predicted RGS line profile for the four considered characteristic turbulent velocities, for both assumed abundance distributions. We simulate spectra with photon statistics comparable to that of the actual observation, using the best fit values for the core of NGC 4636 from Table 5.2 as input parameters, and convolving the 15.01 Å line through these predicted line profiles. By fitting the data simulated with no turbulence, we obtain $(I/I_0)_{15.01\mathring{A}} = 0.69$ and 0.71 for peaked and flat abundance profiles, respectively. The ratios of $(I/I_0)_{15.01\mathring{A}}$ for isotropic turbulent velocity of $M = 0.25$ are 0.76 and 0.78, and for $M = 0.50$ they

[2] http://cxc.harvard.edu/atomdb/WebGUIDE/index.html
[3] www.physics.nist.gov/PhysRefData/ASD/index.html

are 0.80 and 0.82, for peaked and flat abundance profiles, respectively. The systematic uncertainty on these values due to our lack of knowledge about the actual Fe abundance distribution is ± 0.02. We add this uncertainty in quadrature to the uncertainties associated with our modeling of the line broadening, which is at most 0.03, resulting in a total uncertainty of 0.04. Thus we conclude that the turbulent velocities in NGC 4636 are relatively small and that isotropic turbulence with a characteristic velocity of $M > 0.25$ can be ruled out at the 90% confidence level; turbulent gas motions at $M > 0.5$ can be ruled out at the 95% confidence level. (The sound speed in NGC 4636 is $c_{\rm s} \sim 400$ km s^{-1}.)

In Table 5.3, we list the strongest lines observed in the spectrum of NGC 4636, their oscillator strengths and optical depths for different Mach numbers. Clearly, Fe XVII at 15.01 Å is the most optically thick line in the spectrum, but O VIII Lα and Fe XVIII at 14.2 Å also have relatively large optical depths. For $M = 0$, the depth of the Fe XVII line at 17.05 Å line is $\tau = 0.5$, meaning that our assumption that the 17.05 Å and 17.10 Å line blend is optically thin is not completely correct, and our *observed* values of $(I/I_0)_{15.01\mathring{A}}$ are biased slightly high, which further increases the significance of our upper limits on the turbulent velocities. In Table 5.3, we also list the predicted suppression for the strongest emission lines, $(I/I_0)_{\rm circ} = \int I {\rm d}A \,/\, \int I_0 {\rm d}A$, integrated within a circular region of radius 2 kpc, and within the RGS extraction region $(I/I_0)_{\rm RGS}$. The suppression for the RGS is determined in a simplified way, integrating within our $0.5'$ wide, and for line emission effectively about $3'$ long, RGS extraction region. These predicted ratios in Table 5.3 were determined assuming a flat abundance distribution. By adopting an optically thin plasma in the analysis, the best fitting O abundance within the 2 kpc radius can be underestimated by $\sim$10–25%, and the Fe abundance by $\sim$10–20%.

5.6 Discussion and conclusions

High-resolution spectra obtained with *XMM-Newton* RGS reveal that the Fe XVII line at 15.01 Å in the cores of the elliptical galaxies NGC 4636, NGC 1404, NGC 5813, and NGC 4472 is suppressed by resonant scattering. The effects of resonant scattering can be investigated in detail for NGC 4636. The comparison of the measured suppression of the 15.01 Å Fe XVII line in the spectrum of NGC 4636 with the simulated effects of resonant scattering reveals that the characteristic velocity of isotropic turbulence in the core of the galaxy is smaller than 0.25 and 0.5 of the sound speed at the $\sim$90% and 95% confidence levels, respectively. The energy density in turbulence is:

$$\epsilon_{\rm turb} = \frac{3}{2}\,\rho\, V_{\rm 1D,turb}^2 = \frac{3}{4}\,\rho\, c_{\rm s}^2\, M^2 \tag{5.9}$$

where ρ is the density of the plasma. The thermal energy of the plasma is given as:

$$\epsilon_{\rm therm} = \frac{3}{2}\frac{\rho}{\mu m_{\rm p}} kT. \tag{5.10}$$

By combining these equations we obtain the ratio of turbulent to thermal energy:

$$\frac{\epsilon_{\rm turb}}{\epsilon_{\rm therm}} = \frac{\gamma}{2}\, M^2. \tag{5.11}$$

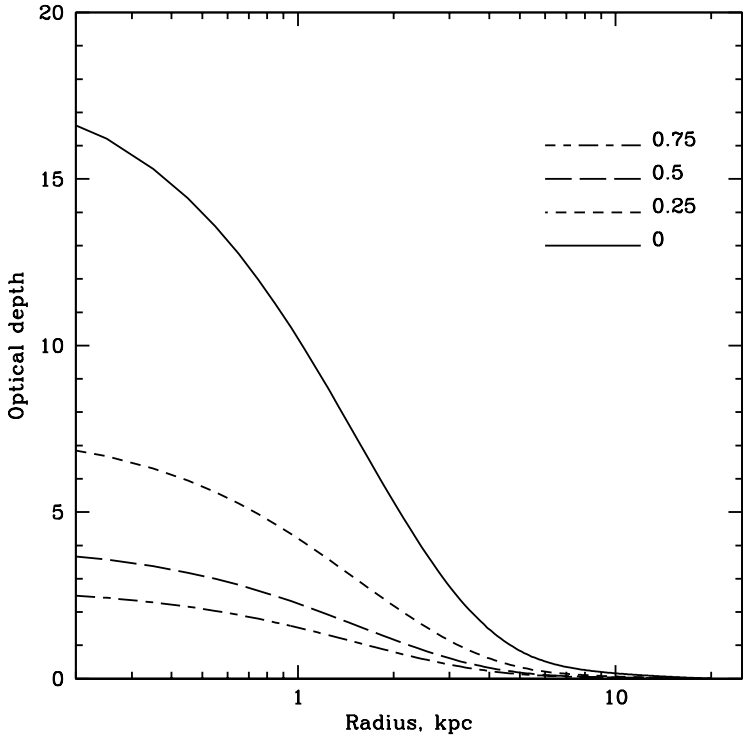

Figure 5.7: Optical depth of the 15.01 Å line calculated from the given radius to infinity, for isotropic turbulent velocities corresponding to Mach numbers 0.0, 0.25, 0.5, and 0.75. A centrally peaked Fe abundance distribution is assumed.

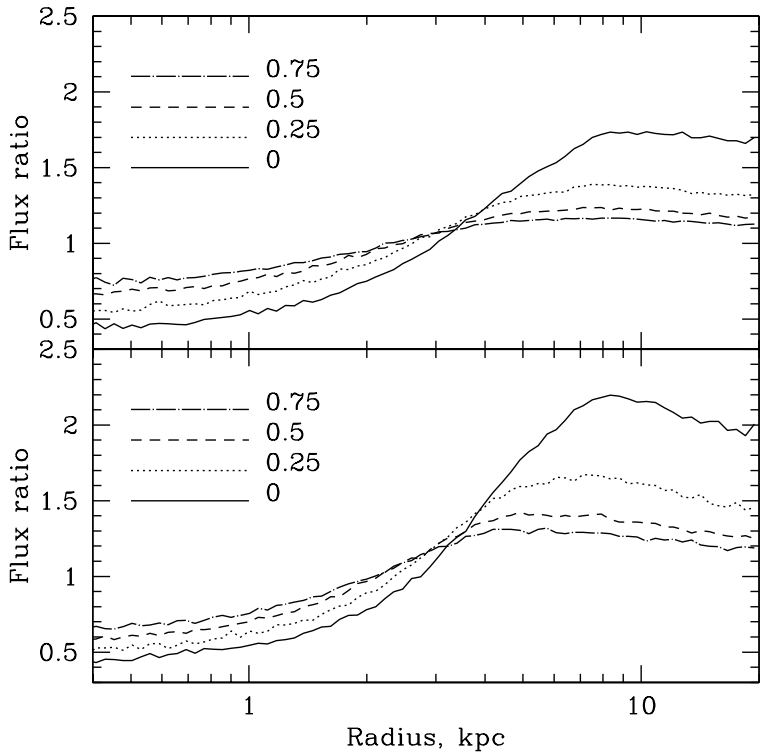

Figure 5.8: Radial profiles of the ratio of the 15.01 Å line intensity with and without the effect of resonant scattering, for isotropic turbulent velocities corresponding to Mach numbers 0.0, 0.25, 0.5, and 0.75. The upper panel shows the profiles for a constant metallicity, and the lower panel for a centrally peaked Fe abundance distribution.

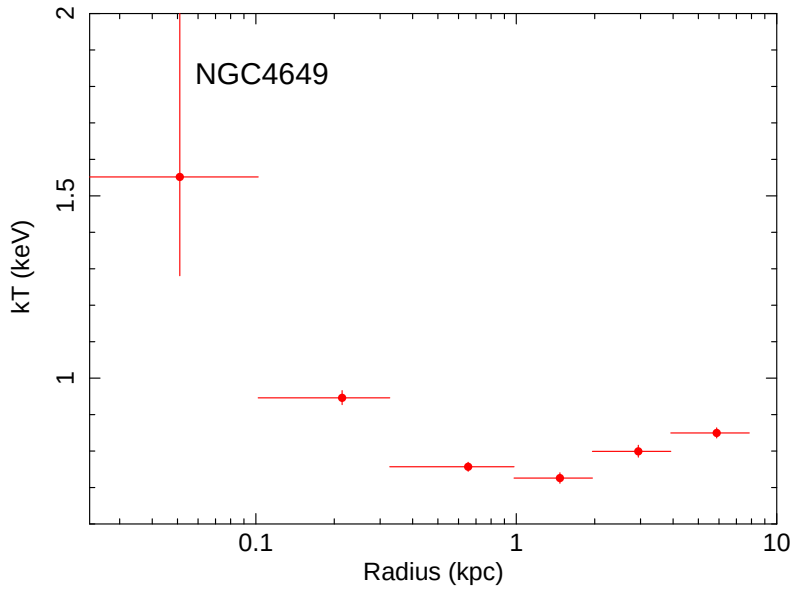

Figure 5.9: The deprojected temperature profile of NGC 4649 determined using *Chandra* data. It shows an unusual central peak.

For the 90% and 95% confidence level upper limits of $M \lesssim 0.25$ and 0.5 on the characteristic velocity of isotropic turbulence in NGC 4636, the upper limit on the fraction of energy in turbulent motions is 5% and 20%, respectively. This is in agreement with the upper limits on the non-thermal pressure component in elliptical galaxies obtained on larger spatial scales by Churazov et al. (2008) and with the properties of AGN induced turbulence in three-dimensional simulations, that use adaptive mesh hydrodynamic code with a subgrid model of turbulence and mixing (Scannapieco & Brüggen 2008).

A small value for the average turbulent velocity dispersion was also inferred in the initial analysis of the RGS spectra for NGC 4636 by Xu et al. (2002). They estimated that the turbulent velocities in the galaxy do not strongly exceed 1/10 of the sound speed. Caon et al. (2000) studied the kinematics of line emission nebulae in NGC 4636 and found an irregular radial velocity curve which indicates turbulent motions in the core. The measured radial velocities of the emission line nebulae are mostly within about $\sim$100 km s^{-1}. The kinematics of emission line nebulae in the sample of elliptical galaxies studied by Caon et al. (2000) indicates chaotic gas motions with velocities of about $M = 0.2$–0.4. In cooling cores, optical emission line nebulae often spatially coincide with soft X-ray emission (e.g. Sparks et al. 2004; Fabian et al. 2006), which indicates a coupling, suggesting that the two gas phases should share the same turbulent velocities.

The dense cores of NGC 4636 and NGC 5813 show strong evidence of recent violent interaction between the hot plasma and the AGN. This interaction is expected to induce turbulence through the mechanical activity of the outflows (Churazov et al. 2001). Our

results indicate that the typical velocities of the AGN induced turbulent motions in the hot plasma on sub-kpc spatial scales are less than 100–200 km s^{-1}. Gas motions on larger spatial scales likely have larger velocities. Observations of the Perseus cluster suggest both turbulent and laminar gas motions with velocities as high as 700 km s^{-1} (Fabian et al. 2003b,a). The observed lack of resonant scattering in the 6.7 keV Fe-K line within the inner $\sim$100 kpc (Churazov et al. 2004) of Perseus confirms the presence of such strong gas motions. AGN induced gas motions with large range of velocities along our line of sight, perhaps even on spatial scales smaller than $\approx$1 kpc, could explain the observed lack of resonant scattering in the 15.01 Å Fe XVII line in M 87 (the analysis of a 0.5′ wide extraction region centred on the core of M 87 gives $(I_{\lambda 17.05} + I_{\lambda 17.10})/I_{\lambda 15.01} = 1.3 \pm 0.3$, Werner et al. 2006). We note that the central AGN in Perseus and in M 87 are more active in X-rays than the AGN in the target galaxies of this study.

The dense cores of galaxies showing smaller disturbance by AGN might be expected to exhibit less turbulence than the heavily disturbed systems. Therefore, we might expect the 15.01 Å line to be more suppressed in the most relaxed galaxies in our sample. While there is a weak indication of the suppression increasing from the least to the most relaxed systems: from NGC 5813 and NGC 4636, to NGC 4472, the large errorbars on the line ratios and the small number of galaxies in the sample do not allow us to draw firm conclusions.

The best fit line ratio in the apparently relaxed galaxy NGC 4649 shows no indication for resonant scattering in its core. The lack of observable optical depth effects in this galaxy can be explained by the unusual temperature profile of its gaseous halo, which exhibits a sharp temperature peak in its centre (see Fig. 5.9, Allen et al. in prep.). Within the central 0.1 kpc of the galaxy, the temperature increases by about a factor of 2 to $\sim$1.5 keV, at which no Fe XVII is present in the gas, implying that all the observed Fe XVII emission is from lower density regions surrounding the hot core. The high temperature might be due to shock heating by the central AGN (e.g. Shurkin et al. 2008). None of the other galaxies in our sample shows such an unusual temperature profile (Allen et al. 2006, Allen et al. in prep.).

Unfortunately, the high temperatures of cluster cores do not allow us to use Fe XVII lines as a diagnostic tool to measure the effects of resonant scattering and thus place firm constraints on turbulent velocities in the intra-cluster medium. No other lines have a comparable sensitivity to the turbulent velocities. However, the dense cores of elliptical galaxies, are in terms of the dominant physical processes like cooling and AGN feedback, sufficiently similar to cooling cores of clusters of galaxies to argue that the turbulent velocities on small spatial scales, and thus the turbulent pressure support in these systems, are also likely to be low. This is encouraging for cosmological studies based on X-ray observations of galaxy clusters (e.g. Allen et al. 2008; Mantz et al. 2008; Henry et al. 2008; Vikhlinin et al. 2008). Simulations predict that turbulent gas motions in the intra-cluster medium can provide 5%–25% of the total pressure support through the virial region of clusters, potentially biasing low hydrostatic mass estimates, even in relaxed systems (e.g. Nagai et al. 2007). However, these predictions depend sensitively on the gas physics assumed. Our results argue that such turbulence may be suppressed in nature, at least within the inner regions of such systems. For the merg-

ing unrelaxed Coma cluster, a ∼10% lower limit on turbulent pressure support was obtained by Schuecker et al. (2004) from a Fourier analysis of pressure maps. In the range 40–90 kpc, the turbulent spectrum was found to be well described by a projected Kolmogorov/Oboukhov-type model.

Future, deeper (of the order of ∼500 ks) observations of large nearby elliptical galaxies with the *XMM-Newton* RGS should provide even tighter constraints on turbulent velocities from resonant scattering. X-ray calorimeters on future missions such as *Astro-H* and *IXO* will enable direct measurements of the velocity-broadening of emission lines in the hot gas in galaxies, groups, and clusters of galaxies (Sunyaev et al. 2003; Inogamov & Sunyaev 2003; Rebusco et al. 2008), thereby allowing an independent check on our results as well as a critical extension to higher mass systems. However, we note that even the excellent (2–5 eV) spectral resolution of these instruments will not allow measurements of turbulent motions with velocities significantly smaller than 100–200 km s^{-1}. Even though, the broad point spread function of the *Astro-H* mirrors will prohibit investigations of the effects of resonant scattering on spatial scales smaller than presented in this paper, it will for the first time allow us to directly measure the gas motions and spatially map them out to larger radii. The next planned X-ray observatory able to produce a real breakthrough by mapping the gas motions in groups and clusters of galaxies at high spatial resolution, will be *IXO*.

An important consequence of resonant scattering is the bias it can introduce in measurements of radial profiles of abundances of chemical elements. As we show in Table 5.3, the integrated emission of several strong resonance lines is significantly suppressed within the inner 2 kpc of NGC 4636. By ignoring the effects of resonant scattering, the Fe and O abundance will be underestimated by 10–20% within this region. This conclusion is in line with the results of Sanders & Fabian (2006). However, while resonant scattering makes abundances appear to be 10–20% lower than the real value, it cannot explain the much stronger abundance dips seen in the cores of several clusters of galaxies (e.g. Sanders & Fabian 2002).

Acknowledgements

Support for this work was provided by the National Aeronautics and Space Administration through Chandra Postdoctoral Fellowship Award Number PF8-90056 issued by the Chandra X-ray Observatory Center, which is operated by the Smithsonian Astrophysical Observatory for and on behalf of the National Aeronautics and Space Administration under contract NAS8-03060. The work of EC is supported by the DFG grant CH389/3-2. SWA acknowledges support from *Chandra* grant AR7-8007X. This work is based on observations obtained with *XMM-Newton*, an ESA science mission with instruments and contributions directly funded by ESA member states and the USA (NASA). This work was supported in part by the U.S. Department of Energy under contract number DE-AC02-76SF00515.

Chapter 6

Deep *Chandra* observation and numerical studies of the nearest cluster cold front in the sky

N. Werner[1,2], *J.A. ZuHone*[3], *I. Zhuravleva*[1,2], *Y. Ichinohe*[4,5], *A. Simionescu*[4], *S.W. Allen*[1,2,6], *M. Markevitch*[7], *A.C. Fabian*[8], *U. Keshet*[9], *E. Roediger*[10,11], *M. Ruszkowski*[12,13], *J.S. Sanders*[14]

[1]Kavli Institute for Particle Astrophysics and Cosmology, Stanford University, 452 Lomita Mall, Stanford, CA 94305-4085, USA
[2]Department of Physics, Stanford University, 382 Via Pueblo Mall, Stanford, CA 94305-4060, USA
[3]MIT Kavli Institute for Astrophysics and Space Research, Massachusetts Institute of Technology, 77 Massachusetts Avenue, Cambridge, Massachusetts 02139, USA
[4]Institute of Space and Astronautical Science (ISAS), JAXA, 3-1-1 Yoshinodai, Chuo-ku, Sagamihara, Kanagawa, 252-5210, Japan
[5]Department of Physics, Graduate School of Science, University of Tokyo, 7-3-1 Hongo, Bunkyo, Tokyo 113-0033, Japan
[6]SLAC National Accelerator Laboratory, 2575 Sand Hill Road, Menlo Park, CA 94025, USA
[7]X-ray Astrophysics Laboratory, NASA Goddard Space Flight Center, Greenbelt, MD 20771, USA
[8]Institute of Astronomy, Madingley Road, Cambridge CB3 0HA
[9]Physics Department, Ben-Gurion University of the Negev, Be'er-Sheva 84105, Israel
[10]Hamburger Sternwarte, Universität Hamburg, Gojensbergsweg 112, D-21029 Hamburg, Germany
[11]Dublin Institute for Advanced Studies, Astronomy and Astrophysics Section, 31 Fitzwilliam Place, Dublin 2, Ireland
[12]Department of Astronomy, University of Michigan, 500 Church Street, Ann Arbor, MI 48109, USA
[13]Michigan Center for Theoretical Physics, 3444 Randall Lab, 450 Church St, Ann Arbor, MI 48109, USA

[14]Max-Planck-Institut für extraterrestrische Physik, Giessenbachstrasse 1, 85748 Garching, Germany

Published in the Monthly Notices of the Royal Astronomical Society, volume 455, pages 846–858, 2016

Abstract

We present the results of a very deep (500 ks) *Chandra* observation, along with tailored numerical simulations, of the nearest, best resolved cluster cold front in the sky, which lies 90 kpc (19′) to the northwest of M 87. The northern part of the front appears the sharpest, with a width smaller than 2.5 kpc (1.5 Coulomb mean free paths; at 99 per cent confidence). Everywhere along the front, the temperature discontinuity is narrower than 4–8 kpc and the metallicity gradient is narrower than 6 kpc, indicating that diffusion, conduction and mixing are suppressed across the interface. Such transport processes can be naturally suppressed by magnetic fields aligned with the cold front. Interestingly, comparison to magnetohydrodynamic simulations indicates that in order to maintain the observed sharp density and temperature discontinuities, conduction must also be suppressed along the magnetic field lines. However, the northwestern part of the cold front is observed to have a nonzero width. While other explanations are possible, the broadening is consistent with the presence of Kelvin-Helmholtz instabilities (KHI) on length scales of a few kpc. Based on comparison with simulations, the presence of KHI would imply that the effective viscosity of the intra-cluster medium is suppressed by more than an order of magnitude with respect to the isotropic Spitzer-like temperature dependent viscosity. Underneath the cold front, we observe quasi-linear features that are $\sim$ 10 per cent brighter than the surrounding gas and are separated by $\sim$ 15 kpc from each other in projection. Comparison to tailored numerical simulations suggests that the observed phenomena may be due to the amplification of magnetic fields by gas sloshing in wide layers below the cold front, where the magnetic pressure reaches $\sim$ 5–10 per cent of the thermal pressure, reducing the gas density between the bright features.

6.1 Introduction

One of the first important results obtained with the *Chandra* X-ray Observatory was the surprising discovery of *cold fronts* - remarkably sharp surface brightness discontinuities, with relatively dense and cool gas on the inner (bright) side and low density hot gas on the outer (faint) side. The first discovered cold fronts in Abell 2142 and Abell 3667 were interpreted as signs of mergers (Markevitch et al. 2000; Vikhlinin et al. 2001a), where the sharp surface brightness discontinuity separates the hotter intracluster medium (ICM) from the low entropy core of a merging subcluster.

However, as more clusters were observed with *Chandra*, cold fronts were also discovered in the centers of cool-core clusters (at r =10–400 kpc) with no signs of recent major mergers (Markevitch et al. 2001). Indeed, such cold fronts are observed in most relatively relaxed cool-core clusters (Ghizzardi et al. 2010), often with several, oppositely placed arcs curved around the central gas density peak, forming a spiral-like pattern (see e.g. Markevitch & Vikhlinin 2007; Owers et al. 2009; Simionescu et al. 2012; Rossetti et al. 2013; Ichinohe et al. 2015). Considering projection effects and the weak density jumps, possibly all cool-core clusters may host some cold fronts.

Cold fronts in cooling cores are believed to be due to the sloshing (or swirling) of the gas in the gravitational potential of the cluster. Numerical simulations show that sloshing can be induced easily by a minor merger where a subcluster falls in with a nonzero impact parameter (Tittley & Henriksen 2005; Ascasibar & Markevitch 2006). Due to this disturbance, the density peak of the main cluster swings on a spiral-like trajectory relative to its center of mass. As the central ICM is displaced from the corresponding dark matter peak, opposite and staggered cold fronts are created where cooler and denser parcels of gas from the centre come into contact with the hotter gas at larger radii. The large-scale coherent flows associated with sloshing and the corresponding cold fronts can persist for Gyrs. By redistributing the ICM, sloshing plays an important role in shaping the cluster cores and may even help prevent significant cooling flows (ZuHone et al. 2010; Keshet 2012).

Markevitch et al. (2001) showed that sloshing cold fronts require significant acceleration of the gas beneath the contact discontinuity. This can be explained as centripetal acceleration of a tangential bulk flow just below the cold front (Keshet et al. 2010), which causes a strong tangential shear along the discontinuity. This strong shear flow should promote the growth of hydrodynamic instabilities, which would broaden and eventually destroy the cold front on short sub-dynamical time scales. But cold fronts are remarkably sharp, both in terms of the density and the temperature jumps: the gas density discontinuity in e.g. the merging cluster Abell 3667 is at least several times narrower than the Coulomb mean free path (Vikhlinin et al. 2001a; Markevitch & Vikhlinin 2007) and the observed temperature jumps require thermal conduction across cold fronts to be suppressed by a factor of order $\sim 10^2$ compared to the collisional Spitzer or saturated values (Ettori & Fabian 2000; Xiang et al. 2007). A layer of magnetic field parallel to the discontinuity could stabilize the front, prevent the growth of instabilities, and suppress transport across the cold front (Vikhlinin et al. 2001b).

Vikhlinin et al. (2001b) and Vikhlinin & Markevitch (2002) used the stability of the merger induced cold front in Abell 3667 to derive a lower limit on the magnetic field of B >7–16 μG at the discontinuity. Magnetic amplification in sloshing cold fronts is achieved through the shear due to the bulk flow of plasma beneath the front, which naturally sustains the strong magnetic fields parallel to cold fronts (Keshet et al. 2010; ZuHone et al. 2011). In the layers underneath cold fronts, fields with initial strengths of 0.1–1 μG may be amplified to tens of μG, and the magnetic pressures may be amplified to values reaching a significant fraction of the thermal pressure, leading to gas depleted bands (ZuHone et al. 2011).

One of the most interesting aspect of cold fronts is that they provide a relatively clean experimental setup. This allows us to address questions about the physics of the

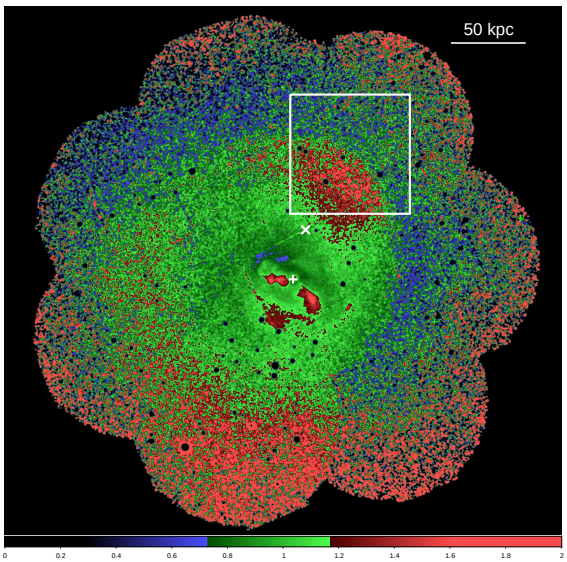

Figure 6.1: *XMM-Newton* EPIC/MOS mosaic image of the central $r \sim 150$ kpc region of the Virgo cluster. The exposure corrected image has been divided by the best-fitting radially symmetric beta model (see Simionescu et al. 2010; Roediger et al. 2011). The white square indicates our *Chandra* ACIS-I pointing shown in Fig. 2. The "+" sign indicates the center of M 87 at the bottom of the global gravitational potential of the Virgo Cluster. The "X" sign indicates the center of curvature (RA: 187.676, DEC: 12.5064) of the part of the cold front imaged by our *Chandra* pointing.

ICM in a more exact way than in cluster cores with complex astrophysical substructure. The closest example of a cluster cold front is the spectacular surface brightness discontinuity that lies 90 kpc ($19'$) to the north of M 87 in the Virgo Cluster and extends 140° in azimuth (see Fig. 6.1, Simionescu et al. 2010). At the distance of 16.1 Mpc (Tonry et al. 2001), 1 arcsec corresponds to only 78 pc, making this the best resolved cluster cold front in the sky. The gas density jump across the discontinuity is $\rho_{\rm in}/\rho_{\rm out} \approx 1.4$ and the gas in the inner, bright side is ∼40% more abundant in Fe than the ICM outside the front (Simionescu et al. 2010). Simionescu et al. (2007) also detected a much weaker cold front $\sim$ 17 kpc to the south-east of the core. The opposite and staggered placement of these fronts, as well as the absence of a remnant sub-cluster, make gas sloshing the most viable explanation for the presence of these edges (Tittley & Henriksen 2005; Ascasibar & Markevitch 2006).

Using constrained hydrodynamical simulations, Roediger et al. (2011) showed that a sloshing scenario can reproduce the radii and the contrasts in X-ray brightness, projected temperature, and metallicity across the observed cold fronts in the Virgo Cluster. By comparing synthetic and real observations, they estimate that the original minor merger event that triggered the sloshing took place about 1.5 Gyr ago, when a subcluster of 2–4 $\times$ 10^{13} $M_\odot$ passed the Virgo core at 100 to 400 kpc distance nearly perpendicular to our line-of-sight. The resulting gas sloshing, with motions primarily in the plane of the sky, creates a contact discontinuity with a surface that is predominantly perpendicular to our line of sight, maximizing the contrast and minimizing projection

Table 6.1: Summary of the *Chandra* observations. Columns list the observation ID, observation date, and the exposure after cleaning.

Obs. ID	Obs. date	Exposure (ks)
15178	2014 Feb. 17	47.1
15179	2014 Feb. 24	41.9
15180	2013 Aug. 1	140.5
16585	2014 Feb. 19	45.6
16586	2014 Feb. 20	49.8
16587	2014 Feb. 22	37.8
16590	2014 Feb. 27	38.1
16591	2014 Feb. 27	23.8
16592	2014 Mar. 1	36.1
16593	2014 Mar. 2	38.1

effects. In subsequent work, Roediger et al. (2013) demonstrated the capability of deep *Chandra* observations to reveal Kelvin-Helmholtz instabilities in the Virgo cold front by detecting multiple edges and shallower than expected surface brightness profiles across the discontinuity. Based on relatively short *XMM-Newton* observations, they also present tentative indications that the northeastern portion of the front is disturbed by instabilities.

Here, we present a very deep (500 ks) *Chandra* observation of the sharpest, northwestern part of the Virgo cold front, designed to test the theoretical predictions in unprecedented detail.

6.2 Observations and data analysis

6.2.1 Chandra data

The *Chandra* X-ray observatory observed the prominent cold front to the northwest of M 87 (see Fig. 6.1) between 2013 August and 2014 March using the Advanced CCD Imaging Spectrometer (ACIS-I). The standard level-1 event lists were reprocessed using the `CIAO` (version 4.7, `CALDB 4.6.5`) software package, including the latest gain maps and calibration products. Bad pixels were removed and standard grade selections applied. The data were cleaned to remove periods of anomalously high background. The observations, along with the dates, identifiers, and net exposure times after cleaning (total net exposure of 500 ks), are listed in Table 1. Background images and spectra were extracted from the blank-sky fields available from the Chandra X-ray Center. These were cleaned in an identical way to the source observations, reprojected to the same coordinate system and normalized by the ratio of the observed to blank-sky count rates in the 9.5–12 keV band.

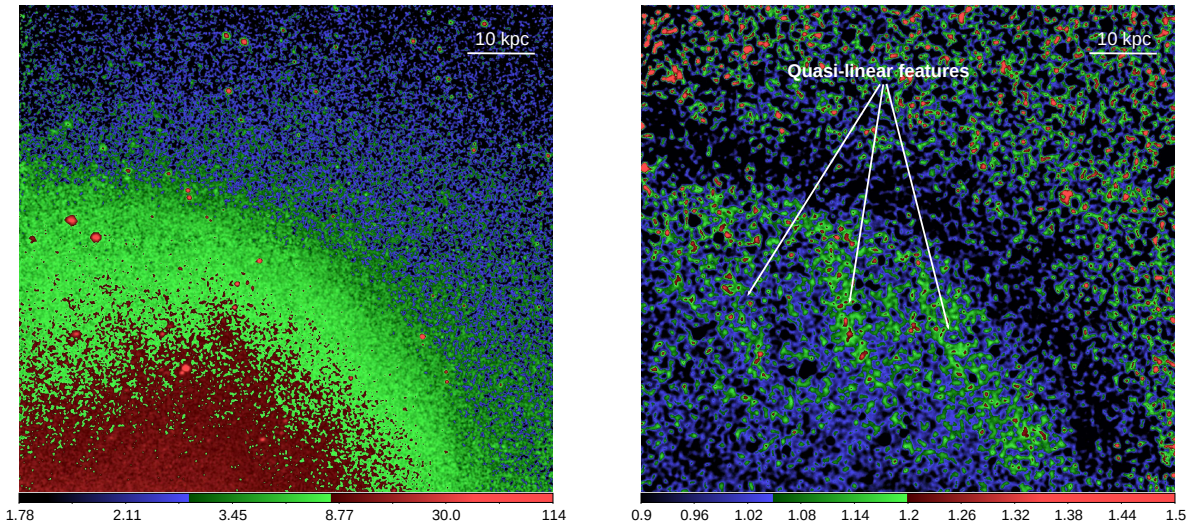

Figure 6.2: *Left panel: Chandra* image of the cold front in the 0.8–4.0 keV energy band. The image was smoothed with a Gaussian function with a 1.5 arcsec window. *Right panel:* The residual image obtained by dividing the image on the left with a beta-model, and patched on large scales with an 80 arcsec scale smoothing window (see Zhuravleva et al. 2015, and the text for details), reveals three X-ray bright quasi-linear features separated from each other by $\sim$ 15 kpc in projection. The dark band outside the cold front is an image processing artifact due to the sharp surface brightness discontinuity. Point sources were removed from the residual image.

Image analysis

Background-subtracted images were created in nine narrow energy bands (0.8–1.0 keV, 1.0–1.2 keV, 1.2–1.5 keV, 1.5–2.0 keV, 2.0–2.5 keV, 2.5–2.75 keV, 2.75–3.0 keV, 3.0–3.5 keV, and 3.5–4.0 keV), spanning 0.8–4.0 keV. The nine narrow-band images were flat fielded with respect to the median energy for each image and then co-added to create the X-ray images shown in Fig. 6.2. In the 0.8–4.0 keV band the signal over background ratio is optimal and the emissivity is nearly independent of the gas temperature, maximizing the contrast at which we detect the contact discontinuity. Identification of point sources was performed using the `CIAO` task `WAVDETECT`. The point sources were excluded from the subsequent analysis.

In order to emphasize structure in the image, we also produced a beta-model subtracted image, shown in the right panel of Fig. 6.2. In order to remove the underlying large-scale surface brightness gradient, we fitted a beta-model to an azimuthally averaged X-ray surface brightness profile extracted from the *XMM-Newton* mosaic image (see Sect. 6.2.2 and Fig. 6.1) and divided our *Chandra* image by this model, patched on large scales with an 80 arcsec smoothing window (see Zhuravleva et al. 2015, for details). Our patched model with which we divide our image is defined as $I_{\rm pm} = I_\beta S_\sigma[I_{\rm X}/I_\beta]$, where I_β is the best fit beta-model to the azimuthally averaged X-ray surface brightness profile, $S_\sigma[.]$ is Gaussian smoothing with window size σ, and $I_{\rm X}$ is the X-ray surface brightness image.

Spectral analysis

Individual regions for the 2D spectral mapping were determined using the contour binning algorithm (Sanders 2006), which groups neighbouring pixels of similar surface brightness until a desired signal-to-noise ratio threshold is met. We adopted a signal-to-noise ratio of 75 (approximately 5600 counts per region), which provides approximately 3 per cent precision for density, 4 per cent precision for temperature, and 10–20 per cent precision for metallicity measurements, respectively. We modelled the spectra extracted from each spatial region with the `SPEX` package (Kaastra et al. 1996). The spectral fitting was performed in the 0.6–7.5 keV band. The spectrum for each region was fitted with a model consisting of an absorbed single-phase plasma in collisional ionization equilibrium, with the spectral normalization (emission measure), temperature, and metallicity as free parameters. The deprojected spectra are obtained following the method described by Churazov et al. (2003) and are fitted using `XSPEC` and the `APEC` plasma model (Smith et al. 2001; Foster et al. 2012). The line-of-sight absorption column density was fixed to the value, $N_{\rm H} = 2 \times 10^{20}$ cm^{-2}, determined by the Leiden/Argentine/Bonn radio survey of H I (Kalberla et al. 2005). Metallicities are given with respect to the proto-Solar abundances by Lodders (2003).

6.2.2 XMM-Newton data

A mosaic of six *XMM-Newton* pointings, each with an exposure time of $\sim$ 20 ks, was performed in June 2008. An additional pointing was obtained in November 2008.

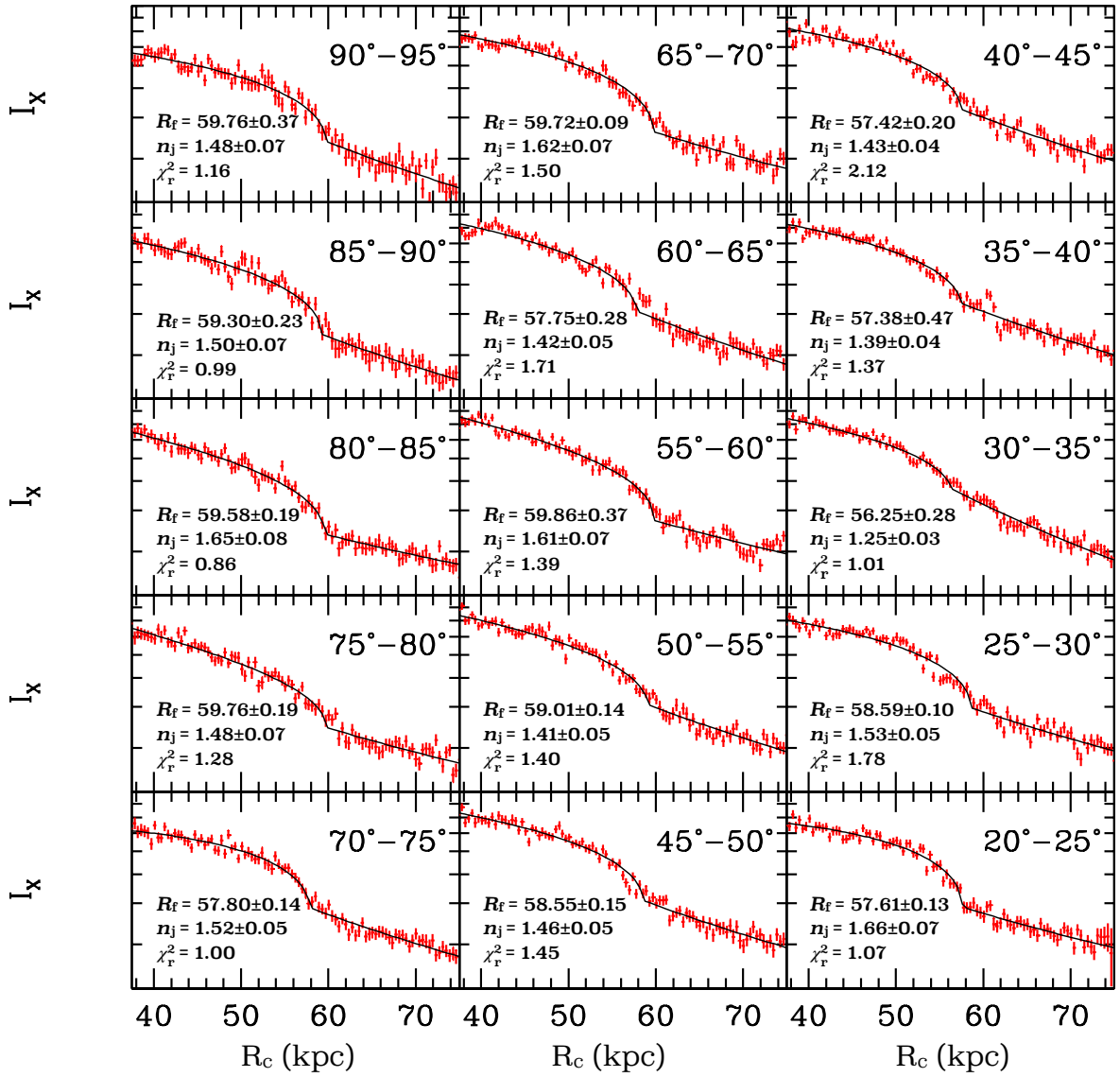

Figure 6.3: Surface brightness profiles across the cold front measured along 15 narrow, 5 degree wedges, each corresponding to $\sim$ 5 kpc along the front. The azimuth angles are measured counterclockwise from the west. Radii are measured from the center of curvature of the cold front (see Fig. 6.1). Over-plotted are the best fit broken power-law models for the ICM density profiles. For each wedge we indicate the best-fit radius of the discontinuity (R_f, measured from the center of curvature of the cold front), density jump (n_j), and the reduced χ^2 for 92 degrees of freedom.

These observations cover an annulus around the deep (net exposure time of 120 ks) pointings on M 87. The full exposure corrected mosaic of *XMM-Newton* observations divided by the best fit radially symmetric beta-model is shown in Fig. 6.1. See Simionescu et al. (2010) for the detailed discussion on the data and the analysis.

6.3 Results

The most prominent sloshing cold front in the Virgo Cluster extends at $r \sim 90$ kpc north of M 87 (see Fig. 6.1). Our *Chandra* observation (indicated by the white square in the figure) targets the part of the front with the largest surface brightness contrast. The deep *Chandra* image, on the left panel of Fig. 6.2, shows clearly this surface brightness discontinuity.

The *Chandra* image also reveals unexpected, relatively bright quasi-linear features underneath the discontinuity. To our knowledge, this is the first time that such substructure has been identified with a cold front. Three of these quasi-linear features can be seen clearly on the residual image on the right panel of Fig. 6.2. They are ~ 10 per cent brighter than the surrounding gas and are separated by ~ 15 kpc from each other in projection. These features are below the detection limit of the existing *XMM-Newton* observation.

To study the detailed cold front interface, we extracted surface brightness profiles along 15 narrow, 5 degree wedges, each corresponding to ~ 5 kpc along the front (see Fig. 6.3). To optimize the sharpness of the surface brightness edge in our profiles, we aligned our annuli with the front interface, choosing the vertex of the wedges at the center of curvature of the highest-contrast part of the cold front (RA: 187°.676, DEC: 12°.5064). The data were binned into 4.92 arcsec radial bins. We fit the surface brightness profiles by projecting a spherically symmetric discontinuous, broken power-law density distribution (see e.g. Owers et al. 2009). The fitting was performed using the `PROFFIT` package (Eckert et al. 2011) modified by Ogrean et al. (2015). We fit the data in the radial range of 8–16 arcmin, corresponding to 38–75 kpc from the center of curvature. The free parameters of our model are the normalization, the inner and outer density slopes, and the amplitude and radius of the density jump. We verified that the best fit parameters are not sensitive to the utilized radial range. The surface brightness profiles over-plotted with their best fit models, along with the values for the best fit density jumps, radii of the discontinuity, and reduced χ^2s (for 92 degrees of freedom) are shown in Fig. 6.3.

Our model provides the best fit to the northern part of the front, at azimuthal angles of 70–95 degrees, indicating that this is the sharpest part of the cold front. In particular, our model provides the best fit to the profile extracted at the azimuthal range of 80–85 degrees. In order to place an upper limit on the width of the front, we fit this profile with a model that includes Gaussian smoothing as an additional free parameter. We find that the 99 per cent upper limit on the smearing of this part of the cold front is 2.5 kpc, which is 1.5 Coulomb mean free paths (see Sect. 6.5.1 for details). Given the quasi-spherical geometry along our line of sight, in this nearby system we observe a steep, few kpc wide surface brightness gradient at the front (in the more distant systems

where the gradient cannot be resolved we only see a sharp surface brightness jump). Because of this resolved gradient, our upper limit on the width is significantly larger than *Chandra's* resolution.

On the other hand, at azimuths of 25–70 degrees, our model mostly provides a poorer fit to the data. Fig. 6.3 shows that around the brightness edge most profiles display deviations from the model, with shallow, smeared discontinuities. The parameters of the best fit model and the structure seen in the profiles also show azimuthal variation. In particular, the northwestern part of the front, at azimuths below 55 degrees, shows significant variation both in the value of the best fit density jump and radius. For the sectors with the least sharp edges the fit significantly improves after including Gaussian smoothing in the model. For example, for the profile extracted in the 65–70 degree wedge, Gaussian smoothing with a best fit width of 4.3 kpc improves the χ^2 from 138 (for 92 degrees of freedom) to 101, for one additional free parameter. According to the F-test, the likelihood that this is a chance improvement is 1.06×10^{-7}. This highly significant improvement strongly suggest that at these azimuths the front has a finite width.

To study the projected thermodynamic properties and the metallicity of the ICM across the cold front, we extracted spectra along three 22.5 degree wide wedges (labeled North, Northwest, and West), the vertex of which is at the same center of curvature of the cold front as for the surface brightness profiles. The best fit projected temperature and metallicity profiles along the three wedges, determined in narrow 2 kpc wide regions, are shown in Fig. 6.4. The projected temperature as a function of radius increases from $\sim$ 2.7 keV to $\sim$ 3.6 keV across the interface, and the metallicity decreases from $\sim$ 0.6 Solar to $\sim$ 0.3 Solar. The projected temperature distribution appears to be smeared across the cold front. The observed gradient of the projected temperature is between $\sim$ 4 kpc (West) and 8 kpc (North) wide.

The 2D maps of the projected thermodynamic properties shown in Fig. 7.4 confirm these trends. While the temperature clearly increases across the front, the best fit metallicity drops from $\sim$ 0.6 Solar to $\sim$ 0.3 Solar. The projected temperature and entropy distributions appear slightly smeared at the edge. The smearing is likely to be at least in part due to projection effects (see Sect. 6.5.1 for more discussion). As expected, the cold front is not visible in the pressure map, indicating that the sloshing gas is in approximate hydrostatic equilibrium within the cluster potential. The linear structures identified in the images (see Fig. 6.2) do not show any significant difference in temperature or metallicity from the surrounding ambient medium.

In order to study the temperature difference of the quasi-linear features and the ambient plasma in more detail, we extracted five spectra from rectangular regions: three spectra from regions centered on the quasi-linear features, and two spectra from the surrounding regions. Based on fitting the combined spectra, the best fit temperature of the quasi-linear features is $kT = 2.77 \pm 0.03$ keV and the best fit temperature of the surrounding gas is $kT = 2.92 \pm 0.03$ keV, qualitatively consistent with the trend expected from the simulations we present in Sect. 6.4 (see Fig. 6.9). However, we caution that because the surface brightness excess associated with these features is only $\sim$ 10 per cent, the measured temperature difference could easily be due to the underlying spatial variation in the temperature of the ambient gas.

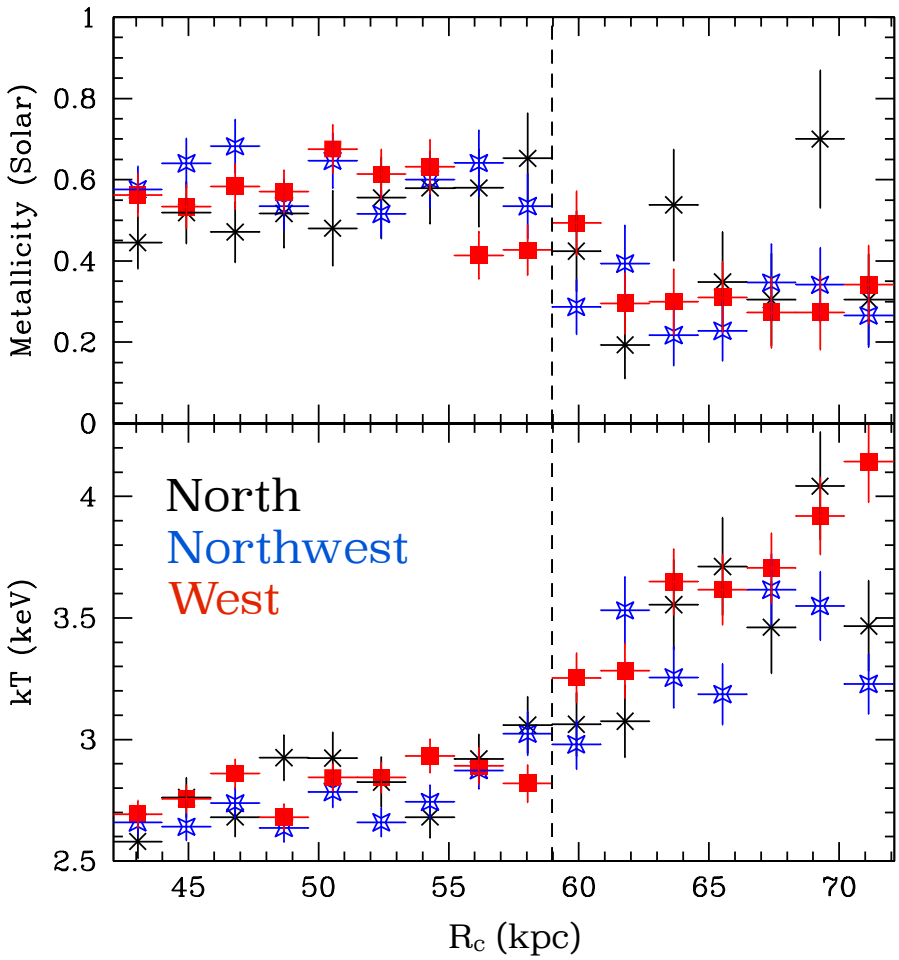

Figure 6.4: Projected temperature and metallicity profiles along three 22.5 degree wide wedges, extracted from the northern direction westward. The profiles extracted from the north, northwest, west are shown in black, blue, and red, respectively. The best fit radius of the front determined by fitting the surface brightness profiles is indicated by the dashed line (the uncertainty on the front radius is ± 2 kpc). Radii are measured from the center of curvature of the cold front.

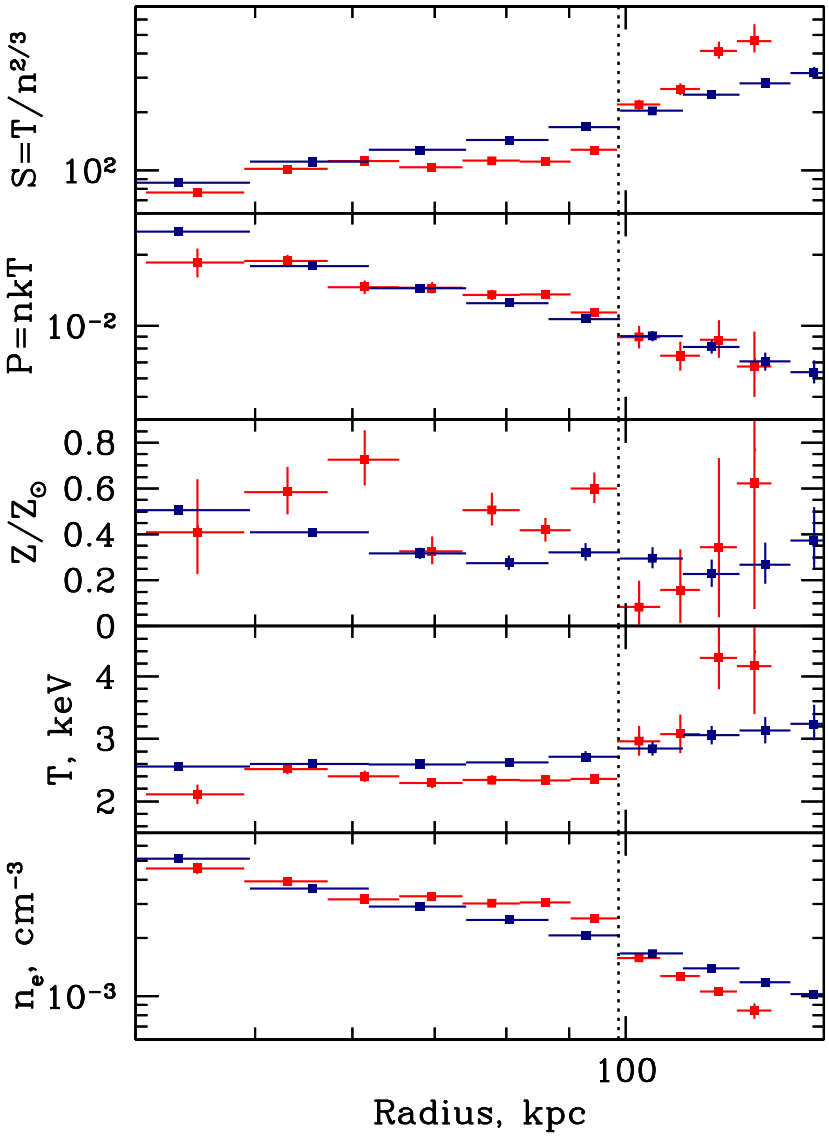

Figure 6.5: Deprojected electron density, temperature, metallicity, pressure, and entropy profiles (from the bottom to the top), respectively. The red datapoints were determined in a 30 degree wedge extending from the north to the west, centered on M 87, using *Chandra* data and the blue datapoints are averaged over the other directions (330 degree region that excludes the wedge) using *XMM-Newton* data. The radius of the cold front is indicated with the dotted line. While the deprojected pressure is continuous across the cold front, the density, temperature, entropy, and metallicity distributions show relatively strong discontinuities. Note that under the cold front ($\sim$ 20 kpc) the ICM entropy is smaller and above the front it is higher than in the other directions.

In order to determine the deprojected spectral properties of the ICM across the cold front, we also extracted spectra from a wedge centered on M 87 at the bottom of the gravitational potential of the Virgo Cluster. Centering the series of partial annuli used for spectral extraction at the bottom of the global gravitational potential enables us to perform the most robust deprojection of the stratified cluster atmosphere. The 30 degrees wide wedge used for extracting the *Chandra* spectra extends from the north towards the west. For this particular wedge, the width of the cold front is the least affected by the choice of the different center. Fig. 6.5 shows the comparison of the deprojected electron density, temperature, metallicity, pressure, and entropy profiles determined in the wedge using *Chandra* data (red datapoints) with the properties determined in the other directions (averaged over a 330 degree region that excludes the wedge) using *XMM-Newton* spectra (blue datapoints). While the deprojected pressure appears continuous across the cold front, the density, temperature, entropy, and metallicity distributions show clear discontinuities. The deprojected entropy profile extracted across the cold front shows a remarkably flat distribution underneath the discontinuity that extends across a radial range of $\sim$ 50 kpc. The comparison also shows that under the cold front ($\sim$ 20 kpc from the discontinuity) the ICM entropy is smaller and above the front it is higher than in the other directions. The pressure appears slightly higher under the cold-front than in the other directions. We verified that the deprojected profiles determined using *Chandra* and *XMM-Newton* data in the 30 degree wedge show consistent results. We caution that while our deprojection procedure assumes spherical symmetry centered on M87, the distribution of the gas uplifted by sloshing is likely to be different and therefore our inferred thermodynamic properties underneath the discontinuity may be biased.

6.4 Numerical simulations

We compare our long exposure of the Virgo cold front to magnetohydrodynamic (MHD) simulations. These simulations were performed using the `Athena 4.1` astrophysical simulation code (Stone et al. 2008). The technical details of the simulation setup are discussed in ZuHone et al. (2015) and the initial conditions, based on the setup from Roediger et al. (2011) and Roediger et al. (2013), were chosen to match the global Virgo Cluster potential and the ICM properties. The cluster is modeled as a cooling-core system with a mass of $\sim 2 \times 10^{14}$ $M_\odot$ and $kT \sim 2$ keV. The sloshing in the simulation is due to the passage of a gas-less dark-matter subcluster with a mass of 2×10^{13} $M_\odot$ at $r \sim 100$ kpc at the time of $t \sim 1$ Gyr after the beginning of the simulation. We note that simulations show that similar cold front features are produced by gas-less perturbers approaching at close distances or gas-filled perturbers approaching at larger distances, indicating that the choice of perturber is not as important as the shape of the potential well and the thermodynamic profiles of the main cluster (ZuHone et al. 2010; Roediger et al. 2011; Roediger & Zuhone 2012). The time at which the properties of the Virgo cold front most resemble the results of the simulation is $\sim$ 1.7 Gyr after the passage of the subcluster. In Fig. 6.7, we show the synthetic X-ray surface brightness residual distributions for the simulation at this time for two pure hydrodynamic runs with

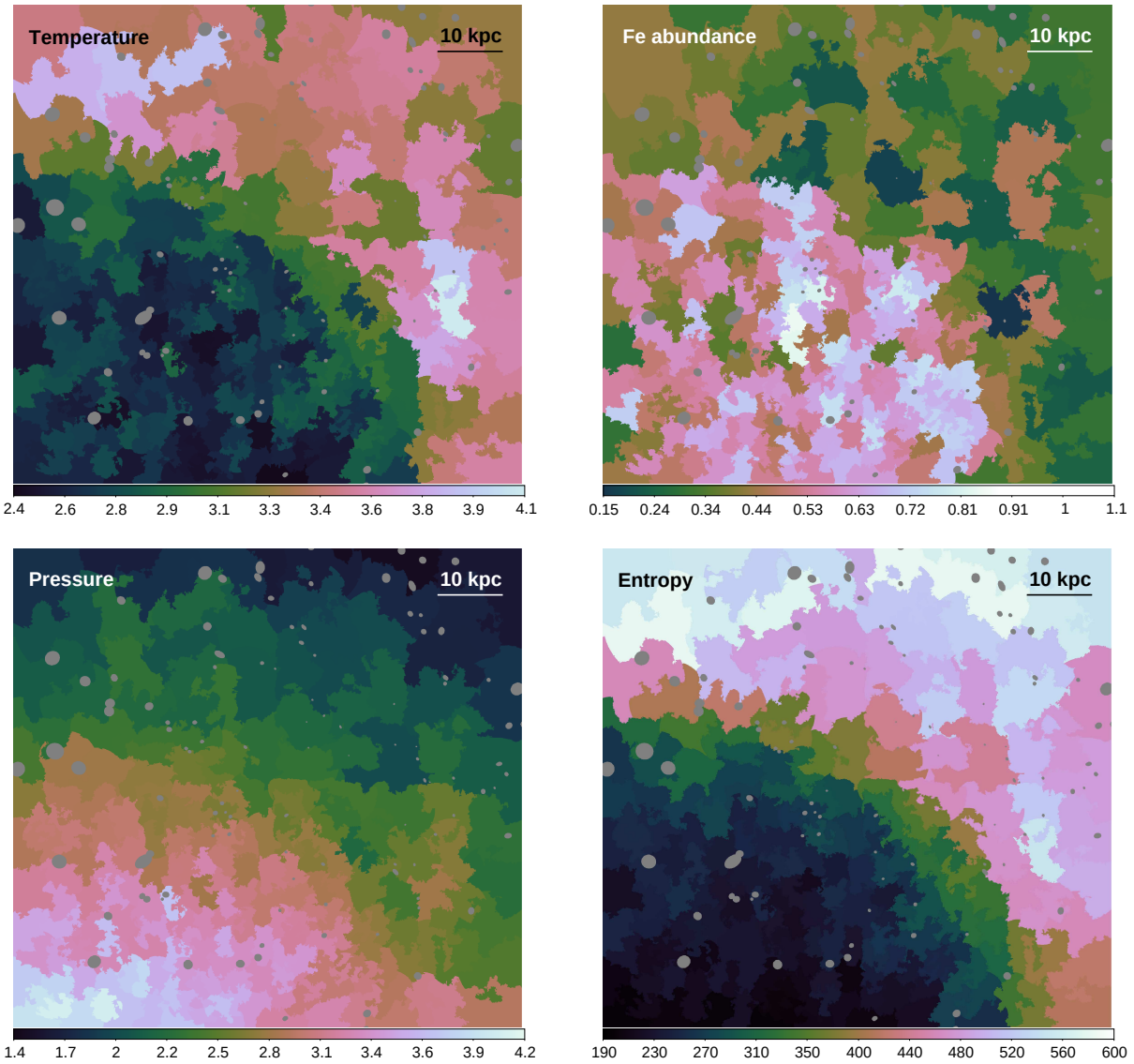

Figure 6.6: Projected thermodynamic maps. Each spatial region contains 5600 net counts (S/N of 75). To compare the pseudo-pressure and pseudo-entropy distributions, we assume the gas uniformly distributed along the line-of-sight depth of $l = 1$ Mpc over the entire field of view. The units of temperature (top left), Fe abundance (top right), pressure (bottom left) and entropy (bottom right) are keV, Solar (Lodders 2003), 1000 keV cm$^{-3}(l/1\,\mathrm{Mpc})^{1/2}$ and keV cm$^{2}(l/1\,\mathrm{Mpc})^{1/3}$, respectively. The fractional 1σ statistical errors are ~ 4 per cent for temperature, 5 per cent for pressure and entropy, and $\sim$ 10–20 per cent for metallicity. Point sources were excluded from the regions shown in grey.

different viscosities (top row), and for two MHD runs (bottom row). The pure hydrodynamic simulations were performed assuming either inviscid ICM ($\mu = 0$), or 10 per cent of the isotropic Spitzer-like temperature dependent viscosity ($\mu = 0.1\mu_{\rm Sp}$). Both MHD runs started with a tangled magnetic field distribution (set up as in ZuHone et al. 2011), one with an initial ratio of thermal to magnetic pressure of $\beta = 1000$ and the other with $\beta = 100$.

The two pure hydrodynamic simulations are visibly inconsistent with the data: the inviscid run shows large, well-developed Kelvin-Helmholtz instabilities (KHI) that are not seen at the Virgo cold front image (the surface brightness profiles extracted from the mock image show a distorted front with multiple strong edges; see also Fig. 4 in Roediger et al. 2013); and the run with 10 per cent of Spitzer viscosity produces a discontinuity that is much smoother than the profiles extracted across the northwestern part of the cold front, seen in Fig. 6.3. Importantly, pure hydrodynamic simulations do not reproduce the bright linear features seen in the right panel of Fig. 6.2, though such features appear in the MHD run with the initial plasma $\beta = 100$; we will discuss this in Section 6.5.5.

6.5 Discussion

6.5.1 The width of the cold front and suppressed diffusion

The observed surface brightness profiles across the cold front show considerable azimuthal variation. While at certain azimuth angles (particularly in the north) the profiles are relatively well described by the model of a spherically symmetric cloud with a power-law density distribution, in other directions they deviate from the model, are wider, and the best fit front parameters show significant azimuthal variation.

For the best fit deprojected temperatures and electron densities, the Coulomb mean free paths inside and outside of the cold front are $\lambda_{\rm in} = 0.77$ kpc and $\lambda_{\rm out} = 2.2$ kpc, respectively. For unsuppressed diffusion, particles diffusing from the bright, dense side of the discontinuity to the low density outer ICM will be especially efficient at broadening the cold front. The Coulomb mean free path for diffusion from the inner bright side to the outer faint side of the discontinuity is:

$$\lambda_{\rm in\rightarrow out} = 15 \left(\frac{T_{\rm out}}{7\,{\rm keV}}\right)^2 \left(\frac{n_{\rm e,out}}{10^{-3}\,{\rm cm}^{-3}}\right) \left(\frac{T_{\rm in}}{T_{\rm out}}\right) \frac{G(1)}{G(\sqrt{T_{\rm in}/T_{\rm out}})} = 1.7\,{\rm kpc}, \qquad (6.1)$$

where $n_{\rm e,out}$ is the electron density outside the cold front, $T_{\rm in}$ and $T_{\rm out}$ are the temperatures inside and outside the cold front, and $G(x) = [\phi(x) - x\phi'(x)]/2x^2$, where $\phi(x)$ is the error function (Spitzer 1962; Markevitch & Vikhlinin 2007). Our conservative upper limit of 2.5 kpc on the intrinsic width of the cold front, determined in the sector with the sharpest brightness edge, corresponds to about 1.5 Coulomb mean free paths.

Part of the apparent broadening of the cold front in the Virgo Cluster may be caused by projection effects and the true intrinsic width of the discontinuity is also likely to be smaller than the Coulomb mean free path. Because the front is seen along the surface in projection, any deviations from the ideal spherical shape will smear the edge.

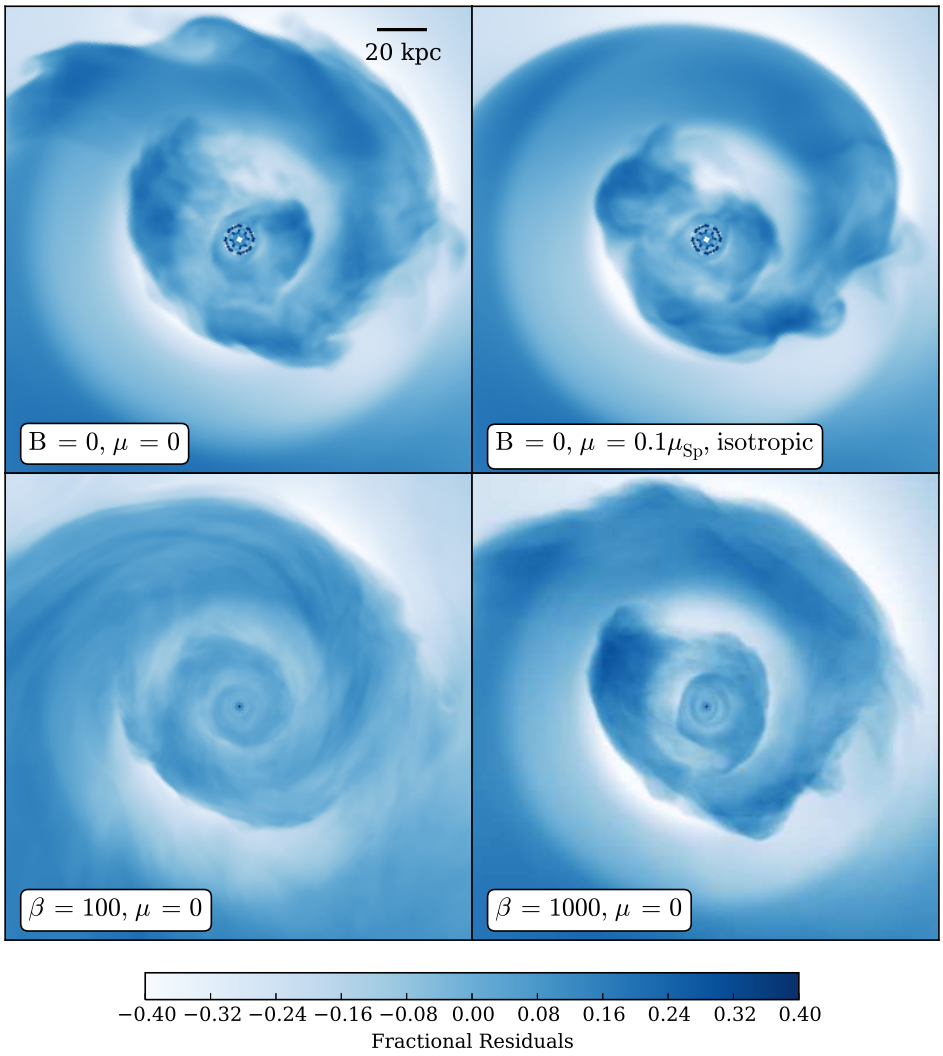

Figure 6.7: Simulated X-ray surface brightness residual distributions for the Virgo Cluster simulation at $t = 1.7$ Gyr after the closest passage of the subcluster for two pure hydrodynamic simulation runs with different viscosities (top row), and two MHD runs with different initial plasma beta parameters (bottom row).

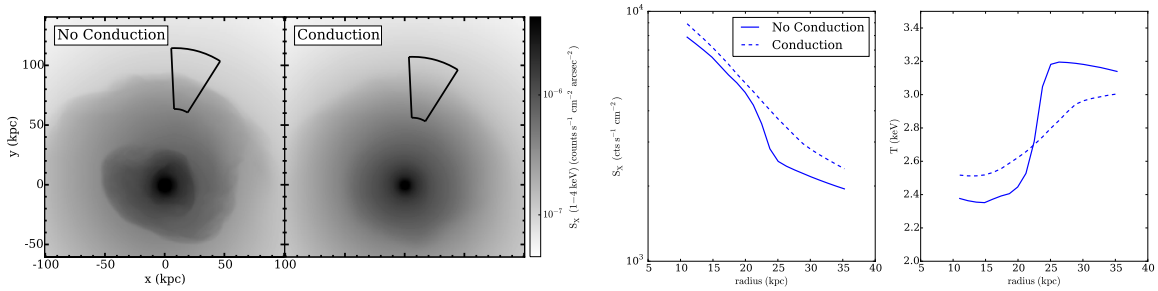

Figure 6.8: Mock surface brightness images (left two panels), and surface brightness and temperature profiles (right two panels) extracted from the black wedges for numerical MHD simulations performed assuming no conduction and full Spitzer conduction along the magnetic field lines. Spitzer conduction along the magnetic field lines would wash out the temperature discontinuity to a degree that is inconsistent with the observations. The observed temperature and surface brightness profiles (see Fig. 6.3, 6.4) are consistent with the conduction along the magnetic field lines being suppressed by a factor $\gtrsim 10$.

Therefore, the observed width is a conservative upper limit on the actual width of the discontinuity. Based on comparisons to numerical simulations, Roediger et al. (2011, 2013) argue for sloshing in the Virgo Cluster close to the plane of the sky, ruling out orbital planes that are further than 45 degrees from the plane of the sky. We verified that the mock X-ray images of sloshing in our simulations, produced for various lines of sight, are consistent with those in Roediger et al. (2011, 2013). For sloshing taking place predominantly in the plane of the sky projection effects are minimized. Their smearing effect gets more important as the shape of the front departs from spherical symmetry and as the inclination of the orbital plane to the plane of the sky gets larger (until the inclination approaches 90 degrees, when sloshing is along the line-of-sight).

Unsuppressed diffusion would smear the density discontinuity by *several* mean free paths. Our upper limit on its intrinsic width therefore indicates that diffusion is suppressed across the cold front. This is consistent with the results obtained for the cold front identified with a subcluster merger in Abell 3667, where Vikhlinin et al. (2001a) showed that the gas density discontinuity is several times narrower than the Coulomb mean free path (see Markevitch & Vikhlinin 2007, for updated results). Churazov & Inogamov (2004) argue that a small but finite width of the interface set by diffusion, that is of the order of a few per cent of the curvature radius ($\sim$ 2 kpc for the Virgo cold front), could strongly limit the growth of perturbations such as KHI (see also Chandrasekhar 1961). Given projection effects that are expected to be broadening the observed width of the discontinuity, the intrinsic width of the Virgo cold front is likely to be too small to be suppressing the development of KHI.

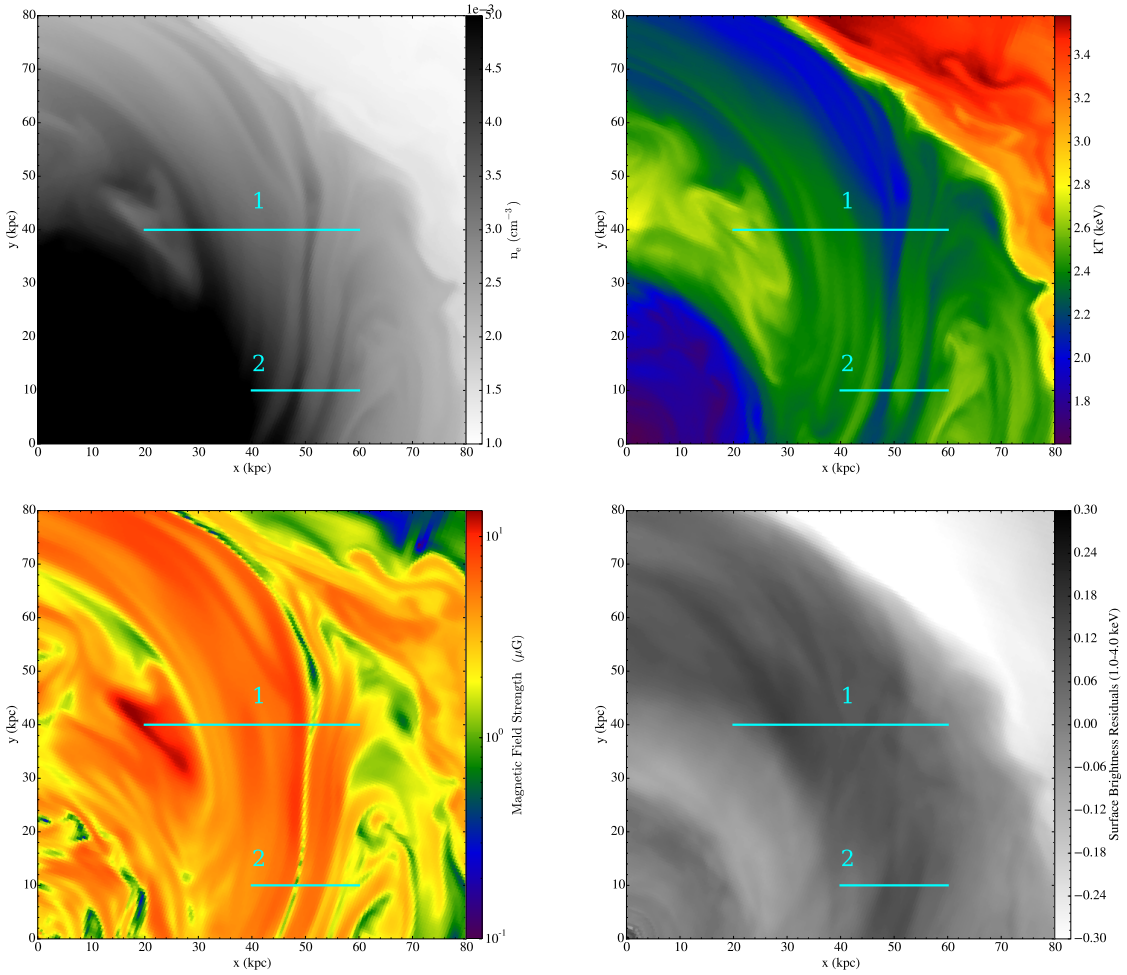

Figure 6.9: A zoom in on a 80×80 kpc^2 region around the cold front located northwest of the cluster center for the MHD simulation run with an initial magnetic to thermal pressure ratio $\beta = 100$ (see the bottom right panel of Fig. 6.7). *Top-left:* slice of gas density; *top-right:* slice of gas temperature; *bottom-left:* slice of magnetic field strength; *bottom-right:* projected surface brightness residuals. The solid cyan lines indicate the extraction regions for the profiles shown in Fig. 6.10.

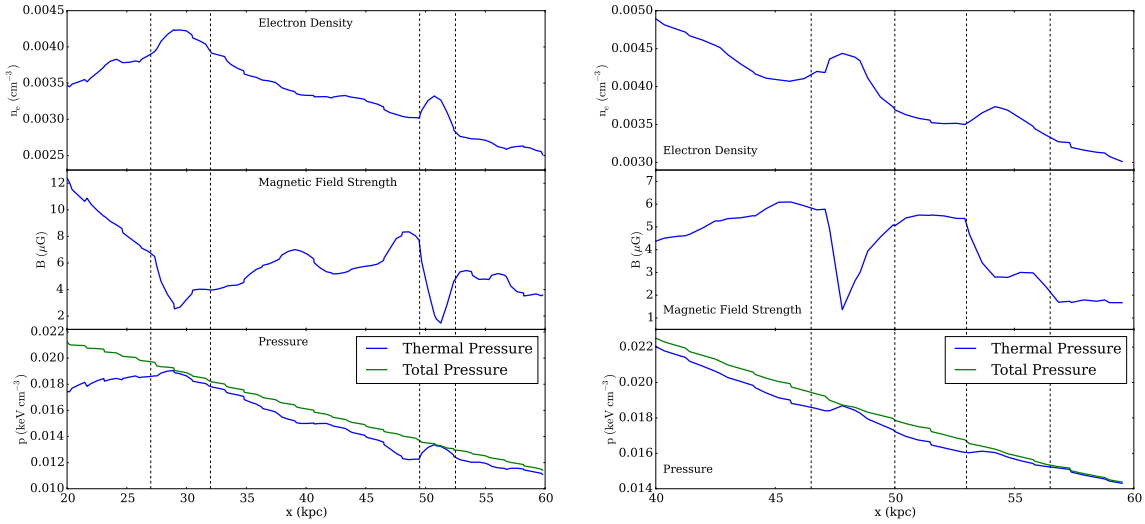

Figure 6.10: Profiles of electron density, magnetic field strength, and pressure along the cyan lines indicated in Fig. 6.9 as '1' (left panel) and '2' (right panel). The difference between the total and thermal pressure is due to magnetic pressure support. Dashed lines indicate approximate boundaries of density enhancements along the profile.

6.5.2 Kelvin-Helmholtz instabilities and ICM viscosity

The primary effect of projection is the broadening of the surface brightness edge and possibly a relatively smooth azimuthal change of the broadening. However, the non-zero width of the cold front, combined with the observed substructure and the azimuthal variations of the best fit radius and density jump seen in Fig. 6.3, require the presence of additional processes, such as KHI. The temperature profiles shown in Fig. 6.4 are consistent with the presence of instabilities on a scale of a few kpc.

Constrained hydrodynamic simulations by Roediger et al. (2012, 2013) demonstrate the efficiency of viscosity at suppressing KHI and show that for viscosities of about 10 per cent of the Spitzer value or larger, at this cold front, KHIs should be suppressed. Our pure hydrodynamic simulation run with 10 per cent Spitzer viscosity is consistent with these conclusions. Based on comparison to these numerical simulations, the presence of KHI would imply that the effective viscosity of the ICM is suppressed by more than an order of magnitude with respect to the isotropic Spitzer-like temperature dependent viscosity. Our conclusions, however, depend on the correctness of the assumed merger model.

The growth of KHIs may be facilitated by the presence of magnetic fields which lower the effective viscosity of the plasma by preventing the diffusion of momentum and heat perpendicular to the field lines. Also, micro-scale MHD plasma instabilities may set an upper limit on the viscosity that is much lower than that expected from ion collisionality (Kunz et al. 2014). However, depending on the field geometry and strength, magnetic fields may also protect cold fronts against instabilities. A layer of strong enough magnetic fields aligned with the cold front could suppress the growth

of KHIs (Vikhlinin & Markevitch 2002; Keshet et al. 2010). However, the suppression of KHI in the simulations of ZuHone et al. (2011) is often partial, indicating that magnetic fields cannot always stabilize cold fronts. Our example in the bottom-right panel of Figure 6.7 shows that if magnetic fields are initially weak ($\beta = 1000$ in our example), they will be unable to suppress KHI. Stronger magnetic fields (see bottom-left panel of Fig. 6.7 for an example with initial $\beta = 100$) suppresses most of the KHI but not all.

Other possible explanations for the broadening and the observed substructure in the surface brightness profiles include plasma depletion due to regions of amplified magnetic fields below the cold front, jet inflated bubbles entrained by the sloshing gas, or clumpy, inhomogeneous ICM distribution.

6.5.3 Gas mixing at the cold front

Well developed, long lasting, large KHI would mix the high metallicity ICM ($\sim$ 0.6 Solar) on the bright side of the interface with the low metallicity gas ($\sim$ 0.3 Solar) on the faint side. The relatively sharp (narrower than 6 kpc) metallicity gradient indicates that if the surface brightness substructure is due to KHI, they are on relatively small, few kpc, scales and are unable to efficiently mix metals across wider regions around the interface. Since cold fronts are transient wave phenomena, the lack of significant mixing across the front is not entirely surprising. Numerical simulations indicate that metallicity jumps remain preserved even for inviscid ICM (Roediger et al. 2011) and they get washed out only on very small scales, consistent with our observation and observations of sloshing cold fronts in other more distant clusters which are also associated with metallicity discontinuities (see e.g. Ghizzardi et al. 2014).

6.5.4 Conduction across the discontinuity

ZuHone et al. (2013) show that while sloshing approximately aligns the magnetic field lines with the cold front surface, perfect alignment is not expected. KHI will re-tangle the field lines, restoring the heat flow between the gas phases above and below the cold front. ZuHone et al. (2015) also performed simulations for the Virgo Cluster with anisotropic conduction, assuming full Spitzer conductivity along the magnetic field lines. In these, the temperature and surface brightness gradients are washed out to such a degree that is inconsistent with our observation (see Fig 6.8). The relatively narrow temperature gradients across the interface (see Fig. 6.4) suggest that the effective conductivity *along* the field lines must be reduced by effects not modeled by the simulation, such as strong curvature of the field lines, stochastic magnetic mirrors on small scales, and/or microscopic plasma instabilities (e.g. Chandran et al. 1999; Malyshkin 2001; Narayan & Medvedev 2001; Schekochihin et al. 2005, 2008). While the observed temperature and surface brightness profiles are consistent with no conduction along the magnetic field lines (see Fig. 6.8), conductivity at or below 0.1 of the Spitzer value along the field lines (which would still result in a steep gradient across the discontinuity, see ZuHone et al. 2013) cannot be excluded and the exact suppression factor remains unknown. Like our conclusions on viscosity, this result also depends strongly

on the correctness of the assumed merger model.

6.5.5 Amplified magnetic fields underneath the cold front

The *Chandra* images in Fig. 6.2 show quasi-linear features that are ~ 10 per cent brighter than the surrounding gas. The simulations of ZuHone et al. (2011) and ZuHone et al. (2015) show that the magnetic field layers amplified by sloshing may be wide and extend relatively far below cold fronts. This can be seen clearly in the Virgo simulation with the initial plasma $\beta = 100$ in Fig. 6.9, which shows slices through a 80×80 kpc^2 region around the cold front for gas density, temperature, and magnetic field strength, as well as residuals of projected surface brightness. Along the lines indicated as "1" and "2", we calculate the distributions of the density, temperature, magnetic field strength and pressure and show them in Fig. 6.10. The quasi-linear features seen in the simulation are very similar to those in our observation, both in terms of width and apparent surface brightness excess. We find that regions of high density/surface brightness correspond to regions of relatively low magnetic field in the map. The thin regions of high density are surrounded by wider bands which are highly magnetized. Here, the increased magnetic pressure has pushed gas out, decreasing its density. This opens up the intriguing possibility that the observed bright bands may be due to denser ICM layers between bands of more magnetized plasma, where the magnetic pressure is amplified to $\sim$ 5–10 per cent of the thermal pressure. Though the magnetic fields in this simulation are strong, they do not completely prevent the development of KHI, consistent with the indications of KHI in our observation.

By extrapolating the pressure profiles outside of cold fronts inwards, up to the edge, Reiss & Keshet (2014) infer that in the inner parts of the spirals most sloshing cold fronts show a pressure jump of $P_{\rm in}/P_{\rm out} \sim 0.8$, which may correspond to the amplification of magnetic fields mainly below the discontinuity. The Virgo cold front does not show any significant pressure jump, which may be due to the amplification of the magnetic fields both above and below the front. Fig. 6.9 shows that such a scenario does occur in our simulation. The magnetic fields above the cold front get amplified due to the shear in the large-scale velocity field produced by the encounter with the subcluster. The same large scale gas motions then draw the amplified magnetic fields inward, towards the cold front.

The observed quasi-linear features may potentially also be due to compressed thermal gas formed in front of bubbles entrained by the magnetized sloshing gas, spiraling outwards below the cold front. Such bubble entrainment was previously suggested by Keshet (2012). Future numerical simulations, that include both jet inflated bubbles and sloshing, will test this possible interpretation.

Alternatively, for geometries where the sloshing occurs along our line-of-sight, KHI would develop predominantly in the plane of the sky, forming rolls projected on the bright side of the front. For such geometries, Kelvin-Helmholtz rolls projected on the sloshing surface could, in principle, appear as quasi-linear features. However, based on the comparison of the numerical simulations to the observations, such geometry is unlikely. None of the simulations that we performed show KHI in projection that would look like the observed quasi-linear features.

6.5.6 The flow of the sloshing gas

Under the cold front interface, the ICM entropy is lower and above the interface it is higher than the radial average. The low entropy gas under the interface also has roughly two times higher metallicity than the gas above the interface. This entropy and metallicity distribution indicates convergent gas flows at the cold front interface, with the low entropy metal rich gas moving outward and, in the same time, the high entropy gas moving inward. Such convergent flows are also seen in numerical simulations (e.g. Ascasibar & Markevitch 2006; Roediger et al. 2011).

The entropy profile shows a remarkably flat distribution underneath the cold front, extending across a radial range of $\sim$ 50 kpc. The flat entropy distribution may indicate that, in this region, the gas uplifted by sloshing originated at the same radius. Similar entropy plateaus have also been seen in e.g. the Perseus and Abell 2142 clusters and interpreted as evidence for gas uplift by sloshing (Simionescu et al. 2012; Rossetti et al. 2013). However, if the distribution of the uplifted gas deviates significantly from spherical symmetry centered on M87 (as assumed by our deprojection analysis), then the shape of the entropy profile measured underneath the cold front may be biased.

6.6 Conclusions

We have analyzed a new, very deep (500 ks) *Chandra* observation, together with complementary archival *XMM-Newton* data, and performed tailored numerical simulations to study the nearest cluster cold front in the sky. We find that:

- The northern part of the front appears the sharpest, with a width smaller than 2.5 kpc (1.5 Coulomb mean free paths; at 99 per cent confidence). Everywhere along the front, the temperature discontinuity is narrower than 4–8 kpc and the metallicity gradient is narrower than 6 kpc, indicating that diffusion, conduction and mixing are suppressed across the interface. Such transport processes can be naturally suppressed by magnetic fields aligned with the cold front. We also find that the temperature jump across the cold front is inconsistent with the temperature jumps produced in simulations with anisotropic thermal conduction, indicating that conduction is also suppressed along the magnetic field lines.

- However, the northwestern part of the cold front is observed to have a nonzero width. The broadening is consistent with the presence of projected KHI eddies on length scales of a few kpc. Based on comparison with simulations, the presence of KHI would imply that the effective viscosity of the ICM is suppressed by more than an order of magnitude with respect to the isotropic Spitzer-like temperature dependent viscosity.

- Underneath the cold front, we observe linear features that are $\sim$ 10 per cent brighter than the surrounding gas and are separated by $\sim$ 15 kpc from each other in projection. Comparison to tailored numerical simulations suggests that the observed phenomena may be due to the amplification of magnetic fields by

gas sloshing in wide layers below the cold front, where the magnetic pressure reaches $\sim$ 5–10 per cent of the thermal pressure, reducing the gas density between the bright features.

- The deprojected entropy distribution and the metallicity of the gas indicate convergent gas flows at the cold front interface, with the low entropy metal rich gas moving outward and, in the same time, the high entropy gas moving inward.

Acknowledgments

NW thanks G. Ogrean, P. Nulsen, O. Urban, and R. Canning for discussions. Support for this work was provided by the National Aeronautics and Space Administration through Chandra Award Number GO3-14142A issued by the Chandra X-ray Observatory Center, which is operated by the Smithsonian Astrophysical Observatory for and on behalf of the National Aeronautics Space Administration under contract NAS8-03060. JAZ acknowledges support from NASA though subcontract SV2-8203 to MIT from the Smithsonian Astrophysical Observatory. Analysis of the simulation data was carried out using `yt`, a visualization and analysis software suite for simulations in astrophysics (http://yt-project.org, Turk et al. 2011). YI is financially supported by a Grant-in-Aid for Japan Society for the Promotion of Science (JSPS) Fellows. E. R. acknowledges the support of the Priority Programme Physics of the ISM of the DFG (German Research Foundation) and a visiting scientist fellowship of the Smithsonian Astrophysical Observatory. U.K. is supported by the European Union Seventh Framework Programme, by an IAEC-UPBC joint research foundation grant, and by an ISF-UGC grant. This work was supported in part by the U.S. Department of Energy under contract number DE-AC02-76SF00515.

Chapter 7

Deep *Chandra* study of the truncated cool core of the Ophiuchus cluster

N. Werner[1,2], *R. E. A. Canning*[1,2], *I. Zhuravleva*[1,2], *S. W. Allen*[1,2,3], *A. King*[1,2], *J. S. Sanders*[4], *A. Simionescu*[5], *G. B. Taylor*[7], *R. G. Morris*[1,3], *A. C. Fabian*[6]

[1]Kavli Institute for Particle Astrophysics and Cosmology, Stanford University, 452 Lomita Mall, Stanford, CA 94305-4085, USA
[2]Department of Physics, Stanford University, 382 Via Pueblo Mall, Stanford, CA 94305-4060, USA
[3]SLAC National Accelerator Laboratory, 2575 Sand Hill Road, Menlo Park, CA 94025, USA
[4]Max-Planck-Institut für extraterrestrische Physik, Giessenbachstrasse 1, 85748 Garching, Germany
[5]Institute of Space and Astronautical Science (ISAS), JAXA, 3-1-1 Yoshinodai, Chuo-ku, Sagamihara, Kanagawa, 252-5210, Japan
[6]Institute of Astronomy, Madingley Road, Cambridge CB3 0HA, UK
[7]Department of Physics and Astronomy, University of New Mexico, Albuquerque, NM 87131, USA

Submitted to the Monthly Notices of the Royal Astronomical Society in March 2016

Abstract

We present the results of a deep (280 ks) *Chandra* observation of the Ophiuchus cluster, the second-brightest galaxy cluster in the X-ray sky. The cluster hosts a truncated cool core, with a temperature increasing from $kT \sim 1$ keV in the core to $kT \sim 9$ keV at $r \sim 30$ kpc. Beyond $r \sim 30$ kpc the intra-cluster medium (ICM) appears remarkably isothermal. The core is dynamically disturbed with multiple sloshing induced cold fronts, with indications for both Rayleigh-Taylor and Kelvin-Helmholtz instabilities. The sloshing is the result of the strongly perturbed gravitational potential in the cluster core, with the central brightest cluster galaxy (BCG) being displaced southward from

the global center of mass. The residual image reveals a likely subcluster south of the core at the projected distance of $r \sim 280$ kpc. The cluster also harbors a likely radio phoenix, a source revived by adiabatic compression by gas motions in the ICM. Even though the Ophiuchus cluster is strongly dynamically active, the amplitude of density fluctuations outside of the cooling core is low, indicating velocities smaller than ~ 100 km s^{-1}. The density fluctuations might be damped by thermal conduction in the hot and remarkably isothermal ICM, resulting in our underestimate of gas velocities. We find a surprising, sharp surface brightness discontinuity, that is curved away from the core, at $r \sim 120$ kpc to the southeast of the cluster center. We conclude that this feature is most likely due to gas dynamics associated with a merger and not a result of an extraordinary active galactic nucleus AGN outburst. The cooling core lacks any observable X-ray cavities and the AGN only displays weak, point-like radio emission, lacking lobes or jets, indicating that currently it may be largely dormant. The lack of strong AGN activity may be due to the bulk of the cooling taking place offset from the central supermassive black hole.

7.1 Introduction

The degree to which cool cores are disrupted by merger events is an outstanding question in cluster physics, with implications for galaxy cluster evolution and cosmology (e.g. Burns et al. 2008; Allen et al. 2011). Some simulations have suggested that cluster cool cores are very difficult to destroy once formed, and are therefore expected to survive major mergers (Burns et al. 2008; Poole et al. 2008). However, these conclusions are sensitive to the hydrodynamical/magnetohydrodynamical treatments employed. Our previous analysis of a short 50 ks *Chandra* observation of the nearby Ophiuchus cluster also challenges this view (Million et al. 2010a).

The Ophiuchus cluster ($z = 0.0296$, Durret et al. 2015) is the second-brightest galaxy cluster in the 2–10 keV sky (Edge et al. 1990). It is the most massive structure in the Ophiuchus Supercluster and is surrounded by many in-falling smaller clusters and groups (Wakamatsu et al. 2005; Hasegawa et al. 2000). Spatially resolved spectroscopy using the previous *Chandra* observation (Million et al. 2010a) revealed remarkably steep temperature and iron abundance gradients within the cool core: in the central 30 kpc, the temperature plunges by more than an order of magnitude, and the metallicity varies by a similar amount. Beyond this radius, however, and out to the edge of the *Chandra* field of view, near constant temperature and metallicity are observed. The cool core of the cluster appears to have been truncated.

The previous *Chandra* observations also revealed a series of cold fronts (Ascasibar & Markevitch 2006; Million et al. 2010a), suggesting substantial 'sloshing' of the X-ray emitting gas (Markevitch et al. 2001; Tittley & Henriksen 2005; Ascasibar & Markevitch 2006; Markevitch & Vikhlinin 2007). The X-ray emission associated with the cool core is very sharply peaked and the X-ray morphology of the inner 10 kpc region is complex. The X-ray and stellar optical/near-IR brightness peaks are offset by ~ 4 arcsec (~ 2.2 kpc; Hamer et al. 2012). These observations indicate that the cool core of the Ophiuchus cluster has been stripped by the violent gas sloshing in the center of the cluster.

Table 7.1: Summary of the *Chandra* observations. Columns list the observation ID, observation date, and the exposure after cleaning.

Obs. ID	Obs. date	Exposure (ks)
3200	2002 Oct. 21	50.5
16142	2014 Jul. 1	32.6
16143	2014 Jul. 13	14.9
16464	2014 Aug. 8	31.7
16626	2014 Jul. 3	30.8
16627	2014 Jul. 5	34.6
16633	2014 Aug. 4	9.5
16634	2014 Jul. 11	22.4
16635	2014 Jul. 12	18.9
16645	2014 Aug. 9	33.6

Here, we present a deep (280 ks) *Chandra* observation of the Ophiuchus cluster along with new high resolution Jansky Very Large Array (JVLA) 1–2 GHz radio data, to study the effects of strong gas dynamics on the evolution of the cool core in detail. At a redshift of $z = 0.0296$ (Durret et al. 2015), assuming the concordance ΛCDM cosmology, one arcsecond corresponds to 0.59 kpc.

7.2 Observations and data analysis

7.2.1 Chandra data

The *Chandra* X-ray observatory pointed at the Ophiuchus cluster in July and August 2014 for 230 ks using the Advanced CCD Imaging Spectrometer (ACIS) in the VFAINT mode, using CCDs 1–4 and 6. We also included in our analysis a 50 ks observation performed in October 2002 using the ACIS S3 chip. The standard level-1 event lists were reprocessed using the `CIAO` (version 4.7, `CALDB 4.6.5`) software package, including the latest gain maps and calibration products. Bad pixels were removed and standard grade selections applied. The data were cleaned to remove periods of anomalously high background. The observations, along with the identifiers, dates, and net exposure times after cleaning (total net exposure of 280 ks), are listed in Table 1. Background images and spectra were extracted from the blank-sky fields available from the Chandra X-ray Center. These were cleaned in an identical way to the source observations, reprojected to the same coordinate system and normalized by the ratio of the observed to blank-sky count rates in the 9.5–12 keV band.

Image analysis

Background-subtracted images, using both the native resolution of the *Chandra* CCDs and using 2×2 pixel binning, were created in 13 narrow energy bands (0.6–0.8 keV,

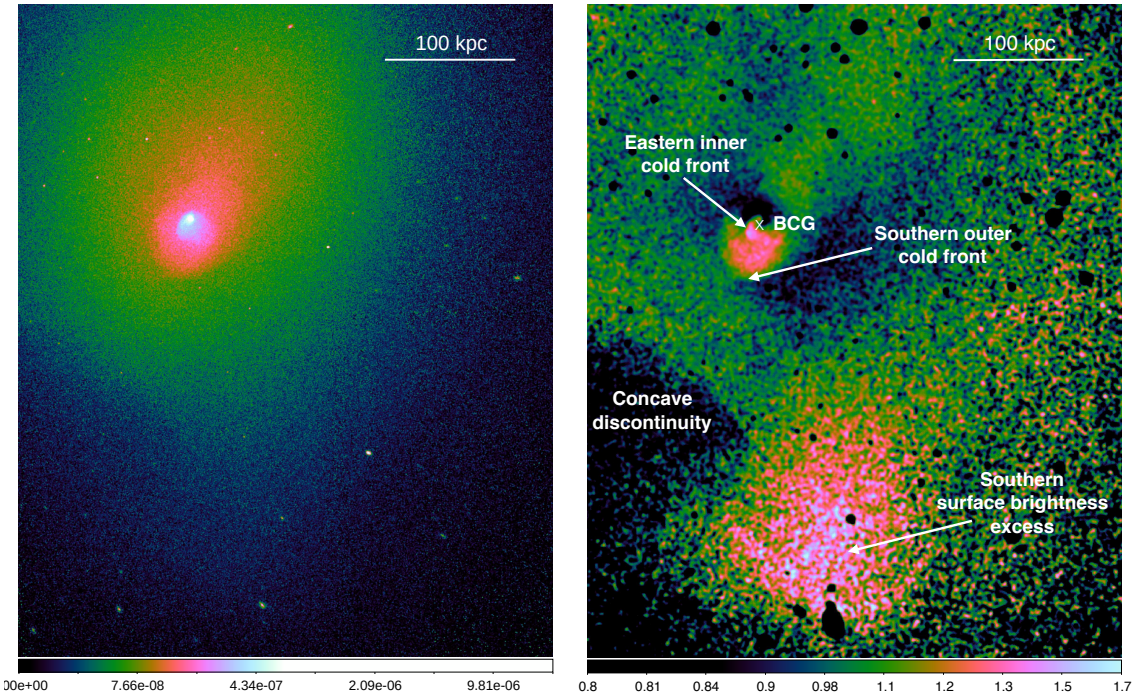

Figure 7.1: *Left panel: Chandra* X-ray image of the Ophiuchus cluster in the 0.6–7.5 keV energy band. The image was smoothed with a Gaussian function with a 1.0 arcsec window. *Right panel:* The residual image obtained by dividing the image on the left with an elliptical double beta-model reveals a prominent surface brightness excess in the south and a surprising, sharp discontinuity southeast of the cluster center, curved away from the core. North is up and east is left in all images.

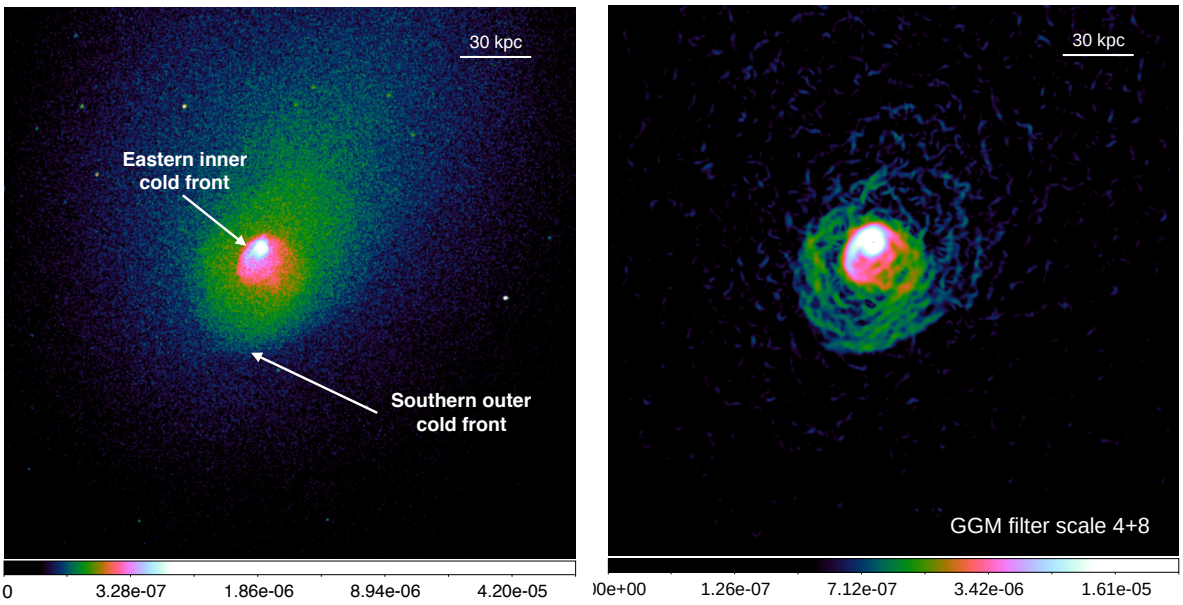

Figure 7.2: The same *Chandra* image as Fig. 7.1, zoomed in on the central part of the cluster (left panel). The right panel shows the GGM filtered image, using $\sigma = 4$ and 8 pixels (a pixel corresponds to 0.984 arcsec), which highlights multiple edges and the disturbed, broken-up cold front to the southeast of the cluster core.

0.8–1.0 keV, 1.0–1.2 keV, 1.2–1.5 keV, 1.5–2.0 keV, 2.0–2.5 keV, 2.5–2.75 keV, 2.75–3.0 keV, 3.0–3.5 keV, 3.5–4.0 keV, 4.0–6.0 keV, 6.0–7.0 keV, 7.0–7.5 keV), spanning 0.6–7.5 keV. The narrow-band images were flat fielded with respect to the median energy for each image and then co-added to create the X-ray images shown in Fig. 7.1. Identification of point sources was performed using the `CIAO` task `WAVDETECT`. The point sources were excluded from the subsequent analysis.

To look for sub-structure in the cluster, we removed the underlying large-scale surface brightness gradient by fitting an elliptical double beta-model to the image using the `Sherpa` package, and subsequently divided the image by the best-fit model (see the right panel of Fig. 7.1).

To highlight the sharp features in the image, we also used a Gaussian Gradient Magnitude (GGM) filter (see Sanders et al. 2016). The GGM filter uses Gaussian derivatives to determine the magnitude of surface brightness gradients in the image. We applied the GGM filter to the exposure-corrected, background subtracted image, from which point sources have been removed, for various Gaussian widths, using $\sigma = 1$, 2, 4, and 8 pixels (a pixel corresponds to 0.984 arcsec). Regions with large gradients, such as discontinuities, are bright, while flatter surface brightness areas are darker (see the right panel of Fig. 7.2).

To study the detailed properties of the surface brightness discontinuities in our X-ray images, we extracted surface brightness profiles at the native resolution of the *Chandra* CCD detectors, in 0.492 arcsec bins. We optimized the sharpness of the surface

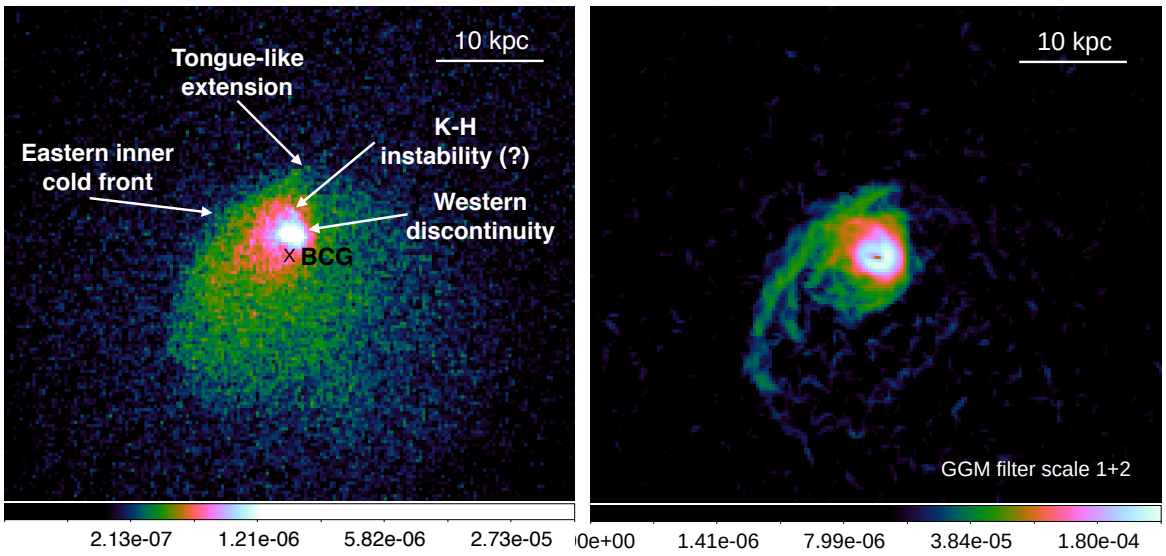

Figure 7.3: The same *Chandra* image as Fig. 7.1, zoomed in on the very central part of the cluster core (left panel). The right panel shows the GGM filtered image, using $\sigma = 1$ and 2 pixels, which highlights the remarkably sharp eastern inner cold front with a 'tongue'-like extension to the north, and the western discontinuity with a possible Kelvin-Helmholtz roll. The X-ray surface brightness peak is offset from the center of the BCG by about 2.2 kpc.

brightness edges in the profiles by aligning our circular annuli with the discontinuities. We fit the surface brightness profiles by projecting a spherically symmetric discontinuous, broken power-law density distribution (see e.g. Owers et al. 2009). The fitting was performed using the `PROFFIT` package (Eckert et al. 2011) modified by Ogrean et al. (2015). In order to place upper limits on the widths of the edges, we included in our models Gaussian smoothing as an additional free parameter.

Spectral analysis

Individual regions for the 2D spectral mapping are determined using the contour binning algorithm (Sanders 2006), which groups neighboring pixels of similar surface brightness until a desired signal-to-noise ratio threshold is met. The Ophiuchus cluster is a very hot system, with $kT \sim 10$ keV (Matsuzawa et al. 1996; Fujita et al. 2008a; Million et al. 2010a), which makes its temperature and metallicity measurement relatively difficult (at such high temperatures the cut-off of the thermal bremsstrahlung spectrum is outside of the energy window of the telescope), requiring a large number of counts. Therefore, we adopt a relatively high signal-to-noise ratio of 200 (approximately 40,000 counts per region), which provides approximately 2 per cent precision for density, 4 per cent precision for temperature, 12 per cent precision for metallicity, and 3 per cent precision for the line-of-sight absorption column density measurements, respectively. To obtain a high resolution 2D spectral map of the cooling core, we also

produced a map of the innermost $r = 10$ kpc region with a signal-to-noise of 50 (approximately 2500 counts per region), which provides 3–9 per cent precision for temperature, and 18–25 per cent per cent for metallicity. The errorbars are the smallest for the lowest temperature regions and grow bigger with increasing temperature. We model the spectra extracted from each spatial region with the SPEX package (Kaastra et al. 1996) in the 0.6–7.5 keV band. The spectrum for each region is fitted with a model consisting of an absorbed single-phase plasma in collisional ionization equilibrium. The Ophiuchus cluster lies close to the plane of our Galaxy, and therefore its line-of-sight absorption column density is high, with $N_{\rm H}$, according to the Leiden/Argentine/Bonn radio survey of H I, of $N_{\rm H} = 2 \times 10^{21}$ cm^{-2} (Kalberla et al. 2005). Radio surveys of H I usually underestimate the total absorption for systems with such high $N_{\rm H}$, because they are not sensitive to molecular and dust absorption. Therefore, the $N_{\rm H}$ has to be a free parameter in our model. Other free parameters include the spectral normalization (emission measure), temperature, and metallicity.

The deprojected spectra are obtained using the PROJCT model in XSPEC and the APEC plasma model (Smith et al. 2001; Foster et al. 2012). The line-of-sight absorption column density is a free parameter in the fit and for a given azimuth it is assumed to have the same value in all annuli except the innermost region where it is allowed to vary independently. Metallicities are given with respect to the proto-Solar abundances by Grevesse & Sauval (1998).

7.2.2 Radio JVLA data

We observed the Ophiuchus cluster with the Jansky Very Large Array (JVLA) in the L band for four hours on 2015 July 30. The observation was taken in the A configuration, resulting in a restoring FWHM beam size of $1.17'' \times 2.48''$. We spent 16 minutes on 3C286 to calibrate the flux, 22 minutes on J1734+0926 to calibrate the polarization leakage, 18 minutes on J1714-2514 to calibrate the phase, and a total of 150 minutes on source. The total bandpass was 1 GHz.

The data analysis was performed using the CASA package (McMullin et al. 2007). After the flux and phase calibrations were transferred to the source and RFI excluded, we used the CLEAN routine to image the cluster. We used a Briggs weighting of Robust $=$ 0.7 to increase the image sensitivity, while still keeping the high resolution to detect any possible extended structure near the BCG. We created the images fitting for both spectral index and correcting for the primary beam attenuation. The final image has an rms of 10 μJy.

7.3 Results

7.3.1 X-ray imaging

The Ophiuchus cluster shows a strongly centrally peaked X-ray surface brightness distribution, elongated north-northwestward (see the left panel of Fig. 7.1). By fitting an elliptical double beta-model to the image, with the cluster center as a free parameter,

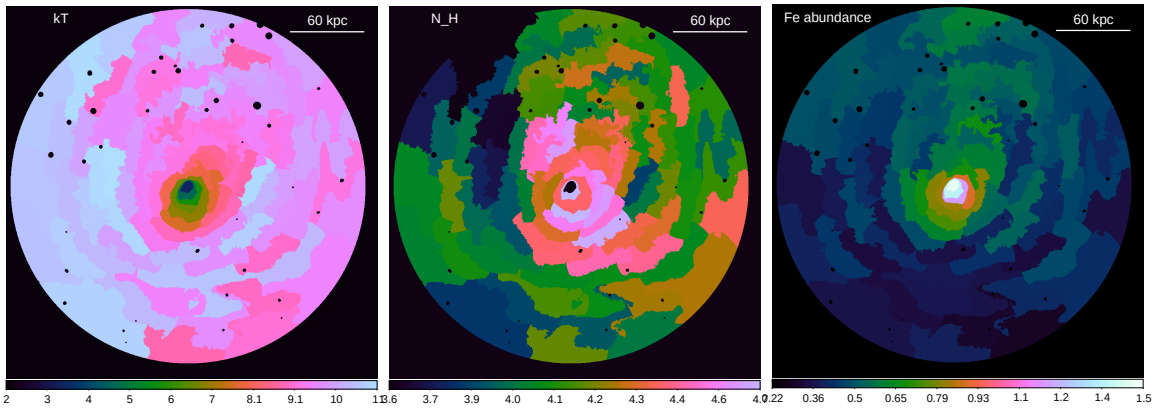

Figure 7.4: 2D maps of the best fit projected temperature, line of sight absorbing hydrogen column density, and iron abundance. Each spatial region contains 40,000 net counts (S/N of 200). The units of temperature, absorbing column density, and Fe abundance are keV, 10^{21} cm^{-2}, and Solar (Grevesse & Sauval 1998). The fractional 1σ statistical errors are $\sim$ 4 per cent for temperature, and $\sim$ 12 per cent for metallicity. Point sources were excluded from the regions shown as black circles.

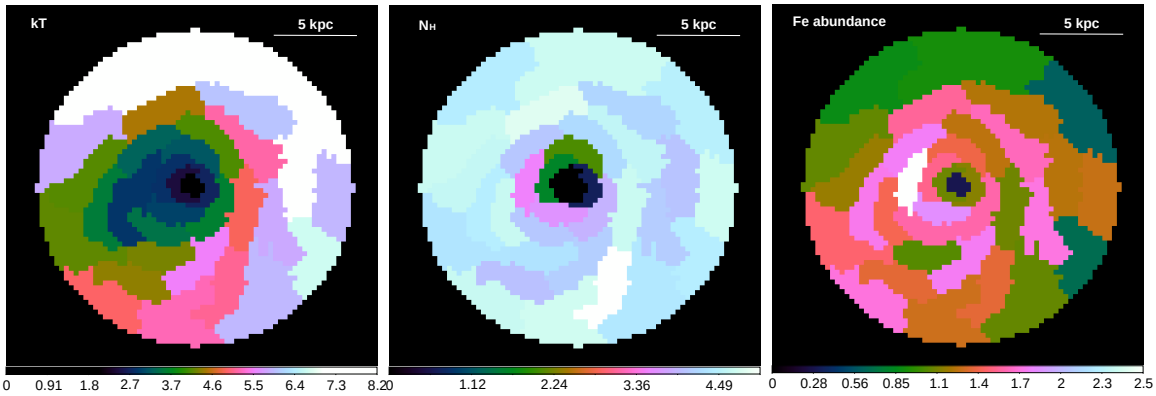

Figure 7.5: The 2D maps zoomed-in on the innermost $r = 10$ kpc core of the Ophiuchus cluster show the best fit projected temperature (left panel), line of sight absorbing hydrogen column density (central panel), and iron abundance (right panel) for spatial regions with 2500 counts (S/N of 50). The units of temperature, absorbing column density, and Fe abundance are keV, 10^{21} cm^{-2}, and Solar (Grevesse & Sauval 1998). The fractional 1σ statistical errors are 3–9 per cent for temperature, and 18–25 per cent per cent for metallicity. The errorbars are the smallest for the lowest temperature regions and grow larger with increasing temperature.

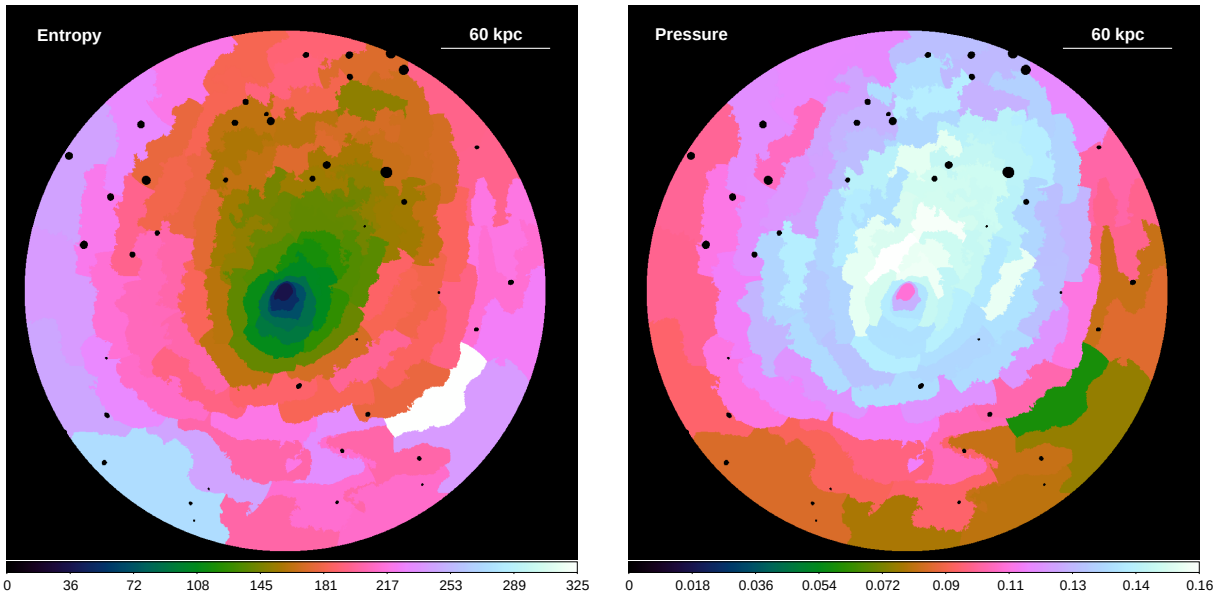

Figure 7.6: 2D maps of the projected entropy and pressure. To study their azimuthal distribution, we assume the gas uniformly distributed along the line-of-sight depth of $l = 100$ kpc over the entire field of view. The units of the entropy and pressure are keV cm^2$(l/100\,\mathrm{kpc})^{1/3}$ and keV cm^{-3}$(l/100\,\mathrm{kpc})^{1/2}$, respectively. The fractional 1σ statistical errors are about 5 per cent.

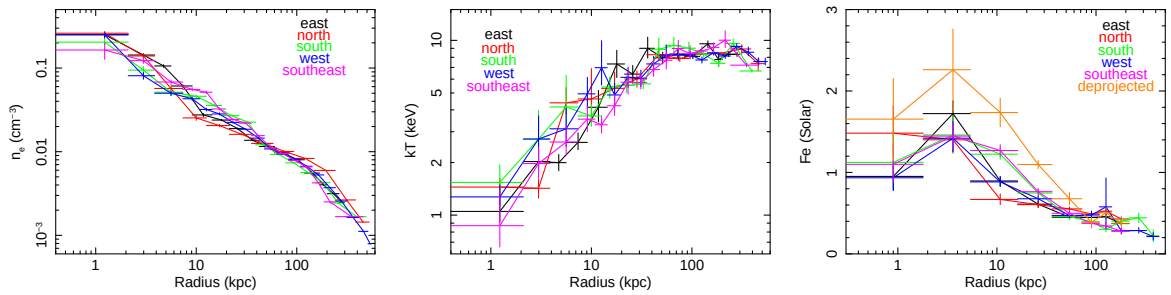

Figure 7.7: Radial profiles of the deprojected electron density and temperature distribution determined along five different azimuths (the azimuth angles are measured counterclockwise from the west): west (305–30 degress), north (30–110), east (110–205), southeast (205–260), and south (260–305). For the iron abundance distribution, in the right panel, we show the projected measurements and the azimuthally averaged deprojected profile.

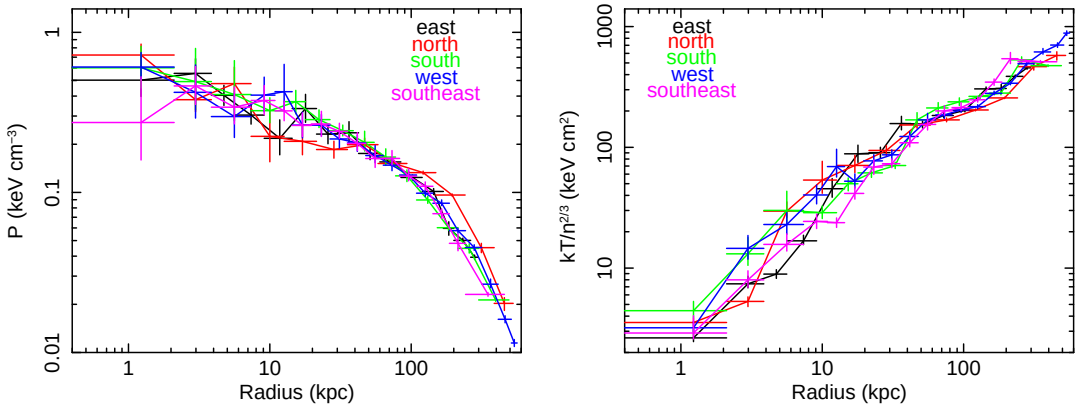

Figure 7.8: Using the electron density n_e and temperature kT_e profiles shown in Fig. 7.7, we determine the radial profiles of the total pressure ($P = nkT$; left panel) and entropy ($K = kT_e/n_e^{2/3}$; right panel).

we find that the center of the large scale emission distribution is offset by 38 kpc to the north-northwest of the central emission peak and the brightest cluster galaxy (BCG). In the residual image, obtained by dividing our *Chandra* image with the best fit elliptical double beta-model (see the right panel of Fig. 7.1), the tail-like excess emission extending north-northwestward practically disappears, indicating that this apparent excess emission is the result of the bright cluster core being displaced southward of the center of the global emission distribution. The residual image reveals a surface brightness excess at the projected distance of $r \sim 280$ kpc to the south of the BCG, which coincides with some bright galaxies identified in 2MASS images. Its southern edge has a hint of a sharp bow-shock shaped morphology. The residual image also reveals a surprising, sharp surface brightness discontinuity that is curved away from the core, at $r \sim 120$ kpc (3.55 arcmin) to the southeast of the BCG. Fitting the surface brightness distribution of the discontinuity with a broken power-law model, we find a steepening from $\gamma_1 = 0.3$ to $\gamma_2 = 2.6$.

The cluster core harbors a series of nested cold fronts (previously discussed in Ascasibar & Markevitch 2006; Million et al. 2010a) that surround the cool core (see Fig. 7.2). The outermost cold front wraps around the core from the east to the west and extends out to $r \sim 43$ kpc in the south. The best fit density discontinuity at its southern part is $n_j = 1.7$ and the 99 per cent upper limit on its width is 5.3 kpc. Southeast of the cluster core, the surface brightness discontinuity appears blurred and the GGM filtered image highlights that the cold front is broken up. The GGM filtering also highlights multiple edges to the south of the core seen in the *Chandra* image.

The sharpest, most prominent cold front extends from the northeast to the southwest of the BCG at $r \sim 4.5$–10 kpc, and has a northward 'tongue'-like extension (see Fig. 7.3). Its best fit density jump is $n_j = 2$ and the front appears remarkably sharp. We find that the 99 per cent upper limit on its width is 1.5 kpc.

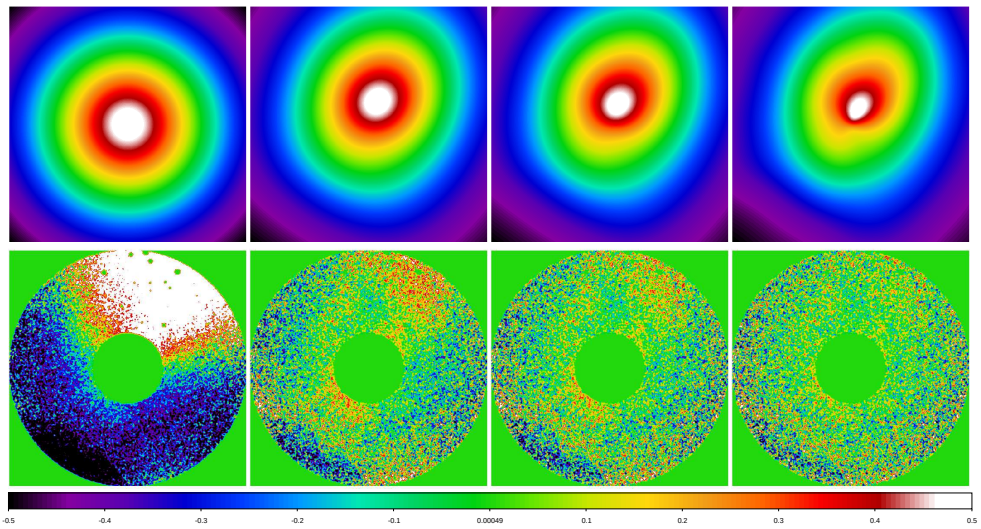

Figure 7.9: *Top*: Underlying models of the "unperturbed" surface brightness distribution of the Ophiuchus cluster. From left to right: spherically-symmetric β-model, patched β-models with $\sigma = 70$ arcsec (removes large-scale asymmetry), $\sigma = 30$ arcsec, and $\sigma = 10$ arcsec (see Zhuravleva et al. 2015, for details). *Bottom:* residual images of the SB fluctuations in the Ophiuchus cluster obtained from the initial image divided by the underlying model on the corresponding upper panel. The smaller the σ, the smaller the structures included to the model and the less structures remain in the residual image.

The compact, bright innermost cluster core is displaced from the center of the BCG by 2.2 kpc in projection (see also Hamer et al. 2012). The compact core has a surface brightness discontinuity at its west side and an extension, a possible Kelvin-Helmholtz roll, to the north. In contrast to the other nearby cooling cores, the core of the Ophiuchus cluster does not show the presence of any *obvious* X-ray cavities produced by the active galactic nucleus (AGN). However, the presence of very small cavities, with radius of up to 1.5 kpc, to the southeast of the core cannot be ruled out.

7.3.2 X-ray spectroscopy

Our temperature map in Fig. 7.4 reveals a remarkably steep temperature gradient in the core of the cluster, with the azimuthally averaged temperature increasing from ~ 2 keV in the core of the cluster up to ~ 8 keV at $r \sim 20$ kpc. Outside $r \sim 30$ kpc the temperature distribution is remarkably uniform with $kT \sim 9.5$–10.5 keV.

Zooming-in on the innermost $r = 10$ kpc core of the cluster, using lower signal-to-noise (S/N=50) maps, the high temperature gradient in the core becomes even clearer (see Fig. 7.5). Along the northwestern direction, the gradient of the projected temperature reaches $\mathrm{d}kT/\mathrm{d}r \sim 1$ keV/kpc. While we model the ICM using a single-temperature plasma model, the plasma in the innermost cluster core is multiphase.

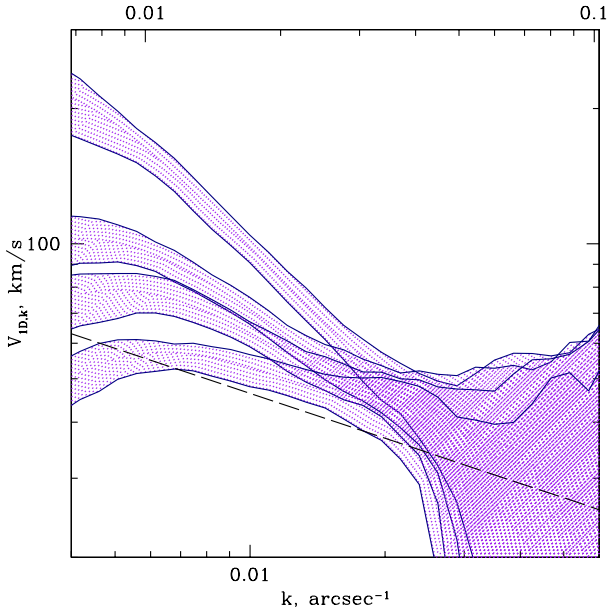

Figure 7.10: The amplitude of velocity fluctuations in the 1.5–5 arcmin annulus in the Ophiuchus cluster obtained by assuming that the amplitudes of the density and velocity fluctuations are proportional to each other on each scale (see the text and Zhuravleva et al. 2014a; Gaspari et al. 2014, for detail). In order to determine the amplitude of density fluctuations, the large scale surface brightness gradient has been modeled with a spherically-symmetric β-model (top hatched region) and with more flexible models shown in Fig. 7.9. While the top hatched region is clearly affected by the large-scale asymmetry in the cluster, all of the models that account for the asymmetry indicate velocities $V_{1D,k} \lesssim 100$ km s^{-1} on scales $\lesssim 100$ kpc. The dashed line indicates the expected shape of a Kolmogorov spectrum.

The soft emission of a multiphase plasma biases the best fit hydrogen column density, $N_{\rm H}$, low. The central panel of Fig. 7.5 shows low best fit $N_{\rm H}$ in the central four spatial bins, at radii $r \lesssim 3.5$–4.5 kpc. Outside this innermost region, the best fit line-of-sight absorbing hydrogen column density distribution is relatively uniform and its value, $N_{\rm H} \sim 4 \times 10^{21}$ cm^{-2}, is approximately two times higher than the column densities measured by the Leiden-Argentine-Bonn survey of Galactic H I (Kalberla et al. 2005). The difference is probably due to molecular gas and dust along our sight-line close to the Galactic plane. Fixing the $N_{\rm H}$ to 4×10^{21} cm^{-2} in our model (the best fit value determined in regions outside the cluster core), we fit a two-temperature model to the spectra extracted from the four central regions (regions where Fig. 7.5 shows a low $N_{\rm H}$). With respect to a fit with a single temperature plasma and free $N_{\rm H}$, for one additional free parameter, the χ^2 of the fit improves by 210 for 4693 degrees of freedom. This best fit model indicated the presence of a 0.82 ± 0.02 keV and a 2.75 ± 0.09 keV plasma phase with a metallicity of 2.14 ± 0.26 Solar. Assuming the 0.82 keV phase is radiatively cooling, we also fit a model of a collisionaly ionized plasma and a cooling flow, cooling from 0.82 keV, and find a best fit mass deposition rate of $\dot{M} = 0.97 \pm 0.12\ M_{\odot}$ yr^{-1}. Similarly to other systems, such as M 87 (Werner et al. 2010), Perseus cluster (Sanders & Fabian 2007), Centaurus cluster (Sanders et al. 2016), the coolest gas phases are associated with Hα filaments in the core of the cluster (Hamer et al. 2012).

The metallicity map in the right panel of Fig. 7.4 reveals a strongly centrally peaked iron abundance distribution. The apparent metallicity dip in the innermost cluster core (see right panel of Fig. 7.5) disappears when fit with a two-temperature model, which indicates a relatively high central metallicity of 2.14 ± 0.26 Solar (see also the previous paragraph). The metallicity distribution shows a relatively sharp discontinuity at the southeastern edge of the outer cold front at $r \sim 43$ kpc and a trail of excess iron abundance extends to the north of the core.

The projected entropy distribution is asymmetric (see the left panel of Fig. 7.6), with a clear discontinuity at the southern cold front and a low entropy 'tail' extending northward. While, as indicated by our deprojection analysis (see the next paragraph), the true pressure peaks at the BCG, the projected pressure in the bright cluster core is biased low (see the right panel of Fig. 7.6). This bias is due to the underestimated density, which is the result of the adopted constant line-of-sight bin size[1]. The detected azimuthal variations are, however, robust. Similar to the entropy distribution, the pressure distribution also shows a prominent excess to the north of the core.

Taking the X-ray surface brightness peak as the center of the system and assuming spherical symmetry, we determine the radial profiles of the deprojected spectral properties along five different azimuths, chosen based on the observed morphological characteristics (the azimuth angles are measured counterclockwise from the west): west (305–30 degress), north (30–110), east (110–205), southeast (205–260), and south (260–305). Fig. 7.7 shows the deprojected electron density ($n_{\rm e}$) and temperature ($kT_{\rm e}$) profiles and both the projected and deprojected iron abundances distributions (the de-

[1]When looking at a spherically symmetric cluster with a centrally peaked density distribution, the effective line-of-sight length, from which the dominant fraction of photons is emitted, is smaller in the core and increases with radius.

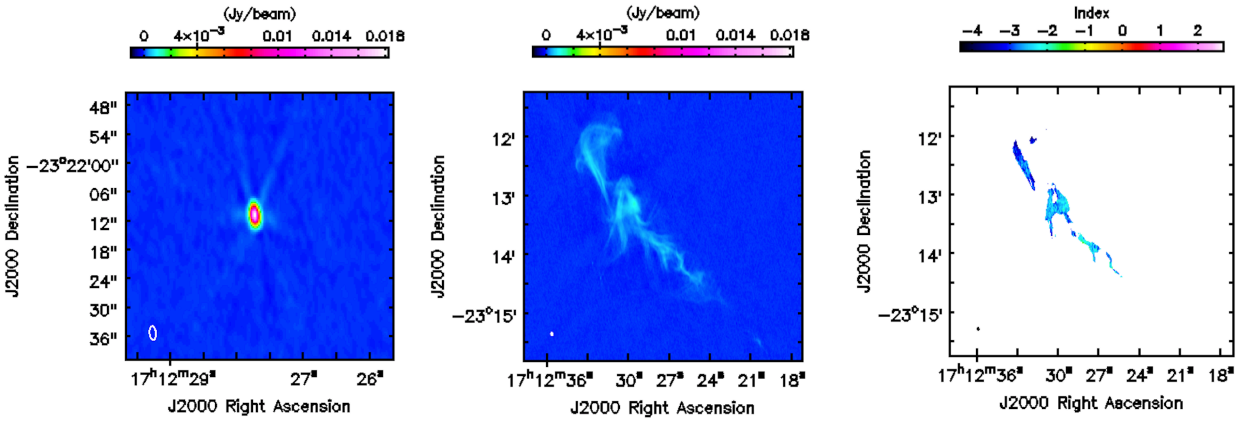

Figure 7.11: *Left panel:* The BCG harbors a relatively faint, point-like, unresolved radio source with a 30 mJy flux density at 1.4 GHz. The white ellipse in the bottom left corner shows the beam size of $1.17'' \times 2.48''$. *Central panel:* A peculiar, filamentary radio source, located about 360 kpc to the north of the cluster core (see also Murgia et al. 2010). This object with no optical or X-ray counterpart is a likely radio phoenix, a source revived by adiabatic compression by gas motions in the ICM. *Right panel:* The spectral index map of the likely radio phoenix shows a relatively steep spectrum across the source.

projection analysis introduces a substantial noise into the measured Fe abundance values). Using these measurements, we determine the total pressure ($P = nkT$) and entropy ($K = kT_{\rm e}/n_{\rm e}^{2/3}$) profiles shown in Fig. 7.8. In the innermost $r \sim$2 kpc region, the best fit iron abundance peaks at $\sim$ 2.3 Solar and the entropy drops to $\sim$ 2.6 keV cm^2 .

7.3.3 The power-spectra of surface brightness fluctuations

Following the methods described in Churazov et al. (2012), Zhuravleva et al. (2015, 2016), and Arévalo et al. (2015), we perform an analysis of the power-spectra of the surface brightness fluctuations in the Ophiuchus cluster. Using theoretical arguments supported by numerical simulations, Zhuravleva et al. (2014b) and Gaspari et al. (2014) show that in galaxy clusters, where the gas motions are subsonic, the root mean squared amplitudes of the density and line-of-sight-component velocity fluctuations are proportional to each other on each scale, $\delta\rho_{\rm k}/\rho_0 \approx \eta V_{\rm 1D,k}/c_{\rm s}$, where ρ_0 is the unperturbed gas density, $c_{\rm s}$ is the sound speed and $\eta \approx 1$ is a proportionality coefficient. Cosmological simulations show that $\eta \approx 1$ with a scatter of 30 per cent (Zhuravleva et al. 2014b) and hydrodynamic simulations confirm that the proportionality coefficient is of the order of unity as long as conduction is completely suppressed (Gaspari et al. 2014).

To avoid complications due to the steep temperature gradient in the core of the cluster, we analyzed an image in the annular region of $r =$ 1.5–5 arcmin around the surface brightness peak, where the ICM appears approximately isothermal (see the left panel of Fig. 7.4). The image was extracted in the 1.5–3.5 keV energy range, where the emissivity is approximately independent of temperature and proportional to the density squared. We ignored the soft band where we are affected by the high Galactic column density. To remove the global surface brightness gradient, we divided the cluster

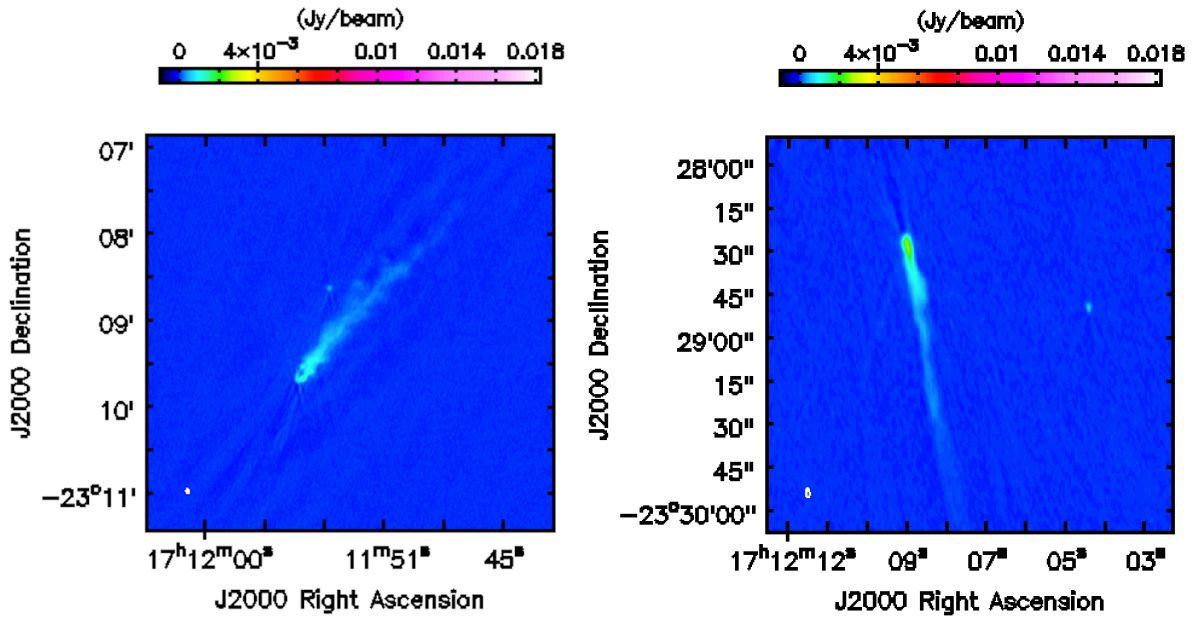

Figure 7.12: The Ophiuchus cluster also harbors two bright narrow-angle tail radio galaxies (see also Murgia et al. 2010). The radio emitting tails of these infalling galaxies are over 60 kpc long.

image by a model of an "unperturbed" surface brightness distribution (see Fig. 7.9). Our simplest assumption is a spherically symmetric β-model which, however, does not account for the prominent global asymmetry. To remove the asymmetry, as shown in Fig. 7.9, we experimented with β-models patched on several different scales (see Zhuravleva et al. 2015, for details).

Assuming volume filling turbulence and a sound speed of 1500 km s^{-1}, we calculate the velocity fluctuations from the density fluctuations obtained by using a range of models for the underlying global density distribution. We find that after accounting for the azimuthal variation in the underlying model, the derived volume filling velocities are $V_{1D,k} \lesssim 100$ km s^{-1} on scales $\lesssim 100$ kpc.

To determine the nature of the southern surface brightness excess (see Fig. 7.1), we used a method introduced in Arévalo et al. (2015) and Zhuravleva et al. (2016), and analyzed the statistical properties of the emissivity fluctuations in two energy bands: 1.5–3.5 keV and 3.5–7.5 keV. For the gas temperatures in the Ophiuchus cluster, we would expect that while 'isobaric' gas perturbations, associated with slow displacement of gas, will result in a ratio of the power-spectra derived in the hard and soft energy bands of $R \sim 0.9$, 'adiabatic' perturbations, associated with weak shocks, will result in $R \sim 1.1$. Our measured ratios, after accounting for the large statistical uncertainties, are $R > 1$ consistent with 'adiabatic' perturbations, suggesting the possible presence of a weak shock or a separate sub-halo moving through the cluster. The statistics associated with this feature is, however, low and a more direct confirmation of the nature of this feature will require deeper observations.

7.3.4 Radio properties

We detect a point-like radio source associated with the center of the BCG with a flux density of 30 mJy and spectral index $\alpha = -0.55$. The source is both compact and optically thin, typical of very low level accretion. As can be seen from the left panel of Fig. 7.11, we find no evidence of extended structure near the BCG above the rms level of 10 μJy. The upper limit on the polarization of the source is 0.2 per cent.

Our radio data also show two head-tail radio galaxies (see Fig. 7.12) previously studied by Murgia et al. (2010) and Govoni et al. (2010). However, the brightest (630 mJy) and perhaps most interesting radio source in the Ophiuchus cluster is a peculiar, filamentary object (see the central panel of Fig. 7.11), located about 360 kpc to the north of the cluster core. It is about 200 arcsec long (120 kpc at the redshift of the cluster) and has no optical or X-ray counterpart. The object has been previously identified in GMRT data by Murgia et al. (2010) as a possible unusual radio relic. We find a steep spectral index of $\alpha \sim -1.8$ to -2.5 that is relatively uniform across the source (see the right panel of Fig. 7.11). This index is steeper than the slope of $\alpha = -1.01 \pm 0.03$ measured between 74 MHz and 1.4 GHz by Murgia et al. (2010), indicating the presence of a break at $\sim$ 1 GHz. The source shows signs of polarization, with the brightest knot, located near the middle of the source, being polarized to roughly 18 per cent.

The core of the Ophiuchus cluster also harbors a faint radio minihalo (see Govoni et al. 2009; Murgia et al. 2009, and our discussion below), however, our high resolution JVLA observation in the A configuration is not sensitive to the faint extended emission.

7.4 Discussion

7.4.1 Dynamical activity and the truncated cooling core

The $\sim$ 38 kpc offset of the centroid of the large scale X-ray emission distribution from the central BCG and the prominent southern surface brightness excess indicate that the gravitational potential in the cluster core has been strongly perturbed. The maps of projected thermodynamic properties support this picture. In a galaxy cluster in approximate hydrostatic equilibrium, with subsonic gas motions, the pressure distribution traces the gravitational potential of the system. However, contrary to most cooling core clusters, the pressure distribution in the Ophiuchus cluster is highly azimuthally asymmetric around the BCG and displays a prominent region of excess pressure in the north. These results strongly indicate that the BCG, which presumably traces the dark matter density peak, is offset from the cluster's global center of mass. Such a perturbed gravitational potential is most likely the result of a relatively recent encounter with an in-falling sub-cluster.

The multiple concentric cold fronts in the core of the cluster are also most likely due to gas sloshing in a changing gravitational potential (e.g. Ascasibar & Markevitch 2006; Markevitch & Vikhlinin 2007) which, following an encounter with a sub-cluster, is expected to be evolving towards a global equilibrium. While the southern outer cold front, at $r \sim 43$ kpc from the BCG, indicates southward gas motions, the prominent

eastern inner cold front, at $r \sim 5$ kpc from the BCG, shows that the gas in the cluster core is swinging northeastward, most likely following the innermost part of the dark matter potential. As the dense low entropy ICM in the cluster core moves through the ambient ICM, it encounters ram-pressure and, as proposed by Million et al. (2010a), the outer layers of the cool core get stripped, resulting in the highly unusual steep temperature and metallicity gradients (for comparison see the entropy profiles in Cavagnolo et al. 2009; Panagoulia et al. 2014). The entropy and metallicity distributions in Fig. 7.4–7.6 also show clear evidence for such ram-pressure stripping. On the large scale maps, we see an excess of low-entropy, high-metallicity gas northwest of the core of the cluster. On smaller scales, we see a similar excess along a perpendicular axis, to the southwest. In the innermost cluster core (see Fig. 7.5), we see an excess of cooler gas to the southeast. The observed disruption of the cool core in the Ophiuchus cluster is particularly interesting in the light of simulations, which indicate that cool cores are remarkably resilient and survive late major mergers (Burns et al. 2008; Poole et al. 2008).

The southern surface brightness excess, seen at the bottom of the residual image in the right panel of Fig. 7.1, is an obvious candidate for a sub-cluster that could have encountered the cluster core relatively recently. The appearance of its southern edge is suggestive of a bow-shock like shape, which would indicate a merger taking place close to the plane of the sky. Furthermore, as discussed in Section 7.3.3, the cross spectrum analysis also suggests the possible presence of a weak shock. Assuming a merger in the plane of the sky, occurring at the sound speed in the $kT = 8.5$ keV ICM ($c_s = 1500$ km s^{-1}), we estimate that the closest passage to the cluster core would have occurred less than ≈ 200 Myr ago. A recent study of spectroscopic redshifts by Durret et al. (2015) indicates that the $1.1 \times 10^{15}\ M_\odot$ Ophiuchus cluster is not undergoing a major merger and the BCG is close to the center of the global gravitational potential, where the BCG velocity is consistent with the mean cluster velocity $\Delta v = 47 \pm 97$ km s^{-1}. However, a merger with a $M \sim 10^{14}\ M_\odot$ system would still be consistent with the optical data.

Although our data clearly show that the Ophiuchus cluster is dynamically active, it is unlikely that the truncation of the cool core has been caused by a single, recent merging event. Comparison to numerical simulations (e.g. Ascasibar & Markevitch 2006; ZuHone et al. 2011; Roediger et al. 2011) indicates that the observed complex, developed sloshing patterns are likely to have been triggered by an encounter over 1 Gyr ago. The merger with the southern sub-cluster might therefore be the latest in a chain of systems merging with the Ophiuchus cluster.

7.4.2 The radio phoenix

Another indication of dynamical activity in the Ophiuchus cluster are the two narrow-angle tail radio sources (see Fig. 7.12 and Murgia et al. 2010) which are infalling towards the cluster center, and the peculiar, filamentary radio source detected at $r \sim 360$ kpc (10 arcmin) north of the BCG (see the central panel of Fig. 7.11). This relic-like source has no optical/near-infrared or X-ray counterpart. The object lacks a clear radio core, and its spectral index of $\alpha \sim -2$ is similar to that of radio relics (see also

Murgia et al. 2010). However, the relatively small size (about 120 × 30 kpc), unusual morphology, high surface brightness, and the central location within the Ophiuchus cluster make it unlikely that this source is a radio relic. It appears more similar to *radio phoenixes* (Kempner et al. 2004; van Weeren et al. 2009; de Gasperin et al. 2015), sources revived by adiabatic compression by a shock or gas motions propagating through the ICM as shown by Ensslin & Gopal-Krishna (2001) and Ensslin & Brüggen (2002). The vortex-like structure at its northern tip might be associated with a $L \sim 15$ kpc turbulent eddy in the ambient ICM. Contrary to the recently identified radio phoenix in Abell 1033 (de Gasperin et al. 2015), the source in the Ophiuchus cluster shows signs of polarization, which may be due to its larger distance from the cluster center resulting in a smaller amount of intervening matter.

7.4.3 The cold fronts

The inner eastern cold front (Fig. 7.3) is remarkably sharp, with a width smaller than 1.5 kpc. This is the tightest measured upper limit on a physical width of a cluster cold front. However, because the ICM density in the cluster core is high, the Coulomb mean free path for particles diffusing from the cooler bright, dense side of the discontinuity to the hotter outer ICM is about an order of magnitude smaller than this upper limit. Diffusion has previously been shown to be suppressed at cold front interfaces with upper limits in Abell 3667 and the Virgo cluster smaller or comparable to the Coulomb mean free path (Vikhlinin et al. 2001b; Markevitch & Vikhlinin 2007; Werner et al. 2016).

The 'tongue'-like extension to the north (Fig. 7.3) may be due to the onset of a Rayleigh-Taylor instability, which develops when the displaced, dense gas subjected to ram-pressure from the ambient ICM spreads sideways, eventually sprouting a tongue of low entropy material which separates and starts sinking towards the minimum of the gravitational potential. Note the remarkable morphological similarity of this feature (although on a much smaller physical scale) to the results of the simulation in Fig. 7 of Ascasibar & Markevitch (2006).

The outer southern cold front appears significantly more disturbed, with multiple edges and azimuthal variation. Fig. 7.2 shows that while the southern edge of the front is relatively sharp (width smaller than 5.3 kpc), its southeastern side appears smeared. Azimuthal variations and smearing has also been observed at the prominent cold fronts in the Virgo and Centaurus clusters by Werner et al. (2016) and Sanders et al. (2016). They propose that the smearing is most likely due to Kelvin-Helmholtz instabilities, which have previously also been observed in NGC 7618 and UGC 12491 (Roediger et al. 2012). Constrained hydrodynamic simulations reproducing the Virgo cluster by Roediger et al. (2013) demonstrate that viscosities of about 10 per cent of the Spitzer value or larger are very efficient at preventing the development of Kelvin-Helmholtz instabilities, indicating that the viscosity is suppressed in that system. Magnetohydrodynamic simulations by ZuHone et al. (2011, 2013) show that magnetic fields provide only partial protection against hydrodynamic instabilities. The apparent breakup of the southern cold front is thus consistent with the previous results which suggest that the viscosity of the ICM is suppressed with respect to the temperature dependent Spitzer value.

While the multiple surface brightness edges to the south of the cluster center, seen in the right panel of Fig. 7.2, could be due to Kelvin-Helmholtz instabilities, as discussed by Roediger et al. (2013), they could also be due to gas depletion by amplified magnetic fields underneath the cold front, as discussed in Werner et al. (2016). Simulations of ZuHone et al. (2011, 2015) show that gas sloshing may result in wide bands of amplified magnetic fields extending relatively far below cold fronts. The increased magnetic pressure in such layers may push gas out, decreasing its density, creating surface brightness edges associated with the magnetized bands.

7.4.4 Turbulence and thermal conduction in the hot ICM

Even though our observations clearly show that the core of the Ophiuchus cluster is strongly dynamically active, the amplitude of density fluctuations in the $r = 1.5$–5 arcmin (53–177 kpc) region is relatively low, indicating velocities smaller than $\sim$ 100 km s^{-1} on scales $\lesssim$ 100 kpc. Given that the cooling core is offset from the global center of mass and the sub-cluster that initiated the unusually strong sloshing is likely to have passed close to the cluster center, we would expect the gas motions associated with the dynamical activity to be higher and to have cascaded down to a volume filling turbulence in the investigated region. Moreover, such low ICM velocities would be surprising in a disturbed cluster with a galaxy velocity dispersion of $\sim 954 \pm 58$ km s^{-1} (Durret et al. 2015). Viscosity is unlikely to suppress gas motions on the relatively large scales that we are probing (see e.g. Gaspari et al. 2014), and the morphology of cluster cold fronts indicates that the viscosity in the ICM is likely lower than the temperature dependent Spitzer value by more than an order of magnitude (see Sect. 7.4.3 and Roediger et al. 2013, 2015; Werner et al. 2016). Our relation between the power spectrum of the density fluctuations and the power-spectrum of velocity fluctuations was derived under the assumption that thermal conduction in the ICM is fully suppressed. However, thermal conduction could damp the density fluctuations by a factor $\sim$ 2–3 on the observed scales, while leaving the velocity cascade unaltered (Gaspari et al. 2014). Such damping would then result in our underestimate of velocities.

The large temperature gradient, of the order of $\mathrm{d}kT/\mathrm{d}r \sim 1$ keV/kpc, in the core of the Ophiuchus cluster indicates that the thermal conduction is suppressed along the radial direction. Such suppression might be the result of azimuthal magnetic fields that will, in the absence of significant turbulence, arise in cooling cores due to heat-flux driven buoyancy instability (HBI; Quataert 2008; Parrish & Quataert 2008; Parrish et al. 2009, 2010). Gas sloshing can also result in azimuthally aligned magnetic fields (ZuHone et al. 2011). Observations of cold fronts (Ettori & Fabian 2000; Xiang et al. 2007) and merging clusters of galaxies (Markevitch et al. 2003) also indicate that thermal conduction in the ICM is significantly suppressed (by a factor of order $\sim 10^2$) with respect to the Spitzer value. The alignment of magnetic field lines alone, however, would not explain the observed suppression of the heat flux. Comparisons of numerical simulations that include anisotropic conduction to observations indicate that thermal conduction is also suppressed by over an order of magnitude *along* the magnetic filed lines (ZuHone et al. 2013; Werner et al. 2016). However, because thermal conduction is a strong function of temperature ($\propto T^{5/2}$), even a suppressed conduc-

tivity would be relatively efficient in the $\sim$ 9 keV ICM outside of the cooling core of the Ophiuchus cluster. Conduction could, in principle, contribute both to the observed isothermality and to the damping of density fluctuations. It would suppress the perturbations preferentially on smaller scales, steepening the observed power-spectrum. Although the observed velocity power-spectrum in Fig. 7.10 appears steeper than the Kolmogorov spectrum, the large systematic uncertainties due the subtraction of the underlying model do not allow us to make a firm conclusion about the slope.

A relatively low level of surface brightness fluctuations is also measured in the $kT \sim 3.5$ keV AWM 7 cluster, where conduction is expected to be much less signifficant (Sanders & Fabian 2012). It is, however, possible that this system is dynamically more relaxed and does therefore not harbor strong volume filling turbulence. Conduction would probably also have a less significant effect on the surface brightness fluctuations in the cool cores of the Perseus and Virgo clusters (see Zhuravleva et al. 2014a, 2015; Arévalo et al. 2015). Comparison of the power-spectra of surface brightness fluctuations and direct line broadening measurements with the *Hitomi* satellite will soon provide important quantitative constraints on transport processes and the microphysics of the ICM (see the discussion in Gaspari et al. 2014; ZuHone et al. 2015).

7.4.5 The concave surface brightness discontinuity: giant AGN outburst or merger related gas dynamics?

Concave surface brightness discontinuities, similar to the one observed at $r \sim 120$ kpc southeast of the core of the Ophiuchus cluster, but on smaller physical scales, are also observed in the Perseus cluster, Abell 1795, Abell 2390, and Centaurus cluster, where they were interpreted as the inner walls of cavities resulting from AGN activity (Walker et al. 2014; Sanders et al. 2016). Low frequency radio observations of the Ophiuchus cluster performed by the GMRT also reveal steep spectrum radio emission beyond this feature (see the radio source E in Murgia et al. 2010). The radius of curvature of the observed concave feature is $\sim$ 180 kpc, therefore, if it is associated with the inner wall of a spherical cavity, then the pV work required to displace the ICM is about 5×10^{61} ergs (comparable with the most powerful AGN outburst known in MS 0735.6+7421; McNamara et al. 2005; Vantyghem et al. 2014). However, a buoyantly rising AGN inflated cavity would more likely have an ellipsoidal shape and a smaller size, requiring less but still a substantial amount of AGN power. Such a powerful AGN outburst would heat and displace a large amount of ICM in the cluster core and, in combination with the ongoing merger, contribute sinificantly to the disruption of the cooling core (see e.g. Ehlert et al. 2011b).

However, the extremely steep metallicity and entropy gradients in the Ophiuchus cluster would most likely get erased by such a powerful AGN outburst, arguing against this scenario. It is more likely that the discontinuity is the result of merger related gas dynamics. Similar concave discontinuities appear at certain stages of mergers in simulations of infall of gas-rich subclusters into cooling core clusters (see Fig. 22 in Ascasibar & Markevitch 2006).

7.4.6 Suppressed AGN feedback

Because of the ram pressure experienced by the ICM (in contrast to the stars and dark matter associated with the BCG, which are effectively collisionless), the gas motions in the changing gravitational potential well can lead to the separation of the ICM density peak from the BCG. Such a separation is clearly observed in the Ophiuchus cluster, where the X-ray surface brightness peak is displaced from the center of the BCG by 2.2 kpc in projection and spatially coincides with Hα nebulae. This dense displaced gas displays multi-temperature structure consistent with a radiative cooling rate of $\dot{M} = 0.97 \pm 0.12\ M_{\odot}$. Because this gas is displaced from the vicinity of the AGN, it can continue cooling without triggering an AGN feedback response. Similar cooling, offset from the AGN, has been seen in Sersic 159-03, Abell 3444 and Abell 1991, Abell 2146 (e.g. Werner et al. 2011; Hamer et al. 2012; McDonald et al. 2015; Russell et al. 2012; Canning et al. 2012). The lack of observed X-ray cavities in the cluster core and the weak point-like radio emission, lacking lobes or jets, indicate that the AGN may currently be largely dormant, which is consistent with the cooling taking place offset from the central supermassive black hole. The innermost surface brightness discontinuity, just 2 kpc west of the X-ray peak, separates the cooling multiphase gas from the ambient ICM.

Mazzotta & Giacintucci (2008) propose that turbulence driven by gas sloshing reaccelerates preexisting cosmic rays from the central AGN producing diffuse radio mini-haloes. The presence of the radio mini-halo in the Ophiuchus cluster, discovered by Govoni et al. (2009) using VLA data at 1.4 GHz in the D configuration, is consistent with this picture. Murgia et al. (2009) concluded that the emissivity of the mini-halo of the Ophiuchus cluster (along with the mini-haloes in Abell 1835 and Abell 2029) is low, similar to the emissivities of radio haloes of merging clusters rather than to other previously known mini-haloes. Within the framework of the turbulent re-acceleration scenario, the relatively low surface brightness of the mini-halo in such a dynamically active cluster core implies the lack of a substantial amount of preexisting cosmic rays, consistent with a picture of a largely dormant AGN.

7.5 Conclusions

- The Ophiuchus cluster hosts a truncated cool core, with a temperature increasing from $kT \sim 1$ keV in the center to $kT \sim 9$ keV at $r \sim 30$ kpc. Beyond $r \sim 30$ kpc the ICM appears remarkably isothermal.

- The core is dynamically disturbed with multiple sloshing induced cold fronts, with indications for both Rayleigh-Taylor and Kelvin-Helmholtz instabilities. The sloshing is the result of the strongly perturbed gravitational potential in the cluster core, with the BCG displaced southward from the global center of mass.

- The residual image reveals a likely sub-cluster south of the core at the projected distance of $r \sim 280$ kpc.

- The cluster harbors a peculiar, filamentary radio source with no optical or X-ray counterpart, located about 360 kpc to the north of the cluster core. The object is a likely radio phoenix, a source revived by adiabatic compression by gas motions in the ICM.

- Even though the Ophiuchus cluster is strongly dynamically active, the amplitude of density fluctuations outside of the cooling core is low, indicating velocities smaller than $\sim$ 100 km s^{-1}. The density fluctuations might be damped by thermal conduction in the hot and remarkably isothermal ICM, resulting in our underestimate of gas velocities.

- We find a surprising, sharp surface brightness discontinuity that is curved away from the core, at $r \sim 120$ kpc to the southeast of the cluster center. We conclude that this feature is most likely due to gas dynamics associated with a merger and not a result of an extraordinary AGN outburst.

- The cooling core lacks any observable X-ray cavities and the AGN only displays weak, point-like radio emission, lacking lobes or jets, indicating that currently it may be largely dormant. The lack of strong AGN activity may be due to bulk of the cooling taking place offset from the central supermassive black hole. The observed unchecked cooling where a largely dormant AGN is offset from the cooling flow solidifies the idea that AGN play a key role in maintaining the cooling/heating balance in cluster cores.

Acknowledgments

Support for this work was provided by the National Aeronautics and Space Administration through Chandra Award Number GO4-15126X issued by the Chandra X-ray Observatory Center, which is operated by the Smithsonian Astrophysical Observatory for and on behalf of the National Aeronautics Space Administration under contract NAS8-03060. This work was supported in part by the US Department of Energy under contract number DE-AC02-76SF00515. The authors thank Georgiana Ogrean and John ZuHone for discussions, and Evan Million and Steven Ehlert for their help with the observing proposal.

Chapter 8

The nature of filamentary cold gas in the core of the Virgo Cluster

N. Werner[1], *J. B. R. Oonk*[2], *R. E. A. Canning*[1], *S. W. Allen*[1,3], *A. Simionescu*[1], *J. Kos*[2,4], *R. J. van Weeren*[5], *A. C. Edge*[6], *A. C. Fabian*[7], *A. von der Linden*[1], *P. E. J. Nulsen*[5], *C. S. Reynolds*[8], *M. Ruszkowski*[9,10]

[1]Kavli Institute for Particle Astrophysics and Cosmology, Stanford University, 452 Lomita Mall, Stanford, CA 94305-4085, USA
[2]ASTRON, Netherlands Institute for Radio Astronomy, P.O. Box 2, 7990 AA Dwingeloo, The Netherlands
[3]SLAC National Accelerator Laboratory, 2575 Sand Hill Road, Menlo Park, CA 94025, USA
[4]Faculty of Mathematics and Physics, University of Ljubljana, Jadranska 19, 1000 Ljubljana, Slovenia
[5]Harvard-Smithsonian Center for Astrophysics, 60 Garden Street, Cambridge, MA 02138, USA
[6]Institute for Computational Cosmology, Department of Physics, Durham University, Durham, DH1 3LE, UK
[7]Institute of Astronomy, Madingley Road, Cambridge CB3 0HA, UK
[8]Department of Astronomy and the Maryland Astronomy Center for Theory and Computation, University of Maryland, College Park, MD 20742, USA
[9]Department of Astronomy, University of Michigan, 500 Church Street, Ann Arbor, MI 48109, USA
[10]Michigan Center for Theoretical Physics, 3444 Randall Lab, 450 Church St, Ann Arbor, MI 48109, USA

Published in the Astrophysical Journal, volume 767, pages 153–162, 2013

Abstract

We present a multi-wavelength study of the emission-line nebulae located ∼38 arcsec (3 kpc in projection) southeast of the nucleus of M 87, the central dominant galaxy of the Virgo Cluster. We report the detection of far-infrared (FIR) [C II] line emission at 158 μm from the nebulae using observations made with the *Herschel* Photodetector Array Camera & Spectrometer (PACS). The infrared line emission is extended and cospatial with optical Hα+ [N II], far-ultraviolet C IV lines, and soft X-ray emission. The filamentary nebulae evidently contain multi-phase material spanning a temperature range of at least 5 orders of magnitude, from $\sim$ 100 K to $\sim 10^7$ K. This material has most likely been uplifted by the Active Galactic Nucleus from the center of M 87. The thermal pressure of the 10^4 K phase appears to be significantly lower than that of the surrounding hot intra-cluster medium (ICM) indicating the presence of additional turbulent and magnetic pressure in the filaments. If the turbulence in the filaments is subsonic then the magnetic field strength required to balance the pressure of the surrounding ICM is $B \sim 30 - 70$ μG. The spectral properties of the soft X-ray emission from the filaments indicate that it is due to thermal plasma with $kT \sim 0.5$–1 keV, which is cooling by mixing with the cold gas and/or radiatively. Charge exchange can be ruled out as a significant source of soft X-rays. Both cooling and mixing scenarios predict gas with a range of temperatures. This is at first glance inconsistent with the apparent lack of X-ray emitting gas with $kT < 0.5$ keV. However, we show that the missing very soft X-ray emission could be absorbed by the cold gas in the filaments with an integrated hydrogen column density of $N_{\rm H} \sim 1.6 \times 10^{21}$ cm^{-2}, providing a natural explanation for the apparent temperature floor to the X-ray emission at $kT \sim 0.5$ keV. The FIR through ultra-violet line emission is most likely primarily powered by the ICM particles penetrating the cold gas following a shearing induced mixing process. An additional source of energy may, in principle, be provided by X-ray photoionization from cooling X-ray emitting plasma. The relatively small line ratio of [O I]/[C II]$<$ 7.2 indicates a large optical depth in the FIR lines. The large optical depth in the FIR lines and the intrinsic absorption inferred from the X-ray and optical data imply significant reservoirs of cold atomic and molecular gas distributed in filaments with small volume filling fraction, but large area covering factor.

8.1 Introduction

Massive giant elliptical galaxies in the centers of clusters with central cooling times shorter than the Hubble time frequently display spectacular optical emission-line nebulae (e.g. Johnstone et al. 1987; Heckman et al. 1989; Donahue et al. 1992; Crawford et al. 1999; McDonald et al. 2010). Associated cold molecular gas has also been detected in many of these systems, from near-infrared (NIR) K-band H_2 line emission (e.g. Jaffe & Bremer 1997; Falcke et al. 1998; Donahue et al. 2000; Hatch et al. 2005; Jaffe et al. 2005; Johnstone et al. 2007; Oonk et al. 2010) and CO observations (e.g. Edge 2001; Edge & Frayer 2003; Salomé & Combes 2003; McDonald et al. 2012). While the NIR spectra show H_2 line ratios characteristic of collisionally excited 1000–2000 K molecular gas,

Table 8.1: Summary of observations and of the properties of the FIR lines integrated over the full 5×5 spaxel (47″×47″) field of view of *Herschel* PACS.

Line	Wavlegth (μm)	Exposure (s)	Flux (10^{-14} erg s^{-1} cm^{-2})	Inst. FWHM (km s^{-1})	Obs. FWHM (km s^{-1})	Shift (km s^{-1})
C II	157.7	3000	5.13 ± 0.5	240	361 ± 27	-62 ± 11
O I	63.2	3312	< 36.7[1]	85	...	...
O IB	145.5	4480	< 2.9[a]	255	...	...

the CO emission traces the coldest (<50 K) molecular gas phases. Optical Hα+[N II] line emission arises from a thin ionized skin of 10^4 K gas on underlying reservoirs of cold neutral and molecular gas. CO observations indicate that the amounts of molecular gas in cluster cores can be large (Edge 2001), e.g. the cold gas mass in the center of the Perseus Cluster is approaching 10^{11} $M_\odot$ (Salomé et al. 2006, 2008, 2011). The observed level of star formation in these systems is, however, typically relatively small (e.g. O'Dea et al. 2008). Despite significant efforts to understand the origin and the excitation mechanism of these nebulae, their nature, energy source, and detailed physics remain poorly understood.

The relatively nearby (d ∼16.7 Mpc, Blakeslee et al. 2009) giant elliptical galaxy M 87 (NGC 4486), at the centre of the Virgo Cluster, harbors a well-known extended optical Hα+[N II] filament system (Ford & Butcher 1979; Sparks et al. 1993). The proximity of this system allows us to study the physics of the emission-line nebulae in greater detail than is possible elsewhere. The Hα+[N II] nebulae in M 87 were found to spatially coincide with filamentary soft X-ray emission (Young et al. 2002; Sparks et al. 2004), which can be modeled as ∼0.5 keV plasma in collisional ionization equilibrium (Werner et al. 2010). The emission-line nebulae also spatially coincide with C IV line emission at far-ultraviolet wavelengths (FUV), which typically arises in gas at temperature $\sim 10^5$ K (Sparks et al. 2009, 2012). C IV line emission has so far not been detected in extended filaments in any other central cluster galaxy. Werner et al. (2010) showed that all of the bright Hα and UV filaments in M 87 are found in the downstream region of a <3 Myr old shock front revealed by X-ray observations with *Chandra* (Million et al. 2010d). This argues that the generation of Hα, UV, and soft X-ray emission in M 87 is coupled to shocks in the hot X-ray emitting plasma. Based on these observations Werner et al. (2010) proposed that shocks induce shearing around the cooler, denser gas filaments, which promotes mixing with the ambient hot intra-cluster medium (ICM) via instabilities. By enhancing the rate at which hot thermal particles come into contact with the colder gas phases, mixing can in principle supply the power and the ionizing particles needed to explain the NIR to FUV line emission (Ferland et al. 2008, 2009; Fabian et al. 2011).

The launch of the *Herschel* space observatory, with its unprecedented sensitivity to far-infrared (FIR) line emission (Pilbratt et al. 2010), has opened new opportunities to study the coldest gas phases in galaxies. *Herschel* has enabled the first detections of atomic cooling lines of [C II], [O I], and [N II] in the X-ray bright cores of Abell 1068,

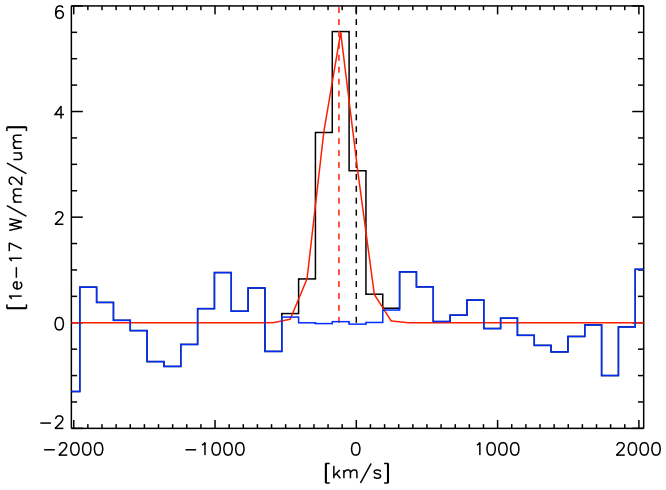

Figure 8.1: The FIR [C II]λ157 μm line obtained from the central spaxel (9.4 $\times$ 9.4 arcsec^2) of the *Herschel* PACS rebinned data cube. The mean line centroid is blue-shifted with respect to M 87 (at $z = 0.004360$) by $v = -123 \pm 5$ km s^{-1}. The blue line indicates the detector noise.

Abell 2597 (Edge et al. 2010), and the Centaurus and Perseus clusters (Mittal et al. 2011, 2012). These lines are the dominant cooling lines for neutral interstellar gas and can be used as diagnostics to infer temperatures, densities, and radiation fields (e.g. Kaufman et al. 1999). Because carbon is the fourth most abundant element in the Universe and has a low ionization potential, the 158 μm [C II] line is the most ubiquitous and best-studied (e.g. Malhotra et al. 1997, 2001). It is a tracer of gas with a temperature of $\sim$ 100 K.

To study the cold gas phases associated with the filamentary line emission nebulae in M 87 we observed the regions of brightest Hα+[N II] filaments, extending to the southeast of the nucleus of the galaxy, with the *Herschel* Photodetector Array Camera & Spectrometer (PACS) at the wavelengths of [C II]λ157μm, [O I]λ63μm and [O IB]λ145μm. Here we report the results of these observations, as well as a reanalysis of deep *Chandra* X-ray, *Hubble Space Telescope (HST)* optical and UV data, and long slit spectra obtained with the William Herschel Telescope (WHT). Sect. 9.2 describes the observations, data reduction, and analysis of the *Herschel* PACS, *HST*, *Chandra*, and WHT data. In Sect. 9.3, we summarize the results, and in Sect. 9.4 discuss the implications of our observations for the nature and the energy sources of the filaments. Our main conclusions are summarized in Sect. 9.5. We assume a distance to M 87 of 16.7 Mpc (Blakeslee et al. 2009), which implies a linear scale of 81 pc arcsec^{-1}. The redshift of M 87 is $z = 0.004360$.

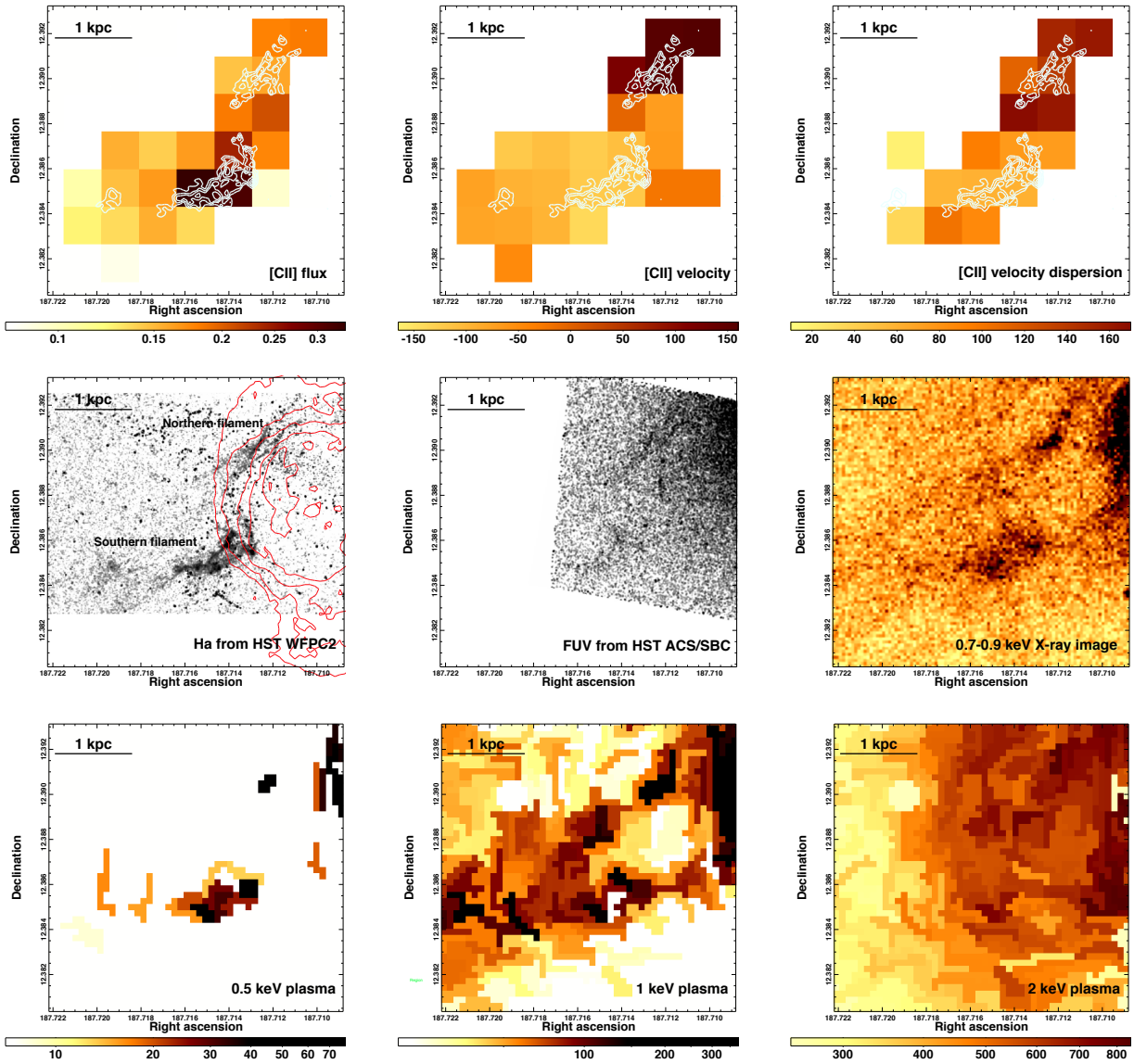

Figure 8.2: FIR [C II] maps (top panels; we only show spatial bins where the signal-to-noise ratio of the integrated [C II] flux is greater than 2) and Hα+[N II], FUV, and X-ray images of the filamentary multiphase gas southeast of the nucleus of M 87. All images show the same 47 $\times$ 47 arcsec region of the sky. The projected distance of the bright filaments from the nucleus is 38 arcsec (3 kpc). *Top left panel:* Map of the integrated [C II] line flux in units of 10^{-14} erg s^{-1} cm^{-2} per 6″$\times$6″spaxel obtained with *Herschel* PACS. *Top central panel:* The velocity distribution of the [C II] emitting gas, in units of km s^{-1}, relative to the systemic velocity of M 87, $v = 1307$ km s^{-1}. *Top right panel:* Map of the velocity dispersion, σ, of the [C II] emitting gas. *Middle row left panel:* Hα+[N II] image obtained with *HST* WFPC2. The contours of these filaments are over-plotted on the *Herschel* PACS maps in the top row. On this *HST* WFPC2 image, contours of 6 cm radio emission from Hines et al. (1989) are over-plotted in red. *Middle row central panel:* FUV image showing C IV line emission obtained with *HST* ACS/SBC. *Middle row right panel: Chandra* soft X-ray image, extracted in the 0.7–0.9 keV band. *Bottom panels:* Spatial distribution of the emission measure, $Y = \int n_{\rm H} n_{\rm e} {\rm d}V$, (in 10^{58} cm^{-3} arcsec^{-2}) of the 0.5 keV *(bottom left)*, 1.0 keV *(bottom central)*, 2.0 keV *(bottom right)* plasma detected at 99.7 per cent confidence.

8.2 Observations and data analysis

8.2.1 Far Infrared spectroscopy with *Herschel* PACS

We observed the FIR cooling lines of [C II]λ157μm, [O I]λ63μm, and [O IB]λ145μm with the PACS integral-field spectrometer (Poglitsch et al. 2010) on the *Herschel* space observatory (Pilbratt et al. 2010). The observations, with a duration of 10880 seconds, were performed on January 4th, 2012 (Obs. ID: 1342236278). Table 9.2 gives a summary of the observations. Columns list the observed lines, their rest frame wavelengths, observation durations, the observed line fluxes and the 2σ upper limits, the spectral resolution full-width-at-half-maximum (FWHM) of the instrument at the given wavelength, the observed FWHM, and the observed line shift with respect to the systemic velocity of M 87 ($v = 1307$ km s^{-1}).

The observations were taken in line spectroscopy mode with chopping-nodding to remove the telescope background, sky background and dark current. A chopper throw of $6'$ was used. All three line observations were taken in pointed mode centered on (α, δ)=(12:30:51.5, +12:23:07) (J2000).

The observations were reduced using the `HIPE` software version 8.2.0, using the PACS `ChopNodLineScan` pipeline script for pointed observations. This script processes the data from level 0 (raw channel data) to level 2 (flux calibrated spectral cubes).

During the final stage of reduction the data were spectrally and spatially rebinned into a $5\times5\times\lambda$ cube. In the following we will refer to this cube as the re-binned cube. Each spatial pixel, termed *spaxel*, in this cube has a size of $9.4''\times9.4''$. The cube thus provides us with a field of view (FoV) of $47''\times47''$.

For the wavelength re-gridding we set the parameters *oversample* and *upsample* equal to 2 and 1 respectively. This means that one spectral bin corresponds to the native resolution of the PACS instrument (see the PACS Data Reduction Guide[2] for further information). Larger values for both these two parameters were investigated and did not change the results.

For the [C II] line we projected the re-binned cube onto the sky using the `specProject` task in HIPE and the `hrebin` task in `IDL`. In the following we will refer to this cube as the projected cube. Upon projecting the observed [C II] data from the telescope frame to the sky we have chosen a resolution of $6''$ in order to Nyquist sample the beam, the FWHM of which is $12''$ at the observed wavelength of the line. We only consider spatial bins where the signal-to-noise ratio of the integrated [C II] flux is greater than 2.

8.2.2 *HST* Hα+[N II] and FUV data

To study the detailed morphology of the filamentary emission-line nebulae, we have also analyzed Hα+[N II] images taken with the Wide Field Planetary Camera 2 (WFPC2) through the F658N filter for 2700 seconds (proposal ID: 5122). The central wavelength of the filter is at 6591 Å and its bandwidth is 29 Å. It transmits the Hα line at $\lambda = 6563$Å,

[2] http://herschel.esac.esa.int/twiki/pub/Public/PacsCalibrationWeb/PDRG_Spec_May12.pdf

with transmission $T = 0.80$, and two [N II] lines at $\lambda = 6584$Å, with $T = 0.20$ and at $\lambda = 6548$Å, with $T = 0.76$, at the systemic velocity of M 87 ($v = 1307$ km s^{-1}). We subtracted the emission of the underlying stellar population of the galaxy using a red continuum image taken with WFPC2 through the filter F814W (proposal ID: 5941).

A FUV image was obtained using the Advanced Camera for Surveys Solar Blind Channel (ACS/SBC) (proposal ID: 11861) through the filter F150LP (1630 seconds), which covers the C IV line at $\lambda = 1549$ Å (see Sparks et al. 2009).

8.2.3 *Chandra* X-ray data

Extensive *Chandra* X-ray observations of M 87 were made between July 2002 and November 2005 using the Advanced CCD Imaging Spectrometer (ACIS). The total net exposure time after cleaning is 574 ks. The data reduction is described in Million et al. (2010d). We extracted six background subtracted, flat-fielded, narrow band images between 0.3 keV and 2.0 keV with a 0.492×0.492 arcsec^2 pixel scale (raw detector pixels). To measure the detailed properties of the soft X-ray emission, we also extracted spectra from regions determined using the Contour Binning algorithm (Sanders 2006), as described in Werner et al. (2010). Spectral modeling has been performed with the `SPEX` package (Kaastra et al. 1996) in the 0.5–7.0 keV band.

8.2.4 Long slit optical spectra

Long slit spectroscopy was performed using the Intermediate dispersion Spectrograph and Imaging System (ISIS) at the 4.2 m William Herschel Telescope on the island of La Palma on February 10, 2011. The total on-source integration time was 3500 s, split into 7 exposures, for the blue and red arm simultaneously. The data were reduced using standard `IRAF` (Image Reduction and Analysis Facility) procedures. The CCD images were bias subtracted, flat fielded, wavelength calibrated, flux calibrated, and merged. Spectra were shifted into the heliocentric velocity frame. Cosmic rays were removed with the `CRNEBULA` subroutine, designed for diffuse objects. Blue and red arm images were treated separately during the whole analysis.

8.3 Results

8.3.1 Cold and warm gas phases

We detect the filamentary emission-line nebulae across all wavebands studied, from the FIR to the soft X-rays. Using *Herschel* PACS, we detect [C II]λ157μm line emission (see Fig. 8.1) and determine 2σ upper limits for the [O I]λ63μm and [O IB]λ145μm cooling lines. The properties of the FIR lines, spatially integrated over the 5×5 spaxel ($47'' \times 47''$) *Herschel* PACS field of view, are summarized in Table 9.2. The 2σ upper limits on the fluxes of the [O I]λ63μm and [O IB]λ145μm lines given in Table 9.2 were determined assuming that their velocity widths are equal to the FWHM of the [C II] line.

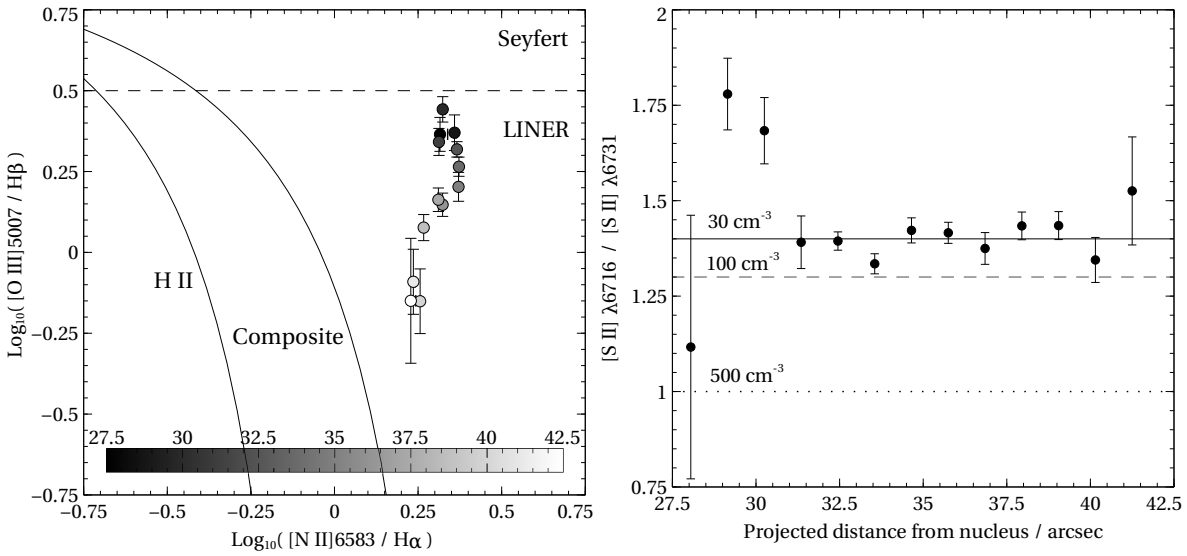

Figure 8.3: *Left panel:* Optical diagnostic diagram (a BPT diagram, Baldwin et al. 1981) showing the [O III]/Hβ against the [N II]/Hα flux observed in the southern filament at different radii from the nucleus. The brightening shades of gray indicate increasing projected distance from the nucleus in arcsec. While the side of the filament closest to the nucleus has spectra similar to Seyfert like AGN, at larger radii the gas has a LINER-like emission spectrum. The solid and dashed lines are from Kewley et al. (2006) and Osterbrock & Ferland (2006), respectively. *Right panel:* The measured [S II]λ6716/[S II]λ6731 line ratios, a good probe of gas density, as a function of radius. The full, dashed, and dotted lines indicate ratios corresponding to electron densities of $n_\mathrm{e} = 30$ cm^{-3}, $n_\mathrm{e} = 100$ cm^{-3}, and $n_\mathrm{e} = 500$ cm^{-3}, respectively (Osterbrock & Ferland 2006).

The [C II]λ157μm line emission is extended and spatially coincident with the Hα+[N II] filaments (see the top left panel of Fig. 8.2). We see two prominent filamentary structures, which we will call the 'southern filament' and the 'northern filament'. The brightest southern filamentary structure falls on the central spaxel of the PACS spectrometer. The [C II] flux detected from the central spaxel (9.4×9.4 arcsec^2) in the rebinned cube is $(8.5 \pm 0.7) \times 10^{-15}$ erg s^{-1} cm^{-2}. The top central panel of Fig. 8.2 shows a map of the velocity distribution of the [C II] line emitting gas with respect to the velocity of M 87. This image shows an interesting dichotomy, with the northern filaments receding at about +140 km s^{-1} and the bright southern filament (most of the emission of which falls on the central 9.4×9.4 arcsec^2 spaxel of the detector) moving in the opposite direction along our line of sight at -123 ± 5 km s^{-1}, with respect to M 87. These velocities show good agreement with the radial velocities of the corresponding optical filaments measured using long-slit spectroscopy (Sparks et al. 1993). The top right panel of Fig. 8.2 shows a map of the velocity dispersion of the [C II] line emitting material. While the northern, receding filaments show a significant velocity dispersion of $\sigma = \mathrm{FWHM}/2.355 \sim 124$ km s^{-1} (FWHM$= \sqrt{377^2 - 240^2} = 291$ km s^{-1}, corrected for the instrumental resolution FWHM of 240 km s^{-1}), the velocity dispersion measured in the southern filaments, $\sigma \sim 55$ km s^{-1} (FWHM$=\sqrt{273^2 - 240^2} = 130$ km s^{-1}), is just marginally above the instrumental resolution.

The middle row left panel of Fig. 8.2 shows the Hα+[N II] image obtained with *HST* WFPC2. Contours of 6 cm radio emission from Hines et al. (1989) are over-plotted, showing that in projection the side of the southern filament closest to the nucleus overlaps with the radio lobes. The narrowest resolved filaments of Hα+[N II] emission have a diameter of only 0.4 arcsec, which corresponds to 32 pc. The total count rate measured in our narrow band image from the bright southern filamentary structure within a $15.7'' \times 5.7''$ box-like region centered at (α, δ)=(12:30:51.48,+12:23:07.33) is 6.94 counts s^{-1}. Assuming an [N II]λ6548/Hα flux ratio of 0.81 and [N II]λ6584/Hα=2.45 (Ford & Butcher 1979) and taking into account the filter throughput at the wavelengths of the lines (see Sect. 8.2.2), the Hα flux of the southern filament is $f_{\mathrm{Hff}} = 9.0 \times 10^{-15}$ erg s^{-1} cm^{-2}.

Sparks et al. (2009) reported that the Hα+[N II] emission-line nebulae are co-spatial with FUV emission (see the middle row central panel of Fig. 8.2). Using subsequent spectroscopic measurements with the *HST* Cosmic Origin Spectrograph, Sparks et al. (2012) showed that the FUV emission in the northern filaments is due to C IV line emission. We find that the C IV flux, measured within the same aperture as the Hα+[N II] flux above, is $f_{\mathrm{CIV}} = 1.2 \times 10^{-14}$ erg s^{-1} cm^{-2}.

The optical spectral properties of the southern filament show an intriguing rapid decrease in the [O III]/Hβ ratio with increasing distance from the nucleus, dropping monotonically from $\sim$2.5 at a projected distance of 28 arcsec to $\sim$0.7 at 43 arcsec (see Fig. 8.3). The diagram in the left panel of Fig. 8.3, showing the [O III]/Hβ over the [N II]/Hα ratios (a BPT diagram, Baldwin et al. 1981), indicates that the side of the filament closest to the nucleus, which also overlaps with the radio lobes (see middle row left panel of Fig. 8.2), has spectra similar to Seyfert like active galactic nuclei (AGN). The [O III]/Hβ line ratios in this part of the filament are larger than in the nucleus of

M 87, where we measure a ratio of $\sim$ 1.75. At larger radii, the gas has a LINER[3]-like emission spectrum, which is more similar to the emission line spectra typically seen in extended filaments around brightest cluster galaxies in cluster cores.

The right hand panel of Fig. 8.3 shows the measured [S II]λ6716/[S II]λ6731 line ratio, a good probe of gas density, as a function of radius. The full, dashed, and dotted lines indicate ratios corresponding to electron densities of $n_{\rm e} = 30$ cm^{-3}, $n_{\rm e} = 100$ cm^{-3}, and $n_{\rm e} = 500$ cm^{-3}, respectively (Osterbrock & Ferland 2006). The value $n_{\rm e} = 30$ cm^{-3} is very close to the low density limit, below which the [S II] line ratios do not provide useful constraints on gas density. Along most of the filament, the line ratios are close to this limit indicating that the electron density of the 10^4 K phase is $n_{\rm e} \lesssim 30$ cm $^{-3}$. At radii between 29–30.5 arcsec, the measured line ratios are outside of the low density limit. The data point closest to the nucleus, at 28 arcsec, indicates a possible increase in density, but with large error bars.

8.3.2 The soft X-ray emission

Young et al. (2002) and Sparks et al. (2004) found good spatial correlation between Hα+[N II] line emission and soft X-ray emission. Here, we have analyzed almost four times as much *Chandra* data, which provides excellent photon statistics in the regions of interest. We extracted six narrow band images between 0.3 keV and 2.0 keV and found that the filaments stand out clearly in the 0.7-0.9 keV band (see the middle row right panel of Fig. 8.2). The spatial correlation between the 0.7–0.9 keV X-rays and the Hα+[N II] line emission is remarkable: everywhere, where we see Hα+[N II] emitting gas, we also see an excess of soft X-rays. On the other hand, in the 0.5–0.7 keV and 0.9–1.2 keV bands the filaments do not stand out clearly against the surrounding emission, indicating that most of their X-ray emission comes from the Fe XVII and Fe XVIII lines in the 0.7–0.9 keV band. The excess X-ray flux of the filaments in this band is 1.1×10^{-14} ergs s^{-1} cm^{-2} and their average X-ray surface brightness is 1.2×10^{-16} ergs s^{-1} cm^{-2} arcsec^{-2}.

Assuming that the soft X-ray emission is of a thermal origin, we follow the analysis of Werner et al. (2010) and fit to each spatial bin a model consisting of collisionally ionized equilibrium plasmas at three fixed temperatures (0.5 keV, 1.0 keV, and 2.0 keV), with variable normalizations and common metallicity. The bottom panels of Fig. 8.2 show the spatial distributions of the emission measures of the individual temperature components. The 0.5 keV component closely follows the distribution of the cold gas phases. This component is required to fit the Fe XVII and Fe XVIII lines in the 0.7–0.9 keV band, which are only present in regions where Hα+[N II] emission has also been detected. The spatial correlation between Hα+[N II] and the softest X-ray emitting component is, however, not perfect: the ratio of Hα+[N II] flux to the $\sim$0.5 keV emission component is $\sim$ 5 times larger in the southern than in the northern filament. The 1 keV component is enhanced as well in the regions where cold gas is present, but it is spatially more extended and is also seen in many regions where cold gas is not detected (see Werner et al. 2010). The spatial distribution of the 2 keV plasma does not

[3]Low-ionization nuclear emission-line region (Heckman 1980)

correlate with the Hα+[N II] emission.

Because the soft X-ray line emission observed in the filaments may be due to cooling gas, we fitted the spectra with a model consisting of a single-temperature plasma in collisional ionization equilibrium plus an isobaric cooling flow, which models cooling between two temperatures at a certain metallicity and mass deposition rate. The upper temperature and the metallicity of the cooling flow component were tied to the temperature and metal abundance of the single-temperature plasma. Both components were absorbed by a Galactic absorption column density $N_{\rm H} = 1.9 \times 10^{20}$ cm^{-2} (Kalberla et al. 2005). Fixing the lower temperature cut-off of the cooling flow model to $kT_{\rm low} = 0.5$ keV, we obtained a best fit upper temperature of $kT_{\rm up} = 1.90 \pm 0.04$ keV, a mass deposition rate of $\dot{M} = (2.46 \pm 0.13) \times 10^{-2}\ M_{\odot}$ yr^{-1}, and a metallicity of $Z = 1.46 \pm 0.09$ Solar (relative to the Solar values by Grevesse & Sauval 1998). Even though the spectra indicate that above $kT \sim 0.5$ keV the gas may be cooling, the spectral signatures of gas cooling below 0.5 keV - soft X-ray emission, including the O VII line - are missing (see also the high resolution spectra in Werner et al. 2006, 2010).

In order to test whether the missing soft X-ray flux might have been absorbed by the cold gas in the filaments, we fixed the mass deposition rate in the model to the best fit value obtained with a lower temperature cut-off set to 0.5 keV, extended this cut-off down to a 1000 times lower temperature of 0.5 eV (the lowest value allowed by the model). Furthermore, we assumed that the cooling X-ray plasma is intermixed with the cold gas and the cooling happens in 13 different regions along our line-of-sight separated from each other by intrinsic cold absorbers (the emission from the first cooling region is affected by one absorber, from the second by two absorbers, from the third by three etc.). The different cooling regions are assumed to have the same cooling rate and the different absorbers are assumed to have the same hydrogen column density. Fitting this model to the data, we find an integrated intrinsic hydrogen column density of $N_{\rm H} = (1.58 \pm 0.21) \times 10^{21}$ cm^{-2} and an absorbed bolometric flux of 3.9×10^{-14} erg s^{-1} cm^{-2}.

8.4 Discussion

8.4.1 Magnetized filaments of multi-phase material

In the filamentary emission-line nebulae to the southeast of the nucleus of M 87, we detect gas spanning a temperature range of at least 5 orders of magnitude, from $\sim$ 100 K to $\sim 10^7$ K. The [C II], Hα+[N II], and C IV emitting gas phases are consistent with being co-spatial, forming a multi-phase medium. Soft X-ray emission in the 0.7–0.9 keV band is also always present in regions where Hα+ [N II] emission is seen. Its spectral shape is consistent with line emission of $\sim$0.5 keV thermal plasma, previously detected in the *XMM-Newton* high resolution reflection grating spectra integrated over the central region of M 87 (Werner et al. 2006, 2010). We see no evidence of X-ray emitting gas with temperature $kT < 0.5$ keV.

The [C II] 158 μm line is about 1500 times stronger than the CO (1$\rightarrow$0) rotational line in normal galaxies and Galactic molecular clouds, and 6300 times more intense in

starburst galaxies and Galactic star forming regions (Crawford et al. 1985; Stacey et al. 1991). Given a [C II] flux of 8.5×10^{-15} erg s^{-1} cm^{-2} observed from the brightest region of the southern filament, the expected CO (1→0) flux is 1.3–5.3 $\times 10^{-18}$ erg s^{-1} cm^{-2}, consistent with the upper limit of 2×10^{-17} erg s^{-1} cm^{-2} for CO (1→0) at 2.6 mm observed in the same region (Salomé & Combes 2008). Using the standard CO luminosity to H_2 conversion factors the inferred range of CO luminosities corresponds to an H_2 mass of 0.4–2 $\times 10^6$ $M_\odot$. However, because the [C II]/CO line ratios in these filaments may be different from those in star-forming galaxies and their heating mechanism may be different from that in more normal molecular clouds, their true molecular mass may be outside of this range.

Assuming that all the observed gas phases are in thermal pressure equilibrium with the ambient ICM (assuming $p = 0.11 - 0.22$ keV cm^{-3}, for a distance range of $r = 3 - 6$ kpc from the nucleus depending on the position of the filament along our line of sight, Churazov et al. 2008), the $\sim$ 100 K [C II] emitting gas forms a network of narrow filaments with densities of the order of $(1.3 - 2.6) \times 10^4$ cm^{-3} (higher than the critical density of 3×10^3 cm^{-3} above which the gas is in local thermal equilibrium with the level populations determined by collisions) with volume filling fraction of $f_V \sim (1 - 2) \times 10^{-4}$ in the bright southern filament. Although the presence of O I 6300 Å lines in the optical spectra (see also Ford & Butcher 1979) indicates the existence of large partially ionized regions in the filaments, the presence of [S II] lines most probably indicates a fully ionized $\sim 10^4$ K phase surrounding the colder gas. The density of this Hα+[N II] emitting gas, assuming thermal pressure equilibrium with the ambient ICM, should be $\sim (1.3 - 2.6) \times 10^2$ cm^{-3}.

The [S II]λ6716/[S II]λ6731 line ratios, however, indicate much lower particle densities in the 10^4 K phase ($n \sim 2n_e \lesssim 60$ cm^{-3}) implying the presence of additional significant non-thermal pressure components in the filaments, such as turbulence and magnetic fields. Assuming isotropic micro-turbulence with a characteristic velocity v_{turb} in a medium with a sound speed c_s, the turbulent pressure support will be $p_{turb} = 1/2\,\gamma\,p_{therm}\,M^2$, where γ is the adiabatic index assumed to be 5/3 and $M = v_{turb}/c_s$ is the Mach number. However, assuming characteristic turbulent velocities of the order of the sound speed in the 10^4 K phase ($c_s = 15$ km s^{-1}), the sum of thermal and turbulent pressure, $p_{turb} + p_{therm} = 0.09$ keV cm^{-3} (1.4×10^{-10} dyne cm^{-2}), is still smaller than the surrounding ICM pressure. If the turbulence in the Hα emitting phase is subsonic, then the additional pressure will be provided by magnetic fields. A magnetic pressure of $p_{mag} = B^2/8\pi \sim (0.3 - 2.1) \times 10^{-10}$ dyne cm^{-2}, needed to keep the filaments in pressure equilibrium with the surrounding ICM, requires magnetic fields of $B = 28 - 73$ μG. This is similar to the values inferred using arguments based on the integrity of Hα+[N II] filaments in the Perseus Cluster (Fabian et al. 2008). Radio observations of the Faraday rotation measure in a number of cooling cores revealed magnetic field strengths of 10–25 μG (Taylor et al. 2001, 2007; Allen et al. 2001; Feretti et al. 1999). Significant imbalance in thermal pressure of the gaseous filaments in cool-core clusters has previously also been inferred between the warm molecular hydrogen gas seen in NIR ($nT \sim 10^{8-9}$ cm $^{-3}$ K) and the ionized gas phases seen in the optical ($nT \sim 10^5$ cm^{-3} K), emphasizing the need for dynamic models for the filaments (Jaffe et al. 2001; Oonk et al. 2010).

The smallest resolved diameter of the Hα+[N II] filaments is 32 pc, about half of the 70 pc diameter observed in the more distant Perseus Cluster (Fabian et al. 2008). However, even the narrowest resolved filaments are likely to consist of many smaller strands. They are surrounded by hotter 10^5 K C IV emitting gas. The space between these filaments is filled by X-ray emitting gas. If the soft X-ray line emission is due to $\sim$0.5 keV gas, then based on our three-temperature fits (see Sect. 9.3) and assuming thermal pressure equilibrium with the ambient ICM, its mass in the southern filament is $\sim 10^5\ M_\odot$ and its emitting volume is $\sim$0.016 kpc^3.

8.4.2 The energy source of the filaments

Sparks et al. (2009) show that no main sequence stars of early spectral type are present in the filaments and therefore neither the FUV nor the Hα+[N II] emission can be due to photoionization by hot UV emitting stars. The [O III]/Hβ emission line ratios are high on the side of the southern filament closest to the nucleus, which also overlaps with the radio lobes (see middle row left panel of Fig. 8.2), and then decrease rapidly with increasing distance from the nucleus. The fact that the line ratios in the filament reach values which are higher than those measured in the nucleus argues against photoionization by the AGN. It seems more likely that the increased [O III]/Hβ ratios are due to internal shocks produced as the radio lobes push against the cold gas. These shocks seem to affect only a part of the filament and the emitted Hα flux does not decrease with the decreasing [O III]/Hβ emission line ratios. Therefore, they can be ruled out as energy source powering the emission of these nebulae.

Ferland et al. (2009) showed that the broad band (optical to mm) emission-line spectra of nebulae around central galaxies of cooling core clusters most likely originate in gas exposed to ionizing particles. Such ionizing particles can be either relativistic cosmic rays or hot particles penetrating into the cold gas from the surrounding ICM. Saturated conduction from the hot into the cold phase of the southern filament would produce a heat flux of $5\phi p c_\mathrm{s} \sim 0.1$ erg s^{-1} cm^{-2}, where $\phi \sim 1$ accounts for the uncertain physics, $p = 0.22$ keV cm $^{-3}$ is the gas pressure and $c_\mathrm{s} = 510$ km s^{-1} is the sound speed in the hot 1 keV phase (Cowie & McKee 1977; Fabian et al. 2011). Following the argument of Fabian et al. (2011), given a typical Hα surface brightness of $\sim 2 \times 10^{-16}$ erg s^{-1} cm^{-2} arcsec^{-2}, corresponding to an emitted flux of 1.1×10^{-4} erg s^{-1} cm^{-2} and assuming that the total broad band emitted flux is 20 times larger 2.2×10^{-3} erg s $^{-1}$ cm^{-2}, the required efficiency with which impinging thermal particles penetrate and excite the cold gas is of the order of $f = 0.022$ ($f = 0.044$ for a filament at $r = 6$ kpc from the nucleus), which is reasonable. However, these particles must somehow overcome the obstacle presented by the magnetic fields believed to be at the interface of the cold and hot gas phases.

Werner et al. (2010) show that all of the bright Hα+[N II] and UV filaments are seen in the downstream region of a < 3 Myr old AGN induced $M \gtrsim 1.2$ shock front (Million et al. 2010d) that seems to have just passed the filaments. Based on these observations they propose that shocks induce shearing around the cold, filamentary, dense gas, thereby promoting mixing of the cold gas with the ambient hot ICM via instabilities (e.g. Friedman et al. 2012). Instabilities and turbulence may also be driven by shear-

ing motions between the hotter X-ray gas and the filaments, as they move through the ambient ICM, both as they are being uplifted and as they fall back. This type of more continuous shear induced mixing could perhaps be in the long term more important for energizing the filaments than shocks. Fabian et al. (2011) propose that the sub-mm through UV emission seen in NGC 1275 in the core of the Perseus Cluster is due to the hot ICM efficiently penetrating the cold gas through reconnection diffusion (Lazarian et al. 2010, 2011). The same process may also be operating in the filaments of M 87 with the fast reconnection induced by shearing instabilities and turbulence. Shearing and magnetic reconnection are, however, not essential to bring the cold gas into contact with the hot ICM. The support from magnetic fields tied to the surrounding ionized phase may become unstable if the layer of dense cold neutral gas is deep enough, and therefore it may fall through into direct contact with the hot gas. The hot ICM particles penetrating the cold gas then produce secondary electrons that excite the observed FIR through UV emission as shown by Ferland et al. (2009). Mixing of the cold and hot gas also naturally account for the presence of the $\sim 10^5$ K intermediate-temperature gas phase (geometric mean of the hot and cold gas temperatures) predicted by the mixing layers calculated by Begelman & Fabian (1990), although mixing layers have most probably a more complicated temperature structure (Esquivel et al. 2006). As the X-ray emitting gas cools through mixing, the mass of the southern filament may grow by as much as $4 \times 10^{-2}\ M_\odot\ \mathrm{yr}^{-1}$.

The particle heating model of Ferland et al. (2009), calculated considering optically thin emission from a cell of gas, predicts [O I]/[C II] $\sim$ 21 and is inconsistent with the 2σ upper limit of 7.2 observed in M 87. The ratios observed in the Perseus and Centaurus clusters, and in Abell 1068 and 2597 are even lower. This discrepancy has been discussed in a recent study of NGC 1275 by Mittal et al. (2012), who conclude that the line ratio suggests that the lines are optically thick, implying a large reservoir of cold atomic gas, which was not accounted for in previous inventories of the filament mass. The same can be concluded for M 87, where the large optical depth of the FIR lines (Canning et al. in prep.) and the intrinsic absorption inferred from the X-ray data (see below) imply significant reservoirs of cold atomic and molecular gas.

8.4.3 X-ray line emission from cold gas due to charge exchange and inner shell ionization?

As ions from the hot ICM penetrate into the filaments, they pick up one or more electrons from the cold gas. The impinging ions thus get into excited states and their deexcitation may produce X-ray radiation. Astrophysical X-ray emission due to this 'charge exchange' process was first discovered in the comet Hyakutake (Lisse et al. 1996; Cravens 1997) and since then it has been identified as the mechanism responsible for X-rays from planets (e.g. Gladstone et al. 2002; Dennerl 2002), the geocorona (Wargelin et al. 2004; Fujimoto et al. 2007), the heliosphere (Robertson et al. 2001), and interstellar medium in particular at interfaces between hot gas and cool clouds (see the review by Dennerl 2010, and references therein). Recently, charge exchange has also been found to possibly contribute significantly to the soft X-ray line emission from

star-forming galaxies (Liu et al. 2011, 2012). Fabian et al. (2011) conclude that in the Perseus Cluster charge exchange may account for a few per cent of the soft X-ray emission from the filaments. They also speculate that if the filaments are composed of many small strands, the same ion might pass from the hot into the cold and back to the hot phase repeatedly, getting collisionally ionized while passing through the hot ICM, thus enhancing the charge exchange emission to the observed level.

After hydrogen and helium, the most abundant ions penetrating the cold gas are O^{8+}, C^{6+}, N^{7+}, Ne^{10+}, Mg^{12+}, Mg^{11+} (with concentrations 8.4×10^{-4}, 3.6×10^{-4}, 1.1×10^{-4}, 1.1×10^{-4}, 2.5×10^{-5}, 1.07×10^{-5} relative to hydrogen by number). Charge transfer onto these ions is expected to produce mainly hydrogen and helium like line emission in the X-ray band. In the 1 keV plasma surrounding the filaments, 23% of Fe is in the form of Fe^{20+}, another 23% in Fe^{21+}, 18% in Fe^{19+}, and 17% in Fe^{22+}, with relative concentrations smaller than 1.1×10^{-5}. The charge exchange line fluxes produced by Fe will therefore be significantly lower, with most of the line flux in Fe IXX to Fe XXII lines, in the spectral band above 0.9 keV. Moreover, laboratory measurements of X-ray spectral signatures of charge exchange in L- shell Fe ions by Beiersdorfer et al. (2008) found that the $n \geq 4 \rightarrow n = 2$ transitions are strongly enhanced relative to $n = 3 \rightarrow n = 2$, shifting the line emission to higher energies. Because charge transfer processes and the corresponding X-ray emission are expected to occur inside of the dense cold clouds, absorption may significantly decrease the observed fluxes of the lowest energy X-ray lines such as C VI, N VII, O VII, and O VIII. The Ne IX, Ne X, Mg XI, and Mg XII lines in the 0.9–1.9 keV band are, however, not expected to be affected by absorption strongly and their enhancement might indicate charge exchange. Given that none of these lines are enhanced in the filaments, and no strong charge exchange emission is expected in the 0.7–0.9 keV band, we conclude that the observed soft X-ray emission is not due to charge transfer onto the impinging ions.

The ions and electrons penetrating from the surrounding hot ICM into the cold filaments will also ionize the inner electron shells of the atoms and molecules in the cold clouds. This inner shell ionization may in principle also contribute to the X-ray emission of the filaments, but given the energetics, it is not expected to be significantly stronger than the X-ray emission due to charge exchange. We would primarily expect to see X-ray lines from few times ionized C, N, O, Ne, and Mg, with the Ne and Mg lines in the band above 0.6 keV. Detailed predictions of this process are beyond the scope of this paper.

Given that the spectral shape of the filaments is consistent with line emission of $\sim$0.5 keV thermal plasma previously resolved within the central region of M 87 with *XMM-Newton* RGS (Werner et al. 2006, 2010) and that charge exchange as a significant source of X-ray emission from the filaments can be ruled out, we conclude that the observed soft X-ray emission is most likely due to thermal plasma. We note, however, that although charge exchange is not responsible for the observed excess X-ray emission in the $0.7 - 0.9$ keV band, the level which is required from the particle heating model is observationally acceptable.

8.4.4 AGN uplift induced cooling instabilities or mixing?

The observed velocity distribution of the [C II] (see top central panel of Fig. 8.2) and optical emission lines (Sparks et al. 1993) indicates that the northern filaments are currently being uplifted by the counter-jet (which is oriented at $< 19^{\circ}$ from our line-of-sight, Biretta et al. 1999) moving away from M 87 with a line-of-sight velocity of $v_{\rm LOS} = +140$ km s^{-1}. The southern filaments, in contrast, are falling back towards M 87 with $v_{\rm LOS} = -123$ km s^{-1}. Assuming uplift at the Keplerian velocity of ~ 400 km s^{-1}, the southern filament would take 8×10^6 yr to get to its current position. Given that this filament is most likely already falling back, its age is $\gtrsim 10^7$ yr. Uplift of low entropy, metal enriched X-ray emitting gas by buoyantly rising relativistic plasma from the AGN jets of M 87 has been previously inferred based on radio and X-ray data (Churazov et al. 2001; Forman et al. 2005; Simionescu et al. 2008; Werner et al. 2010). Optical emission line nebulae also appear to have been drawn out by rising radio bubbles in other nearby systems (e.g. the Perseus and Centaurus clusters, Hatch et al. 2006; Canning et al. 2011).

The initially uplifted material might have already been a multi-phase mixture of low entropy X-ray emitting plasma and dusty cold gas, as is observed in the core of M 87 (Sparks et al. 1993). As the relatively dense, low entropy X-ray emitting plasma was removed from the direct vicinity of the AGN jets it might have cooled radiatively, further contributing to the cold gas mass of the uplifted material (see Revaz et al. 2008). The multi-phase X-ray emitting gas, with the 0.5 keV phase co-spatial with the Hα+[N II] filaments and surrounded by a spatially more extended 1 keV plasma, indicates that such cooling may be taking place. Cooling instabilities are predicted to take place in cooling core clusters within radii where the ratio of the cooling time to free fall time is $t_{\rm cool}/t_{\rm ff} \lesssim 10$ (Sharma et al. 2012a; McCourt et al. 2012; Gaspari et al. 2012, this condition is fulfilled at the radii where the M 87 filaments are seen). AGN induced uplift of multiphase gas may facilitate the onset of such local cooling instabilities. Some Hα+[N II] and soft X-ray filaments lie at the edges of cavities filled by radio emitting plasma, indicating that they might be sheets of gas seen in projection that have been swept up and compressed by the expanding and rising cavities. Even though such compression would first heat the gas, eventually it will accelerate its cooling. This picture of radiatively cooling X-ray gas is, however, complicated by the observed temperature floor at 0.5 keV. Several explanations were proposed to address the missing soft X-ray emission, including mixing (Fabian et al. 2002), anomalous O/Fe abundance ratios, and absorption (Sanders & Fabian 2011).

The mass deposition rate, inferred from the temperature distribution of the X-ray gas in the southern filament above $kT = 0.5$ keV, assuming an isobaric cooling flow model, is $\dot{M} = (2.46 \pm 0.13) \times 10^{-2}\ M_{\odot}$ yr^{-1}. This cooling rate could only be reconciled with the apparent lack of $kT < 0.5$ keV plasma if the cold gas in the filaments absorbs the soft X-rays, modifying the observed spectral shape in a way that results in an apparent temperature cut-off. The X-ray spectral lines providing the most diagnostic power at these temperatures are the Fe XVII and the O VII lines. The ionic fraction of Fe XVII is above 0.3 across a relatively large temperature range of 0.2–0.6 keV, but the O VII line becomes observable only at $kT < 0.4$ keV. Absorption is expected to strongly suppress

the O VII line emitted by the coldest gas phases. The Fe XVII lines will be affected by absorption to a much lesser extent. Therefore when modeling a spectrum that is affected by intrinsic absorption, we may conclude that the cooling stopped at the temperature where we expect to start to see the O VII line[4]. In Sect. 9.3, we show that the required integrated hydrogen column density, distributed in multiple layers (the cooling takes place between the threads) along our line-of-sight is $N_{\rm H} = (1.58 \pm 0.21) \times 10^{21}$ cm^{-2}. If the hot ICM indeed cools radiatively between the cold filaments, then the large area covering fraction of the many small strands may provide a sufficient absorption column to the cooling X-ray emitting plasma to explain the apparent temperature floor at $\sim$0.5 keV.

Soft X-ray photons from the cooling X-ray plasma absorbed by the cold gas would produce energetic photoelectrons which would contribute to the heating and ionization of the cold gas (in a process similar to the secondary electron production by cosmic rays or impinging hot ICM particles, Ferland et al. 2009). Photoionization of emission line nebulae by X-rays has been considered before (e.g. Heckman et al. 1989; Donahue & Voit 1991; Crawford & Fabian 1992; Jaffe & Bremer 1997) and has been found insufficient to ionize and power the observed line emission. However, when considering photoionization by primarily soft X-rays, from cooling plasma which surrounds the cold filamentary gas with a small volume filling fraction, the efficiency of this process increases significantly (Oonk 2011). According to our spectral modeling, where we assumed that all the soft X-ray emission is due to radiative isobaric cooling, intrinsic absorption reduces the observed flux by $\sim 3.9 \times 10^{-14}$ erg s^{-1} cm^{-2}. If the soft X-ray emitting plasma fills the space between the cold filaments and the cold gas absorbs approximately the same amount of energy in all directions, then the total X-ray energy absorbed by the cold gas is $\sim 1.3 \times 10^{39}$ erg s^{-1}. With a total emitted energy from UV to sub-mm about 20 times larger than the observed Hα luminosity of 3.0×10^{38} erg s^{-1}, X-ray photoionization may, in principle, contribute a significant fraction of the energy needed to power the filaments.

The cooling rates above were deduced under the assumption that all the soft X-ray line emitting gas originates from radiative cooling. The $kT \sim 0.5$ keV gas could, in principle, also be produced by mixing of the hot ICM with the cold filaments. More developed mixing might be responsible for the higher ratio of 0.5 keV thermal to Hα+[N II] line emission in the southern filament (which is most likely falling back towards M 87), with respect to the northern filament (which is likely younger, currently being uplifted). Such mixing is, however, not expected to result in a gas with $kT \sim 0.5$ keV - it would result in a mixing layer with a wide range of temperatures (Esquivel et al. 2006). Therefore, both in the cooling and in the mixing scenario for the origin of the soft X-ray emission from the filaments, the explanation of the 0.5 keV cutoff requires intrinsic absorption by cold gas.

The internal reddening in the optical band calculated from the observed line ratio of Hα/H$\beta = 4$ in the filament (Ford & Butcher 1979) is, $E(B-V) = 0.28$. Using the

[4]We note that only a small fraction of the observed X-ray emission originates in the filaments and is affected by intrinsic absorption. The dominant emission component from the ambient ICM remains unaffected by cold gas in the filaments, and therefore fitting the spectra with a Galactic absorption as a free parameter will not result in a significantly higher best fit $N_{\rm H}$.

Galactic transformation between reddening and column density of neutral hydrogen, $N_{\rm H}/E(B-V) = 5.8 \times 10^{21}$ cm^{-2} mag^{-1} (Bohlin et al. 1978), we infer an intrinsic neutral hydrogen column density of $N_{\rm H} = 1.6 \times 10^{21}$ cm^{-2} - sufficient to absorb the soft X-ray emission from gas with $kT < 0.5$ keV. We note that substantial reddening has been observed in a number of Hα nebulae in brightest cluster galaxies of cooling core clusters (e.g. Allen et al. 1995; Crawford et al. 1999).

A similar temperature floor at $\sim$0.5 keV is observed in the Perseus Cluster, Centaurus Cluster, 2A 0335+096, Abell 262, Abell 3581, HCG 62, and Abell 2052 (Sanders & Fabian 2007; Sanders et al. 2008, 2009, 2010a; de Plaa et al. 2010) and in the cooling uplifted multi-phase gas in the core of the galaxy cluster Sérsic 159-03 (Werner et al. 2011). The coolest $\sim$0.5 keV gas phases are co-spatial with filamentary optical emission-line nebulae in all of these systems. In the Perseus and Centaurus clusters, copious amounts of FIR line emission has also been discovered, indicating the presence of large reservoirs of cold atomic gas (Mittal et al. 2011, 2012). Following the arguments outlined above, the low temperature X-ray cutoffs observed in those systems may therefore also, at least partly, result from intrinsic absorption.

8.5 Conclusions

We performed a multi-wavelength study of the emission-line nebulae located southeast of the nucleus of M 87. Our main conclusions may be summarized as follows:

- We detect FIR [C II] line emission at 158 μm with *Herschel* PACS. The line emission is extended and co-spatial with optical Hα+[N II], FUV C IV lines, and soft X-ray emission.

- The filamentary nebulae contain multi-phase material spanning a temperature range of at least 5 orders of magnitude, from $\sim$ 100 K to $\sim 10^7$ K. This material has most likely been uplifted by the AGN from the center of M 87.

- The thermal pressure of the 10^4 K phase appears to be significantly lower than that of the surrounding hot ICM indicating the presence of additional turbulent and magnetic pressure in the filaments. If the turbulence in the filaments is subsonic then the magnetic field strength required to balance the pressure of the surrounding ICM is $B \sim 30 - 70$ μG.

- The spectral properties of the soft X-ray emission from the filaments indicate that it is due to thermal plasma with $kT \sim 0.5$–1 keV, which is cooling by mixing with the cold gas and/or radiatively. Charge exchange can be ruled out as a significant source of soft X-rays.

- Both cooling and mixing scenarios predict gas with a range of temperatures. This is at first glance inconsistent with the apparent lack of X-ray emitting gas with $kT < 0.5$. However, we show that the missing very soft X-ray emission could be absorbed by the cold gas in the filaments with an integrated hydrogen column density of $N_{\rm H} \sim 1.6 \times 10^{21}$ cm^{-2}, providing a natural explanation for the

apparent temperature floor to the X-ray emission at $kT \sim 0.5$ keV. The internal reddening observed in the optical band indicates a similar level of intrinsic absorption.

- The FIR through UV line emission is most likely primarily powered by the ICM particles penetrating the cold gas following a shearing induced mixing process. An additional source of energy may, in principle, be provided by X-ray photoionization from cooling X-ray emitting plasma.
- The relatively small line ratio of [O I]/[C II]< 7.2 indicates a large optical depth in the FIR lines. The large optical depth at FIR and the intrinsic absorption inferred from the X-ray and optical data all imply significant reservoirs of cold atomic and molecular gas distributed in filaments with small volume filling fraction, but large area covering factor.

Acknowledgments

This work is based in part on observations made with *Herschel*, a European Space Agency Cornerstone Mission with significant participation by NASA. Support for this work was provided by NASA through award number 1428053 issued by JPL/Caltech. Support for this work was provided by NASA through Einstein Postdoctoral grant numbers PF9-00070 (AS) and PF2-130104 (RvW) awarded by the Chandra X-ray Center, which is operated by the Smithsonian Astrophysical Observatory for NASA under contract NAS8-03060. SWA acknowledges support from the U.S. Department of Energy under contract number DE-AC02-76SF00515. MR acknowledges NSF grant AST 1008454.

Chapter 9

The origin of cold gas in giant elliptical galaxies and its role in fueling radio-mode AGN feedback

N. Werner[1,2], *J. B. R. Oonk*[3], *M. Sun*[4], *P. E. J. Nulsen*[5], *S. W. Allen*[1,2,6], *R. E. A. Canning*[1,2], *A. Simionescu*[7], *A. Hoffer*[8], *T. Connor*[8], *M. Donahue*[8], *A. C. Edge*[9], *A. C. Fabian*[10], *A. von der Linden*[1,2,11], *C. S. Reynolds*[12], *M. Ruszkowski*[13,14]

[1]Kavli Institute for Particle Astrophysics and Cosmology, Stanford University, 452 Lomita Mall, Stanford, CA 94305-4085, USA
[2]Department of Physics, Stanford University, 382 Via Pueblo Mall, Stanford, CA 94305-4060, USA
[3]ASTRON, Netherlands Institute for Radio Astronomy, P.O. Box 2, 7990 AA Dwingeloo, The Netherlands
[4]Department of Physics, University of Alabama in Huntsville, Huntsville, AL 35899, USA
[5]Harvard-Smithsonian Center for Astrophysics, 60 Garden Street, Cambridge, MA 02138, USA
[6]SLAC National Accelerator Laboratory, 2575 Sand Hill Road, Menlo Park, CA 94025, USA
[7]Institute of Space and Astronautical Science (ISAS), JAXA, 3-1-1 Yoshinodai, Chuo-ku, Sagamihara, Kanagawa, 252-5210 Japan
[8]Physics & Astronomy Department, Michigan State University, East Lansing, MI 48824-2320, USA
[9]Institute for Computational Cosmology, Department of Physics, Durham University, Durham, DH1 3LE, UK
[10]Institute of Astronomy, Madingley Road, Cambridge CB3 0HA, UK
[11]Dark Cosmology Centre, Niels Bohr Institute, University of Copenhagen, Juliane Maries Vej 30, DK-2100 Copenhagen, Denmark
[12]Department of Astronomy and the Maryland Astronomy Center for Theory and Computation, University of Maryland, College Park, MD 20742, USA
[13]Department of Astronomy, University of Michigan, 500 Church Street, Ann Arbor,

MI 48109, USA
[14]Michigan Center for Theoretical Physics, 3444 Randall Lab, 450 Church St, Ann Arbor, MI 48109, USA

Published in the Monthly Notices of the Royal Astronomical Society, volume 439, pages 2291–2306, 2014

Abstract

The nature and origin of the cold interstellar medium (ISM) in early type galaxies are still a matter of debate, and understanding the role of this component in galaxy evolution and in fueling the central supermassive black holes requires more observational constraints. Here, we present a multi-wavelength study of the ISM in eight nearby, X-ray and optically bright, giant elliptical galaxies, all central dominant members of relatively low mass groups. Using far-infrared spectral imaging with the *Herschel* Photodetector Array Camera & Spectrometer (PACS), we map the emission of cold gas in the cooling lines of [C II]λ157μm, [O I]λ63μm, and [O Ib]λ145μm. Additionally, we present Hα+[N II] imaging of warm ionized gas with the Southern Astrophysical Research (SOAR) telescope, and a study of the thermodynamic structure of the hot X-ray emitting plasma with *Chandra*. All systems with extended Hα emission in our sample (6/8 galaxies) display significant [C II] line emission indicating the presence of reservoirs of cold gas. This emission is co-spatial with the optical Hα+[N II] emitting nebulae and the lowest entropy soft X-ray emitting plasma. The entropy profiles of the hot galactic atmospheres show a clear dichotomy, with the systems displaying extended emission line nebulae having lower entropies beyond $r \gtrsim 1$ kpc than the cold-gas-poor systems. We show that while the hot atmospheres of the cold-gas-poor galaxies are thermally stable outside of their innermost cores, the atmospheres of the cold-gas-rich systems are prone to cooling instabilities. This provides considerable weight to the argument that cold gas in giant ellipticals is produced chiefly by cooling from the hot phase. We show that cooling instabilities may develop more easily in rotating systems and discuss an alternative condition for thermal instability for this case. The hot atmospheres of cold-gas-rich galaxies display disturbed morphologies indicating that the accretion of clumpy multiphase gas in these systems may result in variable power output of the AGN jets, potentially triggering sporadic, larger outbursts. In the two cold-gas-poor, X-ray morphologically relaxed galaxies of our sample, NGC 1399 and NGC 4472, powerful AGN outbursts may have destroyed or removed most of the cold gas from the cores, allowing the jets to propagate and deposit most of their energy further out, increasing the entropy of the hot galactic atmospheres and leaving their cores relatively undisturbed.

Table 9.1: Summary of the sample of galaxies. The distances in column 2 are from †Tonry et al. (2001) and ‡Blakeslee et al. (2009). The K-band luminosities in column 5 were determined using the 2MASS survey (Jarrett et al. 2003). The Hα+[N II] luminosities in column 6 are from Macchetto et al. (1996). The luminosities marked with '$\star$' have been revised in Sect. 9.3 and Table 9.4. The 1.4 GHz radio luminosities in column 7 are from Condon et al. (1998) and Condon et al. (2002). Bolometric X-ray luminosities in column 8 are from O'Sullivan et al. (2001). The jet powers for NGC 4636, NGC 4472, and NGC 5846 are from Allen et al. (2006), for NGC 5044 from David et al. (2009), for NGC 1399 from Shurkin et al. (2008), and for NGC 5813 from Randall et al. (2011b). For the jet-powers in NGC 5044 and NGC 5813 no errorbars were published (Randall et al. 2011b; David et al. 2009). Star-formation rates were estimated using a combination of FUV data from *Galex* and MIR data from *Wise*, employing the technique developed by Hao et al. (2011).

Galaxy	d	Scale	z	$L_{\rm K}$	$L_{\rm Hff+[NII]}$	$L_{\rm radio}$	$L_{\rm X}$	$P_{\rm jet}$	SFR
	(Mpc)	(arcsec kpc^{-1})		($\times 10^{40}$ erg s^{-1})	($\times 10^{39}$ erg s^{-1})	($\times 10^{38}$ erg s^{-1})	($\times 10^{41}$ erg s^{-1})	($\times 10^{41}$ erg s^{-1})	$M_\odot$ yr^{-1}
NGC 1399	20.9‡	9.9	0.004753	2.69	9.3*	1.52	5.68	21.9 ± 7	0.171
NGC 4472	16.7‡	12.4	0.003326	3.97	5.8	1.20	2.96	80.7 ± 23.5	0.099
NGC 4636	14.7†	14.0	0.003129	1.20	5.5*	0.28	3.32	3.0 ± 0.8	0.027
NGC 5044	31.2†	6.6	0.009280	1.65	45.6*	0.59	5.87	6.0	0.073
NGC 5813	32.2†	6.4	0.006578	2.30	14.0*	0.26	10.63	1.2	0.063
NGC 5846	27.1†	7.6	0.005717	2.11	24.6	0.26	6.25	7.4 ± 2.6	0.074
NGC 6868	26.8†	5.6	0.009520	1.74	23.8	1.00	1.01	–	0.078
NGC 7049	29.9†	7.1	0.007622	2.32	31.8	0.84	1.23	–	0.117

9.1 Introduction

Recent observations and simulations strongly suggest that the growth and evolution of giant early type galaxies is closely tied to that of their central supermassive black holes through a well regulated feedback cycle (e.g. Silk & Rees 1998; Magorrian et al. 1998; Croton et al. 2006; Sijacki et al. 2007). Many fundamental aspects of this feedback process, such as the nature of the material feeding the black holes in active galactic nuclei (AGN), jet formation, and the heating, cooling and detailed physics of the interstellar medium (ISM) are not well understood. Among the best laboratories to test theories for the formation and growth of massive galaxies are nearby giant ellipticals, groups and clusters of galaxies: systems where hot X-ray emitting plasma may be cooling and accreting onto the galaxies and interacting with their AGN.

In massive galaxy clusters, with central cooling times shorter than the Hubble time, the central brightest cluster galaxies (BCG) are often surrounded by spectacular, filamentary optical Hα+[N II] emission-line nebulae extending up to 70 kpc from the core of the BCG (e.g. Cowie et al. 1983; Johnstone et al. 1987; Heckman et al. 1989; Donahue et al. 1992; Crawford et al. 1999; McDonald et al. 2010). These nebulae of ionized gas seem to be co-spatial with warm (1000-2000 K) molecular hydrogen seen in the near-infrared (e.g. Jaffe & Bremer 1997; Falcke et al. 1998; Donahue et al. 2000; Edge et al. 2002; Hatch et al. 2005; Jaffe et al. 2005; Johnstone et al. 2007; Oonk et al. 2010; Lim et al. 2012) and with large quantities ($10^8 - 10^{11.5}$ M$_\odot$) of cold (< 50 K) molecular gas traced by CO (e.g. Edge 2001; Edge & Frayer 2003; Salomé & Combes 2003; McDonald et al.

Table 9.2: Summary of observations.

Galaxy	*Herschel* Obs. ID	*Herschel* Exp. (s)	*Chandra* Obs. ID	Detector	*Chandra* Exp. (ks)	SOAR/SOI Obs. date	SOAR/SOI filter	SOAR/SOI Exp (s)
NGC1399	1342239492	8161	319	ACIS-S	49.9	2012 Oct. 9	CTIO 656375-4/6916-78	3×600 / 3×600
			4172	ACIS-I	36.7	2013 Aug. 4	Goodman 1.68″ long slit, KOSI600 grating	3×480
			9530	ACIS-S	59.3	2013 Sep. 8	Goodman 3.0″ long slit, KOSI600 grating	4×480
NGC4472	1342234992	8161	321	ACIS-S	19.1			
NGC4636	1342236884	5442	323	ACIS-S	35.8	2009 June 1	CTIO 6600/75	3×780
							CTIO 6120/140	3×500
NGC5044	1342238376	24723	9399	ACIS-S	53.4	2010 April 10	CTIO 6649/76	3×1200
			3926	ACIS-I	54.5		CTIO 6520/76	3×720
			4415	ACIS-I	73.3			
NGC5813	1342238158	10880	5907	ACIS-S	47.4	2008 July 6	CTIO 6600/75	3×900
			9517	ACIS-S	98.8		CTIO 6120/140	3×720
NGC5846	1342238157	5442	788	ACIS-S	17.3	2009 June 1	CTIO 6600/75	3×900
			7923	ACIS-I	75.9		CTIO 6120/140	3×540
NGC6868	1342215929	5442	3191	ACIS-I	18.6	2012 Oct. 9	CTIO 6600/75	2×900, 1×600
			11753	ACIS-I	56.8	2012 Oct. 9	CTIO 6563/75	2×900, 1×600
NGC7049	1342216658	5442	5895	ACIS-I	2.2	2012 Oct. 9	CTIO 6600/75	2×900, 1×600
						2012 Oct. 9	CTIO 6563/75	1×900, 2×600

2012). Recently, observations with the *Herschel Space Observatory* (Pilbratt et al. 2010) also revealed the presence of far-infrared (FIR) cooling lines of [C II], [O I], and [N II] in the X-ray bright cores of Abell 1068, Abell 2597 (Edge et al. 2010), and the Centaurus, Perseus, and Virgo clusters (Mittal et al. 2011, 2012; Werner et al. 2013). In nearby systems, such as the Centaurus, Perseus, and Virgo clusters, where the spatial distribution of the [C II] line could be mapped, it was found to be extended and co-spatial with optical Hα+[N II], far-ultraviolet C IV (in M 87, Sparks et al. 2012), and soft X-ray emission. The filamentary nebulae in the centers of massive cool-core galaxy clusters thus contain multi-phase material spanning a temperature range of over 5 orders of magnitude, from $<$ 50 K to $\sim$ 10^7 K. This gas often appears to be interacting with the jets and the buoyant relativistic plasma from the central AGN (Fabian et al. 2003b; Hatch et al. 2006; Canning et al. 2013). Despite the large quantities of cold gas, many extended nebulae show no evidence for recent star-formation.

The majority of AGN in these systems are in a quiescent, so called 'radio'-mode, where they are accreting at a modest rate. The accretion flows in this mode, though optically faint, often drive powerful relativistic jets, extending to large distances, which can have a profound impact on their surroundings. Using *Chandra* X-ray observations of nine nearby, X-ray luminous elliptical galaxies, Allen et al. (2006) found a tight correlation between the Bondi accretion rates (see Bondi 1952) from the hot X-ray emitting ISM and the power in the relativistic jets (though see Russell et al. 2013a). The jet powers were determined from the work required to inflate bubbles of relativistic plasma associated with the most recent cavities in the hot X-ray emitting atmospheres of the galaxies (Churazov et al. 2002). The relationship between jet power and accretion rate of the hot ISM, however, raises the question: what is the role of the cold gas in the AGN feedback cycle?

Here we present a multi-wavelength study of 8 nearby, X-ray bright, giant elliptical galaxies, all central dominant members of relatively low mass groups. We use FIR data obtained with the *Herschel* Photodetector Array Camera & Spectrometer (PACS) in the lines of [C II]λ157 μm, [O I]λ63μm, and [O Ib]λ145μm that are excellent probes of cold $\sim$ 100 K gas; optical data from the Southern Astrophysical Research (SOAR) telescope in the lines of Hα+[N II] probing warm, ionized $\sim$10,000 K gas; and X-ray data from

the *Chandra X-ray Observatory*, tracing the hot 5-20 million K plasma permeating these systems.

9.1.1 The galaxy sample

Our target list is drawn from the parent sample of Dunn et al. (2010), who identified the optically and X-ray brightest giant elliptical/S0 galaxies within a distance $d \leq 100$ Mpc and with declination Dec. ≥ -45. Motivated by the goal of studying the properties of cold gas in these types of systems in detail, we selected only those galaxies with distance $d < 35$ Mpc and with relatively bright Hα+[N II] emission as reported by Macchetto et al. (1996). All of the systems in our sample are the central dominant galaxies of their respective groups. The properties of the galaxies are summarized in Table 9.1. The table lists the distances of the galaxies (Tonry et al. 2001; Blakeslee et al. 2009), their K-band near-infrared luminosities determined using the magnitudes measured by the 2MASS survey (Jarrett et al. 2003), Hα+ [N II] luminosities (Macchetto et al. 1996), radio luminosities at 1.4 GHz (Condon et al. 1998, 2002), bolometric X-ray luminosities (O'Sullivan et al. 2001), jet-powers (Allen et al. 2006; David et al. 2009; Shurkin et al. 2008; Randall et al. 2011b), and star-formation rates (SFR) estimated using a combination of far-ultraviolet (FUV) data from *Galex* and mid- infrared (MIR) data from *Wise*, employing the technique developed by Hao et al. (2011).

The near-infrared K-band luminosities, and by implication the stellar masses, span a range of approximately a factor of three, with NGC 4636 being the least and NGC 4472 the most luminous. The Hα+[N II] luminosities span a range of a factor of eight, with NGC 5044 being the most luminous, and with NGC 4636 and NGC 4472 on the low luminosity end. NGC 5044 boasts a particularly spectacular network of radial filaments, extending out to a radius of at least $r \sim 10$ kpc (Gastaldello et al. 2009; David et al. 2011). The SFRs are small, typically of the order of 0.1 $M_\odot$ yr^{-1}, and they do not correlate with the Hα luminosities. All eight galaxies have central, active radio jets, also spanning a range of radio luminosities and jet-powers. The X-ray luminosities of the galaxies span a range of an order of magnitude.

9.2 Observations and data analysis

9.2.1 Far-infrared spectroscopy with *Herschel* PACS

We observed the FIR cooling lines of [C II]λ157μm, [O I]λ63μm, and [O Ib]λ145μm in our sample of 8 galaxies with the PACS integral-field spectrometer (Poglitsch et al. 2010) on the *Herschel Space Observatory*. Table 9.2 gives a summary of the observations. The observations were taken in line spectroscopy mode with chopping-nodding to remove the telescope background, sky background and dark current. A chopper throw of 6 arcmin was used. For 7 systems, with a relatively compact Hα emission region, the observations were taken in pointed mode targeting the centers of the galaxies. For NGC 5044, we used raster mapping in 3×3 steps of 23.5 arcsec to match the extent of the Hα nebula. The observations were reduced using the `HIPE` software version

8.2.0, using the PACS `ChopNodLineScan` pipeline script. This script processes the data from level 0 (raw channel data) to level 2 (flux calibrated spectral cubes).

During the final stage of the reduction the data were spectrally and spatially rebinned into $5 \times 5 \times \lambda$ cubes. In the following we will refer to these cubes as the rebinned cubes. Each spatial pixel, termed spaxel, in these cubes has a size of 9.4×9.4 arcsec^2. The cubes thus provide us with a field of view (FoV) of 47×47 arcsec^2. For the wavelength regridding the parameters `oversample` and `upsample` were set to 2 and 1, respectively. This means that one spectral bin corresponds to the native resolution of the PACS instrument.

The integrated [C II] line fluxes were in all cases, except for NGC 5044, obtained by spatially integrating the 5×5 spaxels from the rebinned cubes. For NGC 5044 the integrated line flux is obtained after projecting the individual rebinned cubes onto the sky. No point-spread function (PSF) correction is applied as the [C II] emission, in all cases where it is detected, is found to be extended.

To visualize the extent of the [C II] emission in our galaxies, we have created sky maps of the [C II] emission by using the `specProject` task in `HIPE` and the `hrebin` task in `IDL`. In the following we will refer to these data cubes as the projected cubes. A pixel size of 6 arcsec was chosen in order to Nyquist sample the beam, the full-width-at-half-maximum (FWHM) of which is 12 arcsec at the observed wavelength of the [C II] line. We only consider spatial bins where the signal-to-noise ratio of the integrated line flux is greater than 2. We have compared the integrated line fluxes obtained from the level 2 rebinned cubes with those from the projected cubes and find that they are consistent. Velocity and velocity width maps were constructed by fitting a single Gaussian to the projected data.

For the [O I] and [O Ib] lines, we report line fluxes obtained from either the central spaxel or the central 3×3 spaxels. The PSF corrected fluxes should be viewed as lower limits to the true [O I] and [O Ib] line emission in these galaxies. For NGC 5044 the integrated [O I] and [O Ib] fluxes are obtained after projecting the individual rebinned cubes onto the sky.

9.2.2 Hα+[N II] imaging and spectroscopy

We performed narrow-band imaging observations for all systems in our sample, except for NGC 4472, using the SOAR Optical Imager (SOI) on the 4.1 m SOAR telescope. See Table 9.2 for details on the observations. For each galaxy, we obtained two narrow-band images, one centered on the Hα emission and the other in an adjacent emission-line free band. We reduced the images using standard procedures in the `IRAF MSCRED` package. The pixels were binned by a factor of two, for a scale of 0.154 arcsec per pixel. The typical seeing was $\sim 1''$. Spectrophotometric standard stars were observed for each exposure. More detail on the SOI data reduction can be found in Sun et al. (2007). For continuum subtraction, we follow the isophote fitting method described in Goudfrooij et al. (1994). We assumed line ratios of [N II]λ6583/Hα = 1.5 and [N II]λ6548/[N II]λ6583 = 1/3, which are consistent with the typical values in Goudfrooij et al. (1994).

Table 9.3: Summary of observations with *Herschel* PACS and the properties of the FIR lines.

galaxy	Line	Observation duration (s)	Line Flux in central spaxel (10^{-14} erg s^{-1} cm^{-2})	Observed FWHM (km s^{-1})	Line shift (km s^{-1})	Integrated Line Flux (10^{-14} erg s^{-1} cm^{-2})
NGC 1399	C IIλ157.7μm	2250	< 0.2	300[f]	-	-
	O Iλ63.2μm	2484	< 2.8	300[f]	-	-
	O Ibλ145.5	3360	< 0.2	300[f]	-	-
NGC 4472	C IIλ157.7μm	2250	0.2 ± 0.04	255 ± 36	99 ± 15	1.04 ± 0.16
	O Iλ63.2μm	2484	< 2.5	255[f]	-	-
	O Ibλ145.5μm	3360	< 0.2	255[f]	-	-
NGC 4636	C IIλ157.7μm	1500	2.6 ± 0.06	361 ± 6	22 ± 3	10.52 ± 0.37
	O Iλ63.2μm	1656	1.3 ± 0.2 (1.9)	233 ± 29	75 ± 12	-
	O Ib λ145.5μm	2240	< 0.5	233[f]	-	-
NGC 5044	C IIλ157.7μm	6750	-	-	-	31.73 ± 4.76
	O Iλ63.2μm	7452	-	-	-	7.1 ± 1.8
	O Ibλ145.5μm	10080	-	-	-	1.0 ± 0.5
NGC 5813	C IIλ157.7μm	3000	1.4 ± 0.04	419 ± 10	96 ± 4	8.55 ± 0.26
	O Iλ63.2μm	3312	1.0 ± 0.2 (1.5)	273 ± 36	30 ± 15	-
	O Ibλ145.5μm	4480	0.2 ± 0.04 (0.4)	608 ± 88	100 ± 37	1.4 ± 0.2
NGC 5846	C IIλ157.7μm	1500	2.2 ± 0.06	477 ± 10	-25 ± 4	13.61 ± 0.36
	O Iλ63.2μm	1656	< 2.5	477[f]	-	-
	O Ibλ145.5μm	2240	< 0.3	477[f]	-	-
NGC 6868	C IIλ157.7μ	1500	5.7 ± 0.08	510 ± 6	125 ± 3	21.61 ± 0.44
	O Iλ63.2μm	1656	3.0 ± 0.3	506 ± 31	137 ± 13	5.9 ± 0.8
	O Ibλ145.5μm	2240	0.5 ± 0.06	579 ± 50	125 ± 21	2.0 ± 0.3
NGC 7049	C IIλ157.7μm	1500	2.5 ± 0.06	395 ± 7	78 ± 3	22.49 ± 0.45
	O Iλ63.2μm	1656	< 3.3	395[f]	-	-
	O Ibλ145.5μm	2240	< 0.2	395[f]	-	-

Notes: In brackets, we indicate the PSF corrected fluxes determined assuming the emission comes from a point-source, correcting the measured spaxel flux upward to account for the beam size. The PSF corrected fluxes can therefore be considered a lower limit to the flux integrated over the whole PACS area.

Table 9.4: Hα+[N II] fluxes from the SOAR telescope.

Galaxy	$f_{\mathrm{Hff+[NII]}}$ (10^{-13} erg s^{-1} cm^{-2})
NGC 1399	< 0.34
NGC 4636	2.7 ± 0.4
NGC 5044	7.6 ± 0.9
NGC 5813	2.2 ± 0.3

Table 9.5: Deprojected thermodynamic properties at $r \sim 0.5$ kpc.

Galaxy	n_{e} (cm^{-3})	kT (keV)	P_{e} (keV cm^{-3})	K (keV cm^2)	t_{cool} (10^7 yr)
NGC 1399	0.167 ± 0.005	0.950 ± 0.009	0.158 ± 0.005	3.14 ± 0.07	4.6
NGC 4472	0.154 ± 0.008	0.860 ± 0.012	0.132 ± 0.007	2.99 ± 0.12	4.3
NGC 4636	0.072 ± 0.001	0.535 ± 0.020	0.039 ± 0.001	3.11 ± 0.07	5.2
NGC 5044	0.068 ± 0.005	0.582 ± 0.037	0.039 ± 0.004	3.51 ± 0.27	5.9
NGC 5813	0.074 ± 0.003	0.616 ± 0.041	0.046 ± 0.005	3.50 ± 0.31	5.7
NGC 5846	0.076 ± 0.006	0.677 ± 0.033	0.052 ± 0.005	3.77 ± 0.26	6.2
NGC 6868	0.072 ± 0.002	0.768 ± 0.036	0.055 ± 0.003	4.45 ± 0.22	7.8

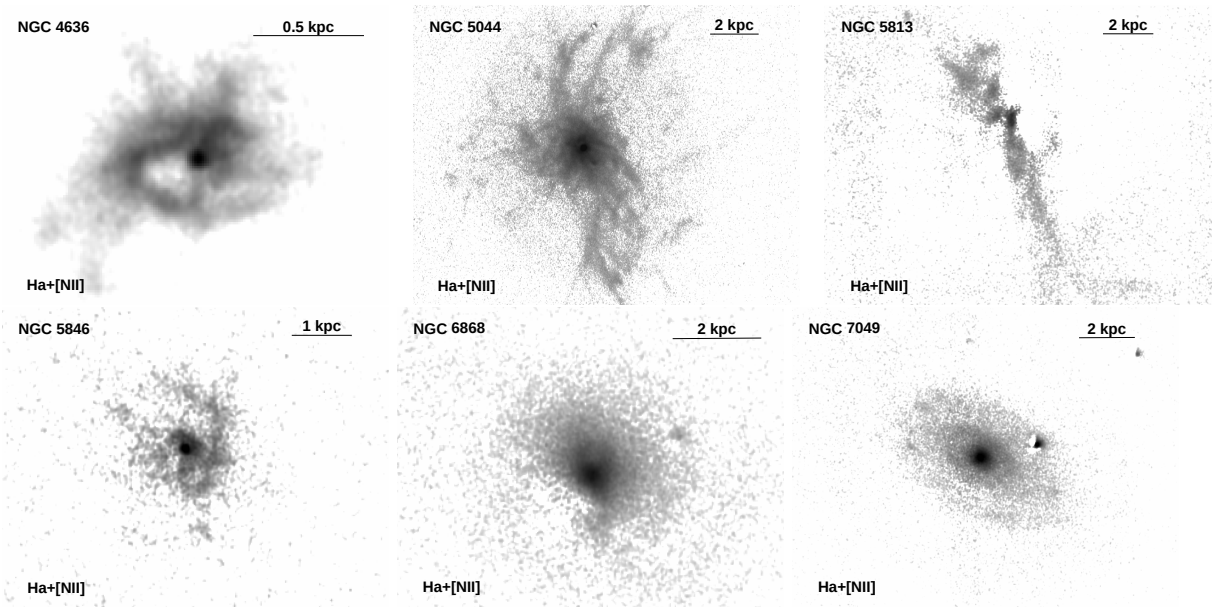

Figure 9.1: Hα+[N II] images of the galaxies with extended emission line nebulae in our sample obtained with the 4.1 m SOAR telescope.

On August 4 and September 8 2013, we also took spectra of NGC 1399 using the Goodman spectrograph on the SOAR telescope. We used a 600 lines per mm grating for the wavelength range of 4350–6950 Å. The first run was taken with a 1.68″ slit, along the NS direction. The second run was taken with a 3.0″ slit, at a position angle of 302 degrees (almost along the major axis of the galaxy). We took three 480 second exposures on the first night and four 480 second exposures on the second night. Before and after each exposure we took a quartz flat and a comparison spectrum of an Fe lamp. Bias correction, flat-fielding, and wavelength calibration were all performed using standard `IRAF` procedures. For flux calibration, we took spectra of the spectrophotometric standard stars LTT7379 and LTT1020.

9.2.3 *Chandra* X-ray data

The archival *Chandra* data were reprocessed using the CIAO (version 4.3) software package. We cleaned the data to remove periods of anomalously high background. Table 9.2 summarizes the net exposure times after cleaning. Our data reduction procedures are described in detail in Million et al. (2010c,d).

To produce 2D maps of projected thermodynamic quantities, we identified spatial regions using the contour binning algorithm (Sanders 2006), which groups neighbouring pixels of similar surface brightness until a desired signal-to-noise ratio threshold is met. We adopted a signal-to-noise ratio of 18–25 ($\sim$320–630 counts per region) in the 0.6–2.0 keV band, which gives us small enough regions to resolve substructure, yet provides enough counts to achieve better than 5 per cent precision on the temperature. Point sources were identified using the CIAO task WAVDETECT and excluded from all regions used for spectral analysis. Separate photon-weighted response matrices and

effective area files were constructed for each spectral region.

We modelled the spectra extracted from each spatial region with the SPEX package (Kaastra et al. 1996). The spectrum for each region was fitted with a model consisting of an absorbed single-phase plasma in collisional ionization equilibrium, with the temperature and spectral normalization (emission measure) as free parameters. The line-of-sight absorption column densities, $N_{\rm H}$, were fixed to the values determined by the Leiden/Argentine/Bonn radio survey of H I (Kalberla et al. 2005).

From the best fit emission measures, $Y = \int n_{\rm H} n_{\rm e} {\rm d}V$, where $n_{\rm H} = n_{\rm e}/1.2$ is the hydrogen number density and V is the emitting plasma volume, we determined the projected electron densities, $n_{\rm e}$, for each region assuming a fixed column depth of $l = 20$ kpc. Using these electron densities and the best fit plasma temperatures (kT), we determined the pressures ($P_{\rm e} = n_{\rm e} kT$) and entropies ($K = kT/n_{\rm e}^{2/3}$). We note that the choice of the assumed column depth for these projected maps is arbitrary and it does not affect the magnitude of the observed azimuthal variations in the derived thermodynamic properties.

Because the statistical quality of the data for the X-ray faintest galaxies in our sample, NGC 6868 and NGC 7049, does not allow us to produce 2D maps of thermodynamic properties, we only present X-ray images for these systems. Background-subtracted images were created in six narrow energy bands, spanning 0.5–2.0 keV. These were flat fielded with respect to the median energy for each image and then co-added to create the broad-band X-ray images.

To determine the deprojected thermodynamic properties of the hot gas, we extracted, for each galaxy (except NGC 7049), a set of azimuthally averaged spectra from concentric annuli. We modeled these spectra simultaneously in the 0.6–2.0 keV band, with the XSPEC (version 12.5 Arnaud 1996) spectral fitting package, using the projct model (see Werner et al. 2012, for details). We have determined the azimuthally-averaged deprojected radial profiles of electron density and temperature, from which we derived the deprojected radial profiles for entropy, electron pressure, and cooling time. We define the cooling time as the gas enthalpy divided by the energy radiated per unit volume of the plasma:

$$t_{\rm cool} = \frac{\frac{5}{2}(n_{\rm e} + n_{\rm i})kT}{n_{\rm e} n_{\rm i} \Lambda(T)}, \tag{9.1}$$

where the ion number density $n_{\rm i} = 0.92 n_{\rm e}$, and $\Lambda(T)$ is the cooling function for Solar metallicity tabulated by Schure et al. (2009). We caution that, because the deprojected thermodynamic properties are determined assuming spherical symmetry, for the 5/7 analyzed galaxies with disturbed morphologies, the derived values have significant systematic uncertainties.

9.3 Results

Using *Herschel* PACS, we detect FIR [C II]λ157μm line emission in 7/8 systems (see Table 9.3). The detections of [O I]λ63.2μm and [O Ib]λ145.5μm lines are relatively weak, and are only seen in 4/8 and 3/8 systems, respectively. No cold neutral gas is detected

in NGC 1399 and the [C II] detection in NGC 4472 is relatively weak. Table 9.3 lists the observed lines for all the target galaxies, their rest frame wavelengths and observation durations. For the central spaxel, we present the observed line fluxes and the 2σ upper limits where appropriate, the observed FWHM, and the observed line shifts with respect to the systemic velocity determined based on optical data. In the brackets, we give the PSF corrected fluxes determined assuming that the emission comes from a point-source, correcting the measured spaxel flux upward to account for the beam size. The PSF corrected fluxes can therefore be considered a lower limit to the flux integrated over the whole PACS area. For sources that allow us to confirm that the emission is extended we report non-PSF corrected fluxes. The last column gives the line fluxes spatially integrated over the 5×5 spaxel ($47'' \times 47''$) *Herschel* PACS field of view.

The [O I]/[C II] line ratios determined from the central spaxel in systems with significant [O I] detections are in the range of 0.4–0.8. The 2σ upper limits on the fluxes of the [O I]$\lambda 63\mu$m and [O Ib]$\lambda 145\mu$m lines given in Table 9.3 were determined assuming that their velocity widths are equal to the FWHM of the [C II] line.

As indicated in Section 9.1.1 and in Table 9.1, according to Macchetto et al. (1996) all our targets are Hα luminous. Fig. 9.1 shows narrow band Hα+[N II] images obtained with the SOAR telescope of our six targets with extended line-emitting nebulae. The nebulae in NGC 6868 and NGC 7049 show regular extended disk-like morphologies reaching radii $r \sim 2 - 3$ kpc (see also Macchetto et al. 1996). On the other hand, NGC 5044, NGC 5813, NGC 5846, and NGC 4636 show filamentary emission. NGC 5044 has the largest optical emission line luminosity, with a rich, dense network of filaments extending from the core out to a radius of ~ 10 kpc (see also David et al. 2011; Gastaldello et al. 2009). The nebulae in NGC 5813 show a radial bipolar distribution in the direction of buoyant bubbles rising in the hot X-ray emitting atmosphere of the galaxy (see also Randall et al. 2011b). The bright Hα+[N II] emission in NGC 4636 and NGC 5846 appears relatively compact, concentrated in the innermost $r \lesssim 1.5$ kpc of the galaxies, but the morphology of the nebulae is clearly filamentary exhibiting signs of interaction with the central AGN.

Our new SOAR data allow robust constraints on the Hα+[N II] flux in four galaxies, NGC 5044, NGC 4636, NGC 5813, and NGC 1399 (see Table 9.4). The NGC 5846 data were not taken in photometric conditions, and for NGC 6868 and NGC 7049, the filters available at the time of the observations made the continuum subtraction less reliable than what is achieved for other galaxies. Our Hα+[N II] flux for NGC 4636 is consistent with the values published by Macchetto et al. (1996) and Buson et al. (1993). For NGC 5813, our result is consistent with Goudfrooij et al. (1994) but is almost a factor of two higher than the flux measured by Macchetto et al. (1996). For NGC 5044, our flux is significantly higher than the values measured by Goudfrooij et al. (1994) and Macchetto et al. (1996), but is consistent with the result of Rickes et al. (2004). The large spatial extent of the nebula surrounding NGC 5044 combined with the small field-of-view of the instrument ($1.4' \times 2.2'$) may have prevented Macchetto et al. (1996) from a robust determination of the local background.

Contrary to the results of Macchetto et al. (1996), we detected no Hα+[N II] emission in NGC 1399. Goudfrooij et al. (1994) derived an Hα+[N II] flux of $4.2 \pm 0.2 \times 10^{-14}$ erg

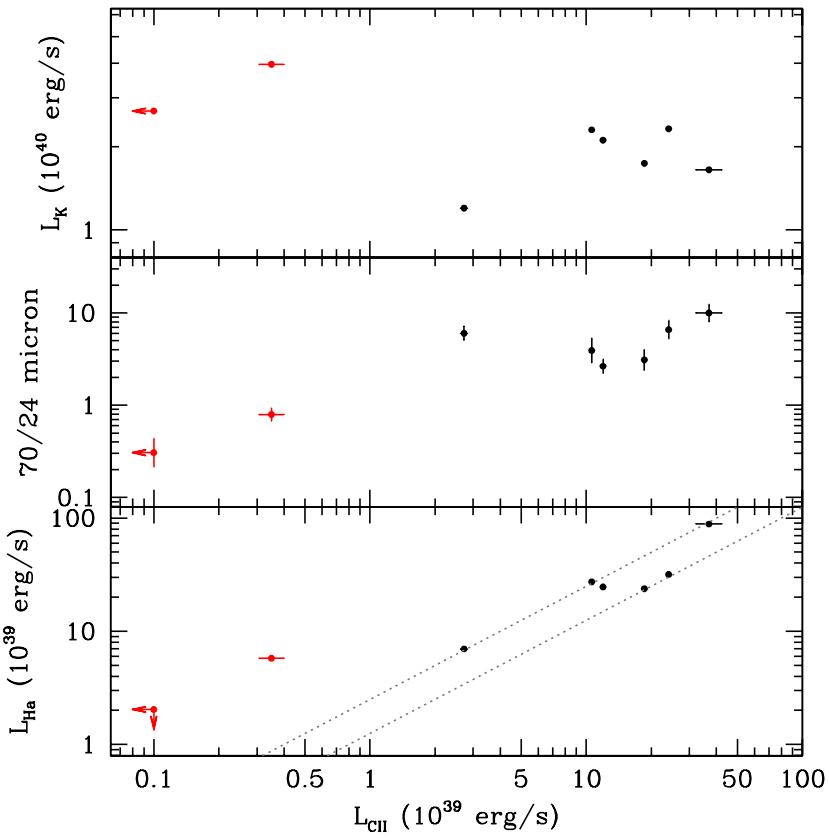

Figure 9.2: The Hα+[N II] luminosity (bottom panel) from SOAR for NGC 1399, NGC 5044, NGC 5813, and NGC 4636 (see Table 9.4) and from Macchetto et al. (1996) for NGC 4472, NGC 5846, NGC 6868, and NGC 7049 (see Table 9.1), 70/24 μm infrared continuum ratio (middle panel, Temi et al. 2007a), and K-band luminosity (top panel, based on the 2MASS survey, Jarrett et al. 2003) plotted against the spatially integrated [C II] luminosity measured by *Herschel* PACS. The grey doted lines on the bottom panel indicate constant [C II] over Hα+[N II] luminosity ratios of 0.4 and 0.8. These ratios are remarkably similar for 6/8 galaxies in our sample. The outliers, NGC 4472 and NGC 1399, have little or no cold gas. They are indicated in red.

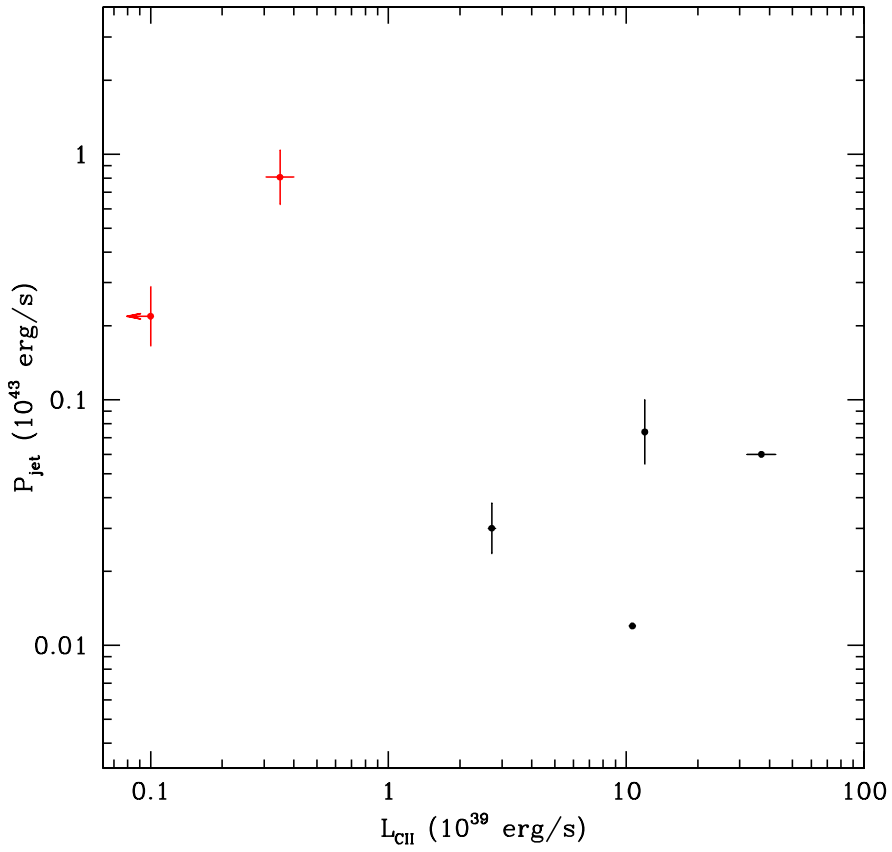

Figure 9.3: Jet powers (Allen et al. 2006; Shurkin et al. 2008; David et al. 2009; Randall et al. 2011b) plotted against the spatially integrated [C II] luminosity measured by *Herschel* PACS. Galaxies with little or no cold gas are indicated in red. For the jet-powers in NGC 5044 and NGC 5813 no errorbars were published (Randall et al. 2011b; David et al. 2009).

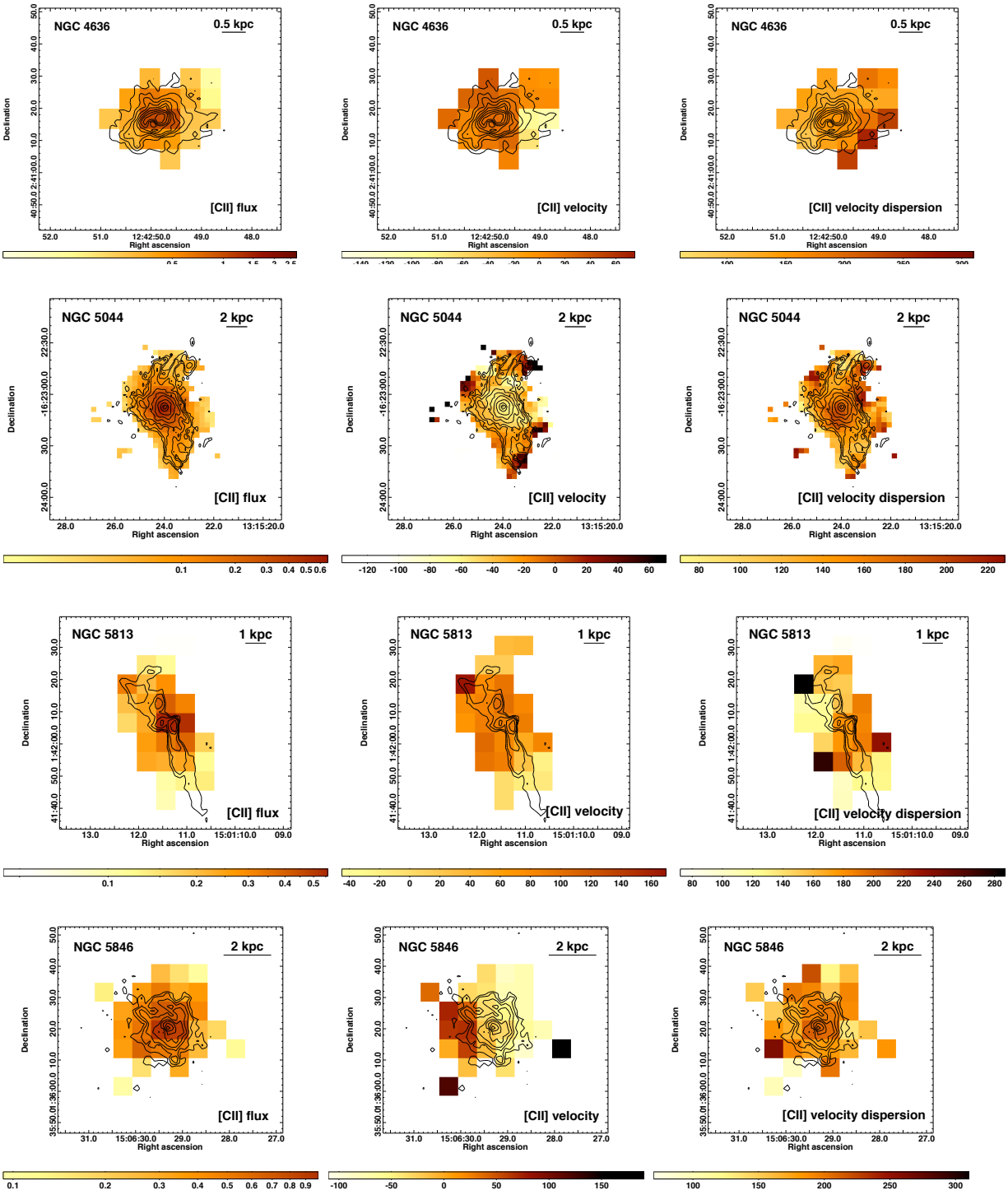

Figure 9.4: Left panels: Maps of the integrated [C II] line flux in units of 10^{-14} erg s^{-1} cm^{-2} per $6'' \times 6''$ spaxel obtained with *Herschel* PACS for NGC 4636, NGC 5044, NGC 5813, and NGC 5846. Central panels: The velocity distribution of the [C II] emitting gas, in units of km s^{-1}, relative to the systemic velocity of the host galaxy. Right panels: Map of the velocity dispersion, σ, of the [C II] emitting gas. Contours of the Hα+[N II] emission are overlaid.

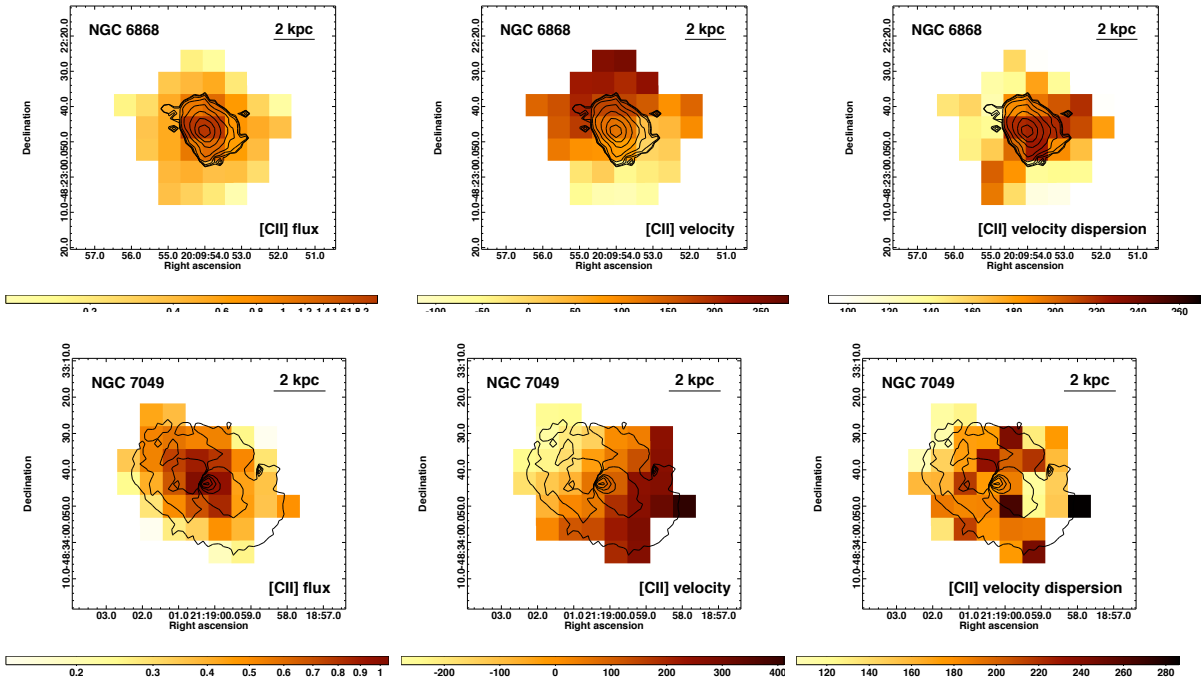

Figure 9.5: Same as Fig. 9.4, but for NGC 6868 and NGC 7049.

s^{-1} cm^{-2}, much smaller than the value measured by Macchetto et al. (1996). Our SOI Hα+[N II] imaging analysis of NGC 1399, with either adjacent narrow-band or R band image for the continuum subtraction, results in negative net flux around the center of the galaxy, indicative of Hα absorption. Therefore, we took additional long-slit spectra with the Goodman spectrograph on SOAR. Our Goodman spectra give a 5 σ limit on the EW of the emission line of 0.1 $\AA$. Assuming that all the Hα+[N II] emission is from the central 12″ radius, as shown by the Hα+[N II] image from Macchetto et al. (1996), this EW upper limit translates to an Hα+[N II] flux limit of 3.4×10^{-14} erg s^{-1} cm^{-2}. The lack of a spectroscopic detection of optical emission lines in NGC 1399 is inconsistent with previous reports of detections through narrow-band filters. We suspect that the previously reported detections of morphologically smooth line emission, where the emitting region has the same morphology as the old stellar populations, may be due to color gradients in the stellar population of the galaxy. Currently, we do not have SOAR data for NGC 4472.

In Fig. 9.2, we plot the Hα+[N II] luminosities (bottom panel), 70/24 μm infrared continuum ratios (middle panel, Temi et al. 2007a), and the K-band luminosity (top panel, based on the 2MASS survey, Jarrett et al. 2003) against the spatially integrated [C II] luminosity measured by *Herschel* PACS. The ratio of the [C II] over Hα+[N II] luminosity is remarkably similar $\sim$ 0.4–0.8 for 6/8 galaxies in our sample. For the same 6/8 systems, the [C II]λ157μm line emission is spatially extended and appears to follow the distribution of the Hα+[N II] filaments (see the left panels of Fig. 9.4 and 9.5). In the extended network of filaments of NGC 5044 at $r \gtrsim 1$ kpc, the [C II]/(Hα+[N II]) ratios also remain similar as a function of position. In the two FIR faint systems (shown

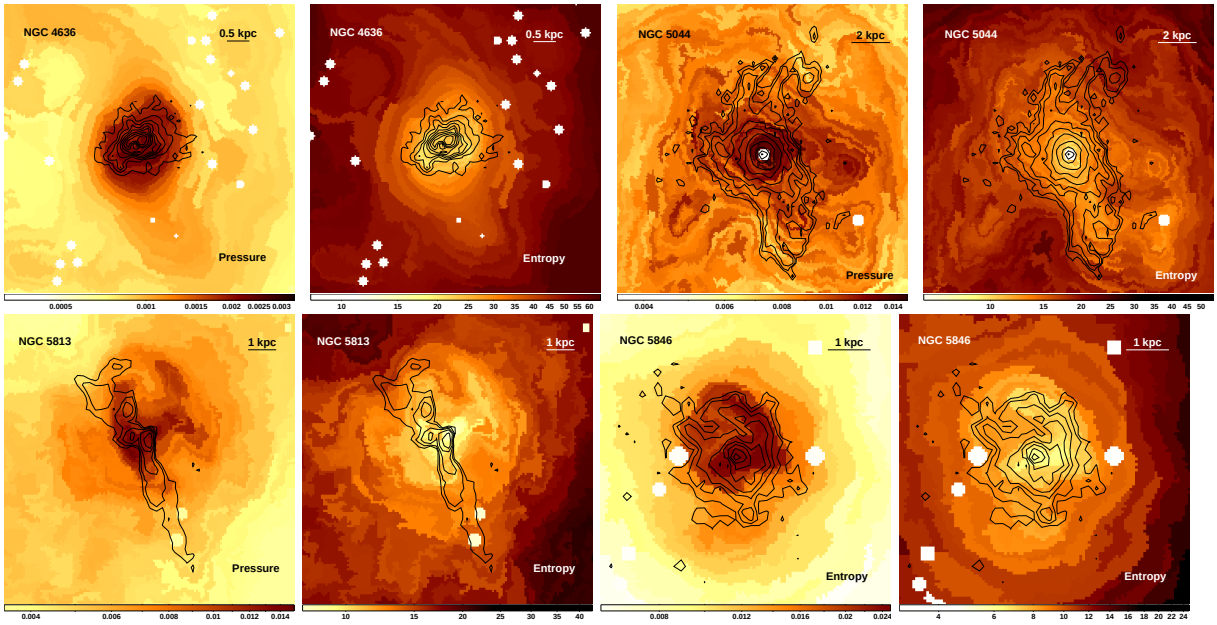

Figure 9.6: 2D map of the hot gas pressure (in units of keV cm^{-3} $\times \left(\frac{l}{20\mathrm{kpc}}\right)^{-1/2}$) and entropy (in units of keV cm^2 $\times \left(\frac{l}{20\mathrm{kpc}}\right)^{1/3}$) with the H$\alpha$+[N II] contours overlaid. The maps were obtained by fitting each region independently with a single temperature thermal model, yielding 1σ fractional uncertainties of $\sim$3–5 per cent in temperature, entropy, and pressure. Point sources were excluded from the spectral analysis and therefore appear as white circles on the maps.

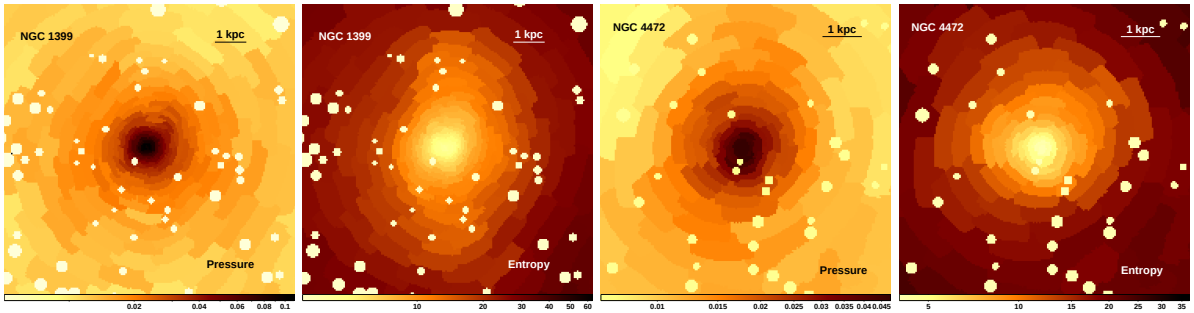

Figure 9.7: 2D maps of the hot gas pressure and entropy for the two galaxies with little or no [C II] emitting cold gas detected.

by the red data points) the ionized Hα emission is either concentrated in the nucleus of the galaxy (NGC 4472, Macchetto et al. 1996) or is not present (NGC 1399).

The [C II] luminosities, which are likely excellent tracers of the cold molecular gas mass (Crawford et al. 1985), do not correlate with the K-band luminosities (see Table 9.1), which trace the stellar masses of the galaxies. There is also no correlation between the [C II] luminosities of systems with extended emission line nebulae and the 70/24 μm infrared continuum ratios. In the FIR faint systems indicated by the red data points these ratios are smaller (see the central panel of Fig. 9.2). The 70/24 μm infrared continuum ratio is a good tracer of interstellar dust (Temi et al. 2007a).

Fig. 9.3 shows that the [C II] luminosities in systems with spatially extended emission do not correlate with the jet powers determined from the work required to inflate bubbles of relativistic plasma associated with the cavities in the hot X-ray emitting atmospheres of the galaxies listed in Table 9.1. In our relatively small sample, the galaxies with little or no cold gas (indicated in red) have higher jet powers than the systems with significant [C II] detections.

The central panels of Fig. 9.4 and 9.5 show the velocity distributions of the [C II] line emitting gas with respect to the velocities of the host galaxies. In NGC 6868 and NGC 7049 the velocity distribution of the [C II] emitting gas indicates that the cold gas forms a rotating disk. This is consistent with the overall morphology of the optical line emission nebulae. The velocity distribution of the [C II] emitting gas in the other four systems with extended emission does not show any coherent structure.

The projected velocity dispersions measured from the [C II] lines along our line of sight are generally in the range between 100 km s^{-1} and 200 km s^{-1}, with the highest measured values reaching $\sim$ 280 km s^{-1}.

Fig. 9.6 shows maps of the pressure and entropy in the hot X-ray emitting intragroup/interstellar medium for the galaxies where the cold gas has a filamentary morphology. In all of these systems, the filaments are co-spatial with the lowest entropy hot X-ray emitting gas. They also appear to anti-correlate and interact with the AGN inflated bubbles of relativistic plasma, which provide significant non-thermal pressure in the X-ray atmospheres of the galaxies and therefore appear as regions of low projected X-ray pressure on our maps. This is most clearly seen for the southwestern filament in NGC 5813, which appears to be pushed aside by the large, older, outer bubble. The inner portion of the filament also appears on the side and partly on the top of the small, younger, inner southwestern bubble that is currently being inflated in the core (for detailed discussion on the bubbles see Randall et al. 2011b). Similar interaction, with the filaments being pushed around by the bubbles, is seen in NGC 5846 and NGC 4636, both of which show 'cavities' in the Hα+[N II] images that coincide with pressure decrements in their X-ray spectral maps. NGC 5044 shows a strongly disturbed morphology due to both AGN activity and the intra-group medium sloshing in the gravitational potential of the system (Gastaldello et al. 2009; David et al. 2009, 2011; O'Sullivan et al. 2013).

Fig. 9.7 shows the pressure and entropy maps for NGC 4472 and NGC 1399 - systems with little or no cold and warm gas. Compared to the systems with filamentary Hα nebulae, their thermodynamic maps have relatively regular morphologies. These systems are among the nearby giant ellipticals with the most relaxed X-ray morpholo-

gies at small radii (Werner et al. 2012).

NGC 6868 and NGC 7049 do not have X-ray data with the quality that would allow us to extract detailed maps of thermodynamic properties and in Fig. 9.8 we only show their X-ray images. The images show extended X-ray haloes, co-spatial with the Hα+[N II] emission, surrounding the galaxies. The X-ray image of NGC 6868 shows a relatively complex disturbed morphology (see also Machacek et al. 2010). The X-ray data of NGC 7049 are very shallow and only allow us to detect the extended X-ray emission. Four galaxies - NGC 5044, NGC 6868, NGC 7049, and NGC 5813 - have an X-ray point source associated with the central AGN.

The deprojected central densities and pressures measured at $r = 0.5$ kpc in the morphologically relaxed NGC 1399 and NGC 4472 appear significantly higher than in the other, more disturbed, [C II] bright systems (see Table 9.5). All [C II] bright galaxies appear to have similar central densities and pressures. The entropies at $r = 0.5$ kpc span a small range of 3.0–4.5 keV cm^2 and the central cooling times are 4–8 $\times$ 10^7 yr. At radii $r \gtrsim 1$ kpc the entropies of the galaxies containing cold gas (except NGC 6868) are systematically lower than those of NGC 1399 and NGC 4472 (see Fig. 9.9). The measured relatively low central densities and pressures of the morphologically disturbed systems may partly be due to the additional non-thermal pressure support in the central regions of the these systems. However, we also suspect a bias due to departures from spherical symmetry. Due to the non-uniform surface brightness within the circular annuli used in the deprojection analysis, densities in the outer shells may be somewhat overestimated, leading to underestimated central densities. For the morphologically disturbed systems, we repeated the deprojection analysis using wedges and found, that despite the systematic uncertainties, at radii $r \gtrsim 1$ kpc the difference in the shapes of the profiles shown in Fig. 9.9 remains robust.

9.4 Discussion

9.4.1 Properties of the cold ISM

The observed high [C II] luminosities indicate the presence of large reservoirs of cold gas. Cold gas is evidently prevalent in massive giant elliptical galaxies with spatially extended Hα+[N II] nebulae, even though their stellar populations are old and appear red and dead (Annibali et al. 2007). NGC 5044 has previously also been detected in the CO(2–1) line with the 30 m IRAM telescope with a total flux of 6.6 $\times$ 10^{-17} erg s^{-1} cm^{-2} (Jeremy Lim & Francoise Combes, private communication). Assuming a CO(2–1) to CO(1–0) ratio of 0.8, we obtain a [C II]λ158μm over CO(1–0) flux ratio of 3817, which is within the range of the ratios (1500–6300) observed in normal and star forming galaxies and in Galactic molecular clouds (Crawford et al. 1985; Stacey et al. 1991).

Assuming the cold $\sim$100 K [C II] emitting gas is in thermal pressure equilibrium with the surrounding hot X-ray emitting plasma, it will presumably form filaments with densities $\sim 10^4$ cm^{-3} and small volume filling fractions. As discussed in Fabian et al. (2003b, 2008, 2011) and Werner et al. (2013), the emission line filaments are likely to consist of many strands that have small volume filling fractions but large area cov-

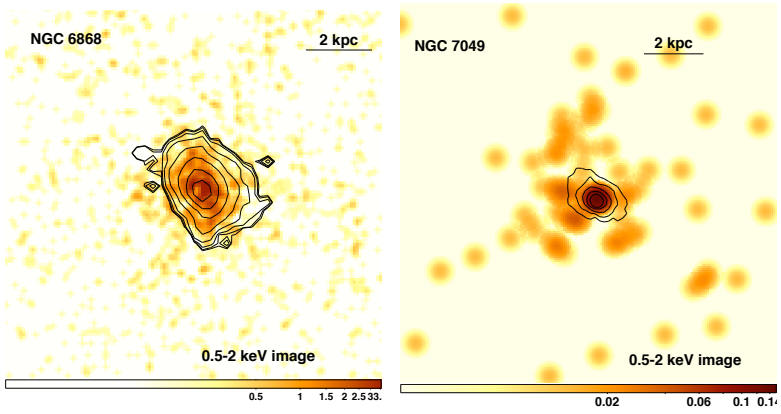

Figure 9.8: 0.5–2 keV *Chandra* images of the X-ray faintest galaxies in our sample, NGC 6868 and NGC 7049, with the Hα+[N II] contours overlaid. The statistical quality of the X-ray data does not allow us to produce 2D maps of thermodynamic properties for these two systems.

ering factors. The soft X-ray emission that is always associated with filaments in cool core clusters (Sanders & Fabian 2007; Sanders et al. 2008, 2009, 2010a; de Plaa et al. 2010; Werner et al. 2011, 2010, 2013) indicates the presence of cooling hot plasma distributed between the threads. The hot plasma may be cooling both radiatively and by mixing with the cold gas in the filaments. Part of the soft X-ray emission from this cooling plasma gets absorbed by the cold gas in the strands (Werner et al. 2013).

The velocities inferred from the [C II] line emission are consistent with those measured from the Hα+[N II] lines by Caon et al. (2000), indicating that the different observed gas phases form multiphase filaments where all the phases move together. The velocity structure measured in NGC 6868 and NGC 7049 indicates that the cold gas in these systems is distributed in large extended rotating disks. Given the expected densities of the [C II] emitting gas, its volume filling fraction must be low and the disks are also likely to be formed from many small clouds, sheets, and filaments.

The observed velocity dispersions of the [C II] emitting gas are similar to the range of values measured from CO line widths and using optical and near-infrared integral field spectroscopy of 2000–10,000 K gas in the cooling cores of clusters (e.g. Edge 2001; Ogrean et al. 2010; Oonk et al. 2010; Farage et al. 2012; Canning et al. 2013). Observations indicate that, due to their small volume filling fraction and large area covering factors, filaments may be blown about by the ambient hot gas, potentially serving as good tracers of its motions (Fabian et al. 2003b). The measured velocity dispersions of the [C II] emitting gas, which reflect the range of velocities of the many small gas clouds/filaments moving through the galaxy, may therefore be indicative of the motions in the hot ISM. They are in general consistent with the limits and measurements

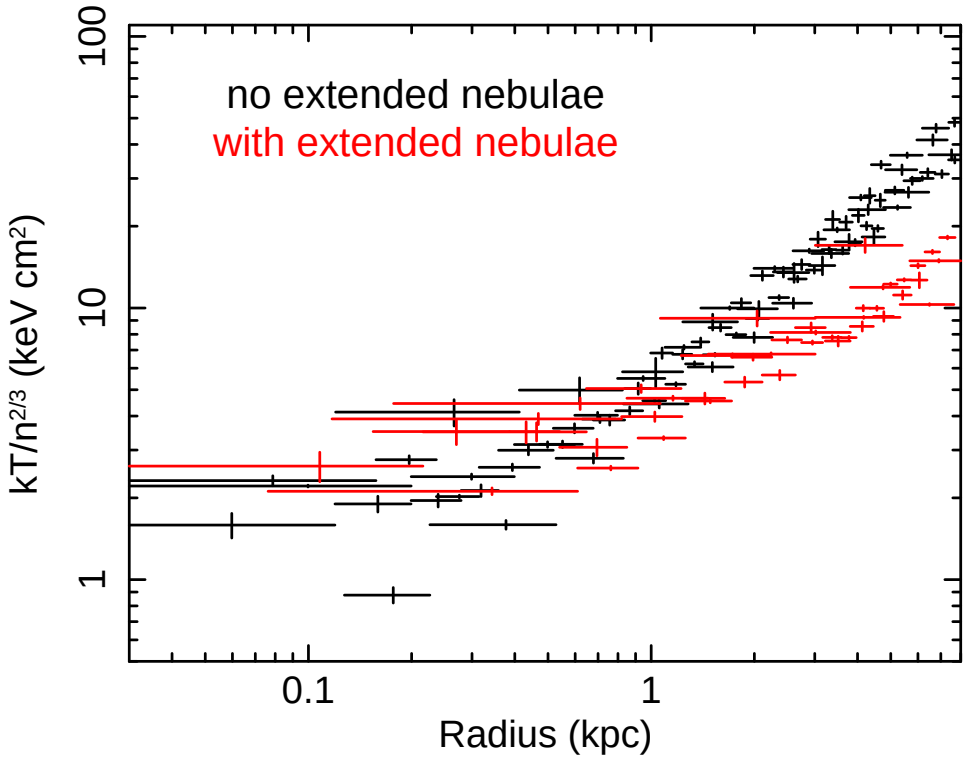

Figure 9.9: Entropy profiles for a sample of morphologically relaxed giant ellipticals (NGC 4472, NGC 1399, NGC 4649, NGC 1407, NGC 4261; Werner et al. 2012), with no extended optical emission line nebulae (in black), and for five galaxies from our sample with [C II] emission indicating the presence of reservoirs of cold gas (NGC 5044, NGC 5813, NGC 5846, NGC 4636, NGC 6868 - in red). The entropy in galaxies containing cold gas is systematically lower at $r \gtrsim 1$ kpc. The only exception is NGC 6868 the entropy profile of which follows that of the cold-gas-poor galaxies.

obtained through X-ray line broadening and resonant line scattering observations with the Reflection Grating Spectrometers on *XMM-Newton* (Werner et al. 2009; de Plaa et al. 2012; Sanders & Fabian 2013).

The mid-infrared *Spitzer* spectra of all of our [C II] bright galaxies overlapping with the sample of Panuzzo et al. (2011) - NGC 4636, NGC 5044, NGC 5813, NGC 5846, NGC 6868 - show the presence of dust, warm H_2 molecular gas, and for NGC 5044, NGC 6868, and NGC 4636 also PAH emission. Temi et al. (2007a) show that, for NGC 4472 and NGC 1399, galaxies with little or no [C II] detected, the infrared spectral energy distributions (SEDs) can be fully explained by circumstellar dust in the context of a steady state model of dust production in normal stellar mass loss followed by sputtering by the hot X-ray emitting gas. However, for all of the galaxies with extended [C II] emission, the infrared SEDs observed with *IRAS* and *Spitzer* indicate the presence of true interstellar dust, well in excess of the predictions of the steady state model (Knapp et al. 1989; Temi et al. 2007a,b). Although there are early reports of detections of H I emission in NGC 5846 and NGC 4636 (Bottinelli & Gouguenheim 1977, 1979; Knapp et al. 1978), they were not confirmed by later re-observations (Krishna Kumar & Thonnard 1983; Lake & Schommer 1984; Knapp et al. 1985).

Werner et al. (2013) showed that the [S II]λ6716/6731 line ratios of the filaments in M 87 indicate very low densities in the Hα+[N II] emitting 10,000 K phase. They concluded that, assuming subsonic turbulence in the filaments, the presence of significant magnetic pressure is required to keep this warm ionized gas in pressure equilibrium with the surrounding intra-cluster medium, indicating that the filaments are supported by magnetic fields of $B = 28 - 73\mu$G. The assumption of subsonic turbulence is motivated by the lack of [O III] line emission, which would be produced by strong shocks. For 5/8 galaxies overlapping with the sample of Annibali et al. (2010), the [S II]λ6717/6731 line ratios point to very low densities, $n_e < 26$ cm^{-3}, in the ionized gas, indicating that it is supported by magnetic fields. Such low densities appear to be common in the ionized, extended emission line nebulae in the cores of galaxy clusters. Significant magnetic fields threading the emission line nebulae were also inferred using arguments based on the integrity of the filaments in the Perseus Cluster (Fabian et al. 2008) and based on radio observations of the Faraday rotation measure in cooling core clusters (Taylor et al. 2001, 2007; Allen et al. 2001; Feretti et al. 1999). This magnetic support may be slowing or preventing the gravitational collapse of any molecular gas clouds traced by the [C II] line emission that exceed the Jeans mass, preventing them from forming stars (e.g. see the discussion for NGC 1275 in Ho et al. 2009).

9.4.2 Heating and ionization of the cold ISM

In the six systems with significant cold gas mass reservoirs, the [C II] line emission appears to be co-spatial with the Hα+[N II] emission, and with the lowest entropy X-ray emitting plasma. In the same galaxies, the ratios of [C II]/(Hα+[N II]) emission appear to be similar (0.4–0.8), indicating that in these systems the [C II] and Hα+[N II] emission are powered by the same energy source.

Photoionization by young hot stars or by the central AGN is negligible as a source of excitation for the nebulae in these galaxies. Ferland et al. (2009) showed that the broad band emission-line spectra of the filamentary nebulae around central galaxies of cooling core clusters most likely originate in gas exposed to ionizing particles, either relativistic cosmic rays or hot X-ray emitting plasma penetrating into the cold gas. If the magnetized, ionized Hα emitting phase forms a thin skin on the underlaying cold neutral gas, then the hot plasma particles must somehow overcome the obstacle presented by the magnetic fields. Based on the observations of the emission line filaments in M 87, Werner et al. (2010) and Werner et al. (2013) propose that shocks propagating within the hot X-ray emitting plasma as well as the movement of the filaments through this ambient hot gas (both as they are being uplifted and as they fall back) induce shearing around the filaments, thereby promoting mixing of the cold gas with the ambient hot medium via instabilities (e.g. Friedman et al. 2012). Fabian et al. (2011) propose that the ionizing hot plasma in the core of the Perseus Cluster penetrates the cold filaments through magnetic reconnection diffusion (Lazarian et al. 2010, 2011), which may be induced by shearing instabilities and turbulence. The penetration of the cold gas by the hot plasma particles implies that the X-ray emitting gas cools through mixing and thus the filaments of cold gas grow continuously in mass. If the mixing of the cold and hot gas phases turns more violent and the energy input rate due to penetrating hot plasma becomes larger than the cooling rate, this process may also lead to the destruction of the filaments.

On the other hand, according to the scenario proposed by Churazov et al. (2013), the filaments may be powered by the reconnection of the stretched magnetic fields in the wakes of AGN inflated buoyantly rising bubbles, and do not necessarily grow in mass. The fact that the ratios of the [C II]/(Hα+[N II]) emission appear similar in both filamentary nebulae and rotating disks indicates that, despite the different morphologies, the gas is heated and ionized by the same energy source in both types of systems. But because the cold gas in the disky nebulae is not distributed in the wakes of AGN inflated bubbles, the scenario proposed by Churazov et al. (2013) could not explain their energy source. However, in the reconnection model, the powering of the cold gas could also be driven by the orbiting motion of the magnetized blobs/filaments through the hot plasma. This may lead to the sliding of the cold gas along the opposite-polarity magnetic fields and to the subsequent reconnection.

Despite its relatively low X-ray luminosity, the central pressure of the hot X-ray emitting plasma in the disky NGC 6868 is similar to the central pressures in the filamentary systems (see Table 9.5) indicating that in the absence of magnetic fields the heat flux from the hot into the cold phase would also be similar in both types of systems. It therefore appears that if the cold and hot phase come into direct contact - either due to turbulence, shearing motions, or the magnetic fields tied to the ionized phase becoming unstable - hot gas particles penetrating into the cold gas provide a viable mechanism for powering the filaments in all of the systems in our sample. The penetrating particles will heat and increase the degree of ionization of the molecular gas clouds present within the filaments, increasing their Jeans mass and slowing down the collapse of the gas clouds in the presence of magnetic fields.

This model, calculated by Ferland et al. (2009) considering emission from an opti-

cally thin cell of gas, however, predicts [O I]/[C II]$\sim$ 21, significantly higher than our observed range of 0.5–0.7. The ratios previously observed in the Perseus and Centaurus clusters, and in Abell 1068 and Abell 2597 are also low, in the range of 0.3–1 (Edge et al. 2010; Mittal et al. 2011, 2012). Mittal et al. (2012) conclude that these line ratios suggest that the lines are optically thick, implying a large reservoir of cold gas, which was not accounted for in previous inventories of the filament masses. Our measured ratios are consistent with the values determined previously in normal and starburst galaxies (Malhotra et al. 2001).

9.4.3 Origin of the cold ISM

A hotly debated question in the literature is whether the cold gas seen in the central giant elliptical galaxies in clusters and groups, and in early type galaxies with X-ray haloes, originated from the radiative cooling of the hot plasma, from stellar mass loss, or whether it was accreted in mergers with gas rich galaxies.

The difference between the entropy profiles of the systems with cool gas and those without it in Fig. 9.9 supports the argument that the cold gas originates by cooling from the hot phase. In more massive clusters, Hα filaments are always co-spatial with soft X-ray emitting $\sim$0.5 keV gas (Sanders & Fabian 2007; Sanders et al. 2008, 2009, 2010a; de Plaa et al. 2010; Werner et al. 2011, 2010, 2013), indicating that the cold gas must be related to the hot phase. Furthermore, significant star formation and line emitting gas around the central galaxy are only found in systems where the central cooling time is short, or, equivalently, the central entropy is low (Rafferty et al. 2008; Cavagnolo et al. 2008).

The parameter

$$\Pi_{\rm F} = \frac{\kappa T}{n_{\rm e} n_{\rm H} \Lambda(T) r^2}, \tag{9.2}$$

where κ is the thermal conductivity, T is the temperature, Λ is the cooling function, and $n_{\rm e}$ and $n_{\rm H}$ are the electron and hydrogen number densities, respectively, is a measure of the ratio of the conductive heating rate to the radiative cooling rate on scales comparable to r, i.e. the "Field criterion" for thermal instability (Field 1965). Fig. 9.10 shows the Field criterion, $\Pi_{\rm F}$, as a function of the radius, where the systems with substantial quantities of cold gas are plotted in red. There is a clear dichotomy with the cold-gas-rich systems remaining unstable out to relatively large radii. This result strongly indicates that the cold gas is produced chiefly by thermally unstable cooling from the hot phase. A similar result was found for a sample of central galaxies in more massive clusters by Voit et al. (2008), who found minimum values of $\Pi_{\rm F} \lesssim 5$ in all systems with star formation. Voit et al. (2008) argued that the effective conductivity is suppressed by a factor of about 5 by magnetic fields, in which case all of their systems with young stars are thermally unstable by the Field criterion.

The Field criterion alone is insufficient to ensure that the gas is thermally unstable. In a spherical atmosphere, the gas is supported by buoyancy, so that an overdense blob tends to fall inwards on the free-fall timescale towards its equilibrium position where the surrounding gas has the same specific entropy and requires the same specific

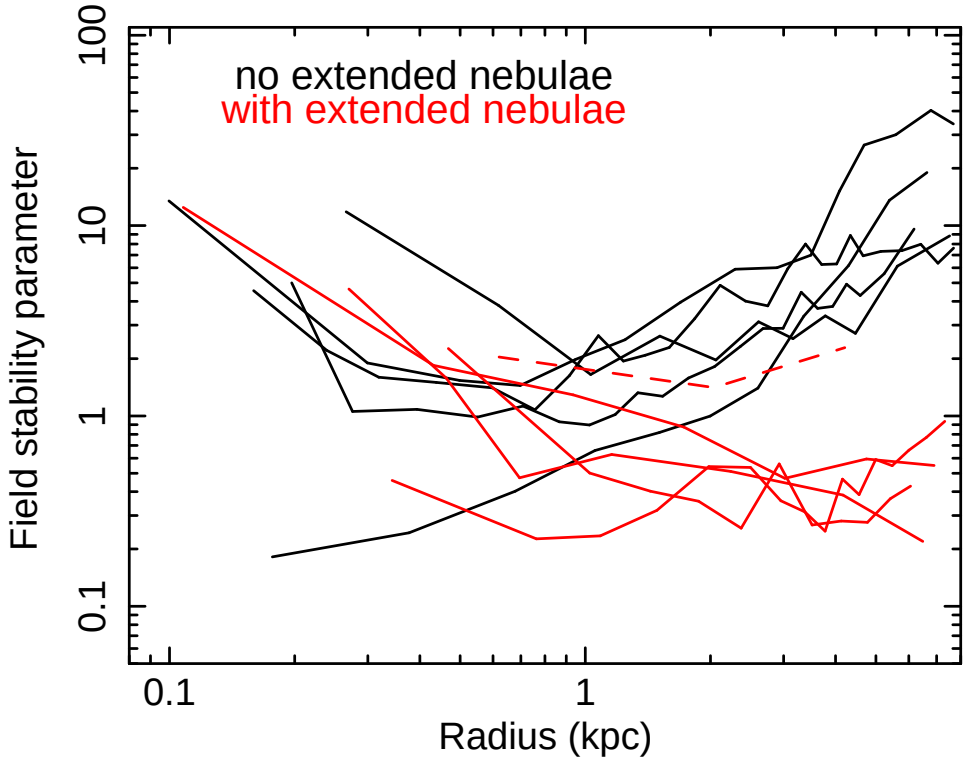

Figure 9.10: The Field criterion, $\Pi_{\rm F} = \kappa T/(n_{\rm e} n_{\rm H} \Lambda(T) r^2)$, as a function of radius for the galaxies that display extended emission line nebulae and [C II] line emission (shown in red) and for a sample of arguably cold-gas-poor systems (shown in black). The clear dichotomy, with the cold gas-rich systems being thermally unstable out to relatively large radii, indicates that the cold gas originates from the cooling hot phase. The galaxy NGC 6868, which shows evidence for a rotating disk of gas, is shown with a dashed line.

heating rate. This suppresses the growth of thermal instability unless the cooling time is comparable to the free-fall time or shorter (Cowie et al. 1980; Balbus & Soker 1989). Using numerical simulations, Sharma et al. (2012b) found that thermal instability is only significant when the cooling time is less than ~ 10 free fall times (see also McCourt et al. 2012; Kunz et al. 2012; Gaspari et al. 2012, 2013). However, this condition can be circumvented if an overdense gas blob is prevented from falling to its equilibrium position by the magnetic fields which pin the cloud to the ambient ICM (Nulsen 1986), or by rotational support in addition to buoyancy.

If a cooling cloud has sufficient angular momentum that is retained while it cools, it can cool unstably onto a non-radial orbit. This provides an alternative condition for thermal instability, that the viscous diffusion length in a cooling time, $\sqrt{\nu t_c}$, where ν is the kinematic viscosity and t_c is the cooling time, must be smaller than the size of a cloud. Analogous to the Field criterion, we define the stability parameter

$$\Pi_v = \frac{\nu t_c}{r^2}, \tag{9.3}$$

which needs to be smaller than about unity for thermal instability to develop on scales comparable to r. Viscous stresses in a plasma (Braginskii 1965) are much less sensitive to the structure of the magnetic field than conduction (e.g., Nulsen & McNamara 2013) and, although the stresses have a different tensor character in magnetized and unmagnetized plasmas, the viscosity itself is the same. Because the underlying process is diffusion controlled by Coulomb collisions in both cases (electrons for Π_F and ions for Π_v), the ratio of these two parameters is almost constant at $\Pi_v/\Pi_F \simeq 0.0253$. Numerical simulations are needed to determine a more accurate stability threshold, but we expect that the viscous diffusion length needs to be somewhat smaller than r for instability by this mechanism. The condition $\Pi_F < 5$ translates to $\Pi_v \lesssim 0.13$, or the diffusion length in one cooling time being $\lesssim 0.36r$. Although it is unclear which stability threshold takes precedence, we conclude that it is sufficient to test only one of these parameters, which we take to be Π_F, for stability.

Our *Herschel* data reveal that in two galaxies, NGC 6868 and NGC 7049, the cold gas forms rotating disks with radii $r \sim 3$ kpc. The disks of cold gas in these systems rotate with orbital velocities of up to 250 km s^{-1}. If this gas cooled from the hot phase, its rotation implies that the hot atmospheres of these systems have significant net angular momentum and the hot gas cools onto non- radial orbits. In the case of NGC 6868, this angular momentum may have been provided by gas sloshing indicated by the *Chandra* data (Machacek et al. 2010). Because the atmosphere is aspherical, heating originating from the center of the galaxy cannot balance the cooling rate locally throughout the atmosphere and so should not be expected to stop hot gas from cooling onto an extended disk. Because of this, and because rotational support prevents infall, instabilities may develop more easily and the gas may become thermally unstable at higher Π_F than in non-rotating systems. This is consistent with our results presented in Fig. 9.10, where Π_F for NGC 6868, shown with a dashed line, is higher than Π_F for the other systems containing non-rotating cold gas. The Field criterion still needs to be met, but the behavior of the stability parameter in NGC 6868 also indicates that the viscous stability criterion takes precedence.

However, in the context of the radiative cooling model, the presence of dust and PAHs within the cold gas clouds (Panuzzo et al. 2011) is intriguing. It suggests that at least some of the cold material originated from stellar mass loss (see also Voit & Donahue 2011; Donahue et al. 2011, for galaxy clusters). Our understanding of dust formation is, however, limited and it cannot be ruled out that dust may somehow form within the cold gas clouds (Fabian et al. 1994). Recent *Herschel* observations suggest that in the most massive galaxies, the dust mass is unconnected to the stellar populations, leading to the suggestion that the dust and the cold gas in these systems have been acquired externally (Smith et al. 2012). Rawle et al. (2012) show that the dust-to-stellar mass ratios in BCGs without line emitting nebulae are much smaller than in systems with cold gas. In the absence of cold gas clouds, the dust produced by stellar mass loss will get destroyed by sputtering and the tenuous gas, lost by stars, may get more easily mixed with and assimilated into the hot ISM. Therefore, if a galaxy loses all of its cold gas content (e.g. due to AGN activity), then stellar mass loss will likely become inefficient in rebuilding its cold gas reservoir. A galaxy that loses its cold gas content will therefore remain free of gas and dust until it again accretes cold material from the cooling hot phase or in a wet merger. This may have happened to NGC 1399 and NGC 4472. On the other hand, if a galaxy already contains clouds of cold gas (it either never lost its cold ISM or it accreted some cold material externally) then these clouds and filaments will help preserving the products of stellar mass loss (both the gas and the dust) by assimilating them as they plow through the galaxy.

In the systems with filamentary cold gas, the AGN jets and the buoyant bubbles of relativistic plasma seem to interact with the filaments, dragging them out from the center of the galaxy. As these filaments move through the hot ISM they may get penetrated by hot particles, which deposit energy into the cold gas heating and ionizing it. This interaction can both destroy the cold gas and contribute to the growth of its mass, depending on the energy input rate from the hot into the cold phase. In the context of this model, the total gas/dust mass will not correlate with the stellar mass of the galaxy, but it will depend on the balance between heating and cooling and on the interaction of the cold nebulae with the AGN (see also Mathews et al. 2013).

9.4.4 Fueling the AGN

The jet-powers, determined from the work required to inflate bubbles of relativistic plasma associated with the cavities in the hot X-ray emitting atmospheres, do not increase with the amount of cold gas in these galaxies. On the contrary, the two galaxies that lack any significant reservoirs of cold gas have the largest jet-powers in our sample. These galaxies, NGC 1399 and NGC 4472, also have the largest hot ISM densities in their cores. Accretion of hot gas in galaxies with high core densities can naturally result in higher jet powers, as has been demonstrated by the correlation between the Bondi accretion rates of hot gas and the observed jet powers in such ellipticals (Allen et al. 2006). The pressure and entropy distributions of the hot ISM in the cores of these two galaxies look remarkably regular, with the X-ray cavities/radio-lobes appearing at larger radii of $\sim$4 kpc and $\sim$8 kpc for NGC 4472 and NGC 1399, respectively.

Other nearby giant elliptical galaxies that appear morphologically relaxed in their

cores, such as NGC 4649, NGC 1407, NGC 4261, or NGC 1404, also do not display extended optical emission line nebulae (Macchetto et al. 1996; Baldi et al. 2009; Tremblay et al. 2009; Moustakas et al. 2010), indicating that they too are relatively depleted of cold gas. Interestingly, some of these morphologically relaxed cold-gas-poor systems, such as NGC 4261, have very large jet powers, with jets puncturing through the X-ray emitting galactic atmosphere to form giant lobes in the surrounding intragroup medium (O'Sullivan et al. 2011). For others, such as NGC 1404, NGC 4649, and NGC 1407, however, the current jet powers are more modest (Shurkin et al. 2008; Giacintucci et al. 2012).

Galaxies containing large reservoirs of cold gas, on the other hand, in general display strongly disturbed X-ray morphologies, possibly relating to earlier AGN outbursts impacting the cores of these systems. In principle, the presence of cold gas may affect both accretion and jet heating in these systems. Accretion of clumpy multiphase gas (hot plasma mixed with cooler, filamentary gas) may result in variable accretion rates and power output of the AGN jets, potentially triggering sporadic, larger outbursts than would be typical from the steady accretion of hot gas alone. Because of the relatively small volume filling fraction of this cooler gas, these outbursts may be relatively short (arguments for sporadic cold/multi-phase accretion in radio mode AGN in galaxy clusters have also been presented by Rafferty et al. 2006; Russell et al. 2013a).

As demonstrated by Morganti et al. (2013), radio-mechanical feedback does not only operate on the hot tenuous atmospheres of galaxies but also on the dense cold gas, which can be accelerated by jets to high speeds. Recent observations using ALMA also show that radio mode AGN activity can drive massive outflows of molecular gas from BCGs (Russell et al. 2013b; McNamara et al. 2013). In systems with large cold gas reservoirs, jets may be more easily slowed by coupling to this material, and may therefore deposit most of their energy at smaller radii. This will result in more disturbed central thermodynamic distributions and, in particular may decrease the central hot ISM density, resulting in lower hot gas accretion rates between the relatively brief periods of multiphase accretion. Any reduction in the accretion rates from the hot gas would result in smaller jet powers, consistent with the observations presented here.

Numerical simulations (Wagner & Bicknell 2011; Wagner et al. 2012) have shown that radio jets can be efficient in clearing the central regions of galaxies of their cold gas, provided that the cold gas clouds are porous, clumpy, and have small volume filling fractions, with individual clouds being relatively small, which again are characteristics consistent with the observations discussed here. Powerful jets may thus eventually destroy or remove most of the cold gas in the cores of the galaxies, allowing the jets to propagate further out and deposit their energy at larger radii, increasing the entropy of the hot galactic atmospheres. This in turn will allow the density of the hot gas in the core of the galaxy to increase, thus increasing the jet power. The central regions of galaxies cleared of cold gas may acquire relaxed morphologies within the central $r \sim 5$ kpc over $\sim 5 \times 10^7$ yr or a few sound crossing times. The similarity of the thermodynamic profiles of elliptical galaxies with highly relaxed X-ray morphologies (see black data points in Fig. 9.9 and Werner et al. 2012) indicates that, after elliptical galaxies are cleared of cold gas, jet heating and cooling of their hot atmospheres comes to an equilibrium in an approximately universal manner. The galaxies may maintain

these equilibria until they are disturbed by a merger event.

9.5 Conclusions

Using FIR, optical, and X-ray data, we study the ISM in eight nearby, X-ray and optically bright, giant elliptical galaxies, all central dominant members of relatively low mass groups. We find that:

- All systems with extended Hα emission in our sample (6/8 galaxies) display significant [C II] line emission that traces $\sim$100 K gas.

- This emission is co-spatial with the optical Hα+[N II] emitting nebulae and the lowest entropy soft X-ray emitting plasma.

- These systems have similar [C II]/(Hα+[N II]) ratios of 0.4–0.8, indicating that the [C II] and Hα+[N II] emission are powered by the same energy source. The likely dominant source of energy is the hot X-ray emitting plasma penetrating into the cold gas.

- The entropy profiles of the hot galactic atmospheres show a clear dichotomy, with the systems displaying extended emission line nebulae having lower entropies beyond $r \gtrsim 1$ kpc than the cold-gas-poor systems. We show that while the hot atmospheres of the cold-gas-poor galaxies are thermally stable outside of their innermost cores, the atmospheres of the cold-gas-rich systems are prone to cooling instabilities. This provides considerable weight to the argument that cold gas in giant ellipticals is produced chiefly by cooling from the hot phase. We show that cooling instabilities may develop more easily in rotating systems and discuss an alternative condition for thermal instability for this case.

- The hot atmospheres of cold-gas-rich galaxies display disturbed morphologies indicating that the accretion of clumpy multiphase gas in these systems may result in variable power output of the AGN jets, potentially triggering sporadic, larger outbursts. The jets may be more easily slowed by coupling to the dense cold material and may therefore deposit most of their energy at smaller radii, resulting in the observed disturbed central thermodynamic distributions.

- In the two cold-gas-poor, X-ray morphologically relaxed galaxies of our sample, NGC 1399 and NGC 4472, powerful AGN outbursts may have destroyed or removed most of the cold gas from the cores, allowing the jets to propagate and deposit most of their energy further out, increasing the entropy of the hot galactic atmospheres and leaving their cores relatively undisturbed. These observations indicate that radio-mechanical AGN feedback is likely to play a crucial role in clearing giant elliptical galaxies of their cold gas, keeping them 'red and dead'.

Acknowledgments

This work is based in part on observations made with Herschel, a European Space Agency Cornerstone Mission with significant participation by NASA. Support for this work was provided by NASA through award number 1428053 issued by JPL/Caltech. This work is based in part on observations obtained at the Southern Astrophysical Research (SOAR) telescope, which is a joint project of the Ministério da Ciência, Tecnologia, e Inovação (MCTI) da República Federativa do Brasil, the U.S. National Optical Astronomy Observatory (NOAO), the University of North Carolina at Chapel Hill (UNC), and Michigan State University (MSU). SWA acknowledges support from the U.S. Department of Energy under contract number DE-AC02-76SF00515. MR acknowledges the NSF grant AST 1008454 and NASA ATP grant (12-ATP12-0017).

Chapter 10

A uniform metal distribution in the intergalactic medium of the Perseus cluster of galaxies

N. Werner[1,2], *O. Urban*[1,2,3], *A. Simionescu*[1,2,4], *S. W. Allen*[1,2,3]

[1]Kavli Institute for Particle Astrophysics and Cosmology, Stanford University, 452 Lomita Mall, Stanford, CA 94305-4085, USA
[2]Department of Physics, Stanford University, 382 Via Pueblo Mall, Stanford, CA 94305-4060, USA
[3]SLAC National Accelerator Laboratory, 2575 Sand Hill Road, Menlo Park, CA 94025, USA
[4]Institute of Space and Astronautical Science (ISAS), JAXA, 3-1-1 Yoshinodai, Chuo-ku, Sagamihara, Kanagawa 252-5210, Japan

Published in Nature, volume 7473, pages 656–658, 2013

Most of the metals (elements heavier than helium) ever produced by stars in the member galaxies of galaxy clusters currently reside within the hot, X-ray emitting intra-cluster gas. Observations of X-ray line emission from this intergalactic medium have suggested a relatively small cluster-to-cluster scatter outside of the cluster centers (Matsushita 2011; Leccardi & Molendi 2008) and enrichment with iron out to large radii (Fujita et al. 2008b; Simionescu et al. 2011; Urban et al. 2011) leading to the idea that the metal enrichment occurred early in the history of the Universe (Fujita et al. 2008b). Models with early enrichment predict a uniform metal distribution at large radii in clusters, while late-time enrichment, favored by some previous studies (Balestra et al. 2007; Maughan et al. 2008), is expected to introduce significant spatial variations of the metallicity. To discriminate clearly between these competing models, it is essential to test for potential inhomogeneities by measuring the abundances out to large radii along multiple directions in clusters, which has not hitherto been done. Here we report a remarkably uniform measured iron abundance, as a function of radius and azimuth, that is statistically consistent with

a constant value of $Z_{\rm Fe} = 0.306 \pm 0.012$ Solar out to the edge of the nearby Perseus Cluster. This homogeneous distribution requires that most of the metal enrichment of the intergalactic medium occurred before the cluster formed, likely over 10 billion years ago, during the period of maximal star formation and black hole activity.

Between 2009 and 2011, we obtained a total of 84 observations of the Perseus Cluster with the *Suzaku* X-ray satellite, as a Key Project for that mission. The pointings covered eight azimuthal directions from the cluster center out to an offset angle of 2 degrees, with a total exposure time of over 1 million seconds. We have analyzed the data from all three functioning X-ray Imaging Spectrometers, extracting spectra from annuli centered on the cluster center. We modeled the spectra from each of the 76 independent regions as a single-temperature thermal plasma in collisional ionization equilibrium, with the temperature, iron abundance, and spectrum normalization included as free parameters (Urban et al. 2014).

The measured radial and azimuthal variation of the iron abundance of the hot intracluster medium (ICM) out to the edge of the Perseus Cluster along the eight different directions is presented in Fig. 10.1. We define this 'edge as r_{200}, the radius within which the mean enclosed mass density of the cluster is 200 times the critical density of the Universe at the cluster redshift (for the Perseus Cluster $r_{200} = 1.8$ Mpc, corresponding to 82 arcmin4). We have tested the statistical uniformity of the measured iron abundance at radii $r > 400$ kpc (i.e. beyond the central metallicity peak associated with the brightest cluster galaxy Simionescu et al. 2011; De Grandi et al. 2004) by modeling the data from all radii and azimuths with a constant abundance. The measured chi-square value of 65.8 for 75 degrees of freedom is consistent with the null hypothesis of a constant iron abundance with a value of $Z_{\rm Fe} = 0.306 \pm 0.012$ Solar (68% confidence limit; we adopt a Solar iron abundance of 3.24×10^{-5} relative to hydrogen by number Feldman 1992). This abundance is also consistent with the mean value measured at intermediate radii ($\sim$ 0.2–0.5r_{200}) for a sample of 48 clusters previously observed with *XMM-Newton* (Leccardi & Molendi 2008). The iron abundance values measured at large radii in the less massive Virgo Cluster are lower, although these are likely biased by the multi-temperature structure of the gas in that system (Urban et al. 2011). The azimuthally averaged iron abundance profile for the Perseus Cluster is shown in Fig. 10.2.

Enrichment scenarios in which the ICM is predominantly enriched with metals after the formation of clusters predict a non-uniform metal distribution, which is inconsistent with the observations presented here. Ram-pressure stripping (Gunn & Gott 1972) would result in a negative gradient in the metal abundance profiles out to large radii, as well as significant azimuthal variations, with higher metal abundances expected along directions connecting to surrounding large scale structure filaments (Domainko et al. 2006). Furthermore, metals ejected by galaxies at later times should roughly follow the distribution of galaxies, producing an approximately constant metal mass to light ratio, which is also inconsistent with observations (Matsushita et al. 2013). Although large scale sloshing motions (Simionescu et al. 2012) may be able to mix metals to some degree, the strong gradients in the entropy distributions of cluster atmospheres (Voit

et al. 2005), including Perseus (Simionescu et al. 2011; Urban et al. 2014), make the ICM convectively stable, prohibiting the efficient mixing of metals that are initially non-uniformly distributed across large radial ranges.

The observed uniform iron abundance distribution at large radii in the Perseus Cluster requires early enrichment of the intergalactic gas in the proto-cluster environment. This enrichment was most likely driven primarily by galactic winds (De Young 1978) - energetic outflows of metal enriched gas - which are expected to be strongest at epochs around the peak of star formation and active galactic nuclei (AGN) activity (redshifts $z \sim 2$–3, or lookback times of 10–12 billion years Madau et al. 1996; Brandt & Hasinger 2005). The combined energy of supernova explosions (De Young 1978) and AGN (Fabjan et al. 2010) must have been strong enough to expel most of the metals from the galaxies at early times, and enrich and mix the intergalactic gas. This gas was later accreted by clusters and virialized (increasing its entropy through shock heating) to form the present ICM.

The total iron mass in the ICM of the Perseus Cluster, calculated from the measured iron abundance and ICM density profiles (Urban et al. 2014), is about 50 billion Solar masses, with about 60% residing beyond $0.5r_{200}$. The dominant fraction of this iron was likely supplied by type Ia supernovae (SNIa), which are thought to have produced 60-90% of iron in the Perseus Cluster (Matsushita et al. 2013) depending on the assumed supernova yields. Based on our measurements, we estimate that at least 40 billion SNIa contributed to the chemical enrichment of the proto-cluster environment that later formed the Perseus Cluster. For such a large iron mass to be expelled by the winds from the galaxies at early times, a significant fraction of these SNIa must have exploded shortly after the epoch of peak star-formation. This is consistent with recent findings based on SNIa delay time distributions (Mannucci et al. 2006; Maoz et al. 2012), which imply that a large fraction of SNIa explode less than $\sim 5 \times 10^8$ years after the formation of the progenitor binary system (prompt SNIa). SNIa with longer delay times will continue contributing to the enrichment of the ICM after clusters virialize, and are expected to be partly responsible for the metallicity peaks surrounding the brightest cluster galaxies in the centers of many clusters (Böhringer et al. 2004).

A unique prediction of the early enrichment scenario is that essentially all galaxy clusters with masses comparable to the Perseus Cluster should have homogeneous iron abundance distributions of about one-third Solar at large radii. Also, contrary to some initial findings (Balestra et al. 2007; Maughan et al. 2008), there should be no substantial redshift evolution in the ICM metallicity outside of the central regions of clusters, out to $z \sim 2$. The presence and strength of such evolution are a matter of ongoing debate (Leccardi & Molendi 2008; Baldi et al. 2012; Andreon 2012). The observed large iron abundance of the high-entropy gas in the outskirts of the Perseus Cluster is also consistent with the idea that the highest-energy cosmic rays (above a few 10^{18} eV) may be primarily iron nuclei (Abraham et al. 2010) accelerated by cluster formation shocks (Norman et al. 1995). Additionally, because much of the metal rich ICM seen at large radii has been accreted from the surrounding large scale structure filaments, our model predicts that the tenuous warm-hot intergalactic medium (WHIM) permeating the cosmic web, in which up to half of the baryons in the Universe currently reside (Cen & Ostriker 1999; Davé et al. 2001), is likely to be substantially enriched in

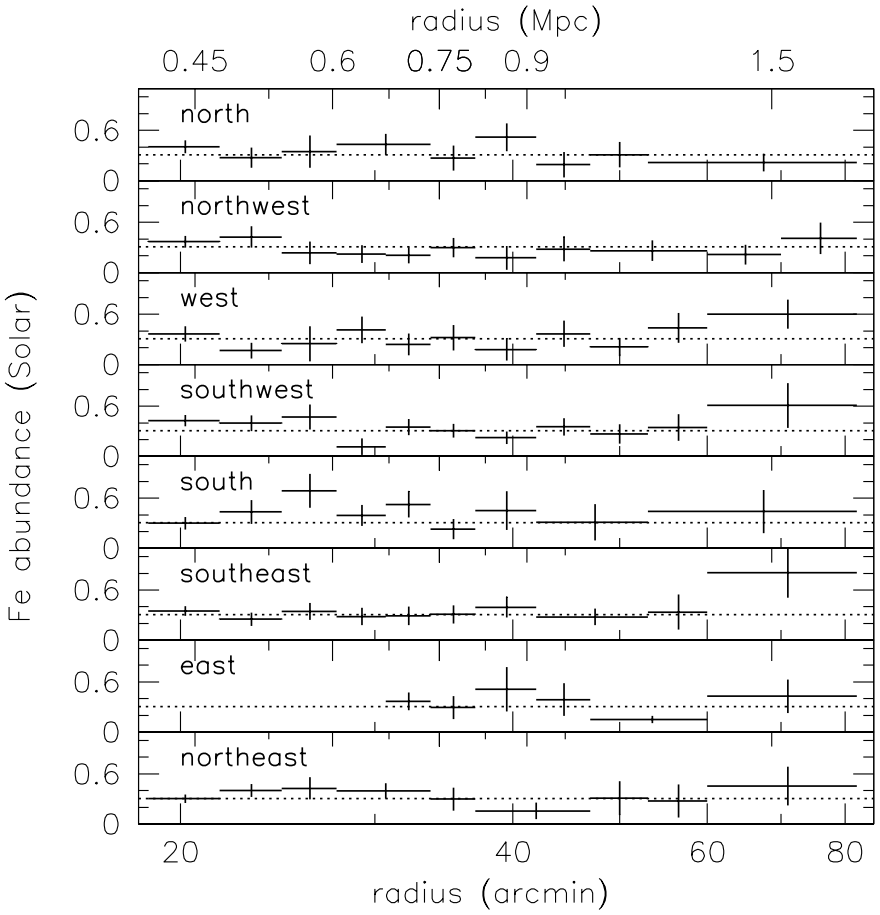

Figure 10.1: Iron abundance profiles expressed in Solar units (Feldman 1992) measured along eight different directions in the Perseus Cluster. At the temperature of the Perseus Cluster, the iron abundance measurement is driven by the Fe-K lines. Compared to the Fe-L lines, these lines are significantly less prone to systematic biases associated with the presence of multi-temperature gas. The spectral extraction regions span a relatively small range in radius and azimuth, where the plasma can be well approximated as single-temperature. There is no evidence for a bias in the temperature measurements due to gas clumping (Urban et al. 2014). We have verified that spectral fits with the Fe-L line complex (0.8–1.5 keV energy range) excluded give consistent results to those in the full 0.7–7 keV band. Collisional ionization and electron-ion equilibrium are likely to hold out to r_{200} in the Perseus Cluster, where the equilibration timescales are only $\sim 3.5 \times 10^8$ yr and $\sim 7.3 \times 10^8$ yr, respectively.Within a radius $r \sim 400$ kpc ($\sim 0.2 r_{200}$; not shown here) metal enrichment is strongly influenced by the brightest cluster galaxy and the metallicity is centrally peaked (Simionescu et al. 2011; De Grandi et al. 2004). Along the eastern direction, large scale sloshing motions are present and are uplifting the ICM from smaller radii out to $r \sim 650$ kpc (Simionescu et al. 2012). Thus we also do not present results for $r < 650$ kpc in this direction. Beyond these radii, the iron abundance measurements are consistent with a radially and azimuthally constant value of $Z_{\rm Fe} = 0.306 \pm 0.012$ Solar, indicated by the dotted lines. Expressed in units of an older, and historically more commonly used Solar iron abundance value (Anders & Grevesse 1989), our best fit constant iron abundance is $Z_{\rm Fe} = 0.212 \pm 0.008$ Solar. The plotted error bars are 68% confidence intervals.

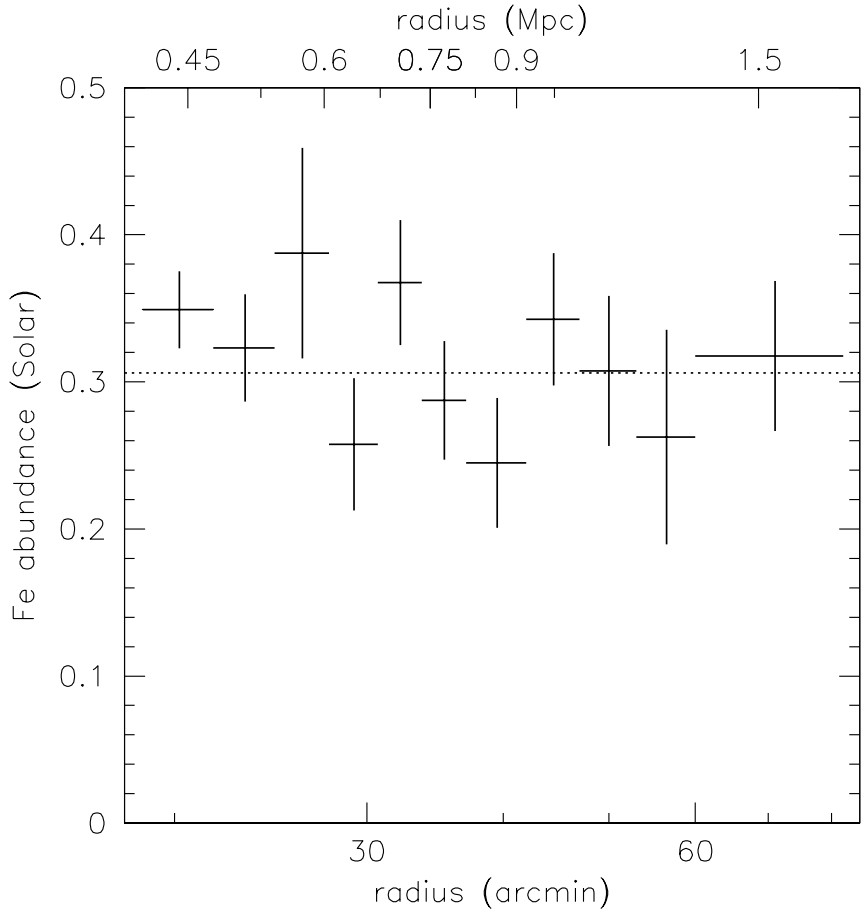

Figure 10.2: Azimuthally averaged iron abundance profile for the Perseus Cluster. The profile was determined by simultaneous fitting of the spectra at a given radius for all eight azimuthal directions. While the iron abundance was assumed to be the same in all directions in the fits, the temperatures and spectral normalizations were allowed to vary independently along the different azimuths. The dotted line shows the best fit constant iron abundance value of $Z_{\rm Fe} = 0.306$ Solar. The plotted error bars are 68% confidence intervals. Our iron abundance values are lower than the value measured in the 650–1100 kpc range with *XMM-Newton* (Matsushita et al. 2013); however, the *XMM-Newton* measurement suffers from significant systematic uncertainties due to the high and variable particle background of that instrument compared to *Suzaku*.

metals. The same is true for the hot circumgalactic gas accreted by galaxies from the intergalactic-medium.

Acknowledgements

The authors are grateful for discussions with other members of the Perseus Cluster Suzaku Key project collaboration, as well as with Yu Lu, Paul Simeon, and Roger Blandford. This work was supported by the Suzaku grants NNX09AV64G, NNX10AR48G, NASA ADAP grant NNX12AE05G, and by the U.S. Department of Energy under contract number DE-AC02-76SF00515.

Chapter 11

Summary and outlook

In the enclosed papers, we advanced our understanding of the radio-mode AGN feedback, and of the microphysics and the chemical enrichment of the ICM. We provided some of the clearest views to date of AGN feedback in action, stripping central cluster galaxies of their lowest entropy gas (Chapter 2 and 3; Werner et al. 2010, 2011); developed the use of resonance scattering of X-ray spectral lines to measure AGN induced turbulence in the hot ISM of giant elliptical galaxies (Chapter 5; Werner et al. 2009); placed constraints on the viscosity, conductivity and the structure of intra-cluster magnetic fields (Chapter 6 and 7; Werner et al. 2015, 2016); discovered large reservoirs of cold gas in nearby giant elliptical galaxies (previously thought to be 'red and dead') and showed that the cold gas observed in giant ellipticals is produced chiefly by thermally unstable cooling from the hot phase (Chapter 9 and 8; Werner et al. 2014, 2013a); and by pioneering the application of X-ray measurements to study the outskirts of galaxy clusters, we discovered that the hot intergalactic medium in cluster outskirts is clumpy and must have experienced the bulk of its metal enrichment over 10 billion years ago (these studies were published in articles in Science and Nature by Simionescu et al. 2011 and Werner et al. 2013b; see Chapter 10).

Our knowledge will be significantly advanced in the coming years due to the improved observing capabilities of the *Hitomi* (*ASTRO-H*) satellite, launched on 2016 February 17. Next to the standard X-ray observables such as the density, temperature, and metallicity, the revolutionary capabilities of *Hitomi*, for the first time, enable direct measurements of the ICM dynamics. The X-ray calorimeters on *Hitomi* provide a factor of 30 improvement in spectral resolution compared to the current state-of-the-art CCD-type detectors. This enables detailed measurements of line centroid shifts and velocity broadening of X-ray emission lines, allowing us to tightly constrain both coherent motions and small scale turbulence in the ICM (see Fig. 11.1). *Hitomi* will thus perform the first direct kinematic measurements of the interaction of the ICM with the jets and the buoyant relativistic plasma.

I led the development of the observing strategy for some of the highest priority galaxy and cluster observations for the *Hitomi* satellite and I am leading the analysis of some of the first data obtained by this mission. Breakthroughs in our understanding of the intimate connection between the IGM, star formation and the growth of supermassive black holes are virtually guaranteed. I plan to use deep observations of the

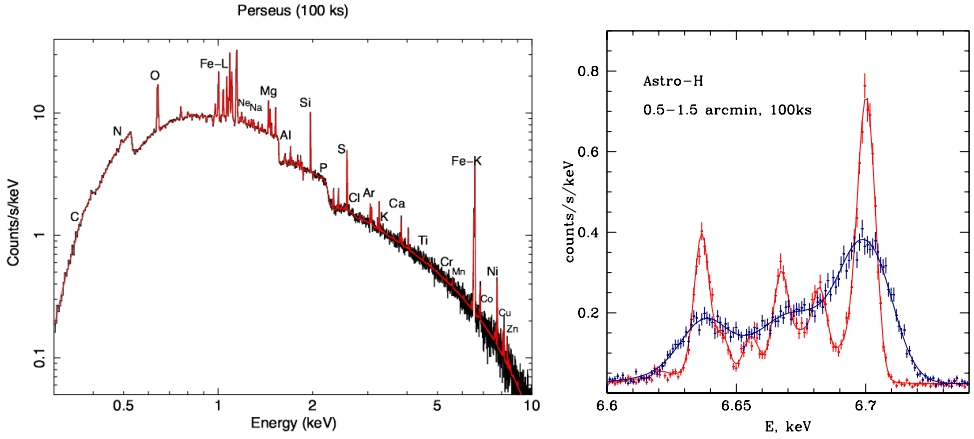

Figure 11.1: These simulated *Hitomi* (*ASTRO-H*) spectra for a 100 ks observation of the core of the Perseus Cluster illustrate the revolutionary diagnostic capabilities of the new calorimeter-type Soft X-ray Spectrometer (SXS). The 5 eV spectral resolution of SXS provides a factor of 30 improvement compared to the current state of-the-art CCD-type detectors, allowing to separate previously unresolved spectral lines. The spectrum in the full energy band (left panel) illustrates the wealth of lines and chemical elements that we will detect. The zoom-in to the energy band of the He-like Fe-K line complex (right panel) shows spectra without velocity broadening and with a broadening of $\sigma_{\rm v} = 330$ km s^{-1}, illustrating the power of high resolution X-ray spectroscopy in measuring the ICM velocities.

Figure 11.2: A composite optical (*HST*), infrared (*Spitzer*), and X-ray (*Chandra*) image of the starburst galaxy M 82. The X-ray emission is shown in blue. The collective energy of exploding supernovae and stellar winds blows the metal rich gas out of the galaxy, enriching and heating the surrounding intergalactic medium. *Hitomi* observations of this galaxy and of NGC 253 will allow us to measure the velocity, thermal state, and the metallicity of the out-flowing hot phase and estimate its momentum.

nearest, brightest galaxy clusters to measure and compare the turbulent velocities on different spatial scales. Mapping the turbulent motions of the ICM in nearby galaxy clusters will provide critical information about the driving and dissipation scales of turbulence, which on small scales is sensitive to viscosity. While for a low-viscosity ICM we expect to see relatively strong small scale turbulence, a highly viscous ICM will be less turbulent, with gas motions, especially on small scales, quickly dissipating into heat. The high-quality *Hitomi* spectra will also allow us to resolve spectral lines from different ionization levels and thus measure the detailed temperature structure of the gas, placing important constraints on radiative cooling, multi-phasedness, and on the dissipation and distribution of heat in the ICM. In the same time, the spectacular, sub-arcsecond imaging capabilities of Chandra will remain unsurpassed for the next 20 years, and ultra-deep observations with this instrument will continue to provide opportunities for breakthroughs in our understanding of the microphysics of the hot plasma (e.g. see Zhuravleva et al. 2014a; Werner et al. 2016).

Most of the metals in the IGM/ICM are believed to have escaped the galaxies due to supernova- and AGN-driven outflows (see the outflows from M 82 in Fig. 11.2) and only a significantly smaller fraction of metals escapes due to ram-pressure stripping and galaxy-galaxy interactions. The physics and the energetics of these outflows, and the mixing of the metals with the ambient IGM, are poorly understood. *Hitomi* will allow us, for the first time, to measure the velocity, thermal state, and the metallicity of the outflowing hot phase and estimate its momentum. These results will provide crucial ingredients for galaxy formation models.

Our experience with *Hitomi*, will be invaluable in the development of the approved, future, L-class (budget of 1 Billion EUR) X-ray mission *Athena* (see Fig. 11.3). I also plan to help in the development of a future satellite aimed at detecting and mapping the tenuous warm-hot intergalactic medium permeating the cosmic web (*DIOS* being proposed to JAXA). Together with new instruments operating in other wavelengths (e.g. the James Webb Space Telescope, 30-meter class optical and near-infrared telescopes), the progress in technology in the next decade will allow the extension of this research to the faint unvirialized intergalactic gas and the high-redshift Universe.

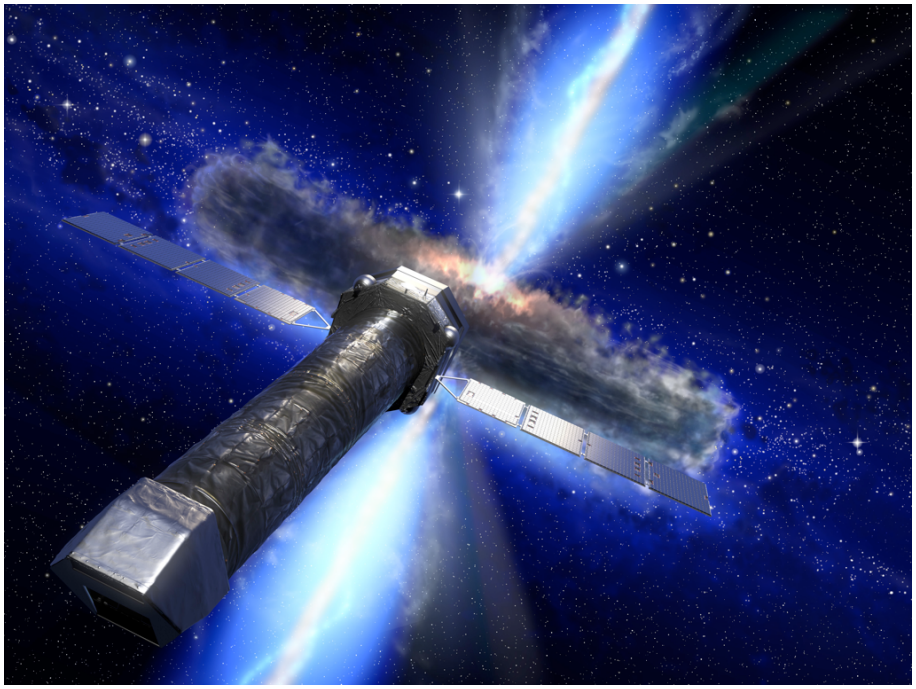

Figure 11.3: *Athena*, the future, large (budget of over 1 Billion EUR) X-ray mission approved by the European Space Agency. *Hitomi* (ASTRO-H) can be considered a pathfinder for *Athena*. We will capitalize on our experience with *Hitomi* in the development of this ambitious European mission.

References

Abraham, J., Abreu, P., Aglietta, M., et al. 2010, Physical Review Letters, 104, 091101
Allen, S. W., Dunn, R. J. H., Fabian, A. C., Taylor, G. B., & Reynolds, C. S. 2006, MNRAS, 372, 21
Allen, S. W., Evrard, A. E., & Mantz, A. B. 2011, ARA&A, 49, 409
Allen, S. W., Fabian, A. C., Edge, A. C., Bohringer, H., & White, D. A. 1995, MNRAS, 275, 741
Allen, S. W., Rapetti, D. A., Schmidt, R. W., et al. 2008, MNRAS, 383, 879
Allen, S. W., Taylor, G. B., Nulsen, P. E. J., et al. 2001, MNRAS, 324, 842
Andernach, H., Baker, J. R., von Kap-Herr, A., & Wielebinski, R. 1979, A&A, 74, 93
Anders, E. & Grevesse, N. 1989, Geochim. Cosmochim. Acta, 53, 197
Andreon, S. 2012, A&A, 546, A6
Annibali, F., Bressan, A., Rampazzo, R., Zeilinger, W. W., & Danese, L. 2007, A&A, 463, 455
Annibali, F., Bressan, A., Rampazzo, R., et al. 2010, A&A, 519, A40
Arévalo, P., Churazov, E., Zhuravleva, I., Forman, W. R., & Jones, C. 2015, ArXiv e-prints
Arnaud, K. A. 1996, in Astronomical Society of the Pacific Conference Series, Vol. 101, Astronomical Data Analysis Software and Systems V, ed. G. H. Jacoby & J. Barnes, 17
Ascasibar, Y. & Markevitch, M. 2006, ApJ, 650, 102
Bîrzan, L., Rafferty, D. A., McNamara, B. R., Wise, M. W., & Nulsen, P. E. J. 2004, ApJ, 607, 800
Baars, J. W. M., Genzel, R., Pauliny-Toth, I. I. K., & Witzel, A. 1977, A&A, 61, 99
Balbus, S. A. & Soker, N. 1989, ApJ, 341, 611
Baldi, A., Ettori, S., Molendi, S., et al. 2012, A&A, 537, A142
Baldi, A., Forman, W., Jones, C., et al. 2009, ApJ, 707, 1034
Baldwin, J. A., Phillips, M. M., & Terlevich, R. 1981, PASP, 93, 5
Balestra, I., Tozzi, P., Ettori, S., et al. 2007, A&A, 462, 429
Balucinska-Church, M. & McCammon, D. 1992, ApJ, 400, 699
Begelman, M. C. & Fabian, A. C. 1990, MNRAS, 244, 26P
Beiersdorfer, P., Schweikhard, L., Liebisch, P., & Brown, G. V. 2008, ApJ, 672, 726
Belsole, E., Sauvageot, J. L., Böhringer, H., et al. 2001, A&A, 365, L188
Bertin, E. 2006, in Astronomical Society of the Pacific Conference Series, Vol. 351, Astronomical Data Analysis Software and Systems XV, ed. C. Gabriel, C. Arviset, D. Ponz, & S. Enrique, 112–+

Bertin, E., Mellier, Y., Radovich, M., et al. 2002, in Astronomical Society of the Pacific Conference Series, Vol. 281, Astronomical Data Analysis Software and Systems XI, ed. D. A. Bohlender, D. Durand, & T. H. Handley, 228–+
Best, P. N., Kauffmann, G., Heckman, T. M., et al. 2005, MNRAS, 362, 25
Biller, B. A., Jones, C., Forman, W. R., Kraft, R., & Ensslin, T. 2004, ApJ, 613, 238
Biretta, J. A., Sparks, W. B., & Macchetto, F. 1999, ApJ, 520, 621
Bîrzan, L., McNamara, B. R., Nulsen, P. E. J., Carilli, C. L., & Wise, M. W. 2008, ApJ, 686, 859
Blakeslee, J. P., Jordán, A., Mei, S., et al. 2009, ApJ, 694, 556
Bland-Hawthorn, J. & Maloney, P. R. 1999, ApJ, 510, L33
Bock, D., Large, M. I., & Sadler, E. M. 1999, AJ, 117, 1578
Bohlin, R. C., Savage, B. D., & Drake, J. F. 1978, ApJ, 224, 132
Böhringer, H., Matsushita, K., Churazov, E., Finoguenov, A., & Ikebe, Y. 2004, A&A, 416, L21
Böhringer, H., Matsushita, K., Churazov, E., Ikebe, Y., & Chen, Y. 2002, A&A, 382, 804
Böhringer, H., Nulsen, P. E. J., Braun, R., & Fabian, A. C. 1995, MNRAS, 274, L67
Bonamente, M., Lieu, R., Mittaz, J. P. D., Kaastra, J. S., & Nevalainen, J. 2005, ApJ, 629, 192
Bondi, H. 1952, MNRAS, 112, 195
Bottinelli, L. & Gouguenheim, L. 1977, A&A, 60, L23
Bottinelli, L. & Gouguenheim, L. 1979, A&A, 74, 172
Braginskii, S. I. 1965, Reviews of Plasma Physics, 1, 205
Brandt, W. N. & Hasinger, G. 2005, ARA&A, 43, 827
Bregman, J. N. & Parriott, J. R. 2009, ApJ, 699, 923
Brüggen, M. 2003, ApJ, 592, 839
Brüggen, M. & Kaiser, C. R. 2002, Nature, 418, 301
Buote, D. A. 2000a, ApJ, 539, 172
Buote, D. A. 2000b, MNRAS, 311, 176
Burns, J. O., Hallman, E. J., Gantner, B., Motl, P. M., & Norman, M. L. 2008, ApJ, 675, 1125
Buson, L. M., Sadler, E. M., Zeilinger, W. W., et al. 1993, A&A, 280, 409
Canning, R. E. A., Fabian, A. C., Johnstone, R. M., et al. 2011, MNRAS, 417, 3080
Canning, R. E. A., Russell, H. R., Hatch, N. A., et al. 2012, MNRAS, 420, 2956
Canning, R. E. A., Sun, M., Sanders, J. S., et al. 2013, ArXiv e-prints
Caon, N., Macchetto, D., & Pastoriza, M. 2000, ApJS, 127, 39
Cappellaro, E., Evans, R., & Turatto, M. 1999, A&A, 351, 459
Cardelli, J. A., Clayton, G. C., & Mathis, J. S. 1989, ApJ, 345, 245
Cavagnolo, K. W., Donahue, M., Voit, G. M., & Sun, M. 2008, ApJ, 683, L107
Cavagnolo, K. W., Donahue, M., Voit, G. M., & Sun, M. 2009, ApJS, 182, 12
Cen, R. & Ostriker, J. P. 1999, ApJ, 514, 1
Chandran, B. D. G., Cowley, S. C., Ivanushkina, M., & Sydora, R. 1999, ApJ, 525, 638
Chandrasekhar, S. 1961, Hydrodynamic and hydromagnetic stability (Oxford: Clarendon, 1961)
Churazov, E., Brüggen, M., Kaiser, C. R., Böhringer, H., & Forman, W. 2001, ApJ, 554, 261

Churazov, E., Forman, W., Jones, C., & Böhringer, H. 2000, A&A, 356, 788
Churazov, E., Forman, W., Jones, C., & Böhringer, H. 2003, ApJ, 590, 225
Churazov, E., Forman, W., Jones, C., Sunyaev, R., & Böhringer, H. 2004, MNRAS, 347, 29
Churazov, E., Forman, W., Vikhlinin, A., et al. 2008, MNRAS, 388, 1062
Churazov, E. & Inogamov, N. 2004, MNRAS, 350, L52
Churazov, E., Ruszkowski, M., & Schekochihin, A. 2013, ArXiv e-prints
Churazov, E., Sunyaev, R., Forman, W., & Böhringer, H. 2002, MNRAS, 332, 729
Churazov, E., Tremaine, S., Forman, W., et al. 2010, MNRAS, 404, 1165
Churazov, E., Vikhlinin, A., Zhuravleva, I., et al. 2012, MNRAS, 421, 1123
Combes, F., Young, L. M., & Bureau, M. 2007, MNRAS, 377, 1795
Condon, J. J., Cotton, W. D., & Broderick, J. J. 2002, AJ, 124, 675
Condon, J. J., Cotton, W. D., Greisen, E. W., et al. 1998, AJ, 115, 1693
Cowie, L. L., Fabian, A. C., & Nulsen, P. E. J. 1980, MNRAS, 191, 399
Cowie, L. L., Hu, E. M., Jenkins, E. B., & York, D. G. 1983, ApJ, 272, 29
Cowie, L. L. & McKee, C. F. 1977, ApJ, 211, 135
Cravens, T. E. 1997, Geophys. Res. Lett., 24, 105
Crawford, C. S., Allen, S. W., Ebeling, H., Edge, A. C., & Fabian, A. C. 1999, MNRAS, 306, 857
Crawford, C. S. & Fabian, A. C. 1992, MNRAS, 259, 265
Crawford, C. S., Sanders, J. S., & Fabian, A. C. 2005, MNRAS, 361, 17
Crawford, M. K., Genzel, R., Townes, C. H., & Watson, D. M. 1985, ApJ, 291, 755
Croton, D. J., Springel, V., White, S. D. M., et al. 2006, MNRAS, 365, 11
Das, P., Gerhard, O., Churazov, E., & Zhuravleva, I. 2010, MNRAS, 409, 1362
Davé, R., Cen, R., Ostriker, J. P., et al. 2001, ApJ, 552, 473
David, L. P., Jones, C., Forman, W., et al. 2009, ApJ, 705, 624
David, L. P., O'Sullivan, E., Jones, C., et al. 2011, ApJ, 728, 162
de Gasperin, F., Ogrean, G. A., van Weeren, R. J., et al. 2015, MNRAS, 448, 2197
De Grandi, S., Ettori, S., Longhetti, M., & Molendi, S. 2004, A&A, 419, 7
De Lucia, G. & Blaizot, J. 2007, MNRAS, 375, 2
de Plaa, J., Werner, N., Bykov, A. M., et al. 2006, A&A, 452, 397
de Plaa, J., Werner, N., Simionescu, A., et al. 2010, A&A, 523, A81
de Plaa, J., Zhuravleva, I., Werner, N., et al. 2012, A&A, 539, A34
De Young, D. S. 1978, ApJ, 223, 47
De Young, D. S. 2003, MNRAS, 343, 719
den Herder, J. W., Brinkman, A. C., Kahn, S. M., et al. 2001, A&A, 365, L7
Dennerl, K. 2002, A&A, 394, 1119
Dennerl, K. 2010, Space Sci. Rev., 157, 57
Dickey, J. M. & Lockman, F. J. 1990, ARA&A, 28, 215
Domainko, W., Mair, M., Kapferer, W., et al. 2006, A&A, 452, 795
Donahue, M., de Messières, G. E., O'Connell, R. W., et al. 2011, ApJ, 732, 40
Donahue, M., Mack, J., Voit, G. M., et al. 2000, ApJ, 545, 670
Donahue, M., Stocke, J. T., & Gioia, I. M. 1992, ApJ, 385, 49
Donahue, M. & Voit, G. M. 1991, ApJ, 381, 361
Doron, R. & Behar, E. 2002, ApJ, 574, 518

Dunn, R. J. H., Allen, S. W., Taylor, G. B., et al. 2010, MNRAS
Dunn, R. J. H. & Fabian, A. C. 2006, MNRAS, 373, 959
Dunn, R. J. H. & Fabian, A. C. 2008, MNRAS, 385, 757
Dunn, R. J. H., Fabian, A. C., & Taylor, G. B. 2005, MNRAS, 364, 1343
Durret, F., Wakamatsu, K., Nagayama, T., Adami, C., & Biviano, A. 2015, A&A, 583, A124
Eckert, D., Molendi, S., & Paltani, S. 2011, A&A, 526, A79
Edge, A. C. 2001, MNRAS, 328, 762
Edge, A. C. & Frayer, D. T. 2003, ApJ, 594, L13
Edge, A. C., Oonk, J. B. R., Mittal, R., et al. 2010, A&A, 518, L46
Edge, A. C., Stewart, G. C., Fabian, A. C., & Arnaud, K. A. 1990, MNRAS, 245, 559
Edge, A. C., Wilman, R. J., Johnstone, R. M., et al. 2002, MNRAS, 337, 49
Edwards, L. O. V., Robert, C., Mollá, M., & McGee, S. L. 2009, MNRAS, 396, 1953
Ehlert, S., Allen, S. W., von der Linden, A., et al. 2011a, MNRAS, 411, 1641
Ehlert, S., Allen, S. W., von der Linden, A., et al. 2011b, MNRAS, 411, 1641
Ensslin, T. A. & Brüggen, M. 2002, MNRAS, 331, 1011
Ensslin, T. A. & Gopal-Krishna. 2001, A&A, 366, 26
Erben, T., Schirmer, M., Dietrich, J. P., et al. 2005, Astronomische Nachrichten, 326, 432
Esquivel, A., Benjamin, R. A., Lazarian, A., Cho, J., & Leitner, S. N. 2006, ApJ, 648, 1043
Ettori, S. & Fabian, A. C. 2000, MNRAS, 317, L57
Fabian, A. C., Allen, S. W., Crawford, C. S., et al. 2002, MNRAS, 332, L50
Fabian, A. C., Johnstone, R. M., & Daines, S. J. 1994, MNRAS, 271, 737
Fabian, A. C., Johnstone, R. M., Sanders, J. S., et al. 2008, Nature, 454, 968
Fabian, A. C., Mushotzky, R. F., Nulsen, P. E. J., & Peterson, J. R. 2001, MNRAS, 321, L20
Fabian, A. C., Sanders, J. S., Allen, S. W., et al. 2003a, MNRAS, 344, L43
Fabian, A. C., Sanders, J. S., Crawford, C. S., et al. 2003b, MNRAS, 344, L48
Fabian, A. C., Sanders, J. S., Taylor, G. B., et al. 2006, MNRAS, 366, 417
Fabian, A. C., Sanders, J. S., Williams, R. J. R., et al. 2011, MNRAS, 417, 172
Fabjan, D., Borgani, S., Tornatore, L., et al. 2010, MNRAS, 401, 1670
Falcke, H., Rieke, M. J., Rieke, G. H., Simpson, C., & Wilson, A. S. 1998, ApJ, 494, L155
Farage, C. L., McGregor, P. J., & Dopita, M. A. 2012, ApJ, 747, 28
Feigelson, E. D., Wood, P. A. D., Schreier, E. J., Harris, D. E., & Reid, M. J. 1987, ApJ, 312, 101
Feldman, U. 1992, Phys. Scr, 46, 202
Feretti, L., Dallacasa, D., Govoni, F., et al. 1999, A&A, 344, 472
Ferland, G. J., Fabian, A. C., Hatch, N. A., et al. 2008, MNRAS, 386, L72
Ferland, G. J., Fabian, A. C., Hatch, N. A., et al. 2009, MNRAS, 392, 1475
Ferrarese, L., Ford, H. C., & Jaffe, W. 1996, ApJ, 470, 444
Ferrari, C., Govoni, F., Schindler, S., Bykov, A. M., & Rephaeli, Y. 2008, SSR, 134, 93
Field, G. B. 1965, ApJ, 142, 531
Ford, H. C. & Butcher, H. 1979, ApJS, 41, 147
Forman, W., Jones, C., Churazov, E., et al. 2007, ApJ, 665, 1057
Forman, W., Nulsen, P., Heinz, S., et al. 2005, ApJ, 635, 894
Foster, A. R., Ji, L., Smith, R. K., & Brickhouse, N. S. 2012, ApJ, 756, 128

Friedman, S. H., Heinz, S., & Churazov, E. 2012, ApJ, 746, 112
Fujimoto, R., Mitsuda, K., Mccammon, D., et al. 2007, PASJ, 59, 133
Fujita, Y., Hayashida, K., Nagai, M., et al. 2008a, PASJ, 60, 1133
Fujita, Y., Tawa, N., Hayashida, K., et al. 2008b, PASJ, 60, S343
Gaspari, M., Churazov, E., Nagai, D., Lau, E. T., & Zhuravleva, I. 2014, A&A, 569, A67
Gaspari, M., Ruszkowski, M., & Oh, S. P. 2013, MNRAS, 432, 3401
Gaspari, M., Ruszkowski, M., & Sharma, P. 2012, ApJ, 746, 94
Gastaldello, F., Buote, D. A., Temi, P., et al. 2009, ApJ, 693, 43
Gastaldello, F. & Molendi, S. 2004, ApJ, 600, 670
Gavazzi, G., Boselli, A., Vílchez, J. M., Iglesias-Paramo, J., & Bonfanti, C. 2000, A&A, 361, 1
Ghizzardi, S., De Grandi, S., & Molendi, S. 2014, A&A, 570, A117
Ghizzardi, S., Rossetti, M., & Molendi, S. 2010, A&A, 516, A32
Giacintucci, S., O'Sullivan, E., Clarke, T. E., et al. 2012, ApJ, 755, 172
Gilfanov, M. R., Sunyaev, R. A., & Churazov, E. M. 1987, Soviet Astronomy Letters, 13, 3
Gitti, M., Brighenti, F., & McNamara, B. R. 2012, Advances in Astronomy, 2012, 950641
Gladstone, G. R., Waite, J. H., Grodent, D., et al. 2002, Nature, 415, 1000
Gonzaléz-Riestra, R. 2004, http://xmm.vilspa.esa.es/docs/documents/CAL-TN-0058-1-0.ps.gz
Goudfrooij, P., Hansen, L., Jorgensen, H. E., & Norgaard-Nielsen, H. U. 1994, A&AS, 105, 341
Govoni, F., Dolag, K., Murgia, M., et al. 2010, A&A, 522, A105
Govoni, F., Murgia, M., Markevitch, M., et al. 2009, A&A, 499, 371
Greisen, E. W. 2003, Information Handling in Astronomy - Historical Vistas, 285, 109
Grevesse, N. & Sauval, A. J. 1998, Space Science Reviews, 85, 161
Gunn, J. E. & Gott, III, J. R. 1972, ApJ, 176, 1
Hamer, S. L., Edge, A. C., Swinbank, A. M., et al. 2012, MNRAS, 421, 3409
Hao, C.-N., Kennicutt, R. C., Johnson, B. D., et al. 2011, ApJ, 741, 124
Hasegawa, T., Wakamatsu, K.-i., Malkan, M., et al. 2000, MNRAS, 316, 326
Hatch, N. A., Crawford, C. S., Fabian, A. C., & Johnstone, R. M. 2005, MNRAS, 358, 765
Hatch, N. A., Crawford, C. S., Johnstone, R. M., & Fabian, A. C. 2006, MNRAS, 367, 433
Heckman, T. M. 1980, A&A, 87, 152
Heckman, T. M., Baum, S. A., van Breugel, W. J. M., & McCarthy, P. 1989, ApJ, 338, 48
Heinz, S. & Churazov, E. 2005, ApJ, 634, L141
Henry, J. P., Evrard, A. E., Hoekstra, H., Babul, A., & Mahdavi, A. 2008, ArXiv e-prints
Hicks, A. K. & Mushotzky, R. 2005, ApJ, 635, L9
Hines, D. C., Eilek, J. A., & Owen, F. N. 1989, ApJ, 347, 713
Ho, I.-T., Lim, J., & Dinh-V-Trung. 2009, ApJ, 698, 1191
Humphrey, P. J., Buote, D. A., Brighenti, F., Gebhardt, K., & Mathews, W. G. 2008, ApJ, 683, 161
Humphrey, P. J., Buote, D. A., Brighenti, F., Gebhardt, K., & Mathews, W. G. 2009, ApJ, 703, 1257
Humphrey, P. J., Buote, D. A., Gastaldello, F., et al. 2006, ApJ, 646, 899
Ichinohe, Y., Werner, N., Simionescu, A., et al. 2015, MNRAS, 448, 2971

Inogamov, N. A. & Sunyaev, R. A. 2003, Astronomy Letters, 29, 791
Irwin, J. A., Athey, A. E., & Bregman, J. N. 2003, ApJ, 587, 356
Jaffe, W. & Bremer, M. N. 1997, MNRAS, 284, L1
Jaffe, W., Bremer, M. N., & Baker, K. 2005, MNRAS, 360, 748
Jaffe, W., Bremer, M. N., & van der Werf, P. P. 2001, MNRAS, 324, 443
Jaffe, W., Ford, H. C., Ferrarese, L., van den Bosch, F., & O'Connell, R. W. 1993, Nature, 364, 213
Jaffe, W. & McNamara, B. R. 1994, ApJ, 434, 110
Jarrett, T. H., Chester, T., Cutri, R., Schneider, S. E., & Huchra, J. P. 2003, AJ, 125, 525
Johnstone, R. M., Fabian, A. C., & Nulsen, P. E. J. 1987, MNRAS, 224, 75
Johnstone, R. M., Hatch, N. A., Ferland, G. J., et al. 2007, MNRAS, 382, 1246
Jones, C., Forman, W., Vikhlinin, A., et al. 2002, ApJ, 567, L115
Kaastra, J. S., Ferrigno, C., Tamura, T., et al. 2001, A&A, 365, L99
Kaastra, J. S., Mewe, R., & Nieuwenhuijzen, H. 1996, in UV and X-ray Spectroscopy of Astrophysical and Laboratory Plasmas p.411, K. Yamashita and T. Watanabe. Tokyo : Universal Academy Press
Kaastra, J. S., Tamura, T., Peterson, J. R., et al. 2004, A&A, 413, 415
Kaiser, C. R. 2003, MNRAS, 343, 1319
Kalberla, P. M. W., Burton, W. B., Hartmann, D., et al. 2005, A&A, 440, 775
Kaufman, M. J., Wolfire, M. G., Hollenbach, D. J., & Luhman, M. L. 1999, ApJ, 527, 795
Kempner, J. C., Blanton, E. L., Clarke, T. E., et al. 2004, in The Riddle of Cooling Flows in Galaxies and Clusters of galaxies, ed. T. Reiprich, J. Kempner, & N. Soker
Kennicutt, Jr., R. C. 1998, ApJ, 498, 541
Keshet, U. 2012, ApJ, 753, 120
Keshet, U., Markevitch, M., Birnboim, Y., & Loeb, A. 2010, ApJ, 719, L74
Kewley, L. J., Groves, B., Kauffmann, G., & Heckman, T. 2006, MNRAS, 372, 961
Kim, D.-W. & Fabbiano, G. 2004, ApJ, 611, 846
Knapp, G. R., Faber, S. M., & Gallagher, J. S. 1978, AJ, 83, 11
Knapp, G. R., Guhathakurta, P., Kim, D.-W., & Jura, M. A. 1989, ApJS, 70, 329
Knapp, G. R., Turner, E. L., & Cunniffe, P. E. 1985, AJ, 90, 454
Krishna Kumar, C. & Thonnard, N. 1983, AJ, 88, 260
Kunz, M. W., Bogdanović, T., Reynolds, C. S., & Stone, J. M. 2012, ApJ, 754, 122
Kunz, M. W., Schekochihin, A. A., & Stone, J. M. 2014, Physical Review Letters, 112, 205003
Lake, G. & Schommer, R. A. 1984, ApJ, 280, 107
Large, M. I., Mills, B. Y., Little, A. G., Crawford, D. F., & Sutton, J. M. 1981, MNRAS, 194, 693
Lazarian, A., Kowal, G., Vishniac, E., & de Gouveia Dal Pino, E. 2011, Planet. Space Sci., 59, 537
Lazarian, A., Santos-Lima, R., & de Gouveia Dal Pino, E. 2010, in Astronomical Society of the Pacific Conference Series, Vol. 429, Numerical Modeling of Space Plasma Flows, Astronum-2009, ed. N. V. Pogorelov, E. Audit, & G. P. Zank, 113
Leccardi, A. & Molendi, S. 2008, A&A, 487, 461
Lim, J., Ohyama, Y., Chi-Hung, Y., Dinh-V-Trung, & Shiang-Yu, W. 2012, ApJ, 744, 112
Lisse, C. M., Dennerl, K., Englhauser, J., et al. 1996, Science, 274, 205

Liu, J., Mao, S., & Wang, Q. D. 2011, MNRAS, 415, L64
Liu, J., Wang, Q. D., & Mao, S. 2012, MNRAS, 420, 3389
Liuzzo, E., Taylor, G. B., Giovannini, G., & Giroletti, M. 2009, A&A, 501, 933
Lodders, K. 2003, ApJ, 591, 1220
Macchetto, F., Pastoriza, M., Caon, N., et al. 1996, A&AS, 120, 463
Machacek, M. E., O'Sullivan, E., Randall, S. W., Jones, C., & Forman, W. R. 2010, ApJ, 711, 1316
Madau, P., Ferguson, H. C., Dickinson, M. E., et al. 1996, MNRAS, 283, 1388
Magorrian, J., Tremaine, S., Richstone, D., et al. 1998, AJ, 115, 2285
Maia, M. A. G., da Costa, L. N., Willmer, C., Pellegrini, P. S., & Rite, C. 1987, AJ, 93, 546
Malhotra, S., Helou, G., Stacey, G., et al. 1997, ApJ, 491, L27
Malhotra, S., Kaufman, M. J., Hollenbach, D., et al. 2001, ApJ, 561, 766
Malyshkin, L. 2001, ApJ, 554, 561
Mannucci, F., Della Valle, M., & Panagia, N. 2006, MNRAS, 370, 773
Mantz, A., Allen, S. W., Ebeling, H., & Rapetti, D. 2008, MNRAS, 387, 1179
Maoz, D., Mannucci, F., & Brandt, T. D. 2012, MNRAS, 426, 3282
Markevitch, M., Mazzotta, P., Vikhlinin, A., et al. 2003, ApJ, 586, L19
Markevitch, M., Ponman, T. J., Nulsen, P. E. J., et al. 2000, ApJ, 541, 542
Markevitch, M. & Vikhlinin, A. 2007, Phys. Rep., 443, 1
Markevitch, M., Vikhlinin, A., & Mazzotta, P. 2001, ApJ, 562, L153
Mathews, W. G. 1990, ApJ, 354, 468
Mathews, W. G. & Brighenti, F. 2003, ARA&A, 41, 191
Mathews, W. G., Temi, P., Brighenti, F., & Amblard, A. 2013, ApJ, 768, 28
Matsushita, K. 2011, A&A, 527, A134
Matsushita, K., Belsole, E., Finoguenov, A., & Böhringer, H. 2002, A&A, 386, 77
Matsushita, K., Sakuma, E., Sasaki, T., Sato, K., & Simionescu, A. 2013, ApJ, 764, 147
Matsuzawa, H., Matsuoka, M., Ikebe, Y., Mihara, T., & Yamashita, K. 1996, PASJ, 48, 565
Mauch, T., Murphy, T., Buttery, H. J., et al. 2003, MNRAS, 342, 1117
Maughan, B. J., Jones, C., Forman, W., & Van Speybroeck, L. 2008, ApJS, 174, 117
Mazzotta, P. & Giacintucci, S. 2008, ApJ, 675, L9
McCourt, M., Sharma, P., Quataert, E., & Parrish, I. J. 2012, MNRAS, 419, 3319
McDonald, M. & Veilleux, S. 2009, ApJ, 703, L172
McDonald, M., Veilleux, S., Rupke, D. S. N., & Mushotzky, R. 2010, ApJ, 721, 1262
McDonald, M., Wei, L. H., & Veilleux, S. 2012, ApJ, 755, L24
McDonald, M., Werner, N., Oonk, J. B. R., & Veilleux, S. 2015, ApJ, 804, 16
McMullin, J. P., Waters, B., Schiebel, D., Young, W., & Golap, K. 2007, in Astronomical Society of the Pacific Conference Series, Vol. 376, Astronomical Data Analysis Software and Systems XVI, ed. R. A. Shaw, F. Hill, & D. J. Bell, 127
McNamara, B. R. & Nulsen, P. E. J. 2007, ARA&A, 45, 117
McNamara, B. R., Nulsen, P. E. J., Wise, M. W., et al. 2005, Nature, 433, 45
McNamara, B. R., Russell, H. R., Nulsen, P. E. J., et al. 2013, ArXiv e-prints
Merloni, A., Heinz, S., & di Matteo, T. 2003, MNRAS, 345, 1057
Million, E. T. & Allen, S. W. 2009, MNRAS, 399, 1307
Million, E. T., Allen, S. W., Werner, N., & Taylor, G. B. 2010a, MNRAS, 405, 1624

Million, E. T., Allen, S. W., Werner, N., & Taylor, G. B. 2010b, MNRAS, 405, 1624
Million, E. T., Allen, S. W., Werner, N., & Taylor, G. B. 2010c, MNRAS, 405, 1624
Million, E. T., Werner, N., Simionescu, A., et al. 2010d, MNRAS, 407, 2046
Mittal, R., O'Dea, C. P., Ferland, G., et al. 2011, MNRAS, 418, 2386
Mittal, R., Oonk, J. B. R., Ferland, G. J., et al. 2012, ArXiv e-prints
Molendi, S. 2002, ApJ, 580, 815
Morganti, R., Fogasy, J., Paragi, Z., Oosterloo, T., & Orienti, M. 2013, ArXiv e-prints
Moustakas, J., Kennicutt, Jr., R. C., Tremonti, C. A., et al. 2010, ApJS, 190, 233
Murgia, M., Eckert, D., Govoni, F., et al. 2010, A&A, 514, A76
Murgia, M., Govoni, F., Markevitch, M., et al. 2009, A&A, 499, 679
Nagai, D., Vikhlinin, A., & Kravtsov, A. V. 2007, ApJ, 655, 98
Narayan, R. & Medvedev, M. V. 2001, ApJ, 562, L129
Norman, C. A., Melrose, D. B., & Achterberg, A. 1995, ApJ, 454, 60
Nulsen, P. E. J. 1986, MNRAS, 221, 377
Nulsen, P. E. J. & McNamara, B. R. 2013, Astronomische Nachrichten, 334, 386
Nulsen, P. E. J., McNamara, B. R., Wise, M. W., & David, L. P. 2005, ApJ, 628, 629
O'Dea, C. P., Baum, S. A., Privon, G., et al. 2008, ApJ, 681, 1035
Ogrean, G., van Weeren, R., Jones, C., et al. 2015, arXiv: 1505.05560
Ogrean, G. A., Hatch, N. A., Simionescu, A., et al. 2010, MNRAS, 406, 354
Oonk, J. B. R. 2011, PhD thesis, Ph. D. thesis, University of Leiden (2011). Advisor: W. Jaffe. ISBN: 9789461910318. pp. 226
Oonk, J. B. R., Jaffe, W., Bremer, M. N., & van Weeren, R. J. 2010, MNRAS, 405, 898
Osterbrock, D. E. & Ferland, G. J. 2006, Astrophysics of gaseous nebulae and active galactic nuclei
O'Sullivan, E., David, L. P., & Vrtilek, J. M. 2013, ArXiv e-prints
O'Sullivan, E., Forbes, D. A., & Ponman, T. J. 2001, MNRAS, 328, 461
O'Sullivan, E., Ponman, T. J., & Collins, R. S. 2003, MNRAS, 340, 1375
O'Sullivan, E., Worrall, D. M., Birkinshaw, M., et al. 2011, MNRAS, 1180
Owen, F. N., Eilek, J. A., & Kassim, N. E. 2000, ApJ, 543, 611
Owen, F. N., Eilek, J. A., & Keel, W. C. 1990, ApJ, 362, 449
Owers, M. S., Nulsen, P. E. J., Couch, W. J., & Markevitch, M. 2009, ApJ, 704, 1349
Panagoulia, E. K., Fabian, A. C., & Sanders, J. S. 2014, MNRAS, 438, 2341
Panuzzo, P., Rampazzo, R., Bressan, A., et al. 2011, A&A, 528, A10
Parriott, J. R. & Bregman, J. N. 2008, ApJ, 681, 1215
Parrish, I. J. & Quataert, E. 2008, ApJ, 677, L9
Parrish, I. J., Quataert, E., & Sharma, P. 2009, ApJ, 703, 96
Parrish, I. J., Quataert, E., & Sharma, P. 2010, ApJ, 712, L194
Peterson, J. R. & Fabian, A. C. 2006, Phys. Rep., 427, 1
Pilbratt, G. L., Riedinger, J. R., Passvogel, T., et al. 2010, A&A, 518, L1
Poglitsch, A., Waelkens, C., Geis, N., et al. 2010, A&A, 518, L2
Pollack, L. K., Taylor, G. B., & Allen, S. W. 2005, MNRAS, 359, 1229
Poole, G. B., Babul, A., McCarthy, I. G., Sanderson, A. J. R., & Fardal, M. A. 2008, MNRAS, 391, 1163
Pratt, G. W., Arnaud, M., Piffaretti, R., et al. 2010, A&A, 511, A85+
Pratt, G. W., Arnaud, M., & Pointecouteau, E. 2006, A&A, 446, 429

Quataert, E. 2008, ApJ, 673, 758
Quillen, A. C., Zufelt, N., Park, J., et al. 2008, ApJS, 176, 39
Rafferty, D. A., McNamara, B. R., & Nulsen, P. E. J. 2008, ApJ, 687, 899
Rafferty, D. A., McNamara, B. R., Nulsen, P. E. J., & Wise, M. W. 2006, ApJ, 652, 216
Randall, S. W., Forman, W. R., Giacintucci, S., et al. 2011a, ApJ, 726, 86
Randall, S. W., Forman, W. R., Giacintucci, S., et al. 2011b, ApJ, 726, 86
Rawle, T. D., Edge, A. C., Egami, E., et al. 2012, ApJ, 747, 29
Rebusco, P., Churazov, E., Sunyaev, R., Böhringer, H., & Forman, W. 2008, MNRAS, 384, 1511
Reiprich, T. H. & Böhringer, H. 2002, ApJ, 567, 716
Reiss, I. & Keshet, U. 2014, Physical Review Letters, 113, 071302
Revaz, Y., Combes, F., & Salomé, P. 2008, A&A, 477, L33
Rickes, M. G., Pastoriza, M. G., & Bonatto, C. 2004, A&A, 419, 449
Robertson, I. P., Cravens, T. E., Snowden, S., & Linde, T. 2001, Space Sci. Rev., 97, 401
Roediger, E., Brüggen, M., Simionescu, A., et al. 2011, MNRAS, 413, 2057
Roediger, E., Kraft, R. P., Forman, W. R., Nulsen, P. E. J., & Churazov, E. 2013, ApJ, 764, 60
Roediger, E., Kraft, R. P., Machacek, M. E., et al. 2012, ApJ, 754, 147
Roediger, E., Kraft, R. P., Nulsen, P. E. J., et al. 2015, ApJ, 806, 104
Roediger, E. & Zuhone, J. A. 2012, MNRAS, 419, 1338
Rossetti, M., Eckert, D., De Grandi, S., et al. 2013, A&A, 556, A44
Russell, H. R., McNamara, B. R., Edge, A. C., et al. 2013a, MNRAS, 432, 530
Russell, H. R., McNamara, B. R., Edge, A. C., et al. 2013b, ArXiv e-prints
Russell, H. R., McNamara, B. R., Sanders, J. S., et al. 2012, MNRAS, 423, 236
Ruszkowski, M., Brüggen, M., & Begelman, M. C. 2004a, ApJ, 611, 158
Ruszkowski, M., Brüggen, M., & Begelman, M. C. 2004b, ApJ, 615, 675
Sakelliou, I., Peterson, J. R., Tamura, T., et al. 2002, A&A, 391, 903
Salomé, P. & Combes, F. 2003, A&A, 412, 657
Salomé, P. & Combes, F. 2008, A&A, 489, 101
Salomé, P., Combes, F., Edge, A. C., et al. 2006, A&A, 454, 437
Salomé, P., Combes, F., Revaz, Y., et al. 2011, A&A, 531, A85
Salomé, P., Revaz, Y., Combes, F., et al. 2008, A&A, 483, 793
Sanders, J. S. 2006, MNRAS, 371, 829
Sanders, J. S. & Fabian, A. C. 2002, MNRAS, 331, 273
Sanders, J. S. & Fabian, A. C. 2006, MNRAS, 371, 1483
Sanders, J. S. & Fabian, A. C. 2007, MNRAS, 381, 1381
Sanders, J. S. & Fabian, A. C. 2008, MNRAS, 390, L93
Sanders, J. S. & Fabian, A. C. 2011, MNRAS, 412, L35
Sanders, J. S. & Fabian, A. C. 2012, MNRAS, 421, 726
Sanders, J. S. & Fabian, A. C. 2013, MNRAS, 429, 2727
Sanders, J. S., Fabian, A. C., Allen, S. W., et al. 2008, MNRAS, 385, 1186
Sanders, J. S., Fabian, A. C., Allen, S. W., & Schmidt, R. W. 2004, MNRAS, 349, 952
Sanders, J. S., Fabian, A. C., Frank, K. A., Peterson, J. R., & Russell, H. R. 2010a, MNRAS, 402, 127
Sanders, J. S., Fabian, A. C., Smith, R. K., & Peterson, J. R. 2010b, MNRAS, 402, L11

Sanders, J. S., Fabian, A. C., & Taylor, G. B. 2009, MNRAS, 396, 1449
Sanders, J. S., Fabian, A. C., Taylor, G. B., et al. 2016, [arXiv: 1601.01489]
Scannapieco, E. & Brüggen, M. 2008, ApJ, 686, 927
Schekochihin, A. A., Cowley, S. C., Kulsrud, R. M., Hammett, G. W., & Sharma, P. 2005, ApJ, 629, 139
Schekochihin, A. A., Cowley, S. C., Kulsrud, R. M., Rosin, M. S., & Heinemann, T. 2008, Physical Review Letters, 100, 081301
Schuecker, P., Finoguenov, A., Miniati, F., Böhringer, H., & Briel, U. G. 2004, A&A, 426, 387
Schure, K. M., Kosenko, D., Kaastra, J. S., Keppens, R., & Vink, J. 2009, A&A, 508, 751
Serra, P. & Oosterloo, T. A. 2010, MNRAS, 401, L29
Sharma, P., McCourt, M., Quataert, E., & Parrish, I. J. 2012a, MNRAS, 420, 3174
Sharma, P., McCourt, M., Quataert, E., & Parrish, I. J. 2012b, MNRAS, 420, 3174
Sharma, P., Parrish, I. J., & Quataert, E. 2010, ApJ, 720, 652
Shepherd, M. C., Pearson, T. J., & Taylor, G. B. 1995, in Bulletin of the American Astronomical Society, Vol. 27, Bulletin of the American Astronomical Society, ed. B. J. Butler & D. O. Muhleman, 903–+
Shurkin, K., Dunn, R. J. H., Gentile, G., Taylor, G. B., & Allen, S. W. 2008, MNRAS, 383, 923
Sijacki, D., Springel, V., Di Matteo, T., & Hernquist, L. 2007, MNRAS, 380, 877
Silk, J. & Rees, M. J. 1998, A&A, 331, L1
Simionescu, A., Allen, S. W., Mantz, A., et al. 2011, Science, 331, 1576
Simionescu, A., Böhringer, H., Brüggen, M., & Finoguenov, A. 2007, A&A, 465, 749
Simionescu, A., Roediger, E., Nulsen, P. E. J., et al. 2009a, A&A, 495, 721
Simionescu, A., Werner, N., Böhringer, H., et al. 2009b, A&A, 493, 409
Simionescu, A., Werner, N., Finoguenov, A., Böhringer, H., & Brüggen, M. 2008, A&A, 482, 97
Simionescu, A., Werner, N., Forman, W. R., et al. 2010, MNRAS, 405, 91
Simionescu, A., Werner, N., Urban, O., et al. 2013, ApJ, 775, 4
Simionescu, A., Werner, N., Urban, O., et al. 2012, ApJ, 757, 182
Simionescu, A., Werner, N., Urban, O., et al. 2015, ApJ, 811, L25
Sirothia, S. K. 2009, MNRAS, 398, 853
Smith, M. W. L., Gomez, H. L., Eales, S. A., et al. 2012, ApJ, 748, 123
Smith, R. K., Brickhouse, N. S., Liedahl, D. A., & Raymond, J. C. 2001, ApJ, 556, L91
Soker, N., Blanton, E. L., & Sarazin, C. L. 2004, A&A, 422, 445
Sparks, W. B., Donahue, M., Jordán, A., Ferrarese, L., & Côté, P. 2004, ApJ, 607, 294
Sparks, W. B., Ford, H. C., & Kinney, A. L. 1993, ApJ, 413, 531
Sparks, W. B., Pringle, J. E., Carswell, R. F., et al. 2012, ApJ, 750, L5
Sparks, W. B., Pringle, J. E., Donahue, M., et al. 2009, ApJ, 704, L20
Spitzer, L. 1962, Physics of Fully Ionized Gases (New York: Interscience (2nd edition))
Stacey, G. J., Geis, N., Genzel, R., et al. 1991, ApJ, 373, 423
Stone, J. M., Gardiner, T. A., Teuben, P., Hawley, J. F., & Simon, J. B. 2008, ApJS, 178, 137
Sun, M. 2009, ApJ, 704, 1586
Sun, M., Donahue, M., & Voit, G. M. 2007, ApJ, 671, 190

Sun, M., Voit, G. M., Donahue, M., et al. 2009, ApJ, 693, 1142
Sunyaev, R. A., Norman, M. L., & Bryan, G. L. 2003, Astronomy Letters, 29, 783
Sutherland, R. S. & Dopita, M. A. 1993, ApJS, 88, 253
Tamura, T., Bleeker, J. A. M., Kaastra, J. S., Ferrigno, C., & Molendi, S. 2001, A&A, 379, 107
Tamura, T., Kaastra, J. S., Makishima, K., & Takahashi, I. 2003, A&A, 399, 497
Taylor, G. B. 1996, ApJ, 470, 394
Taylor, G. B., Barton, E. J., & Ge, J. 1994, AJ, 107, 1942
Taylor, G. B., Fabian, A. C., Gentile, G., et al. 2007, MNRAS, 382, 67
Taylor, G. B., Govoni, F., Allen, S. W., & Fabian, A. C. 2001, MNRAS, 326, 2
Temi, P., Brighenti, F., & Mathews, W. G. 2007a, ApJ, 660, 1215
Temi, P., Brighenti, F., & Mathews, W. G. 2007b, ApJ, 666, 222
Tittley, E. R. & Henriksen, M. 2005, ApJ, 618, 227
Tonry, J. L., Dressler, A., Blakeslee, J. P., et al. 2001, ApJ, 546, 681
Tremblay, G. R., Chiaberge, M., Sparks, W. B., et al. 2009, ApJS, 183, 278
Turk, M. J., Smith, B. D., Oishi, J. S., et al. 2011, ApJS, 192, 9
Urban, O., Simionescu, A., Werner, N., et al. 2014, MNRAS, 437, 3939
Urban, O., Werner, N., Simionescu, A., Allen, S. W., & Böhringer, H. 2011, MNRAS, 414, 2101
van Weeren, R. J., Röttgering, H. J. A., Brüggen, M., & Cohen, A. 2009, A&A, 508, 75
Vantyghem, A. N., McNamara, B. R., Russell, H. R., et al. 2014, MNRAS, 442, 3192
Vikhlinin, A., Kravtsov, A. V., Burenin, R. A., et al. 2008, ArXiv e-prints
Vikhlinin, A., Markevitch, M., & Murray, S. S. 2001a, ApJ, 551, 160
Vikhlinin, A., Markevitch, M., & Murray, S. S. 2001b, ApJ, 549, L47
Vikhlinin, A., Markevitch, M., Murray, S. S., et al. 2005, ApJ, 628, 655
Vikhlinin, A. A. & Markevitch, M. L. 2002, Astronomy Letters, 28, 495
Voit, G. M., Cavagnolo, K. W., Donahue, M., et al. 2008, ApJ, 681, L5
Voit, G. M. & Donahue, M. 2011, ApJ, 738, L24
Voit, G. M., Kay, S. T., & Bryan, G. L. 2005, MNRAS, 364, 909
Wagner, A. Y. & Bicknell, G. V. 2011, ApJ, 728, 29
Wagner, A. Y., Bicknell, G. V., & Umemura, M. 2012, ApJ, 757, 136
Wakamatsu, K., Malkan, M. A., Nishida, M. T., et al. 2005, in Astronomical Society of the Pacific Conference Series, Vol. 329, Nearby Large-Scale Structures and the Zone of Avoidance, ed. A. P. Fairall & P. A. Woudt, 189
Walker, S. A., Fabian, A. C., & Kosec, P. 2014, MNRAS, 445, 3444
Wargelin, B. J., Markevitch, M., Juda, M., et al. 2004, ApJ, 607, 596
Werner, N., Allen, S. W., & Simionescu, A. 2012, MNRAS, 425, 2731
Werner, N., Böhringer, H., Kaastra, J. S., et al. 2006, A&A, 459, 353
Werner, N., Durret, F., Ohashi, T., Schindler, S., & Wiersma, R. P. C. 2008, Space Sci. Rev., 134, 337
Werner, N., Kaastra, J. S., Takei, Y., et al. 2007, A&A, 468, 849
Werner, N., Oonk, J. B. R., Canning, R. E. A., et al. 2013, ApJ, 767, 153
Werner, N., Simionescu, A., Million, E. T., et al. 2010, MNRAS, 407, 2063
Werner, N., Sun, M., Bagchi, J., et al. 2011, MNRAS, 415, 3369
Werner, N., Zhuravleva, I., Churazov, E., et al. 2009, MNRAS, 398, 23

Werner, N., ZuHone, J. A., Zhuravleva, I., et al. 2016, MNRAS, 455, 846
Xiang, F., Churazov, E., Dolag, K., Springel, V., & Vikhlinin, A. 2007, MNRAS, 379, 1325
Xu, H., Kahn, S. M., Peterson, J. R., et al. 2002, ApJ, 579, 600
Young, A. J., Wilson, A. S., & Mundell, C. G. 2002, ApJ, 579, 560
Zhuravleva, I., Churazov, E., Arevalo, P., et al. 2015, arXiv: 1501.07271
Zhuravleva, I., Churazov, E., Arevalo, P., et al. 2016, ArXiv e-prints
Zhuravleva, I., Churazov, E., Schekochihin, A. A., et al. 2014a, Nature, 515, 85
Zhuravleva, I., Churazov, E. M., Schekochihin, A. A., et al. 2014b, ApJ, 788, L13
ZuHone, J. A., Kunz, M. W., Markevitch, M., Stone, J. M., & Biffi, V. 2015, ApJ, 798, 90
ZuHone, J. A., Markevitch, M., & Johnson, R. E. 2010, ApJ, 717, 908
ZuHone, J. A., Markevitch, M., & Lee, D. 2011, ApJ, 743, 16
ZuHone, J. A., Markevitch, M., Ruszkowski, M., & Lee, D. 2013, ApJ, 762, 69